ASTERO–ARCHAEOLGY: READING THE GALACTIC HISTORY RECORDED IN THE WHITE DWARF STARS

by

Matthew Alan Wood, B.Sci., M.A.

DISSERTATION

Presented to the Faculty of the Graduate School of
The University of Texas as Austin
in Partial Fulfillment
for the Degree of

DOCTOR OF PHILOSOPHY
THE UNIVERSITY OF TEXAS AT AUSTIN
May 1990

Astero–Archaeology: Reading The Galactic History Recorded in the White Dwarf Stars

Approved By

Supervisory Committee:

D. E. Winget

Gilles Fontaine

A. M. Van Horn

R. E. Mather

J. Craig Wheeler

When we try to pick out anything by itself, we find it hitched to everything else in the universe.

— John Muir

ACKNOWLEDGMENTS

I would like to take a few words to thank those who helped me make this work possible. First, of course, I thank my wife, Clara, who has been a great stabilizing influence on me — I cannot thank her enough for her love and support. I must thank my parents for always being there, and for always allowing me (encouraging me) to make my own decisions and then for respecting those decisions unconditionally. I couldn't have wished for a better mom and dad. The rest of my family has also been a continual source of enthusiasm and support, and no doubt they underestimate the positive influence they have had on my life.

Graduate school in astronomy is in many respects an apprentice system. I have been fortunate to have had as mentors two great men, Don Winget and Ed Nather. Don, my formal advisor, has always been a source of inspiration to me, and I only hope that over the years I can give back to him some small measure of all that he's given me. He's a good friend and an outstanding scientist. Ed, although not officially my advisor, has nonetheless been just that alongside Don. Being at an age when some are ruefully considering retirement and many more have already retired on the job, Ed is "in the trenches" doing science the world over as he orchestrates his most recent scientific achievement, The Whole Earth Telescope. Like Don a leader by example, Ed too is a source of inspiration. What a guy. What a team.

I would like to thank Pierre Bergeron, Rex Saffer, and Jim Liebert for kindly sending me their data in advance of publication — they and the rest

of the "good guys" make the white dwarf community a pleasant place to live and work.

I would like to thank all the friends I have made in the Astronomy Department at The University of Texas. You are all fine people and I will miss you.

Finally, I thank the NASA Graduate Student Researchers Program for providing financial support for the last three years.

Preface

A few words on the structure of this thesis are warranted before you begin reading. This work is approximately equally divided into two Parts. Part I concerns the details of white dwarf evolution and spans chapters 1 through 5. Chapters 6 and 7 make up Part II, and in these I discuss the information obtainable from the white dwarf luminosity function; specifically, the age and evolution of the Galactic disk and halo.

Because Parts I and II are to be submitted separately for publication (after suitable modifications have been made) it is inevitable that there is some measure of repetition, although I have tried to keep this to a minimum as much as possible. While Part I is to be a multi-author paper, Part II is to be a single author paper. Because of this, the voice changes upon going between parts from first person plural to first person singular.

ASTERO–ARCHAEOLGY: READING THE
GALACTIC HISTORY RECORDED IN
THE WHITE DWARF STARS

Publication No. ———

Matthew Alan Wood, Ph.D.
The University of Texas at Austin, 1990

Supervising Professors: Donald E. Winget and Gilles Fontaine

Galactic history is written in its oldest stars, the white dwarfs. Although we are still some years away from reading the details of that history, we can already place significant limits on both the Galactic age and star formation history. The following is a complete analysis of the problem, starting with a fresh exploration of the physics of white dwarf stars. I present an extensive grid of numerical model sequences and use these to describe in detail the behavior of the white dwarf stars as a function of mass, core composition, surface layer masses and compositions, and uncertainties in the constitutive physics.

In the second part of this work, I use these model sequences to decode the information contained in the white dwarf luminosity function. I establish a theoretical context for current and future observations by presenting luminosity functions computed with differing choices for the input white dwarf evolutionary sequences, the assumed age of the local disk, the star formation

rate as a function of time, and the possibility of scale height inflation of the disk with time. The results suggest that the star formation rate over the history of the Galaxy has been constant to within an order of magnitude, and that conservatively, the disk age lies in the range 6–13.5 Gyr. The principle uncertainties are the core composition and surface helium layer mass, which seismological observations will remove in the near future. Using the best *current* estimates as input, the disk ages range from 8–11 Gyr — *i.e.*, substantially younger than most estimates for the halo globular clusters but in reasonable agreement with those for the disk globular clusters and open clusters. Within the next decade, luminosity functions will be determined for the halo white dwarfs, and comparison with the theoretical halo luminosity functions herein will determine the relative ages and star formation histories of the two populations.

Finally, I discuss white dwarf cosmochronology within the context of other, conflicting, methods of cosmochronology. I show how this work can help resolve these conflicts and shed light on fundamental problems in galaxy formation and cosmology.

Table of Contents

List of Figures

1. The Physics of White Dwarf Stars

1.1 Introduction

Considerable strides have been made in recent years in our understanding of the evolution of white dwarf stars and their importance to the overall picture of stellar and Galactic evolution. Ever improving observational and theoretical studies have allowed us to determine that these cooling embers of prior nuclear burning are a remarkably homogeneous class. It at first appears that there is a clear division by spectral type, as ~80% have spectra dominated by strong hydrogen lines in the absence of helium (type DA, using the nomenclature of Sion *et al.* 1983) and most of the remaining ~20% show lines of helium in the apparent absence of hydrogen (type DB, or more generally type non-DA). However, the mass functions derived for *both* spectral classes are similarly narrow ($\sigma \sim 0.1$) and peak at a mass of roughly 0.55 $M_\odot$ (Koester, Shultz and Weidemann 1979; Shipman and Sass 1980; Weidemann and Koester 1984; Oke, Weidemann and Koester 1984; McMahan 1989; Bergeron, Saffer, and Liebert 1990). Further, the observed ratio of DAs to non-DAs is a strong function of effective temperature (*e.g.*, Greenstein 1984, Fontaine and Wesemael 1987), leading some to suggest that a significant fraction of the white dwarf stars have their dominant photospheric constituent change as they evolve along the cooling track — a

process that has come to be known as spectral evolution (see Fontaine and Wesemael 1987).

The discovered turndown in the white dwarf luminosity function near $\log(L/L_{\odot}) \approx -4.5$ (Liebert 1979; Liebert, Dahn, and Monet 1988, 1989) reflects the beginning of Galactic star formation history (Winget *et al.* 1987). Preliminary fitting of theoretical luminosity functions to the turndown suggest that the onset of sustained star formation occurred approximately 9×10^9 years (9 Gyr) ago (Winget *et al.* 1987; Iben and Laughlin 1989; Yuan 1989; Wood 1990). Although nominally this age is determined for a sample of nearby white dwarf stars, the ellipticity of stellar orbits in the Galactic potential (see, for example, Carney *et al.* 1990) essentially guarantees that this age is in fact representative of a wide annulus of the Galactic disk at our galactocentric radius. The recent broad-based surge of interest in white dwarf evolution stems largely from its application to the problem of the age and evolution of the Galaxy. The method of using white dwarfs as cosmochronometers is particularly appealing because observations of rates of period change in the *pulsating* white dwarf stars will provide solid observational constraints to the problem at the temperatures of the two white dwarf instability strips, as has already been obtained for the pulsating pre-white dwarf PG1159-035 (Winget *et al.* 1985).

A primary component of these studies is the *theoretical model sequences* against which the observations can be compared. A number of researchers have published their numerical model sequence results, including: Vila (1971); Koester (1972); Lamb and Van Horn (1975); Kovetz and Shaviv (1976); Sweeney (1976); and more recently Iben and Tutukov (1984); Iben and MacDonald (1985, 1986); Koester and Schönberner (1986); Mazzitelli and D'Antona (1986); D'Antona and Mazzitelli (1989); Wood, Winget, and

Van Horn (1987); Wood and Winget (1989); and Tassoul, Fontaine, and Winget (1990). The physics of white dwarf evolution has been reviewed most recently by D'Antona and Mazzitelli (1990) and Koester and Chanmugam (1990). The variety among the calculated sequences is wide enough that a meaningful comparison is difficult to make. However, Winget and Van Horn (1987) determined the differential effects of the various constitutive physics and input model parameter choices on the ages of the models at the luminosity function turndown. Using a simple first-order perturbational approach, they found that the differences among research groups are understandable and are attributable to the different assumptions that people made in constructing their models. This suggests that we are well on our way towards converging to an agreed-upon cooling theory.

In this work, we present the results of an extensive numerical exploration into the details of white dwarf evolution. We hope to provide a complete and varied picture of all stages of evolution, and further hope that through your perusal of the numerous figures your intuition into the physics of the fundamental cooling process will be sharpened and invigorated. Our method is perturbational in that we sample each input parameter over the range that it is uncertain or unknown and then intercompare the results of a large number of sequences to shape our working model for the overall picture of white dwarf evolution. In the model sequences that we present, we vary the stellar masses between 0.4 $M_{\odot}$ and 1.2 $M_{\odot}$, vary the core composition between carbon and oxygen, and vary the masses of the surface helium and hydrogen layers over the ranges of plausible values. In addition, we also explore the effects on the age–luminosity relation of uncertainties in the opacities (radiative and conductive) and in the process of crystallization. To fill a long-standing void in the literature, we include a large set of these

evolutionary summary results in tabulated form in the Appendix. As a prelude to planned major observational surveys it is our hope that these calculations may be of some use to guide them. Finally, as the observational constraints tighten-up, the parameters nature has selected will be a subset of our calculations, and this work will provide a context within which to interpret them.

1.2 Historical Background

1.2.1 *Discovery Observations*

As discussed by Schatzman (1958), it was in 1910 that H. N. Russell and his benefactor E. C. Pickering first noted the peculiar nature of the star 40 Eridani B, which had been observed as part of a parallax program. They found that although the star was of spectral type A, it had the luminosity of an M dwarf. It was not until 1915 that this information was published as a footnote by Hertzsprung (1915), and in the intervening time the spectrum of Van Maanan 2 (Van Maanan 1913) and that of Sirius B (Adams 1914, 1915) were published. Adams, knowing the distance to Sirius and the surface temperature of Sirius B, was able to derive a radius for the object of order 10^9 cm — nearly two orders of magnitude smaller than the Sun. This radius estimate when combined with the mass determined from the orbit, lead Eddington to write in *The Internal Constitution of the Stars*, "Adams ... has confirmed our suspicion that matter 2000 times denser than platinum is not only possible, but is actually present in the Universe." Eddington further realized that although only three white dwarf stars were then currently known, their proximity to the Sun and their intrinsic faintness suggested

that their total space density was likely to be quite high (contemporary estimates are $N_{\rm WD} \approx 3.2 \times 10^{-3}$ pc^{-3}; Liebert, Dahn, and Monet 1988). These first three objects, all with surface temperatures a few times Solar and luminosities roughly one-onehundredth Solar, initially defined the class and gave rise to the somewhat misleading name *white dwarf stars.*

1.2.2 *The Electron Degeneracy of the White Dwarf Stars*

The theoretical explanation of the nature of the white dwarf stars was presented by Fowler in his landmark 1926 paper entitled "Dense Matter," Fowler used the Fermi-Dirac statistics (Dirac 1926) to solve the puzzle of the white dwarf support mechanism by suggesting that it arises from the *degenerate pressure of electrons.* In presenting the equations describing electron degeneracy we follow Chandrasekhar (1984), but also recommend Chandrasekhar (1939), Clayton (1968), and Hansen and Kawaler (1990) for more detailed discussions.

In a completely degenerate gas (the idealized "zero-temperature" degenerate gas), all energy states up to a threshold momentum p_0 (called the Fermi momentum) are occupied as described by the Pauli exclusion principle: two electrons only (one for each spin orientation) can occupy each phase-space cell of volume h^3 in any isolated quantum mechanical system. Under terrestrial conditions atoms are themselves largely isolated quantum-mechanical systems. Their electron clouds are composed of discrete energy levels called orbitals, and each orbital is occupied by at most two electrons. In contrast to terrestrial standards, the conditions in white dwarf interiors are extreme. The atoms are compressed so tightly that they become completely pressure ionized: nearly all of the electrons are shared equally among nearly all of

the nuclei, and *the entire star becomes an isolated quantum-mechanical system.* Even though the separation between "energy levels" is of the order of order Plank's constant $h = 6.626 \cdot 10^{-27}$ erg s, the sheer number of electrons ($\sim 10^{58}$) insures that those with the highest energies are moving at near light speed and carrying considerable momentum, and so are able to provide support against collapse through a balancing of the gravitational and electric fields. As Fowler wrote in summing up his 1926 paper (see Chandrasekhar 1984):

> The black-dwarf material is best likened to a single gigantic molecule in its lowest quantum state. On the Fermi-Dirac statistics, its high density can be achieved in one and only one way, in virtue of a correspondingly great energy content. But this energy can no more be expended in radiation than the energy of a normal atom or molecule. The only difference between black-dwarf matter and a normal molecule is that the molecule can exist in a free state while the black-dwarf matter can only so exist under very high external pressure.

More quantitatively, if $n(p)dp$ is the number of electrons per unit volume which have momenta between p and $p + dp$, then the condition of complete degeneracy is expressed by

$$n(p) = \begin{cases} \frac{8\pi}{h^3}\, p^2, & p \leq p_0; \\ 0 & p > p_0. \end{cases} \tag{1.1}$$

where the Fermi momentum p_0 is determined by the total number n of electrons per unit volume

$$n = \int_0^{p_0} n(p)\ dp = \frac{8\pi}{3h^3} p_0^3. \tag{1.2}$$

In the completely-degenerate gas, the pressure is given by

$$P = \frac{8\pi}{3h^3} \int_0^{p_0} p^3 v_p dp, \tag{1.3}$$

where in general

$$v = \frac{\partial E}{\partial p} \tag{1.4}$$

and where in the non-relativistic regime we can use $v = p/m$ to find

$$P_{\rm nr} = \frac{8\pi}{15mh^3} p_0^3, \tag{1.5}$$

or,

$$P_{\rm nr} = \frac{h^2}{20m} \left(\frac{3}{\pi}\right)^{2/3} n_e^{5/3} \tag{1.6}$$

$$= 1.004 \cdot 10^{13} \left(\frac{\rho}{\mu_e}\right)^{5/3} \text{ dynes cm}^{-2} \tag{1.7}$$

where m is the rest mass of the electron and where μ_e is the mean molecular weight per electron ($\mu_e \approx 2$ for everything but hydrogen). In the extreme-relativistic limit, $v_p \approx c$ and equation (1.3) becomes

$$P_{\rm r} = \frac{8\pi c}{3h^3} \int_0^{p_0} p^3 dp = \frac{2\pi c}{3h^3} p_0^4, \tag{1.8}$$

which, through equation (1.2) gives

$$P_{\rm r} = \frac{1}{8} \left(\frac{3}{\pi}\right)^{1/3} hcn^{4/3} \tag{1.9}$$

$$= 1.244 \cdot 10^{15} \left(\frac{\rho}{\mu_e}\right)^{4/3} \text{ dynes cm}^{-2}. \tag{1.10}$$

Both of these relations are independent of temperature, and are *polytropic equations of state* of order $n = \frac{3}{2}$ and 3 (see Chandrasekhar 1939, or Shapirio and Teukolsky 1983):

$$P = K\rho^{1+\frac{1}{n}} \tag{1.11}$$

such that the non-relativistic and relativistic relations become, respectively,

$$P_{\rm nr} = K_1 \rho^{5/3}, \tag{1.12}$$

$$P_{\rm r} = K_2 \rho^{4/3}, \tag{1.13}$$

where

$$K_1 = \frac{1}{20}\left(\frac{3}{\pi}\right)^{2/3} \frac{h^2}{m(\mu_e H)^{5/3}}, \tag{1.14}$$

$$K_2 = \frac{1}{8}\left(\frac{3}{\pi}\right)^{1/3} \frac{hc}{(\mu_e H)^{4/3}}. \tag{1.15}$$

Note that the extreme relativistic expression is a polytrope with

$$\Gamma \equiv \frac{d\ln P}{d\ln \rho} = \frac{4}{3}, \tag{1.16}$$

which implies neutral stability against perturbation. In other words, if the star is compressed while in this precarious state (say by accretion), the electron degeneracy will not be sufficient to halt the contraction. The mass at which this occurs is termed the *Chandrasekhar mass* in honor of its discoverer, S. Chandrasekhar, who in 1931 constructed the first (zero-temperature polytropic) models of white dwarf stars and found the maximum mass to be $M_{\rm Ch} \approx 1.44\, M_\odot$ (Chandrasekhar 1931a,b). Recently, Chandrasekhar (1984) used the forum of his Nobel lecture to provide a very readable account of the pioneering early efforts in the study of white dwarf evolution.

It is difficult to predict the details of white dwarf collapse — some models predict a nearly homologous collapse until the degenerate pressure of the recombined neutrons provide support at neutron star radii while other predict total collapse to the black hole stage. Although the endpoint of this collapse is not known with certainty, it is perhaps suggestive that for the neutron stars whose masses we can estimate, the masses are clustered about $1.4\, M_\odot$.

1.3 A Generalized Mestel Cooling Relation

The next major theoretical contribution to our understanding of the evolution of white dwarfs dates from the work of Mestel (1952; see also Mestel and Ruderman 1967). He derived the now well-known $\log(t) \propto -\frac{5}{7}\log(L/L_\odot)$ relation in terms of a simple, physical model wherein the thermal energy of the degenerate, (nearly) isothermal core gradually radiates away through the blanketing non-degenerate surface layers. The Mestel cooling theory contains a number of concepts fundamental to the study of white dwarf cooling, and we begin with a somewhat generalized derivation of the cooling law before discussing the numerical model results (see also Van Horn 1971; Iben and Tutukov 1984).

We begin by writing the four basic equations of stellar structure and evolution (cf. Clayton 1968, p. 436):

$$\frac{dM_r}{dr} = 4\pi r^2 \rho, \tag{1.17}$$

$$\frac{dP}{dr} = -\rho \frac{GM_r}{r^2}, \tag{1.18}$$

$$\frac{dT}{dr} = -\frac{3}{4ac}\frac{\kappa\rho}{T^3}\frac{L_r}{4\pi r^2}, \tag{1.19}$$

$$\frac{dL_r}{dr} = 4\pi r^2 \rho(\epsilon - T\frac{\partial s}{\partial t}). \tag{1.20}$$

Here M_r is the mass interior to a sphere of radius r; L_r is the luminosity passing through that sphere; κ, ϵ, and s are the opacity, net nuclear minus neutrino energy production rate, and entropy, respectively; $a = 7.565 \times 10^{-15}$ erg cm^{-3} deg^{-4} is the radiation constant (Allen 1973);

and the remaining symbols have their usual meaning (all units are c.g.s. unless otherwise noted). Equation (1.19) yields a useful approximation for the thermal structure of the envelope, although we note that in adopting it, we are implicitly assuming, as Mestel did, that the energy transport processes are radiative transfer and electron conduction. We have known since the work of Schatzman (1958) and later Böhm (1968) that a convection zone develops on the surface of a star as the effective temperature drops below the dominant species' ionization temperature, and that this convection zone lowers the temperature gradient between surface and core, and hence shortens the evolutionary timescale. However, because this does not occur until $T_{\rm eff} \approx 15{,}000$ for the majority of white dwarf stars, the derivation using equation (1.19) is not only instructive but also widely applicable. The set of equations (1.20) through (1.17) take on different forms in the interior and envelope, and we consider each in turn.

1.3.1 *The Interior*

Matter in the interiors of white dwarf stars is highly-degenerate, and because degenerate electrons are excellent conductors of heat — just as they are in a normal metal — the interiors are nearly isothermal, and the core temperature approximately equals the temperature at the core/envelope boundary. Furthermore, because the pressure of degenerate matter is nearly independent of the temperature, we may use the zero-temperature density–pressure relation $P = K\rho^{5/3}$ [cf. equations (1.12) and (1.14)] and equations (1.17) and (1.18) to derive the mechanical structure of the star in the form of an *Emden polytrope.* Within these approximations, equation (1.19) is superfluous, and we are left with equation (1.20) to solve. Two additional approximations allow us to solve this equation analytically.

The conditions in typical white dwarf cores (temperature, density, and composition) are such that nuclear reactions do not occur. In addition, for the purpose of this derivation, we assume that neutrino losses are negligible [note that detailed models suggest that this assumption only holds true below a luminosity $\log(L/L_\odot) \approx -1.5$]. Within these approximations, we may write $\epsilon = 0$. Furthermore, because to a good approximation the white dwarf stars evolve at constant radius, we can ignore gravitational contraction as a luminosity source, and write for the time rate of change of entropy:

$$T\frac{\partial s}{\partial t} = T\left(\frac{\partial s}{\partial T}|_\rho \frac{dT}{dt} + \frac{\partial s}{\partial \rho}|_T \frac{d\rho}{dt}\right) \approx C_V \frac{dT}{dt}. \tag{1.21}$$

Here C_V is the specific heat at constant volume. For a plasma of strongly degenerate electrons plus an ideal gas of ions of atomic mass A, this is given by

$$C_V = \frac{3}{2}\frac{k}{AH}. \tag{1.22}$$

With these approximations, equation (1.20) can be integrated over radius to obtain

$$L_\star = \int_0^{R_\star} \frac{dL_r}{dr} \tag{1.23}$$

$$= -\int_0^{R_\star} dr \cdot 4\pi r^2 \rho C_V \frac{dT}{dt} \tag{1.24}$$

$$= -\int_0^{M_\star} dM_r C_V \frac{dT}{dt}. \tag{1.25}$$

Within the approximations given above, the integrand is independent of position in the star, and we have

$$L_\star = -M_\star \frac{3}{2}\frac{k}{AH}\frac{dT}{dt}. \tag{1.26}$$

Equation (1.26) gives the expression for the luminosity of the star in terms of the changing core temperature. Next, we need to derive the equations of energy transport through the non-degenerate envelope to derive the age–luminosity relation for the model.

1.3.2 *The Non-Degenerate Envelope*

The non-degenerate envelope which surrounds the core has a mass of typically $M_{\rm env} \sim 10^{-4}$, and so to a good approximation we can neglect the fractional envelope mass. We can also neglect energy production and loss in the envelope (nuclear shell burning sources, if present, are important only the hottest white dwarfs). Thus, we can write for equations (1.17) and (1.18),

$$M_r \approx M_\star, \tag{1.27}$$

$$L_r \approx L_\star, \tag{1.28}$$

where $M_\star$ and $L_\star$ are the white dwarf mass and luminosity, respectively.

With these approximations, the ratio of equations (1.18) and (1.19) can be written in the form

$$\frac{dT}{dP} = \frac{3}{4ac}\frac{L_\star}{4\pi G M_\star}\frac{\kappa}{T^3}. \tag{1.29}$$

Note that all of the terms on the right-hand side except the opacity κ and temperature T are constants. Mestel chose for the opacity the form given by the Kramers' Law, $\kappa \propto \rho/T^{3.5}$, but because the Kramers' law opacity is not a good approximation if the envelope is convective at the core/envelope (*i.e.*, degeneracy/non-degeneracy) boundary, we generalize this somewhat and write

$$\kappa = \kappa_0 P^\alpha / T^\beta. \tag{1.30}$$

We are now in a position to solve equation (1.29) by integrating using the "radiative zero" surface boundary condition, $T = 0$ and $P = 0$, to obtain

$$T^{4+\beta} = \frac{4+\beta}{1+\alpha} C P^{1+\alpha}, \tag{1.31}$$

where

$$C \equiv \frac{3}{4ac}\frac{\kappa_0 L_\star}{4\pi G M_\star}. \tag{1.32}$$

These two equations give approximately the run of temperature and pressure in the envelope.

The non-degenerate envelope behaves as an ideal gas

$$P_{\rm ideal} = \frac{k}{\mu H}\rho T, \tag{1.33}$$

where $k = 1.38 \times 10^{-16}$ erg K^{-1} is Boltzmann's constant, μ is the mean molecular weight of the gas [$\mu \approx 2/(1 + 3X + 0.5Y)$], and $H = 1.66044 \times 10^{-24}$ gm is the unit of atomic mass. Conversely, in the non-relativistic outer part of the electron degenerate core, the pressure is independent of temperature and is related to the density by the expression

$$P_{\rm nr} = K\rho^{5/3}, \tag{1.34}$$

using $K \equiv K_1$ from equation (1.14).

In the spirit of the approximations of the Mestel model, we define the degeneracy boundary as the point at which expressions (1.33) and (1.34) are equal. Solving both for ρ and setting them equal yields the following approximate relationship between the pressure and the temperature at the degeneracy boundary:

$$P = K\left(\frac{kT}{K\mu H}\right)^{5/2}. \tag{1.35}$$

We use this relation to eliminate P from equations (1.31) and (1.32), we may then write

$$L_\star = \Lambda T^{(3+2\beta-5\alpha)/2}, \tag{1.36}$$

where

$$\Lambda \equiv \frac{1+\alpha}{4+\beta}\frac{4ac}{3}\frac{4\pi G M_\star}{\kappa_0}K^{-1+\alpha}\left(\frac{K\mu H}{k}\right)^{\frac{5(1+\alpha)}{2}}. \tag{1.37}$$

For a Kramers' Law opacity, we have $\alpha = 1$ and $\beta = 4.5$, giving from (1.36) the relation $L_\star \propto T^{-3.5}$.

1.3.3 *The Mestel Age–Luminosity Relation*

Now we are in a position to combine equations (1.36) and (1.26) to obtain the age–core temperature relation and the age–luminosity relation. We consider each in turn.

Writing equations (1.36) and (1.26) in terms of the core temperature, we can integrate analytically to obtain the time t required for the model to cool from an initial core temperature T_0 to a final core temperature T. We obtain

$$t = \frac{3/2}{\nu - 1} \frac{M_\star}{\Lambda} \frac{k}{AH} \left[\frac{1}{T^{\nu-1}} - \frac{1}{T_0^{\nu-1}} \right], \tag{1.38}$$

where $\nu - 1 \equiv (1 - 5\alpha + 2\beta)/2$. If we assume a Kramers' Law opacity, the exponent is $\nu - 1 = 2.5$, and this dependence is sufficiently steep so that the age of the star rapidly becomes independent of the initial core temperature T_0 as the star cools.

On the other hand, if we write the equations in terms of the stellar luminosity $L_\star$, we obtain the age–luminosity relation

$$t = \frac{3/2}{\nu - 1} \frac{M_\star}{\Lambda^{1/\nu}} \frac{k}{AH} \left[L_\star^{(1/\nu)-1} - L_0^{(1/\nu)-1} \right]. \tag{1.39}$$

Typically, the initial luminosity L_0 is assumed to be large compared to the current luminosity $L_\star$ of the white dwarf. Again, if we consider the specific Kramers' Law opacity, we have the steep relation given by $\nu = 3.5$ ($\frac{1}{\nu} - 1 = -\frac{5}{7}$), and again the star rapidly "forgets" its initial luminosity.

If we assume that we are several e–folding timescales away from the initial models, then we can neglect the terms in equations (1.38) and (1.39)

resulting from the initial conditions, and obtain simple power law relations between the temperature or luminosity and the age of the white dwarf. These then allow us to obtain a remarkably accurate expression for the white dwarf luminosity function. If we write for the luminosity function of white dwarfs $\Phi \equiv dN_{WD}/d\log(L_\star/L_\odot)$, then we can rewrite this as

$$\Phi = \frac{dN_{WD}/dt}{d\log(L_\star/L_\odot)/dt}, \tag{1.40}$$

where dN_{WD}/dt is the birthrate of white dwarfs. If the birthrate has been constant in time, then equation (1.40) shows that the luminosity function is inversely proportional to the white dwarf cooling rate. Using the results from above, we find

$$\Phi = \frac{dN_{WD}}{dt}\frac{3/2}{\nu \log e}\frac{M_\star}{\Lambda^{1/\nu}}\frac{k}{AH}L_\star^{(1/\nu)-1}. \tag{1.41}$$

With a Kramers' Law opacity, we have $(1/\nu) - 1 = -5/7$ — remarkably close to the observed form of the white dwarf luminosity function.

To summarize, we have shown that using the standard equations of stellar structure and evolution along with a number of simplifying assumptions, we can derive an age–luminosity relation which is an excellent match to detailed numerical-model results over the luminosity range where the approximations are valid, approximately $-1 \gtrsim \log(L/L_\odot) \gtrsim -3$.

1.3.4 *A Mestel Relation for Crystallized White Dwarfs*

The Mestel age–luminosity relation doesn't get used much these days because we have available the results of detailed model calculations over the entire range in which the Mestel relation is applicable. However, because the model sequences that we compute do not include crystallization in the envelope equation of state, our sequences necessarily stop shortly after the

crystallization front crosses the core/envelope boundary, and because these white dwarf sequences will be used in studies of the white dwarf luminosity function which may require extensions of the mass-dependent cooling curves to arbitrarily low luminosities, we must be able to extrapolate these sequences in a physically self-consistent manner. We can derive just such a relation using an approach similar to the above, although now we must use information from the last computed model to make the extrapolation.

We begin with the general relation

$$L_\star = -\frac{\partial}{\partial t}(E_{\rm therm}), \tag{1.42}$$

where approximately, $E_{\rm therm} \approx C_V T M_\star$, as we saw above in equation (1.25). Here we assume that our models are fully crystallized and evolving in the Debye cooling regime, where the heat capacity behaves like that of a metal near zero temperature (see Reif 1965, p. 411; Landau and Lifshitz 1980, p. 195):

$$C_V \approx \frac{2\pi^2 T^3 V}{5(\hbar\overline{u})^3}. \tag{1.43}$$

For the derivation of the extrapolation formula for the fully-crystallized models, we can write this as

$$C_V \approx C_{V,0}\left(\frac{T}{T_0}\right)^\gamma, \tag{1.44}$$

where nominally $\gamma = 3$ in the Debye regime, and where $C_{V,0}$ and T_0 are the mass averages over the final model in a sequence:

$$C_{V,0} \equiv \frac{1}{M_\star}\int_0^{M_\star} C_V \; dM, \tag{1.45}$$

$$T_0 \equiv \frac{1}{M_\star}\int_0^{M_\star} T_r \; dM. \tag{1.46}$$

Note that in equation (1.46) we use "T_r" as distinct from "T" which in this section denotes the mean temperature. Within this approximation, we can substitute into equation (1.42) and solve to obtain

$$L_\star \approx -M_\star C_{V,0}(1+\gamma)\left(\frac{T}{T_0}\right)^\gamma \frac{dT}{dt}, \tag{1.47}$$

similar to equation (1.26) above. This equation, together with equation (1.36), forms a system of two ordinary differential equations which we can solve as above.

We first solve for the age as a function of core temperature by setting equations (1.47) and (1.36) equal and integrating analytically to obtain

$$t - t_0 = \frac{M_\star C_{V,0}}{\Lambda T_0^\gamma}\frac{1+\gamma}{\delta-\gamma}(T^{\gamma-\delta} - T_0^{\gamma-\delta}) \tag{1.48}$$

where we have defined $\delta \equiv (3+2\beta-5\alpha)/2$ for convenience. If, for example, we assume a Kramers' Law opacity is appropriate and that we are in the Debye cooling regime (*i.e.*, $\gamma = 3$), then equation (1.48) simplifies to

$$t - t_0 = 8\frac{M_\star C_{V,0}}{\Lambda T_0^3}(T_0^{1/2} - T^{1/2}). \tag{1.49}$$

We note first that the dependence on T is much shallower than in the standard Mestel model [see equation (1.38)]. Second, and more importantly, note that the form of the equation is such that the star cools to invisibility in a *finite time* (cf. Mestel and Ruderman 1967, Van Horn 1971, Iben and Tutukov 1984). Finally, note that in this regime, the Kramers' Law opacity is not the best choice, because the base of the surface convection zone is degenerate and hence the controlling opacity is the conductive opacity at the base of the envelope.

As above, we can also use equations (1.47) and (1.36) to solve for the age–luminosity extrapolation relation of a fully crystallized model. Solving equation (1.36) for T and substituting into (1.47), we obtain the relation

$$t - t_0 = \frac{M_\star C_{V,0}}{T_0^\gamma} \frac{1+\gamma}{\gamma+\delta} \left(\frac{1}{\Lambda}\right)^{\frac{\gamma+1}{\delta+1}} \left(L_0^{\frac{\gamma+\delta}{\delta+1}} - L_\star^{\frac{\gamma+\delta}{\delta+1}}\right), \tag{1.50}$$

which, using the Kramers' opacity law in the Debye cooling regime, reduces to

$$t - t_0 = \frac{8}{11} \frac{M_\star C_{V,0}}{T_0^3} \left(\frac{1}{\Lambda}\right)^{8/7} \left(L_0^{11/7} - L_\star^{11/7}\right). \tag{1.51}$$

Again, the form of the equation is such that the luminosity goes to zero in a finite time as a result of the T^3 dependence of the specific heat in the Debye cooling regime. Further, note again that in practice we typically fit the last two models with a relation of the form

$$t - t_0 = A \left[1 - \left(\frac{L}{L_0}\right)^B\right]$$

where A and B are free parameters which are typically $A \approx 3$ Gyr and $B \approx 1$ (see §6.2 below).

In this section we have presented a generalized derivation of Mestel cooling theory, and extended it into the crystallized regime where our detailed numerical models cannot go. This extrapolation relation should be particularly useful in studies of the white dwarf luminosity function.

2. *The White Dwarf Evolution Code and Related Topics*

2.1 The Evolution Code

To construct our numerical white dwarf models we use an updated version of the Rochester/Texas White Dwarf Evolution Code (WDEC); this has been described most thoroughly in Lamb and Van Horn (1975). The envelope integrator in WDEC is an updated version of that developed by Fontaine (1973; see also Fontaine and Van Horn 1976). Although we discuss our improvements here, we refer the reader to these papers for the details of the basic codes. In brief, WDEC uses a Newton-Raphson iterative method to solve the four differential equations describing the structure and evolution of a spherically-symmetric stellar model. The models are non-rotating, non-magnetic, and do not include nuclear shell burning sources. They can have essentially arbitrary carbon/oxygen (C/O) mixtures in the core and hydrogen (H) and helium (He) layer masses in the envelope. We use the method of triangles developed by Kippenhahn, Weigert, and Hofmeister (1967) to provide the surface boundary conditions for the evolving cores.

In the Fontaine envelope code the calculation begins with a gray atmosphere integration from optical depth $\tau = 10^{-4}$ to either a depth $\tau = 10$ or

to the point at which convection begins, whichever comes first. The calculation proceeds inward from this point using a Runge-Kutta-Gill integration of the four stellar structure equations for the static case, assuming the luminosity to be constant throughout the envelope. Because our envelopes are static, the gravitational contraction of the envelope with time does not contribute to the luminosity in the form of released gravitational potential energy. We computed two parallel sequences to test the magnitude of this effect. Comparing the two pure-C, 0.6 $M_{\odot}$models, one which had the fitting mass set to $M_{\rm env} = 10^{-6} M_{\star}$ and the other which had $M_{\rm env} = 0.05\ M_{\star}$ (our deepest, used for models with $10^{-2}\ M_{\star}$ He layer mass), we find that the age differences are typically less than 5 percent. This corresponds to an absolute age difference on the order of 0.5 Gyr at the Galactic WDLF turndown luminosity, which is non-negligible but not a great concern because it is a monotonic and calculable effect. In general, we try to keep our envelope masses as small as possible.

2.2 Stellar Evolution Preceding the WD Phase

White dwarf stars are the remnants of main sequence stars with masses ranging from less than 1 $M_{\odot}$ to about 6–8 $M_{\odot}$ (Romanishin and Angel 1980; Anthony-Twarog 1982, Weidemann and Koester 1983). The evolution of these low- to intermediate-mass stars is a topic which is central to a number of textbooks (see Schwarzchild 1958; Cox and Guili 1968; Clayton 1968; Hansen and Kawaler 1990) and review papers (Iben 1967; Iben and Renzini 1984; Mazzitelli 1989), and so we will be mercifully brief here.

Lower-mass stars are thought to form primarily in the cold, dense cores of interstellar molecular clouds (*e.g.*, Shu, Adams, and Lizano 1987; Boss

1989). Because proto-stellar collapse involves processes with distance scales and timescales each spanning several orders of magnitude and because the cores themselves are currently observationally unresolvable, the details of star formation are quite uncertain. Newly on the main-sequence, the star will quietly burn hydrogen to helium in the core until roughly 10% of the stellar mass is consumed. The reaction 4H $\rightarrow$ He proceeds by either the *p–p* chain or the CNO cycles, depending on the total stellar mass (or availability of CNO species, if born in the first $\sim 10^9$ years after the onset of star formation in the Galaxy). With the exhaustion of hydrogen in the core after some $10^{10} \left(\frac{M}{M_\odot}\right)^{-2.5}$ years comes the ascension of the giant branch as hydrogen burns in a shell and builds a degenerate helium core (see Figure 2.1).

At the tip of the giant branch, the helium core ignites under degenerate conditions, and in a flash the star moves onto the horizontal branch, possibly losing a substantial fraction of its mass in the process. Horizontal branch evolution is characterized by core helium burning and shell hydrogen burning. Following helium exhaustion in the core comes an epoch of double-shell burning as the star ascends the asymptotic giant branch (AGB; see Iben and Renzini 1984; Mazzitelli 1989). The C/O profile in the core is determined during the core-He and double-shell burning epochs, as some fraction of the carbon created through the triple-α process burns on to oxygen in the reaction $^{12}C(\alpha,\gamma)^{16}O$ (Fowler *et al.* 1975, Harris *et al.* 1983, Caughlan and Fowler 1988, D'Antona and Mazzitelli 1990). When the C/O core mass grows large enough ($\sim$0.5–0.6 $M_\odot$; see, for example, Mazzitelli 1989), the helium burning can no longer be continuously sustained, and the late stages of AGB evolution are characterized by thermal shell flashes (also called thermal pulses). In addition to the shell flashes which occur on timescales of

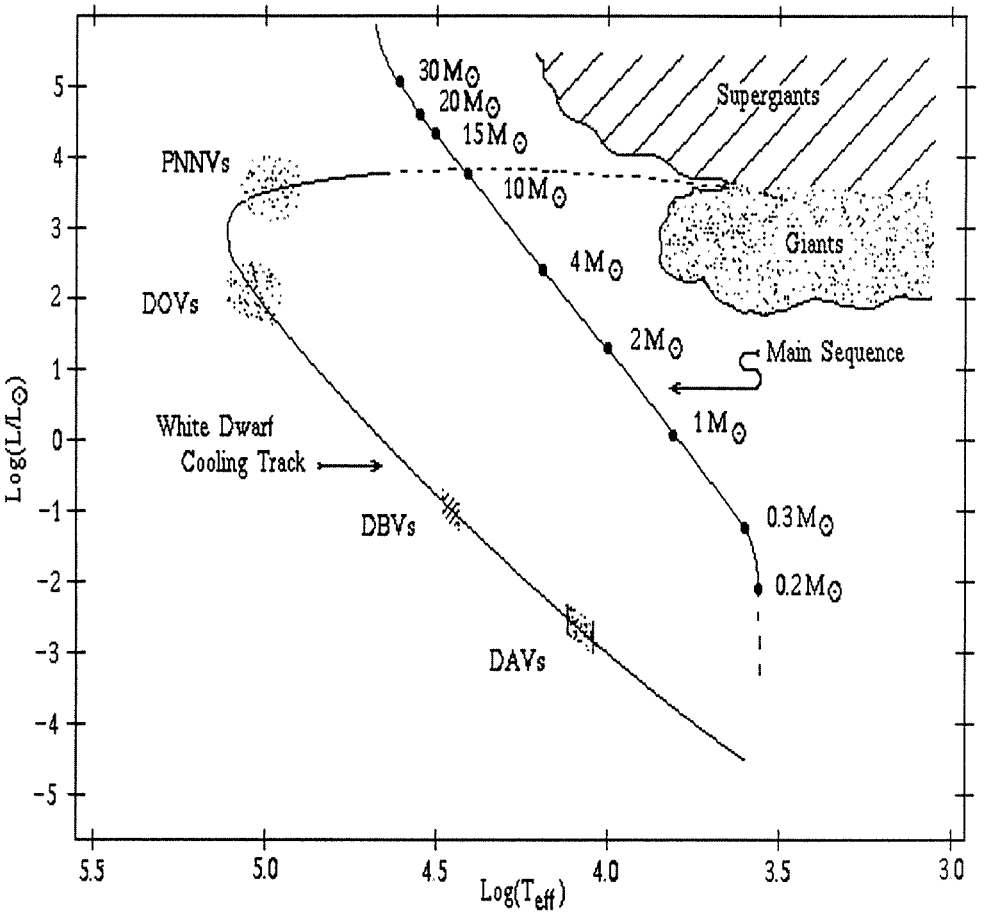

Figure 2.1: Theoretical Hertzsprung-Russell Diagram Including White Dwarf Cooling Track. In this schematic H–R diagram we show the white dwarf cooling track in relation to the main sequence stars, giants, and supergiants. Along the pre-white dwarf track we have indicated the approximate locations of the PNNV and DOV instability strips, and on the white dwarf cooling track we show the locations of the DBV and DAV instability strips. The densities of the boundaries to these regions is a loose indicator of the precision to which we believe we know the temperatures of the boundaries.

order 10^5 years, these stars are also often pulsationally unstable in the form of Mira variables, irregular variables, and OH-IR sources. Schild (1989) has suggested that these objects in fact form an evolutionary sequence, and that the mass-loss rate builds from 10^{-6} $M_\odot$ yr^{-1} to 10^{-4} $M_\odot$ yr^{-1} along the sequence (see also Kwok 1987; Knapp 1990).

Because mass loss is a dynamical process and therefore extremely difficult to model, our knowledge of the details of the process and its termination is sparse (see, for example, Barkat and Tuchman 1980). Evidence obtained from stars further on down the white dwarf cooling track suggests that the hydrogen layers remaining after the planetary nebula (PN) ejection are quite small in mass — less than roughly 10^{-8} $M_\odot$ and possibly as small as $\sim 10^{-13}$ $M_\odot$ (see below). The best estimate for the helium-layer mass is given by Pelletier *et al.* (1986) as $\log(M_{\rm He}/M_\odot) = -3.5 \pm 0.5$. These hydrogen- and helium-layer masses are *much* smaller than the maximum masses which could remain unburned (a few $\times$ 10^{-4} $M_\odot$ and 10^{-2} $M_\odot$, respectively) and could suggest that the final episode of mass loss occurs as a direct result of a helium shell flash instead of the usual picture wherein mass loss stops with the extinguishing of the hydrogen-burning shell (see *e.g.*, D'Antona and Mazzitelli 1979).

To summarize, we believe that main sequence stars with masses up to about 8 $M_\odot$ evolve to become carbon/oxygen white dwarf stars with thin hydrogen and helium surface layers. Gravitational settling and ordinary diffusion quickly sort out the envelope, leaving any remaining hydrogen "floating" on top of helium, itself surrounding the carbon/oxygen core. Most evolutionary models suggest that there is also a trend for oxygen enrichment with depth in the star, although the uncertainties in the $^{12}C(\alpha,\gamma)^{16}O$ reaction rate suggest that specific predictions are not likely to be unique.

2.3 Starting Models

We start our sequences as polytropes of order $n = \frac{3}{2}$ (*i.e.*, $P \propto \rho^{5/3}$). The early evolution of these objects is characterized by a contraction phase at a constant luminosity of order $10^2 L_\odot$ before rounding the "knee" in the cooling track. The growing degeneracy in the core halts the contraction and the surface temperature reaches a maximum of $T_{\rm eff} \gtrsim 100{,}000$ K (see Winget and Cabot 1980, Wesemael *et al.* 1982). In contrast, researchers who have modelled the mass loss using phenomenologically within evolutionary codes find that the cores of asymptotic giant branch models typically evolve across the H-R diagram at a luminosity of order 10^3 to 10^4, and reach a peak surface temperature well in excess of $T_{\rm eff} \sim 100,000$ K (Schönberner 1981, 1983; Wood and Faulkner 1986).

The question naturally arises: how do sequences with polytropic starting models compare with those which start as evolved post-AGB cores? The answer is that as we would have suspected, the thermal structures of models in the two sequences are very similar by the time they have cooled to a luminosity of 1 $L_\odot$ because the neutrino energy losses dominate the early evolution (Kawaler 1986). The assignment of the "time of zero" for theoretical white dwarf sequences is always fairly arbitrary, but is usually chosen to be somewhere near the knee in the pre-white dwarf cooling track. In this as in previous publications (Wood, Winget, and Van Horn 1987; Wood and Winget 1989) our ages are computed relative to the polytropic starting model. As we discuss below in §4.3, our age–luminosity relations merge with those of other researchers at a luminosity of $\log(L/L_\odot) \approx -1$.

2.4 The Composition Transition Zones

The high surface gravities of the white dwarf stars ($\log g \approx 8$) leads to a rapid gravitational segregation of the elements in the envelope (Schatzman 1958; Fontaine and Michaud 1979; Vauclair, Vauclair, and Greenstein, 1979; Muchmore 1982, 1984, Pelletier *et al.* 1986). Any hydrogen remaining in the stellar envelope after the expulsion of the planetary nebula bubbles to the surface on a timescale of order 10^5 years. Similarly, the helium will feather into the C/O core which it overlays. Thus, realistic models of white dwarfs must include compositionally-stratified envelopes.

Most of our sequences have been computed with the composition transition zones idealized as discontinuities because this reduces computing time and has a relatively small effect on the evolution of the interior. Models with discontinuous transitions between compositional layers are too crude for meaningful pulsational analyses, however, and so we have included in WDEC the ability to compute models with the composition transition zones approximating the equilibrium diffusion profile as determined by the gravitational and electric forces and the forces induced by the concentration gradient. The timescale for this process is a strong function of depth in the models such that we do not expect that the helium tail will have time to penetrate below a depth of order $5 \times 10^{-2} M_\star$ in the stars. The detailed derivation of the equilibrium profiles is presented in Arcoragi and Fontaine (1980). Briefly, the derivation assumes that the stellar plasma consists of two ionic species of average charge Z_1 and Z_2 and of atomic weight A_1 and A_2, respectively. Proceeding under the assumption that one element is trace

in the other, we find that the abundance profile of element 2 in the background of element 1 is given by (see Tassoul, Fontaine and Winget 1990, Equation 26):

$$\frac{\partial \ln c_2}{\partial r} = \alpha_2 \frac{\partial \ln q}{\partial r}, \tag{2.1}$$

where

$$\alpha_2 = \frac{A_2}{A_1}(1 + Z_1) - Z_2 - 1. \tag{2.2}$$

The relations for the trace abundance of element 1 in the background of element 2 are of course symmetric to these relations. In these relations, c_i is the fractional abundance of element i by number $[c_i \equiv n_i/(n_1 + n_2)]$ and q is the mass fraction. We next assume that the trace approximation holds over the entire transition region. This is obviously inconsistent, but gives profiles with a minimum amount of computation which are reasonable approximations to those resulting from recent time-dependent calculations (Pelletier *et al.* 1986, Vennes *et al.* 1988). Within this approximation, the abundance profiles are given by the solutions to equation (2.1) and its symmetric partner, giving

$$c_2 = k_2 q^{\alpha_2}, \tag{2.3}$$

$$c_1 = k_1 q^{\alpha_1}. \tag{2.4}$$

The system of equations is closed by requiring that at a given mass, q_m, the abundances of the two elements will both be $X_1 = X_2 = 1/2$, where q_m is determined by specifying that the integral over the abundance profile of the element must equal the specified layer mass.

In our models we can only treat carbon and oxygen in the interior calculations, and so to avoid discontinuities in composition at the core/envelope boundary, we must force the helium abundance to zero there. Because we

also want to have our core/envelope boundary as far out in mass as possible, we often will set the He/C transition zone to be much thinner than the equilibrium profile (see Figure 2.2). This configuration may actually be more representative of the real stars, because the helium-burning shell should have left a sharp transition zone, and the diffusion timescales at this depth are of the order of the evolutionary timescale (Paquette *et al.* 1986). We discuss our detailed comparisons below in §5.1.5.

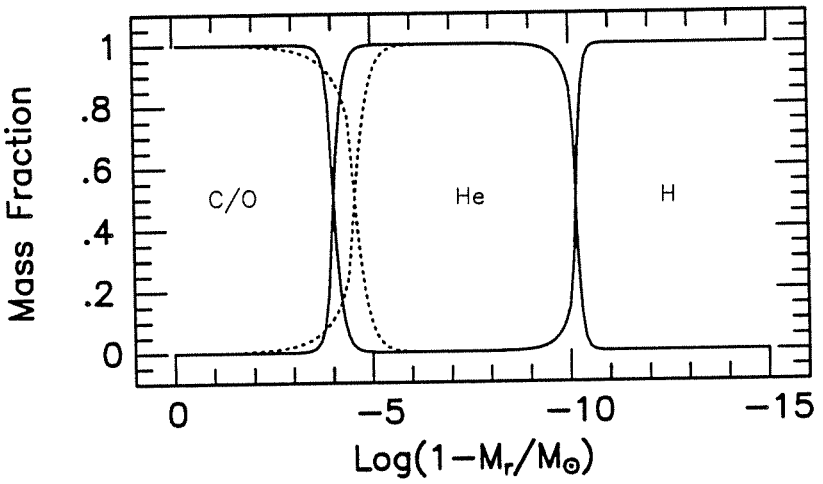

Figure 2.2: Two Approximations to Diffusive Equilibrium Composition Profiles. We show the nominal equilibrium composition profile (*dashed line*) for a sequence with $\log(M_{\rm He}/M_\star) = -4$ and $\log(M_{\rm H}/M_\star) = -10$ calculated in the trace approximation as described in Arcoragi and Fontaine (1980). Also shown is the profile we used in practice (*solid line*) for reasons described in the text.

2.5 Spectral Evolution

The relative fraction of DAs to non-DAs is a function of effective temperature, suggesting that the dominant photospheric constituent may change with evolution as a result of the competition between gravitational settling and convective mixing (Strittmatter and Wickramasinghe 1971, Baglin and Vauclair 1973, Winget and Fontaine 1982, Fontaine and Wesemael 1987). In particular, at a temperature below ~10,000 K, the surface convection zone in DA models begins to move inward into the star in step with the base of the partial ionization zone. If the hydrogen layer is sufficiently "thin" ($M_{\rm H} \lesssim 10^{-8}\ M_\star$) then the base of the convection zone digs below the H/He transition layer as the star cools (Koester 1976; Vauclair and Reisse 1977; and D'Antona and Mazzitelli 1979; Tassoul, Fontaine, and Winget 1990). Are the hydrogen layers so thin? The answer appears to be a qualified yes.

Winget and Fontaine (1982) showed unambiguously that models with hydrogen-layer masses greater than $M_{\rm H} = 10^{-8}\ M_\star$ were not pulsationally unstable at the observed temperatures of the DA instability strip. On the basis of these calculations, they suggested that the observed narrowness of the instability strip combined with the observational fact that most, if not all, stars in the strip are photometric variables (Fontaine *et al.* 1982, 1985) probably indicates that most, and possibly all, DA variables have thin hydrogen layers. The fact that the DAVs differ from the entire population of DAs only in effective temperature further suggests that all DA stars have thin hydrogen layers. The "yes" above must be qualified, however, because the stars in the instability strip are only ~0.5 Gyr old, as compared with the ~9 Gyr age of the white dwarf stars at the luminosity of

the turndown in the white dwarf luminosity function. It is possible that the initial-final mass relation has evolved with the metallicity increase over the history of the Galaxy, and also possible that the details of the separation between the asymptotic giant branch stars' expanding envelopes and the pre-white dwarfs that live within them have changed as well. The observational/theoretical results of Bergeron *et al.* (1990), however, indicate that the photospheres of essentially all of the coolest DA stars have a significant helium content, with $\log N(He)/N(H)$ spanning $\sim 10^{-2}$ (the detection limit) to $10^{1.4}$, compared to the more typical limit of 10^{-5}. These authors suggest that essentially *all* cool white dwarfs have hydrogen layers thin enough to allow convective mixing with the subsurface hydrogen layer at an effective temperature of $T_e \approx 11{,}500$. This suggests that the initial→final mass relation has *not* changed dramatically, nor have the details of the planetary nebula separation process.

2.6 Constitutive Physics

A number of theoretical calculations have been published over the years, and the more-recent of these have included quite detailed treatments of the microscopic physics of both the envelope and interior. A representative subset of such calculations includes Iben and Tutukov (1984), Iben and MacDonald (1985, 1986), Koester and Schönberner (1986), Mazzitelli and D'Antona (1986), D'Antona and Mazzitelli (1989), Winget *et al.* (1987), and Wood, Winget, and Van Horn (1987). Although the age–luminosity relations from these studies appear at first glance to be incommensurate, Winget and Van Horn (1987) showed through a first-order perturbation analysis that if everyone had adopted the same constitutive physics relations

and had computed the same model, they likely would have arrived at the same age–luminosity relationship. We compare our results against the above in detail in §5.3; for the remainder of this section, we discuss the specific choices we have made for our equation of state (EOS), opacities, neutrino rates, and convective treatment.

2.6.1 *Interior Equation of State*

We will maintain consistency with the calculation of Lamb and Van Horn (1975) and use the same expressions for the various physical properties. We use the equation of state (EOS) generator of Lamb (1974) to compute the carbon and oxygen interior EOS tables, and interpolate in composition to a specific C/O mixture using the additive-volume technique described in Fontaine, Graboske, and Van Horn (1977). The EOS incorporates contributions from the kinetic energies of the electrons (which may be arbitrarily degenerate and relativistic — see Eggleton, Faulkner, and Flannery 1973) the radiation field, electron exchange interactions (Kovetz, Lamb, and Van Horn 1972) and Thomas–Fermi contributions (Salpeter 1961). In the ion liquid phase we add to this the ions' ideal gas contribution, the Coulomb liquid term (Hansen 1973; Slattery, Doolen, and DeWitt 1982), and the quantum liquid correction (Wigner 1932). Alternatively, in the ion solid phase we include the Madelung energy of the body-centered-cubic (*bcc*) lattice and the corresponding phonon contributions (Carr 1961; Cohen and Keffer 1955; Kugler 1969), with screening of the optical modes of the lattice treated similarly to Kovetz and Shaviv (1970) but using a semirelativistic Thomas-Fermi model.

For each of carbon and oxygen, we compute the transition between the liquid and solid phases using exact thermodynamics (see Landau and

Lifshitz 1980, p. 257), given our expressions for the EOS. The value of $\Gamma \equiv (Ze)^2/akT$, the ratio of Coulomb to thermal energies, varies somewhat along the crystallization curve marking the boundary between the liquid and solid phases but is in the range $\Gamma_m = 160 \pm 15$. Here $[(4\pi/3)a^3]^{-1} \equiv n_i = \rho/AH$ is the ion number density. The most accurate Monte Carlo calculations of the fluid/solid phase transition in the one-component plasma, a hypothetical system closely related to white dwarf matter, have recently given $\Gamma_m = 178 \pm 1$ (Slattery, Doolen, and DeWitt 1982) and $\Gamma_m = 180 \pm 1$ (Ogata and Ichimaru 1987).

Recently, Ichimaru *et al.* (1983) have raised the possibility that the white dwarfs may not freeze into a *bcc* lattice, which is the lowest energy state, but instead form a metastable, amorphous, glassy state. Because the state is metastable, it eventually makes the transition to the *bcc* configuration. For example, Ichimaru *et al.* compute that for ^{56}Fe at $\Gamma = 210$, the transition should take of order 10^5 years, which is negligible compared to white dwarf cooling times. Thus, the maximum effect this suggested state might cause is to delay the release of latent heat of crystallization by at most a few 10^8 years, which is small compared to other uncertainties in the calculations. Thus, we do not consider this state further in our calculations.

We compute our crystallizing models by assuming that the liquid phase undergoes a first-order phase transition to the *bcc* solid. Our treatment of the crystallization front advancing through pure-C or pure-O interiors is as described in Lamb and Van Horn (1975). When the temperature and pressure of a given mass shell j are on the solid side of the pre-computed crystallization boundary, the thermodynamic quantities corresponding to that shell are interpolated from the solid portion of the EOS table. Alternatively, if the (P, T) point indicates that the material has not yet crystallized, we

interpolate in the liquid portion of the EOS table. Our EOS tables are on a $(\log P, \log T)$ grid, and we use a two-dimensional, 4-point Aitken-Lagrange interpolation procedure to extract the needed thermodynamic quantities. To insure that each interpolation uses (P,T) points from only one or the other portion of the EOS table, no matter how close to the crystallization boundary, the table includes a 16-isotherm overlap region in which thermodynamic quantities have been calculated for both states, regardless of which state is formally applicable. In the case of C/O mixtures we assume that the matter crystallizes as an alloy if, for the temperature that it is at, $P_{C/O}^{\rm crit} \geq X_C \cdot P_C^{\rm crit} + X_O \cdot P_O^{\rm crit}$, where $P^{\rm crit}$ is the pressure at crystallization for a given temperature.

It was suggested by Stevenson (1980) that C/O ionic mixtures might be immiscible in the solid phase. In this picture, the white dwarf stars would start with some C/O profile before freezing and end with an oxygen core surrounded by a carbon mantle, itself surrounded by the surface helium and hydrogen layers. The release of gravitational potential energy associated with the restructuring could in principle be large and have a significant effect on the age of the Galactic disk as inferred from the white dwarf stars (Mochkovitch 1983, Garcia-Berro *et al.* 1988). However, as discussed by Ichimaru *et al.* (1988), Stevenson made some unwarranted (and incorrect) assumptions in deriving his phase diagram. Recently, two groups have calculated the C/O phase diagram using the density functional approach, and concluded that although the phase diagram is either of the spindle (Barrat, Hansen, and Mochkovitch 1988) or azeotropic (Ichimaru *et al.* 1988) kind, they do not expect there to be a chemical separation of the elements upon freezing. We consider the matter thus to be settled.

2.6.2 *Envelope Equation of State*

The physical conditions in white dwarf envelopes are quite complex and the demands on the equation of state are substantial. In our envelope integrations, we used the tabular equation of state developed by Fontaine, Graboske, and Van Horn (1977) for pure H, He, and carbon compositions and which includes the effects of incomplete ionization, electron degeneracy, pressure ionization, and other non-ideal-gas effects. Although it does not include the crystallization transition, we regard this equation of state as the best currently available for matter under such conditions. Thermodynamic quantities used in the envelope calculation are obtained by two-dimensional, three-point, Aitken-Lagrange interpolation, which tests have shown to yield fractional errors less than 10^{-3} in the interpolated quantities. As suggested by Fontaine, Graboske, and Van Horn (1977), we have used the additive volume prescription to interpolate in composition in the non-discontinuous transition zones.

2.6.3 *Opacities*

The total opacity is given by the relation:

$$\frac{1}{\kappa} = \frac{1}{\kappa_{\mathrm{r}}} + \frac{1}{\kappa_{\mathrm{c}}}. \tag{2.5}$$

where κ_{r} is the radiative opacity and κ_{c} is the conductive opacity. We have used the conductive opacities of Itoh *et al.* (1983, 1984) and supplemented them below $\log \rho = 1.6$ with the older Hubbard and Lampe (1969) opacities as fit by Lamb (1974; for C) and Fontaine and Van Horn (1976; H and He). In practice, we use the Itoh *et al.* opacities exclusively above $\log \rho = 1.8$, the Hubbard and Lampe opacities below $\log \rho = 1.5$, and interpolate linearly in

the logarithm in the transition region (the fitting formulae they give extend to only $\log \rho \approx 1.6$).

The Itoh opacity calculation includes the best understanding of the structure factor of the ions in the high-temperature, classical limit, and the dielectric screening due to degenerate electrons. They are in good agreement with the calculations of Yakovlev and Urpin (1980) and Nandkumar and Pethick (1984) in the high-density regime, but differ in the low-density regime as a result of the inclusion of the relativistic dielectric screening function. Yakovlev and Urpin set the dielectric function to unity, which is invalid in the low-density limit. In the calculation of the electrical and thermal conductivities of matter in the crystalline phase, Itoh *et al.* (1984) included the Debye–Waller factor, resulting in a reduction of the opacities by a factor of ~2–4 near the melting curve. To determine the effects of switching to the newer opacities from the Hubbard and Lampe (1969) opacities, we include a pair of parallel sequences which differ only in the conductive opacities used. As discussed in §5.2.1 below, we find that the Itoh *et al.* opacities are somewhat less than a factor of two larger than those of Hubbard and Lampe in regions of interest (see Figure 4.18).

The radiative opacities we use are those provided by Huebner (1980) supplemented below 12,000 K with the opacities of Cox and Stewart (1970). The mixtures we have used are Iben I ($X_H = 0.999$), Iben V ($X_{He} = 0.999$), and Weigert V ($X_C = 0.999$). We interpolate in the tables using a two-dimensional, two-point logarithmic interpolation and extrapolation, yielding accuracies of 20–30 percent. We interpolate the opacities in composition linearly by mass fraction for each of the radiative and conductive contributions, and then obtain the total opacity using equation (2.5).

D'Antona and Mazzitelli (1989) have recently suggested that differences in the interpolated or extrapolated radiative opacities between their models and ours account for the differences in ages between our sequences and theirs (their sequences are generally younger at a given luminosity). We show in Figures 2.3, 2.4, and 2.5 our opacities for comparison with D'Antona and Mazzitelli's Figure 1. The hydrogen opacities compare quite favorably, whereas the helium opacities show some differences. The primary difference between their helium opacities and ours appears as a ridge in their opacity table at a density near $\log \rho = 1$. Our radiative opacity tables do not go to such high densities for these low temperatures, and we extrapolate off the table linearly in the logarithm of the variables. Although it is difficult to read specific values off the D'Antona and Mazzitelli opacity plots, it seems that if anything, our helium opacities are of the same order or smaller than those they used.

2.6.4 *The Treatment of Convection*

We computed our convective transport properties using the standard mixing-length theory of Böhm-Vitense (1958). We set the mixing length ℓ to be equal to one pressure scale height,

$$H_P \equiv -\frac{dr}{d\ln P} = \frac{P}{\rho g}, \tag{2.6}$$

or the geometric depth of the convection zone (whichever is less). When integrating the envelope the step size is typically $\frac{1}{8}H_P$, which is sufficient to give the pressure at the base of the envelope to better than a few percent. As we discuss below, an accurate treatment of the envelope physics is essential in computing accurate cooling times for the models — the envelope controls the outflow of heat from the stellar interior. The sensitivity of

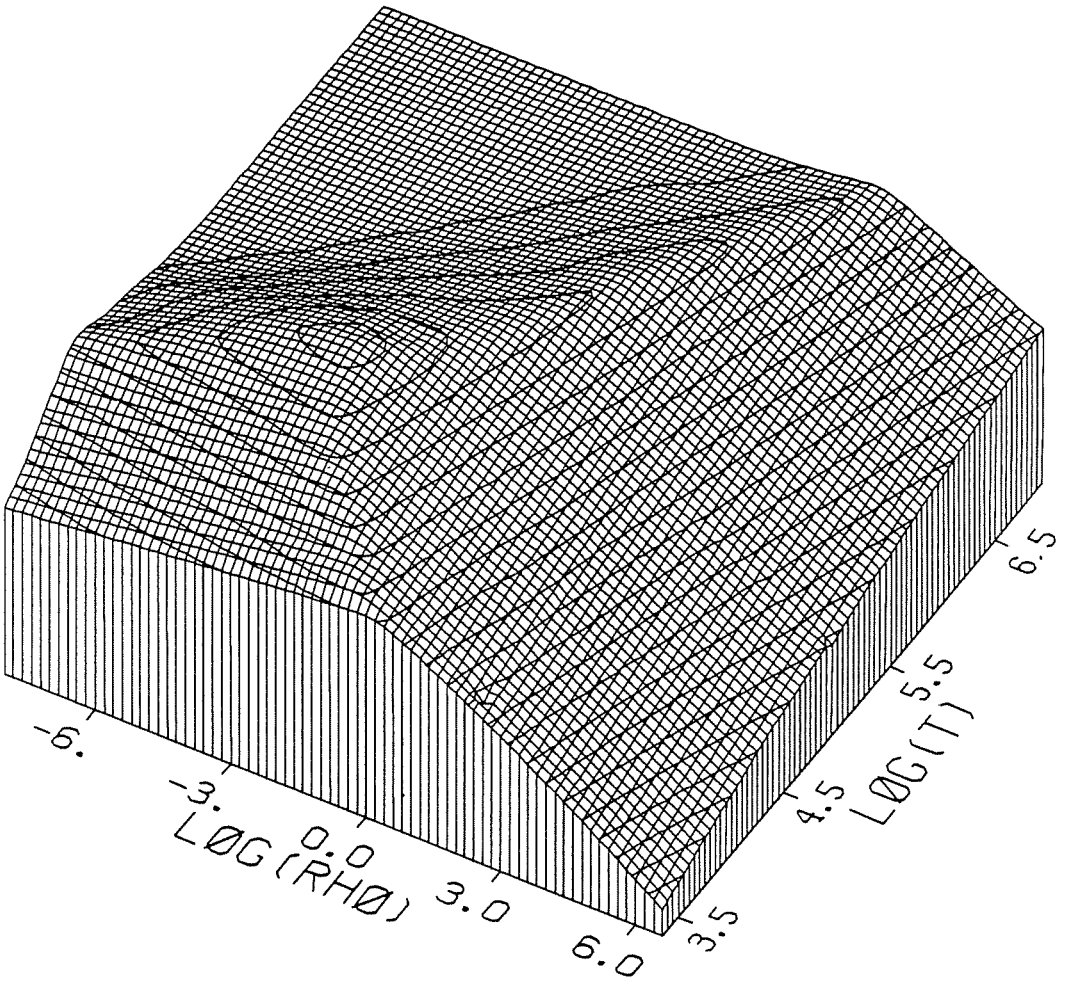

Figure 2.3: Logarithm of the total opacity for a hydrogen-rich composition ($X = 0.999$, $Y = 0.0$, $Z = 0.001$). In this figure, density runs from $-8 \leq \log \rho \leq 6.6$ in equal steps of $\Delta \log \rho = 0.2$, and temperature runs from $3.4 \leq \log T \leq 7.0$ in steps of $\Delta \log T = 0.05$. The logarithm of the opacity runs in the $+z$ direction from a minimum of $z_{\rm min} = \log \kappa_{\rm min} = -17.2$, to a maximum of $z_{\rm max} = \log \kappa_{\rm max} = 5.41$, and contour levels are plotted at integer values of $\log \kappa$ in between.

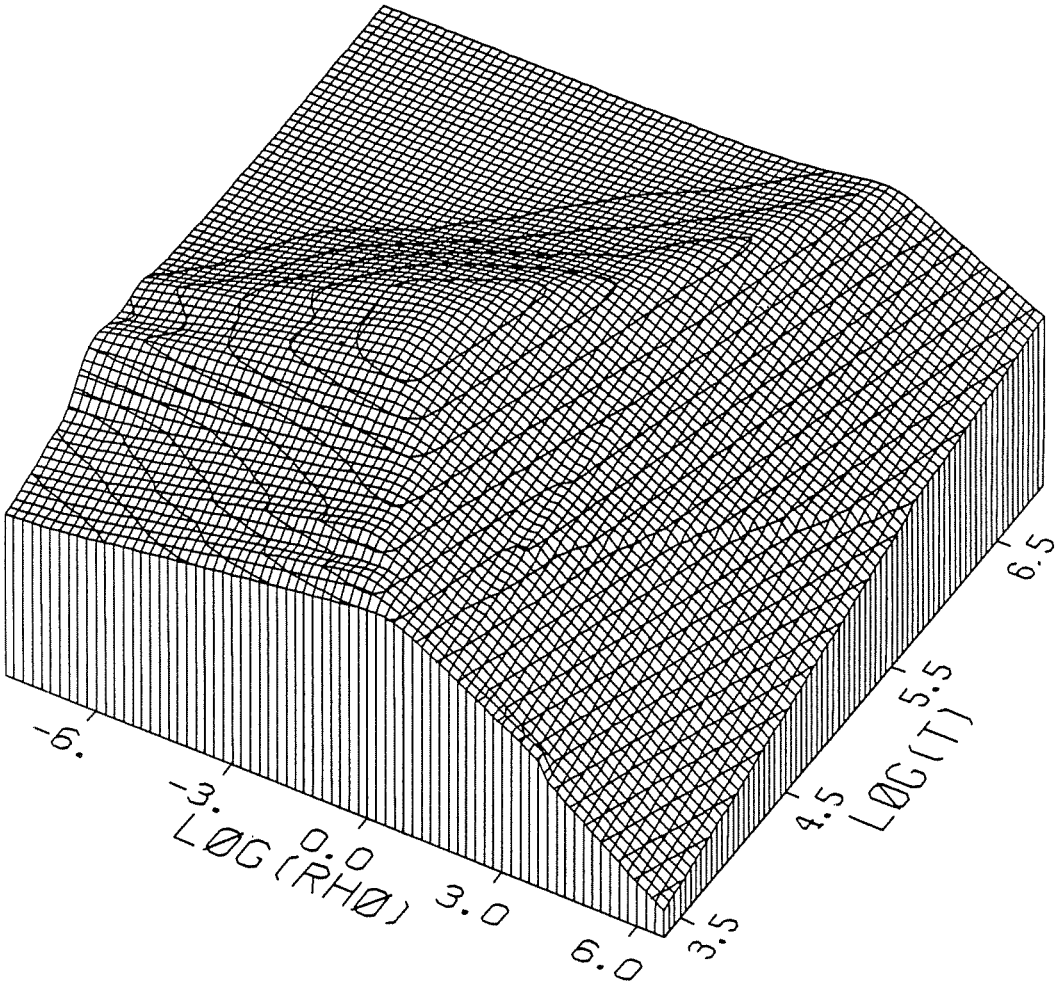

Figure 2.4: Similar to Figure 2.3, but for the composition $X = 0.0$, $Y = 0.999$, and $Z = 0.001$. Here, $\log \kappa_{\rm min} = -18.0$, $\log \kappa_{\rm max} = 4.89$, and again $\Delta \log \kappa = 1$.

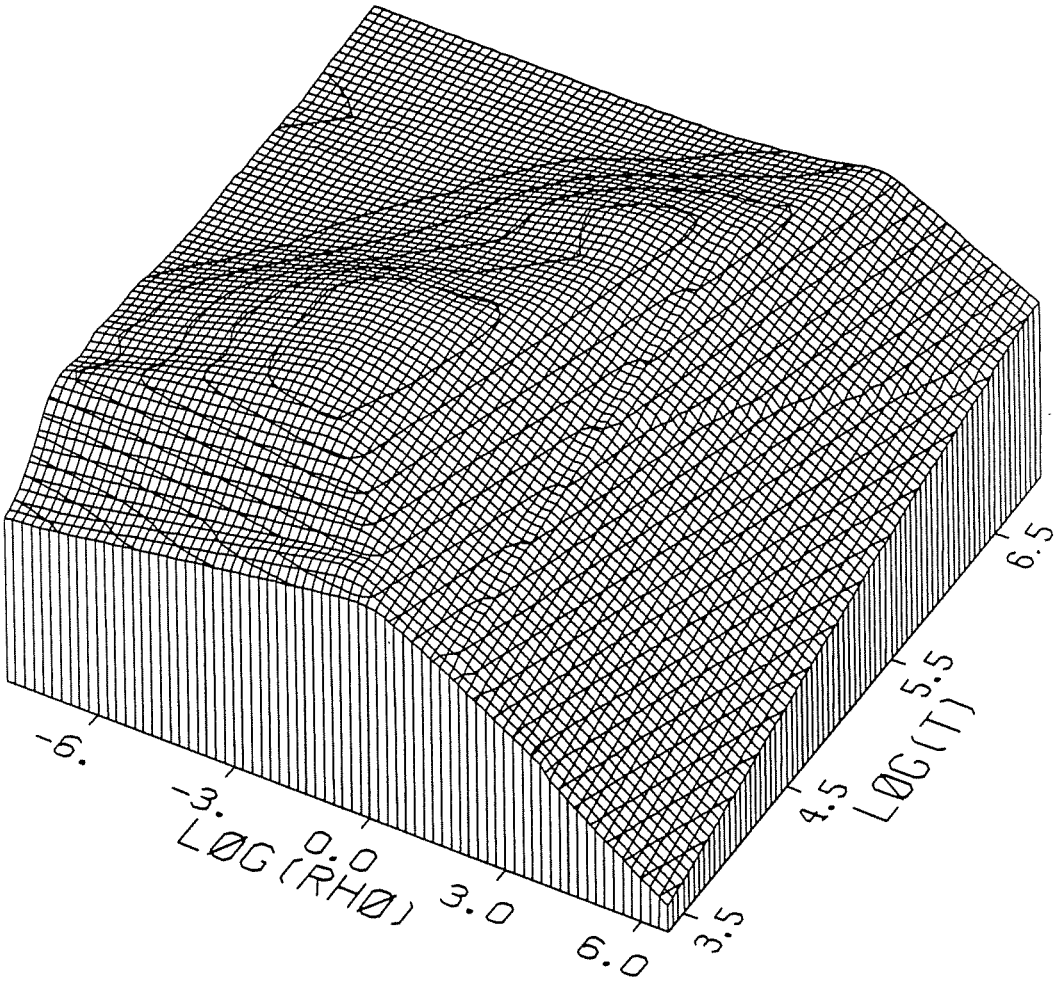

Figure 2.5: Similar to Figure 2.3, but for the carbon composition $X_C = 0.999$ and 0.001 heavier metals. Here, $\log \kappa_{min} = -17.8$, $\log \kappa_{max} = 4.92$, and $\Delta \log \kappa = 1$. Note the wrinkle present at $\log \rho \approx 1.5$, the overlap region between the conductive opacities of Hubbard and Lampe (1969) and those of Itoh *et al.* (1983, 1984). Note that the H and He transitions are comparatively smooth across the transition.

envelope models to differences in the treatment of the microscopic physics has previously been discussed by Fontaine *et al.* (1974).

Most of our sequences do not include convective mixing, and in those that do the treatment is extremely crude. The question of mixing is only relevant for the DA models and occurs at temperatures below $T_{\rm eff} \lesssim$ 11,500 (see Bergeron *et al.* 1990). Having computed a number of sequences without regard to mixing considerations, we found that hydrogen layers with masses of interest should mix completely at low luminosities. Because our envelopes are static, we could not compute the compositional mixing case accurately. We switch straight to a DB composition when the surface and subsurface composition zone boundaries touch (see Figure 4.16 below). Although this may not be correct in detail, we do expect it to be a reasonable approximation, because the fractional hydrogen abundance in the mixed convective region is several orders of magnitude less than the fractional helium abundance, and the mixing occurs on a timescale short with respect to the subsequent evolution.

2.6.5 *Neutrinos*

Neutrino energy losses in the hottest models can exceed the photon luminosity by a factor of up to 50 or more. We have included neutrino energy losses for the photon, plasmon, pair, and recombination processes from Beaudet, Petrosian, and Salpeter (1967) and for the bremsstrahlung process from De Zotti (1972). We have not included the modifications necessary for consistency with the recently confirmed "electroweak" theory (see Dicus 1973; Weinberg 1974); however, they introduce only moderate reductions in the neutrino rates in the hottest models (D'Antona and Mazzitelli 1990), and quickly become unimportant. Neither did we include URCA process

neutrino losses, because these are negligible in the regimes we encounter (Beaudet, Salpeter, and Silvestro 1972).

3. The Fiducial Model Sequence: X6400B

3.1 Model Parameters

Having finished discussing the code and the constitutive physics that goes into it, we are now ready to begin discussing the results. Space constraints prohibit a detailed accounting of all of the sequences which we have computed, but as a point of reference we describe in detail one model sequence. This fiducial model sequence is intended to represent a reasonable approximation to the structure of real white dwarf stars as we currently understand them, yet is still simple enough that we may draw meaningful conclusions when comparing it with other model sequences. The choices for the input parameters which characterize the sequence are as follows. We chose to compute a 0.6 $M_\odot$ sequence, consistent with the mean mass determination of Weidemann and Koester (1984). The particular C/O profile that we used in the core was guided but not dictated by the full MS $\rightarrow$ WD evolutionary calculations of Mazzitelli and D'Antona (1986; see their Figure 4) and D'Antona and Mazzitelli (1989; see their Figure 4). We chose for the oxygen abundance profile

$$X_O = \begin{cases} 0.8, & 0.0 \leq q \leq 0.5, \\ 0.8 - 2(q - 0.5) & 0.5 < q \leq 0.9, \\ 0. & 0.9 < q \leq 1.0, \end{cases} \tag{3.1}$$

where $X_C = X_O - 1$ for all but the outermost 10^{-4} $M_\star$, which is helium. Because the $^{12}C(\alpha,\gamma)^{16}O$ reaction rate is larger at lower temperatures, the products of core-helium burning are more oxygen-rich than are the products of shell-burning, which occurs at higher temperatures and lower pressures (D'Antona and Mazzitelli 1990). Another consequence of this temperature dependence is that we expect larger total mass fractions of oxygen in *lower mass* main sequence stars. The total oxygen mass fraction specified by equation (3.1) is ~56% (see Figure 3.1), and is probably representative of a remnant of a main sequence progenitor in the mass range 1.5–4 $M_\odot$. Because helium photospheres are in the majority at low effective temperatures, we decided to compute a DB model sequence with the helium-layer mass of $\log(M_{He}/M_\star) = -4$, consistent with the results of Pelletier *et al.* (1986). We treated the helium/carbon composition transition as a discontinuity to minimize the numerical noise introduced by interpolating in composition and so that we could set the core/envelope fitting point M_e to be as close to the surface as is practical $M_e = 5M_{He}$.

We evolved the sequence from a maximum luminosity of $\log(L/L_\odot) \approx 2$ to a minimum luminosity of $\log(L/L_\odot) \approx -5.4$ in 78 timesteps (see Table A.1 in the Appendix). In the interest of saving space, we have interpolated the summary listing onto a uniform luminosity grid using splines. During crystallization, certain models would not converge because of numerical oscillations at the crystallization boundary (see Lamb and Van Horn 1975 for details). In these cases, we found that if we temporarily lengthened the timestep, the new model usually converged without further problems.

In the following sections, we explore the detailed results of the fiducial sequence through plots of the evolutionary quantities. We begin with the global results and show log(age), $\log(T_c)$, and the crystallization mass

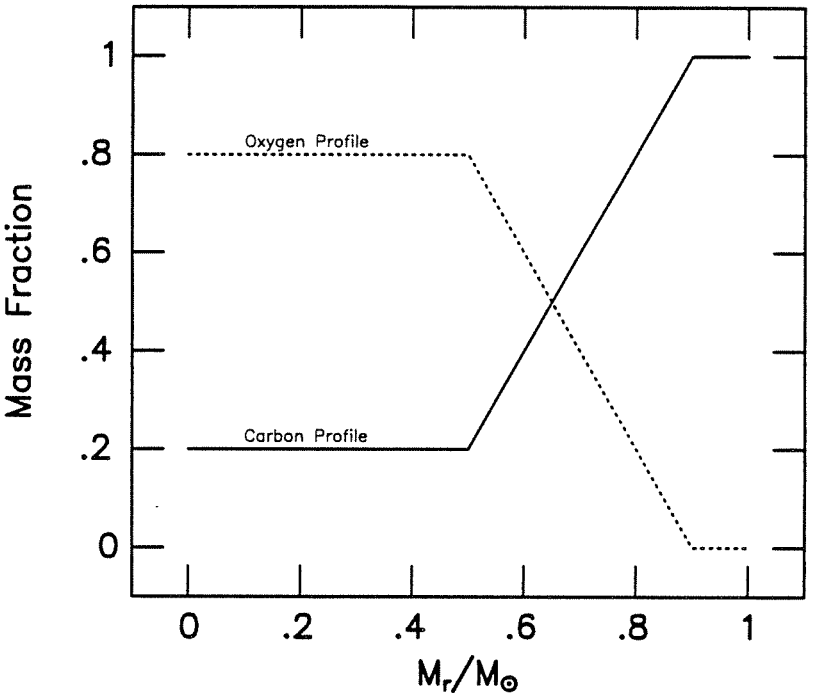

Figure 3.1: Mass Fraction of Carbon (*dashed line*) and Oxygen (*solid line*) as a Function of $M_r/M_\star$. The adopted C/O profile is intermediate between the results of the detailed numerical calculations of Mazzitelli and D'Antona (1986) and D'Antona and Mazzitelli (1989). We have made no attempt to represent the surface helium layer in this Figure.

fraction $M_{\rm xtal}/M_\star$ *versus* $\log(L/L_\odot)$. We then discuss the evolution of the envelope structure with cooling, before showing and discussing the evolution of the interior and envelope quantities using surface plots similar in form to the opacity plots above.

3.2 Global Results

In Figure 3.2, we show the logarithm of the age τ, the logarithm of the core temperature T_c, and the crystallization mass fraction $M_{\rm xtal}/M_\star$ *versus* decreasing luminosity. Before discussing the curves themselves, we should discuss our choice of independent variable. We believe that the independent variable should be an observable quantity instead of time. The two choices are then $\log(L/L_\odot)$ and $\log(T_{\rm eff})$, and we chose $\log(L/L_\odot)$ over $\log(T_{\rm eff})$ because the former is used in the presentation of the observed white dwarf luminosity function (Liebert, Dahn, and Monet 1988), and because the theoretical luminosity function is in the simplest approximation given by equation (1.40). The choice is of course arbitrary, and to the extent that $\delta\log(L/L_\odot) = 4\delta\log(T_{\rm eff})$ (*i.e.*, to the extent $R_\star$ is constant), inconsequential. However, because the two representations do differ appreciably in the high-luminosity phase, we include Figure 3.3 for comparison. Further, the sequence summary Tables below contain redundant information in the form of $\log(L/L_\odot)$, $\log(T_{\rm eff})$, and $\log(R_\star)$, in addition to the age, $\log(T_{\rm c})$, neutrino luminosity $\log(L_\nu/L_\odot)$, and crystallization mass fraction.

Figure 3.2 shows the effects of neutrino energy losses at high luminosities and of crystallization effects at low luminosities, but is in reasonable agreement with the Mestel prediction between these two extremes. Note that in the crystallization regime the models are much closer together because the release of latent heat slows the evolution (the timesteps, though monotonically increasing with decreasing luminosity, are nevertheless approximately constant over small luminosity intervals). The core temperature is initially held relatively flat with time from the neutrino emission,

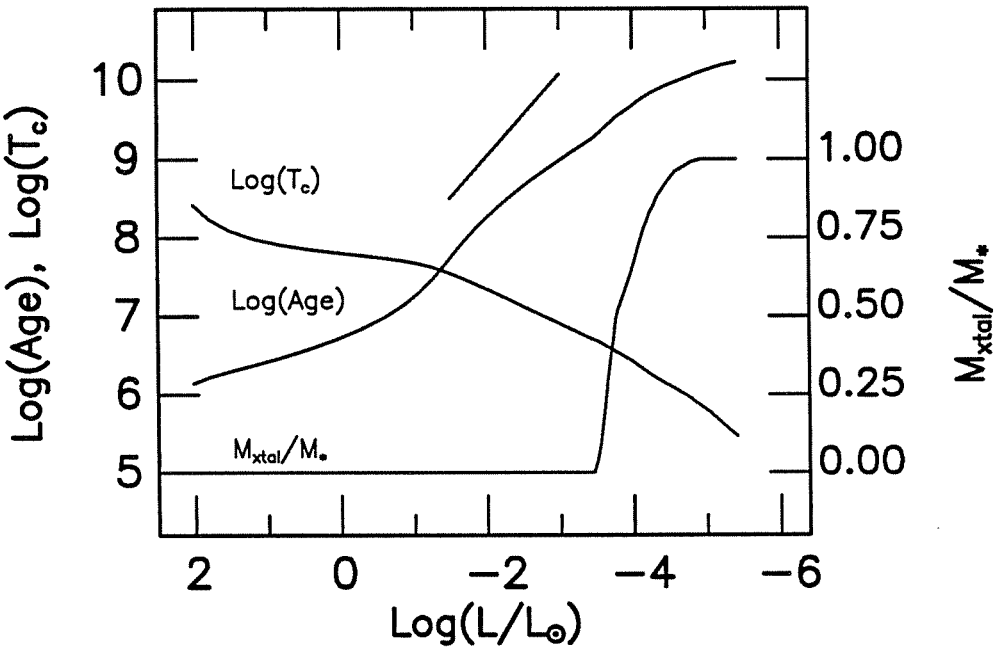

Figure 3.2: Evolutionary Summary Plot of the Fiducial Sequence x6400b. The points which correspond to the converged models in the sequence are also shown here connected. In addition to showing the age, core temperature, radius, and crystallization mass fraction as functions of luminosity, we also include in this Figure a line segment that has the Mestel age–luminosity relation slope [$\log \tau = -\frac{5}{7}\log(L/L_\odot) + \text{cst.}$]. To the extent possible, we put all of our plots on one scale to simplify intercomparison.

but begins to decline more steeply near $\log(L/L_\odot) \sim -1.0$ as neutrinos become less important. The slope in the $\log(T_c)$–$\log(L/L_\odot)$ relation during first the crystallization process and then again early in the Debye cooling regime [$\log(L/L_\odot) \approx -3.9$ and -4.5, respectively] is slightly less steep than the norm because of the $T\frac{ds}{dt}$ luminosity source associated with the jump in entropy at the crystallization phase transition and later from the decline of the heat capacity in the interior in the Debye cooling regime. We can see the composition profile from Figure 3.1 reflected in the progression of the

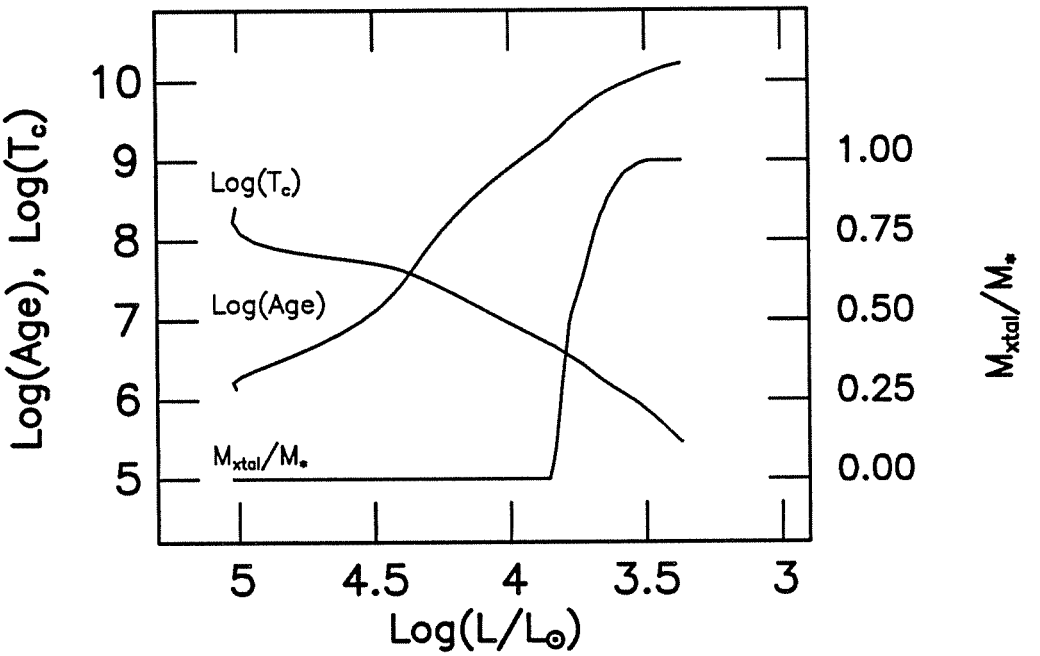

Figure 3.3: Similar to Figure 3.2, but here $\log(T_{\rm eff})$ is the independent variable.

crystallization front. At the half-mass point, the slope of the curve changes abruptly as the mass fraction of carbon changes.

With cooling the radii of the models (see Table A.1) asymptotically approach the radius of a fully-degenerate (zero temperature) object (Hamada and Salpeter 1961), but they do so on a long timescale. At $\log(L/L_{\odot}) \approx 2$, the radius of the 0.6 $M_{\odot}$ fiducial model is nearly a factor of 3 larger than its final radius, and it is still ~5% larger than its final radius at a luminosity of $\log(L/L_{\odot}) \sim -2$ ($T_{\rm eff} \approx 16{,}000$ K; $t_{\rm cool} = 0.18$ Gyr). As discussed by Koester and Schönberner (1986), it is important that observers use these radii instead of the Hamada and Salpeter radii when dealing with hot white dwarfs. We discuss this further in the next Chapter when covering the behavior of the models as a function of mass.

3.3 Envelope Evolution

In Figure 3.4 we show the evolution of the envelope on the same luminosity scale as in Figure 3.2. Here, we have plotted $\log(1-q)$ on the ordinate (where $q \equiv M_r/M_\star$) to resolve the envelope and de-emphasize the core. We show the He/C composition transition zone as a dashed line at $\log(1-q) = -4$ and the convective regions as hatched areas. From left to right, the curves running from lower central to upper right are the loci of $\eta = 0$, 10, and 20, respectively. We see that at high luminosities the material is fully ionized out to the photosphere, and there is no surface convection zone. As the temperature drops below that of second and then first helium ionization, the convection zone digs deep into the envelope, flattening the true temperature gradient, and so enhancing the rate of energy loss. Shortly thereafter, at a luminosity $\log(L/L_\odot) \approx -2.7$, the degeneracy boundary ($\eta = 0$) reaches the base of the convection zone. With no radiative buffer zone between the degenerate interior and the convective envelope, the controlling opacities become the conductive opacities at the base of the convection zone — the temperature structure is adiabatic from that point outward. This change in efficiency in the energy transport through the envelope at $\log(L/L_\odot) \approx -2.7$ is reflected in Figure 3.2 in both the age–luminosity relation and in the T_c–luminosity relations, as was first noted in Winget and Van Horn (1987).

3.4 A Detailed Look Inside

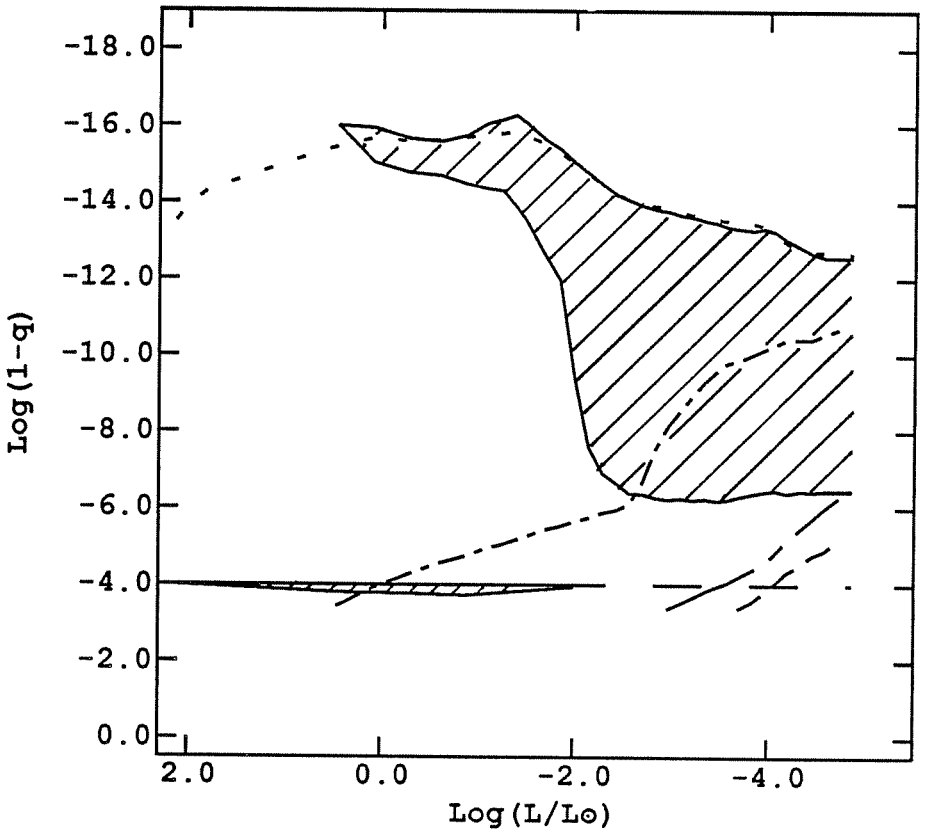

Figure 3.4: Evolution of the Envelope *versus* Log($L/L_{\odot}$) for x6400b. Here we show the dependence of the envelope structure on the luminosity of the fiducial model. We show the He/C transition mass as a long-dashed line, the photosphere ($\tau = 2/3$) as a short-dashed line, and the convective regions as hatched areas. We also include in the envelope region the curves for $\eta = 0$ (*medium/short dashed line*), $\eta = 10$ (*long/medium dashed line*), and $\eta = 20$ (*medium dashed line*) as a function of luminosity, showing the degeneracy boundary reaches the base of the surface convection zone at a luminosity of $\log(L/L_{\odot}) = -2.7$ for this model. Looking back at Figure 3.2, we see a change in the age–luminosity relation at this luminosity.

3.4.1 *A Few Words on Presentation*

We will compare these results with those of other sequences in the following section, but for the remainder of this section we focus on the details of the evolution of the thermodynamic quantities throughout the models. In looking at these quantities, we will be using surface plots similar to those used in Figures 2.3, 2.4, and 2.5. We show the variables in two different ways using these surface plots. First, we show them as functions of both q and $\log(L/L_\odot)$, and define our coordinate system such that q increases in the $+x$ direction, $\log(L/L_\odot)$ decreases in the $+y$ direction, and the dependent quantity increases in the $+z$ direction. These plots emphasize the evolution of the interiors. In fact, *only* the interiors are plotted on these plots: q runs from a minimum of $\sim 10^{-4}$ (the innermost mass shell) to the core/envelope boundary, which in the fiducial model sequence is at a depth in the star $M_{\rm env} = 5 \times 10^{-4}\ M_\star$. Not including the envelope has the effect that quantities which peak in the envelope (*e.g.*, the opacity or the heat capacity) are misrepresented. The other method of presentation picks up where the first leaves off. Again we plot the dependent variable along the z-axis and $\log(L/L_\odot)$ along the y-axis, but here instead of using linear mass along the x-axis, we use $\log(1 - q)$, thus emphasizing the envelope (see also Tassoul, Fontaine, and Winget 1990). We call these two methods of representation the "interior" and "envelope" surface plots of the thermodynamic quantities, respectively.

Although there is the potential for confusion between the two methods of display, we felt it better to keep the Figures grouped by thermodynamic quantity rather than by method of presentation. We do not use both displays for all the variables, because in most cases one or the other is sufficient.

To maximize the usefulness of these figures and to minimize confusion, we have provided reference coordinate systems, labels for the x and y axes, and contour levels in the z direction. To plot these values, we first used splines to interpolate each model to a specified mass grid [*i.e.*, one with equal steps in either q or $\log(1-q)$]. We chose to use 51 grid points in the mass interpolation in q (for 50 mass steps of 0.02 $M_\star$), and 69 grid points in the interpolation of $\log(1-q)$ spanning the range $0 \geq \log(1-q) \geq -17$ (for 68 mass steps of 0.25 dex). We include lines tying the grid points of one evolutionary model to the next to make it possible to read numerical values easily from the figures.

Finally, we note that in the lower-luminosity models, the starting mass in the envelope routine as given by the gray atmosphere routine can be as large as 10^{-15} from the compression with cooling in the envelope. In the highest luminosity models, the starting mass can also be larger than our boundary at $\log(1-q) = -17$ because the envelope is radiative and the gray atmosphere routine integrates to the mass where the optical depth is 10. For the purpose of the figures plotted against $\log(1-q)$, we simply set the height outside the interpolation region to the level of the skirt drawn around the base.

3.4.2 *Temperature*

We first show the evolution of the interior temperature as a function of both mass and decreasing luminosity in Figure 3.5. The Figure shows the core temperature inversion at high luminosities resulting from the neutrino energy losses. Depending on the stellar mass, the neutrino luminosity can exceed the photon luminosity by a factor of ~5–10 in this luminosity regime (see Figure 3.6). The dominant reaction involves losses by the

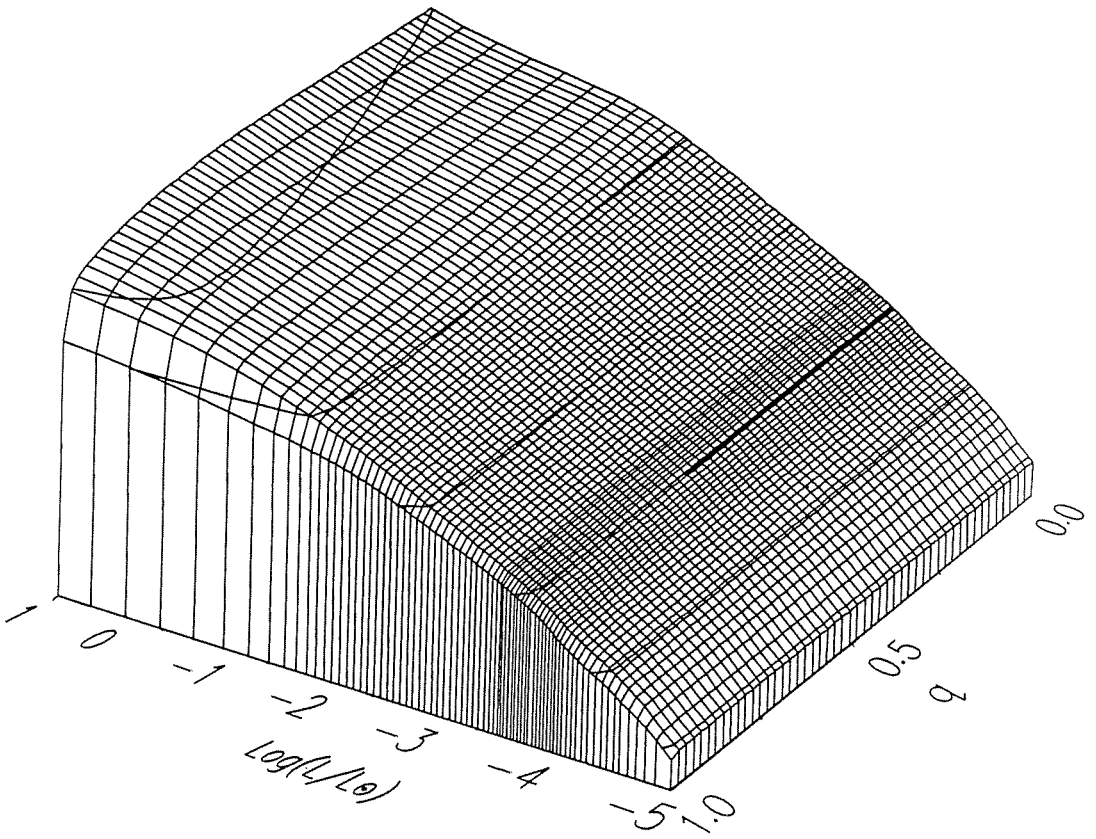

Figure 3.5: Interior Surface Plot of $\log(T)$ *vs.* q and $\log(L/L_{\odot})$. Note the core temperature inversion at the highest luminosities (back corner) caused by neutrino energy losses. Once the core is cool enough that neutrinos are no longer a factor, the interior temperature structure becomes nearly isothermal for the remainder of the evolution. In this Figure which does not include the envelope, we can only see the beginnings of the sharp temperature drop in the last mass shell (but see Figure 3.7).

plasmon neutrinos; contributions by bremsstrahlung neutrinos and pair-process neutrinos, however, are non-negligible, especially at the highest luminosities. After the neutrino regime, the interior temperature is nearly constant for most of the mass of the star, but drops precipitously through the envelope (we see only a hint of this in this interior plot).

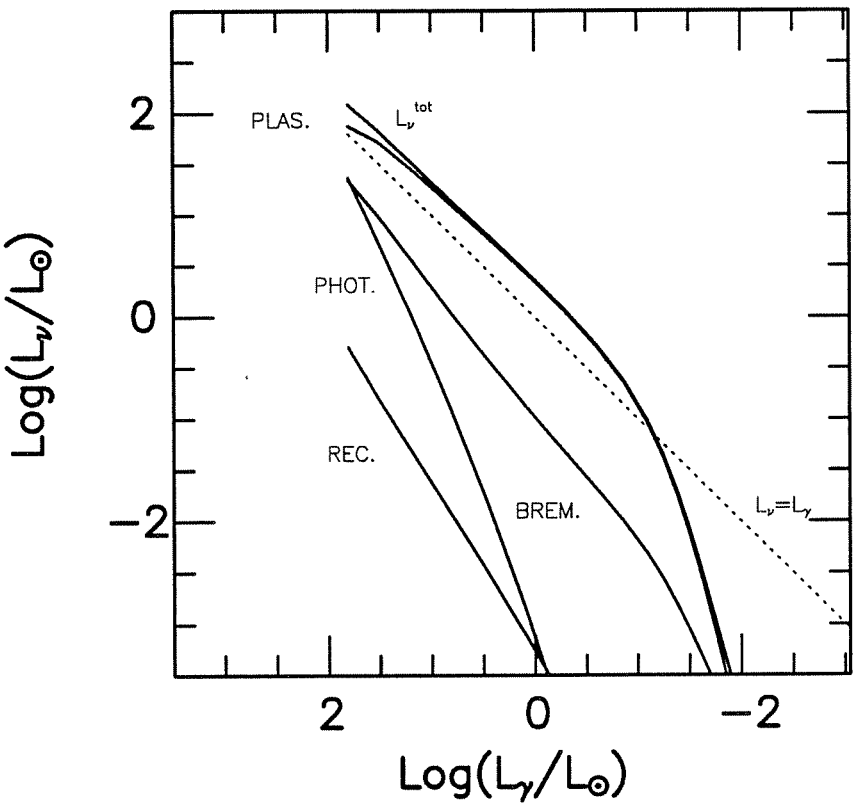

Figure 3.6: Fractional Contributions of the Various Energy Loss Mechanisms for the Hottest Models. We see that for our models, the plasmon neutrinos provide the largest contribution to the neutrino emission.

We next show the envelope surface plot of $\log(T)$ in Figure 3.7. A number of features are notable in this Figure. Again we start at the high-luminosity end where we clearly see the core temperature inversion as a folding over of the surface at the back corner. We see in the contour lines the growth of the isothermal core. In the outer envelope, we see effects of the second and first ionizations of helium moving inward in mass as the luminosity drops below $\log(L/L_{\odot}) \approx 0$. These ionization zones merge at $\log(L/L_{\odot}) \approx -1.7$ as the result of increased pressure ionization. As we would expect, these ionization fronts coincide with regions of convective instability, and efficient convection causes a steeper temperature gradient — the convective region is clearly visible as a depressed region in the Figure (cf. the envelope evolution plot in Figure 3.4), and the post crystallization models show the effects of the degeneracy boundary pushing out the base of the convection zone. Because the base of the convection zone becomes (weakly) degenerate at $\log(L/L_{\odot}) \sim -3$, the temperature gradient flattens somewhat as a function of the increasing degeneracy. Noting the behavior of the contour lines in the coolest models, we find that they follow the behavior of the core temperature T_c as we discussed above (cf. Figure 3.2); specifically, the overall decline in the temperature profile is slowed up first in the crystallization process and second as the heat capacity begins to drop and the thermal energy is in effect forced out. In the last few models the temperature profile again drops rapidly with luminosity as the core moves well into Debye cooling regime and as the base of the convection zone becomes more strongly degenerate. These effects are most easily seen by looking first at the feature caused by the temperature depression corresponding to the inward-moving convection zone base [near $\log(L/L_{\odot}) \approx -2$] and then at the cool end of the sequence.

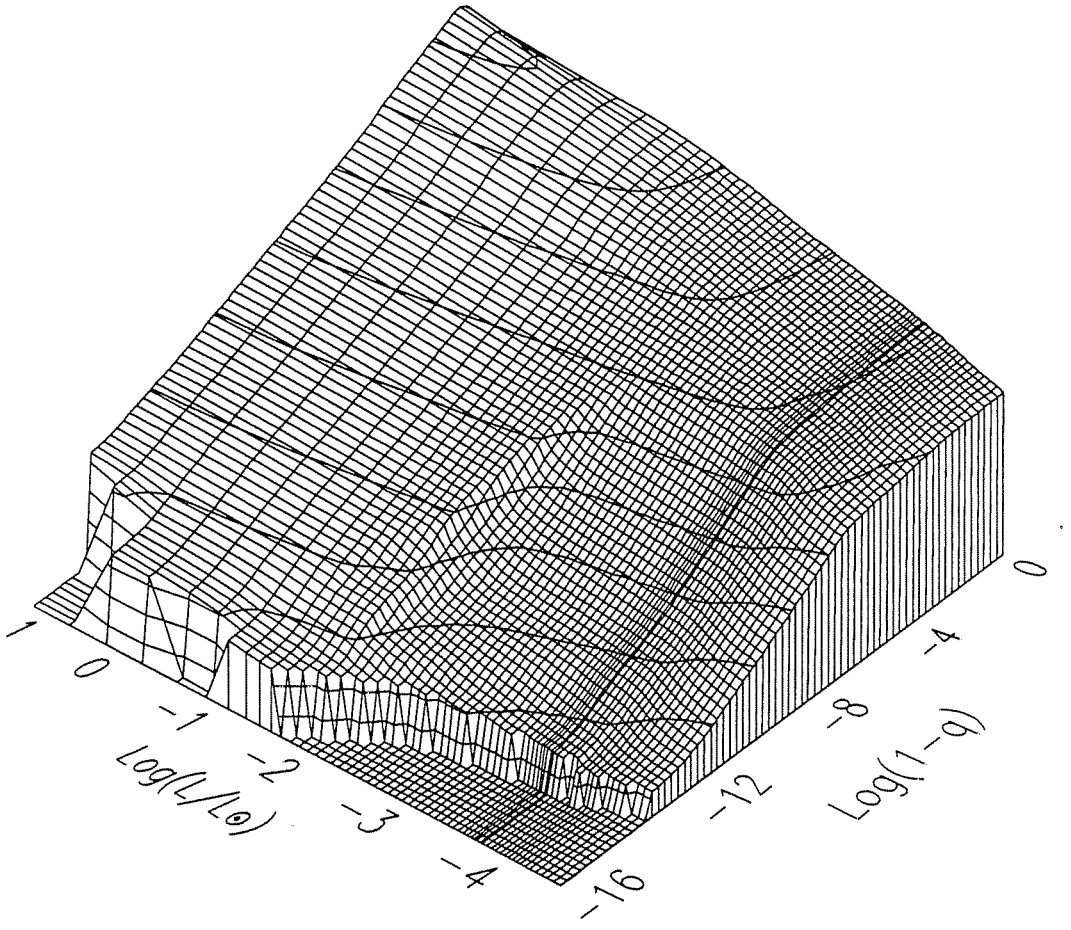

Figure 3.7: Envelope Surface Plot of the Logarithm of the Temperature. The core temperature inversion is apparent in the cores of the high-luminosity models, the growth of the isothermal cores is reflected in the contour lines, and the convection zone is apparent as the large depressed region in the outer envelope (cf. Figure 3.4).

3.4.3 *Density, Pressure, and Radius*

In the next two Figures, we show the behavior of $\log(P)$ and $\log(\rho)$ in the envelope surface plots in Figures 3.8, and 3.9, respectively. We see that, as expected, the pressure and density structures change very little during the evolution of the model. The initial contraction causes the pressures and densities to increase globally at high luminosities. Once the contraction phase is over, the subsequent evolutionary changes in the plot of pressure are small, as we would expect for a constant-radius object in hydro-static equilibrium; there is only a modest increase in the outer envelopes of the cool models. Because the outer envelopes are well approximated by an ideal gas equation of state, it follows that for the pressure to remain relatively constant while the temperature decreases (as we saw in Figure 3.7), the density must increase. We see just such an increase in Figure 3.9.

3.4.4 *Entropy*

Itself proportional to the logarithm of the number of states in the system, the entropy and specifically its change with time reflect the evolution through stellar structure equation (1.20) relating the luminosity of the star $L_\star$ to $T\frac{\partial s}{\partial t}$ (recall the discussion in the Mestel section above). We show the interior surface plot of the logarithm of the entropy in Figure 3.10. The entropy is relatively constant over the degenerate interior but increases in the outer few percent (in mass) of the model where the degeneracy is lower. The entropy is also only slowly declining with evolution until the onset of crystallization. The freezing is a first-order phase transition from liquid metal to solid, and acts as a luminosity source through equation (1.20). The crystallization front proceeds out through the model with only a slight

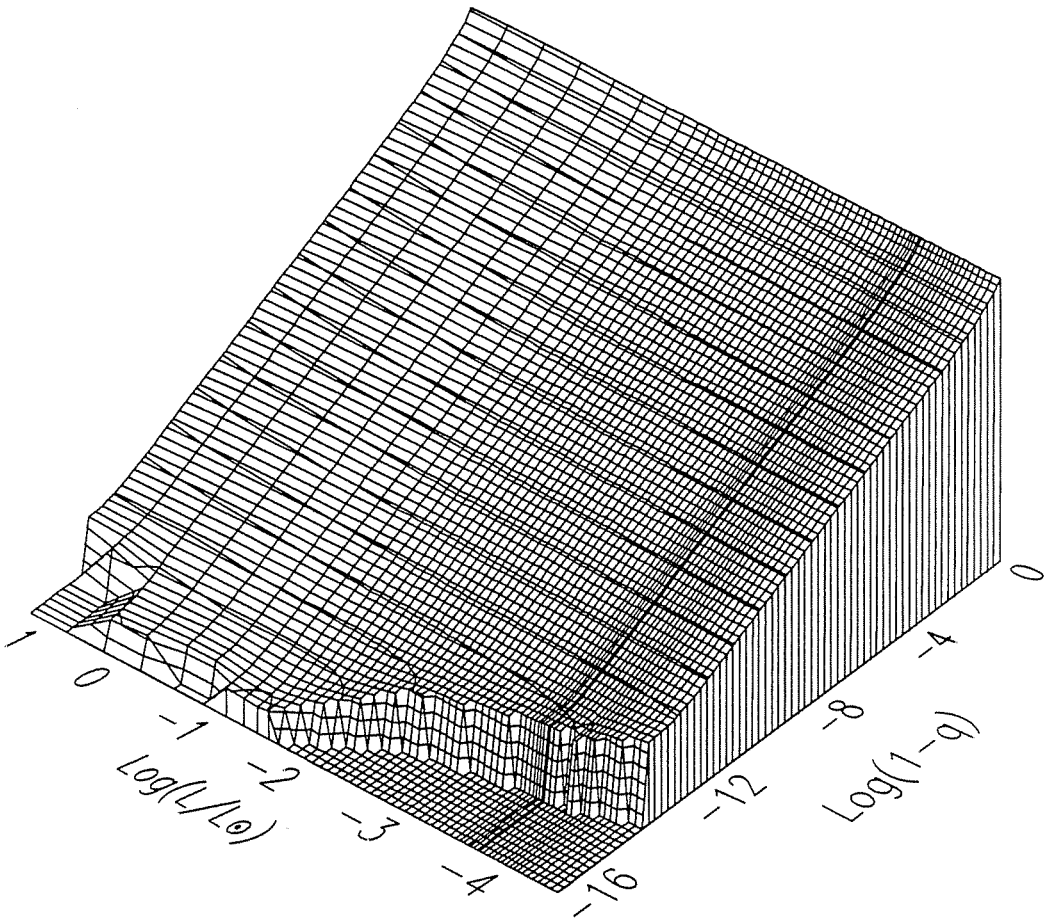

Figure 3.8: Envelope Surface Plot of the Logarithm of the Pressure. This Figure emphasizes that the structure of these models changes very little over the course of the evolution. There is a slight increase in the pressure in the cool models' outer envelopes.

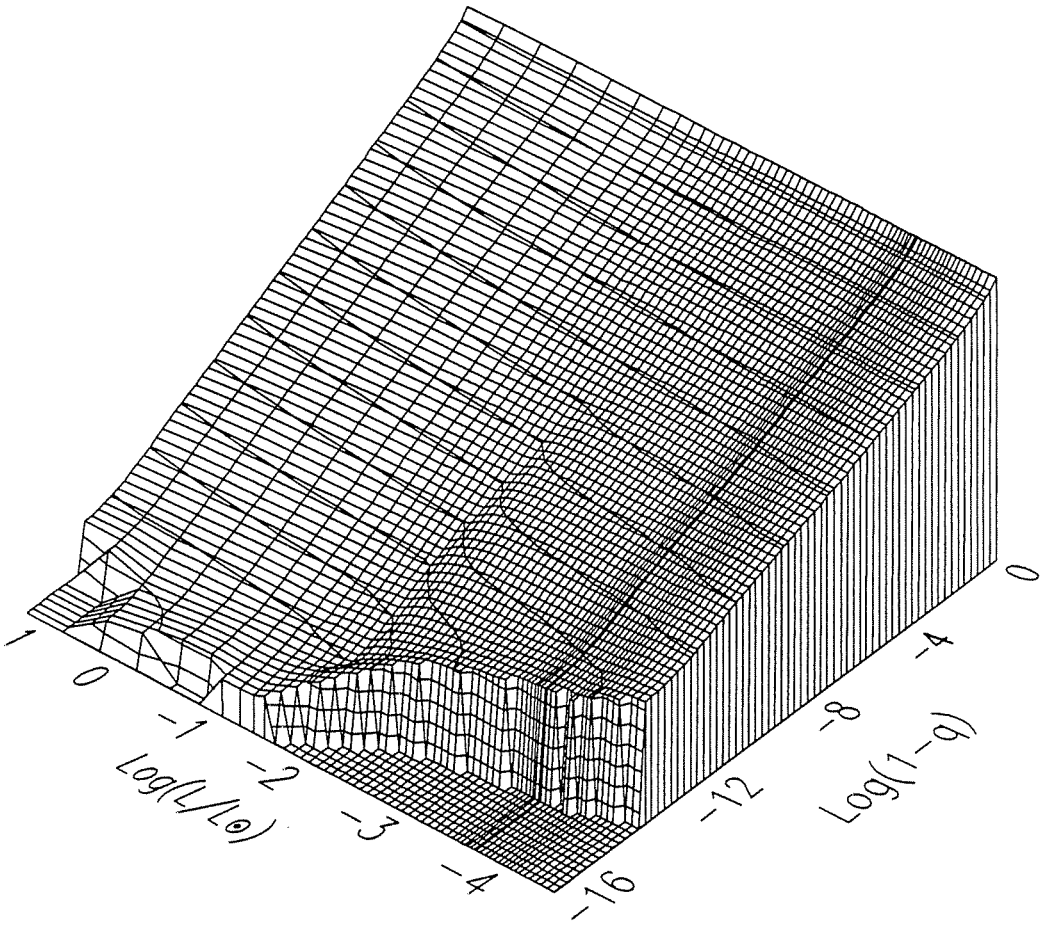

Figure 3.9: Envelope Surface Plot of the Logarithm of the Density. The dominant feature in this plot is the density enhancement in the convection zone. The density structure of the degenerate interior is only a weak function of luminosity, as expected.

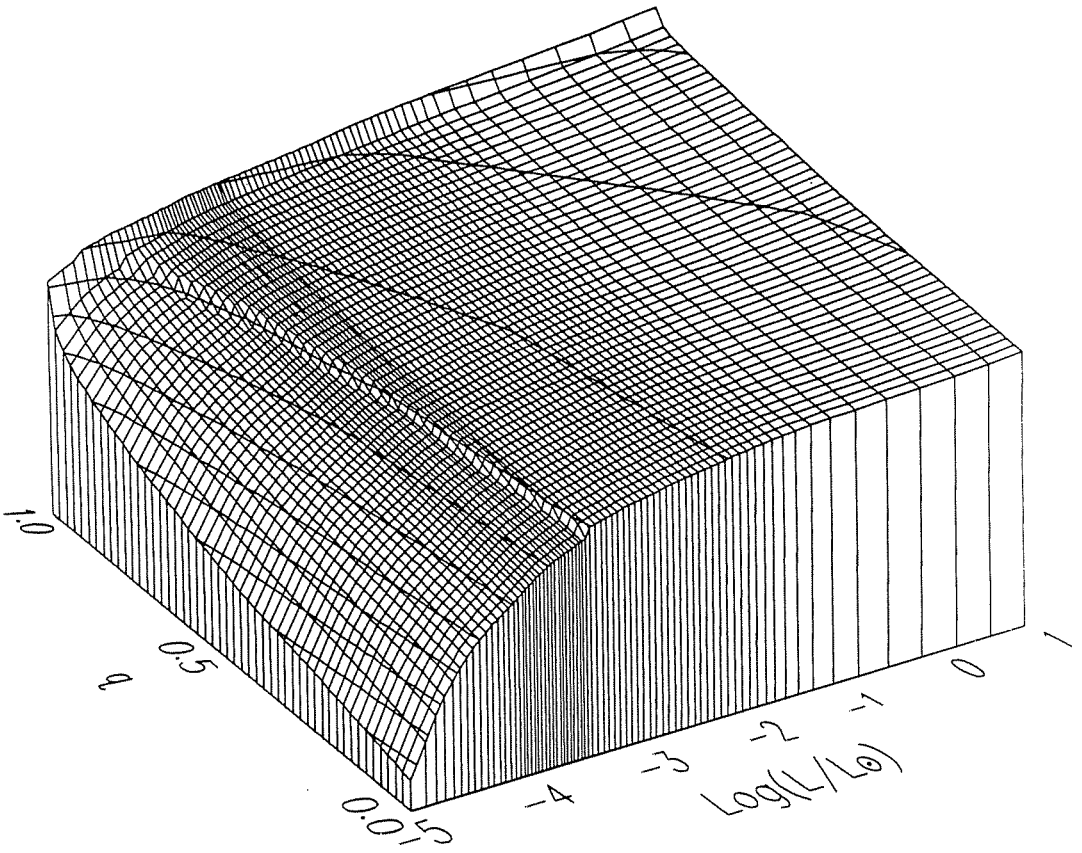

Figure 3.10: Interior Surface Plot of the Logarithm of the Entropy. The entropy is only slowly declining with luminosity until the crystallization jump. This jump and the subsequent overall decline in the Debye cooling phase act as luminosity sources through (1.20). Note the change in axes.

increase in the local entropy, and as the front advances outward in the models, the size of the entropy discontinuity across it increases and the rate of advancement slows, both reflecting the transition to a pure-C composition. After crystallization, the material enters the Debye cooling regime where the heat capacity drops dramatically with temperature, and because the thermal energy is in effect forced out from the model, this too acts to slow the evolution and we see the effect as a small secondary bump in the age–luminosity relation, following the crystallization bump (cf. Figure 3.2).

3.4.5 *Heat Capacity*

The quantity $C_V T$ is a measure of the thermal energy stored per gram of material. In Figure 3.11 we show the interior surface plot of the logarithm of the heat capacity. Not surprisingly, the plot looks similar in form to the entropy surface plot (recall that $C_v \equiv \frac{\partial s}{\partial \ln T}|_\rho$). At high luminosities (hence high temperatures) the dominant term in the calculated heat capacity is the electronic contribution. At the high-luminosity end near the half-mass point and evolving outward in cooler models, we see the effect of the transition from gas to dense liquid near $\Gamma \approx 1$. The transition between the two states is smooth, and Figure 3.10 shows that it occurs at approximately constant entropy. The transition is therefore *not* a first-order phase transition and causes no overt modifications to the evolution of the models through the release of latent heat, as is the case when the models crystallize.

In the dense liquid regime, which spans the largest luminosity interval, the heat capacity is relatively constant, changing slowly from that characteristic of an ideal gas ($C_V \approx \frac{3}{2}k$ per ion) to that of a high-temperature solid ($C_V \approx 3k$) (see, for example, Van Horn 1968, 1971). Upon crystallization, C_V decreases by about 5 percent. Afterwards, the heat capacity continues to

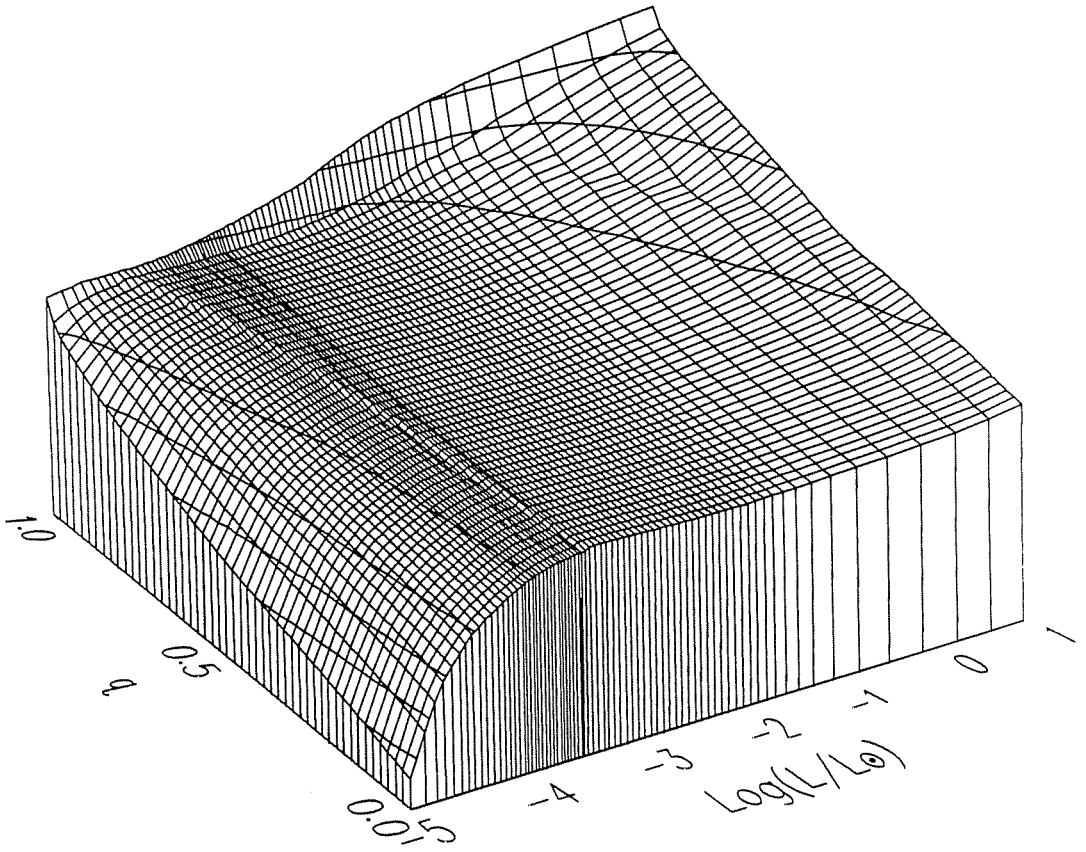

Figure 3.11: Interior Surface Plot of the Logarithm of the Heat Capacity. Near the surface of the high-luminosity models, we see the effect of the gas-to-dense liquid transition near $\Gamma \approx 1$ as an outward-moving bend in the surface plot which falls between the second- and third-highest contour lines. In the dense liquid regime, which spans the largest luminosity interval, the heat capacity is relatively constant, and rises slightly before crystallization. There is a discontinuity in the heat capacity across the crystallization boundary reflecting the discontinuity in the entropy. Once a solid, the heat capacity begins declining as the model enters the Debye cooling regime.

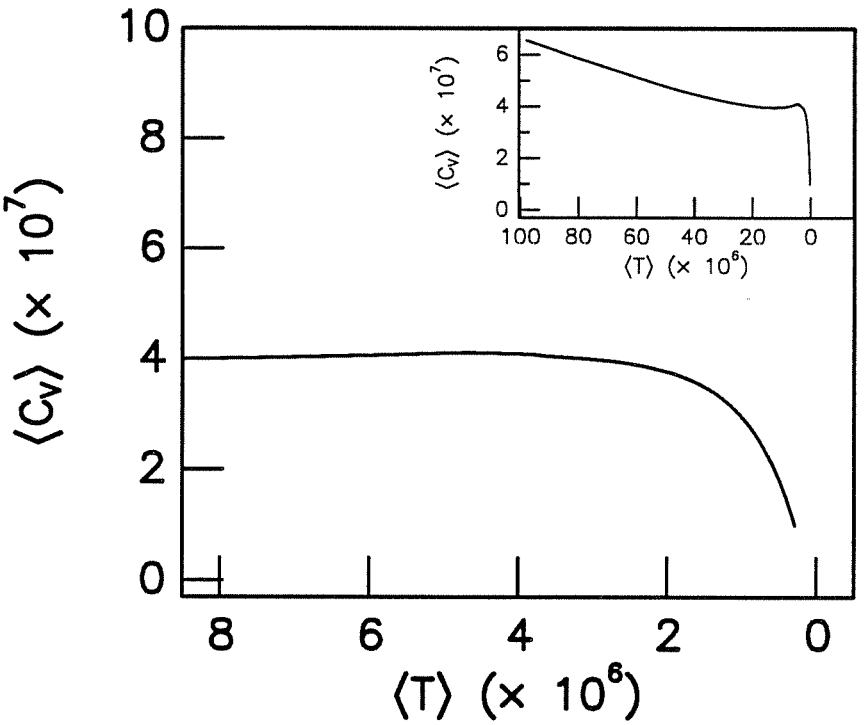

Figure 3.12: Behavior of the Integrated Average Heat Capacity Over the Evolution of the Sequence. In this Figure we show the behavior of $\langle C_V \rangle$ over the evolutionary sequence as a function of $\langle T \rangle$ (*inset*), and in the coolest models only (*main panel*). The integrated heat capacity plummets for temperatures approaching zero. Note however that because we are plotting the integrated average, even in the coolest models the heat capacity is not falling as T_c^3, but more nearly as T_c.

decline as excitation of the higher phonon energy levels becomes impossible, but note that in contrast to the entropy (Figure 3.10), the heat capacity remains relatively constant during the crystallization epoch, and does not begin its rapid decline until crystallization is nearly complete. As we discussed above, the temperature dependence in the Debye cooling regime formally goes as T^3. We show the behavior of the integrated average heat capacity, $\langle C_V \rangle$, of the fiducial model as a function of the integrated average temperature, $\langle T \rangle$, in Figure 3.12, and find that as the temperature goes to

zero, the integrated heat capacity falls more as a linear function of T than as T^3.

3.4.6 *Opacity*

The rate at which the internal energy is released from the surface of the star is intimately related to the opacity of the stellar material over the structure of the model. The interiors of the models are strongly degenerate and the material therefore highly conductive; hence, the conductive opacities (Itoh *et al.* 1983, 1984; Hubbard and Lampe 1969) determine the interior temperature structure. The envelope is non-degenerate and the controlling opacities are the radiative opacities (Huebner 1980, Cox and Stewart 1970). We show the interior surface plot of the logarithm of the total opacity in Figure 3.13. Although flaring up in the envelope, $\log(\kappa)$ is relatively constant (and low) in the degenerate interior, increasing with decreasing density and increasing temperature. The controlling opacity in the interior is the conductive opacity, and as we noted above we are using the fitting formulae of Itoh *et al.* (1983) for the dense liquid regime and those of Itoh *et al.* (1984) for the solid regime. There is a factor of ~2–4 drop in the opacities at the crystallization front as a result of accurately taking into account the Debye-Waller factor (see Itoh *et al.* 1984 for details). Further, the opacities continue to decrease in the Debye cooling regime as the Coulomb parameter Γ increases.

In Figure 3.14, we show the envelope surface plot of the total opacity. We see here the steep rise in the opacities in the non-degenerate envelope. In the outer layers of the hottest models the helium is fully ionized and the opacity is dominated by electron scattering processes. In slightly cooler models, we see the opacity ridges corresponding to the two ionization stages of helium.

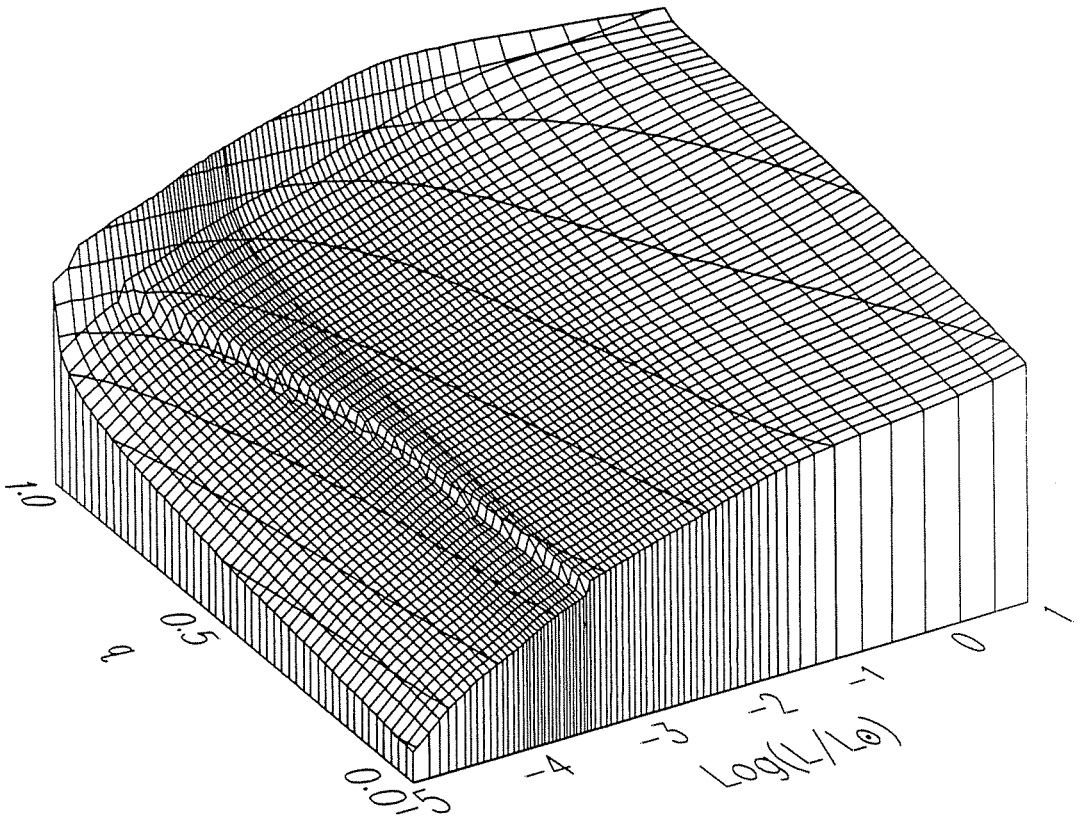

Figure 3.13: Interior Surface Plot of the Logarithm of the Opacity for the Fiducial Model Sequence. As discussed in the text, we see the opacity increasing for decreasing luminosity and for increasing temperature, and a discontinuity in the opacity at the crystallization front.

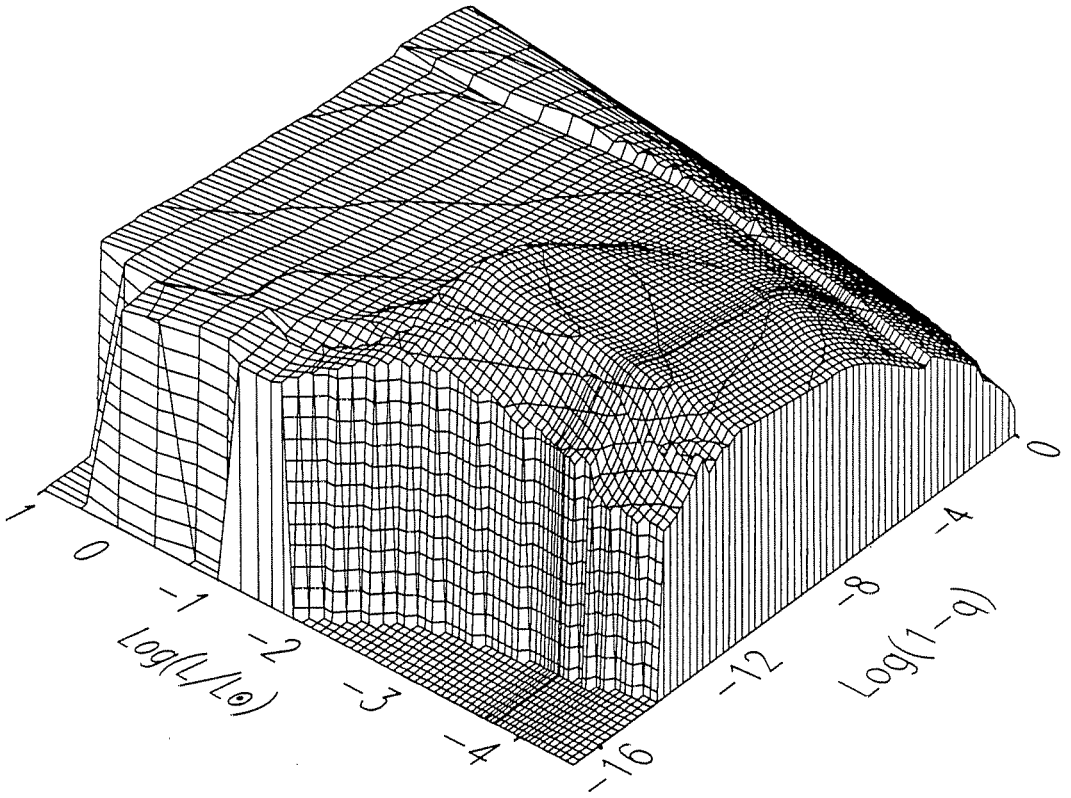

Figure 3.14: Envelope Surface Plot of the Logarithm of the Opacity. At the highest luminosities the opacity in the envelope is relatively constant. The opacities are largest at the ionization front as it begins progressing inward in mass in slightly cooler models, and the opacity maximum digs deep when the model get to $\log(L/L_{\odot}) \approx -2$.

The opacities are at their largest and the adiabatic temperature gradients are at their lowest in regions of partial ionization, and as is well known, matter in this state violates the Schwarzschild convective stability criterion that $\nabla < \nabla_{\rm ad}$ in regions of convective stability. It is the resulting surface convection zone that is the cause of the plateaus we discussed in the envelope temperature plot above (Figure 3.7). Near $\log(L/L_{\odot}) \approx -2$, the opacity maximum digs deep into the star and brings the convection zone with it. Once the material is convective, the temperature gradient is adiabatic and the magnitude of the opacities only matters in determining the convective velocities. Note that in the low-luminosity models, the envelope opacities are lower, suggesting that convection may be somewhat less efficient there, although the temperature structure remains fully adiabatic and convection still carries 100% of the flux. Tassoul, Fontaine, and Winget (1990). plot convective velocities in their evolutionary models and in their Figures 19a and 19b show that the convective velocities are relatively small in the the envelopes of the coolest models. Look back at Figure 3.4 and note that the photosphere in the cool models is formally outside the convective region. Although we expect that some mixing should occur from overshooting (in particular, the densities are high), and that the in a non-gray atmosphere the photosphere would be further out in mass, it is interesting to speculate that some fraction of the remaining (or accreted) hydrogen can exist in this radiative region, unmixed with the convection zone below. This may help explain the observations of Bergeron *et al.* (1990) who found that all the cool DA stars they observed show spectral evidence for a significant helium mass fraction. Their observations further support the idea that most if not all white dwarf stars have hydrogen-layer masses $\log(M_{\rm H}/M_{\star}) \lesssim -11$.

3.4.7 *Temperature Gradients* ∇ *and* $\nabla_{\rm ad}$

By examining the behavior of the true ($\nabla \equiv \frac{d\ln T}{d\ln P}$) and adiabatic ($\nabla_{\rm ad} \equiv \frac{d\ln T}{d\ln P}\Big|_{\rm ad}$) temperature gradients in the envelope we learn of the convection zone structure of the models. As the well-known Schwarzschild criterion states, regions where $\nabla_{\rm ad} < \nabla_{\rm rad}$ are convectively unstable and through convective energy transport rapidly establish an adiabatic temperature gradient. We show the evolution of ∇ and $\nabla_{\rm ad}$ in the envelope surface plots in Figures 3.15 and 3.16, respectively. The core temperature inversion causes negative values of ∇ and so has a dramatic effect in the cores of the highest luminosity models (however note that in the interior $\nabla_{\rm rad} < \nabla_{\rm ad}$, always). Also in the interior region, we see a plateau in $\nabla_{\rm ad}$ after crystallization resulting from the near equality of C_P and C_V in solids (see Landau and Lifshitz, 1980, p. 195). The progression of the front does not continue into the envelope because crystallization is not included in the envelope equation of state. Indeed, in models cooler than this, the mass shells at base of the envelope use thermodynamic quantities which are extrapolated off the envelope EOS table, and as a result are correspondingly noisy. This extrapolation is relatively stable when we compute models with discontinuous He/C transitions, but gives unsatisfactory results when computing models with composition transition zones that approximate diffusive equilibrium, because these must rely on interpolations in the extrapolated quantities (see §5.1.5 below).

In the outer envelopes of the hottest models in Figure 3.15 the helium is fully-ionized to the photosphere and ∇ is relatively constant throughout, but with a ridge corresponding to the transition between He and C. Note that this ridge decreases in size as the He/C boundary becomes strongly

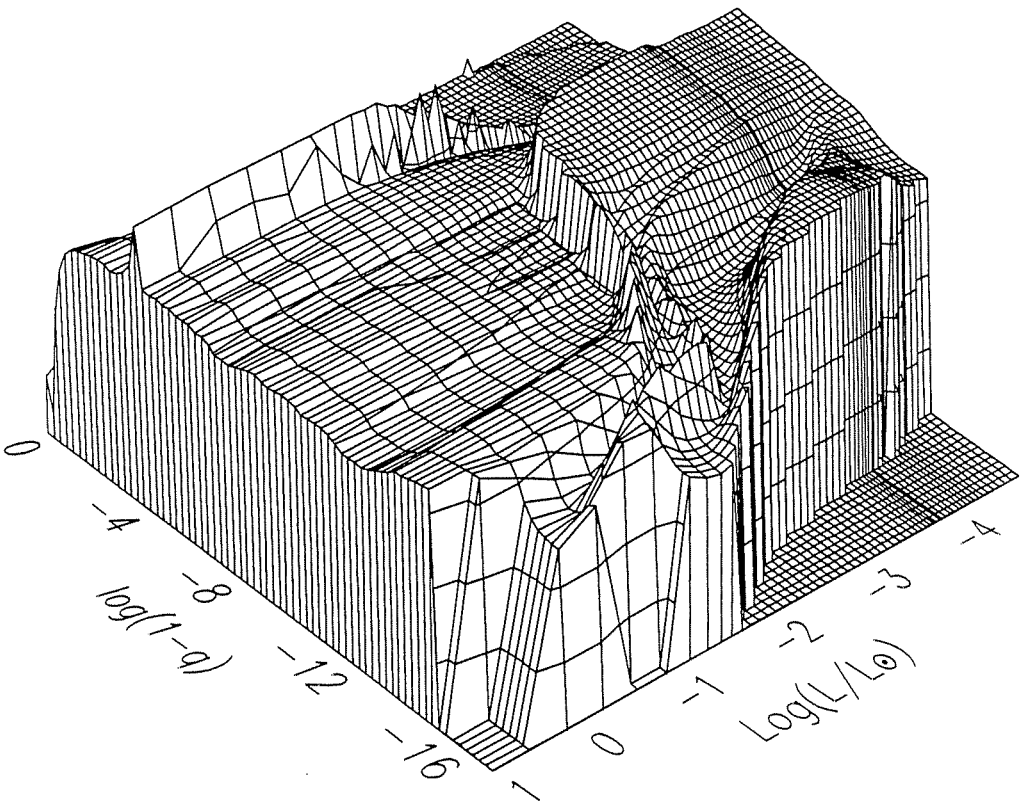

Figure 3.15: Envelope Surface Plot of ∇. The true temperature gradient is relatively constant in the envelope at high luminosities. The base convective region is easily discerned as the plateau in the Figure, and the He/C transition discontinuity is also readily apparent in the hotter models.

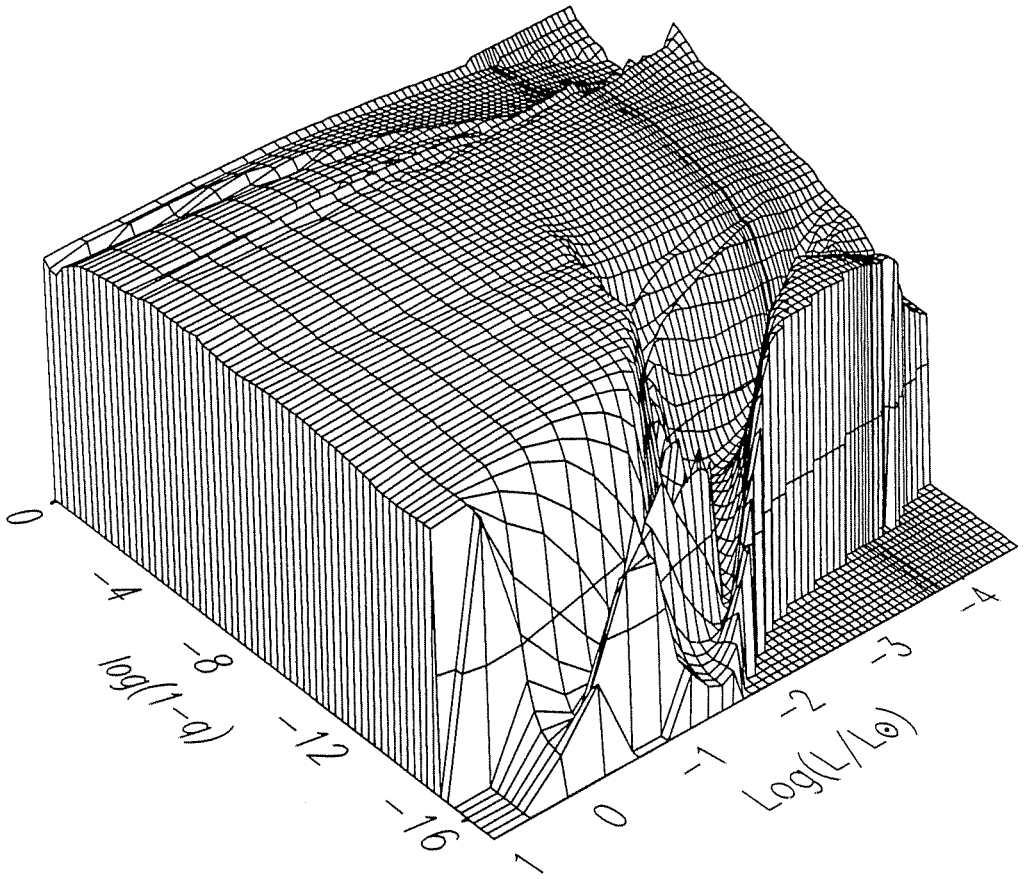

Figure 3.16: Envelope Surface Plot of ∇_{ad}. The adiabatic temperature gradient is relatively constant in convectively stable regions. In regions of partial ionization, however, ∇_{ad} drops significantly. Compare with the envelope surface plot of the opacity (Figure 3.14).

degenerate, thus flattening the temperature profile. The partial ionization regions begin moving inward in mass and are reflected as ridges in the temperature gradient. The outline of the convective region is clear as is the ridge corresponding to first ionization. Although the vertical scales in the two Figures are very different, we can see that the ridges and depressions in the convective region of Figure 3.15 correspond to the the depressed region in the envelope surface plot of ∇_{ad} (Figure 3.16). The adiabatic temperature gradient is low in regions of partial ionization because small increases in pressure act more to increase the ionization fraction than to increase the temperature. In the plot of ∇_{ad}, we find a plateau near the surface of the convective region. This region is fully convective, but not strongly because the atoms are only incompletely ionized. Because of this, the convective velocities are very low and the temperature gradient is essentially the radiative temperature gradient ($\nabla \approx \nabla_{rad}$). As the models cool further, the densities increase (at a fixed mass envelope mass) thus pushing the ionization front out towards the surface again.

4. Variation of Model Parameters and Constitutive Physics

4.1 Variation of the Model Parameters

In this chapter we intercompare the results of our sequences. In the sections below, we discuss the effects of variations in stellar mass, core composition, surface layer masses, composition transition zone profiles, and the effect of convective mixing. In particular, we are interested in the effects that these variations have on the age–luminosity relations for the models. The large number of sequences preclude an exhaustive intercomparison, but we have included summary listings of most of the sequences we discuss in the Appendix. We also include a brief discussion of our nomenclature there, and suggest that you may wish to review this discussion now before proceeding.

4.1.1 *Variations in Stellar Mass*

We now discuss the effects on the evolutionary time scale of variations in the stellar mass, and begin by showing in Figure 4.1 the H–R diagram of these sequences including age contours. In this Figure, we see that as a

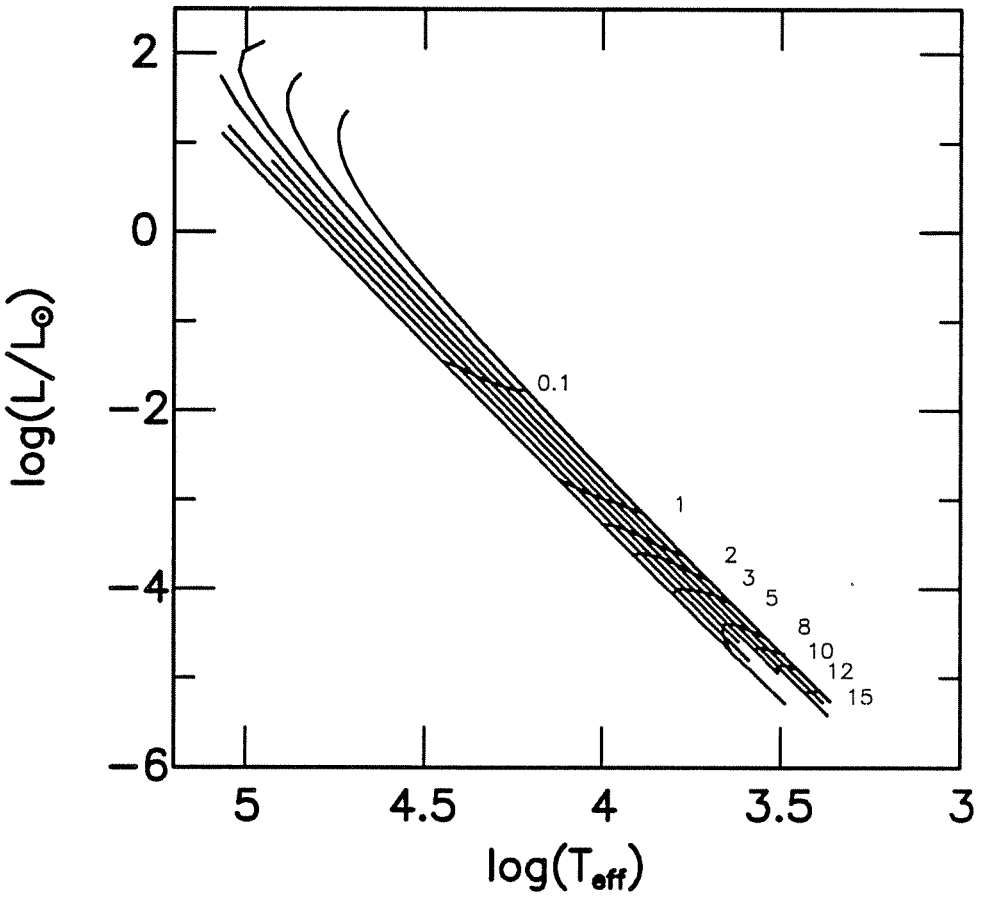

Figure 4.1: Hertzsprung–Russel Diagram of the C/O Model Sequences. We show in this Figure the luminosity–effective temperature tracks of C/O core sequences calculated with the fiducial C/O profile for masses of 0.4–1.0 $M_{\odot}$, sampled at intervals of 0.1 $M_{\odot}$. Also shown are age contours (in units of 10^9 yr) spanning the range 0.1 Gyr to 15 Gyr.

function of luminosity, the low-mass models initially evolve the most quickly because of their lower neutrino luminosities, larger radii, and lower total thermal heat content. The age contours show that this trend reverses once

the more massive models begin crystallizing, and we see clearly the effects of Debye cooling in these models.

In Figures 4.2 to 4.4, we show the evolutionary summary diagrams of DB sequences of masses 0.4, 0.8, and 1.0 $M_\odot$ calculated with the fiducial interior composition profile [see equation (3.1) and Figure 3.1], helium layer masses of 10^{-4} $M_\odot$ and discontinuous He/C transition zones. In addition to the Figures, we present evolutionary summary listings in the Appendix for sequences of mass 0.4 to 1.0 $M_\odot$ sampled at intervals of 0.1 $M_\odot$ (Tables A.2 to A.7).

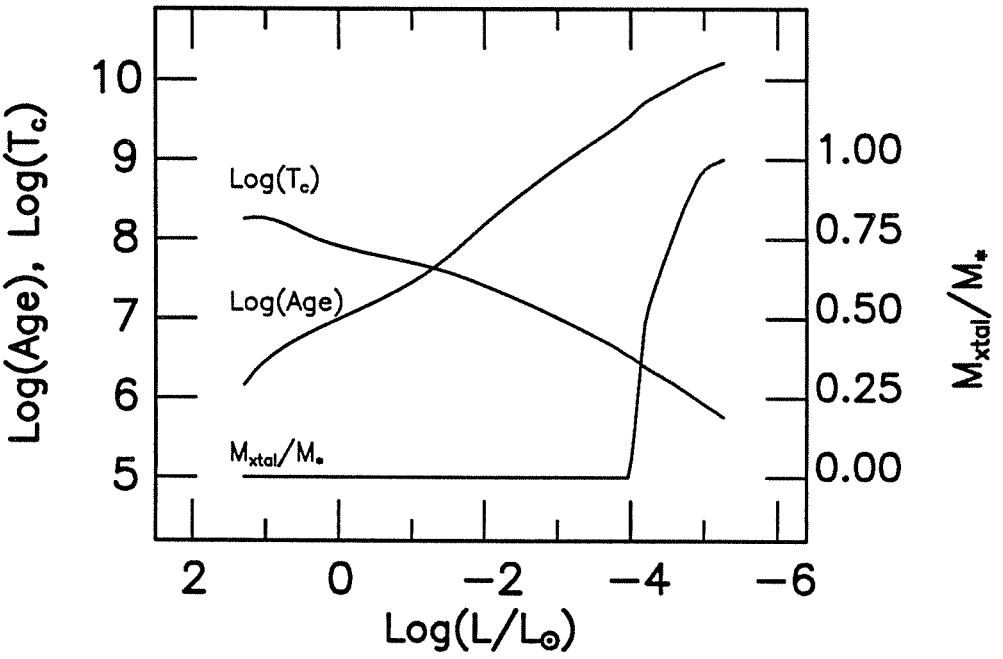

Figure 4.2: Similar to Figure 3.2, but for a 0.4 $M_\odot$ model sequence.

As we inspect the Figures, we see that the core temperature at a given luminosity is a function of mass. At high luminosities, the more massive models have *lower* core temperatures at a given luminosity resulting from

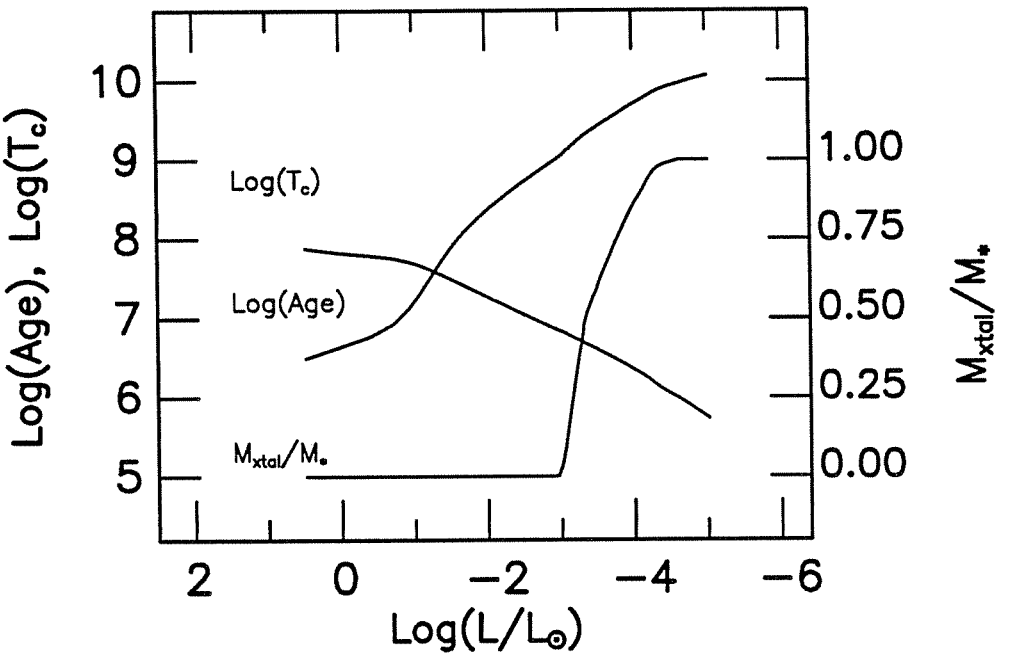

Figure 4.3: Similar to Figure 3.2, but for a 0.8 $M_\odot$ model sequence.

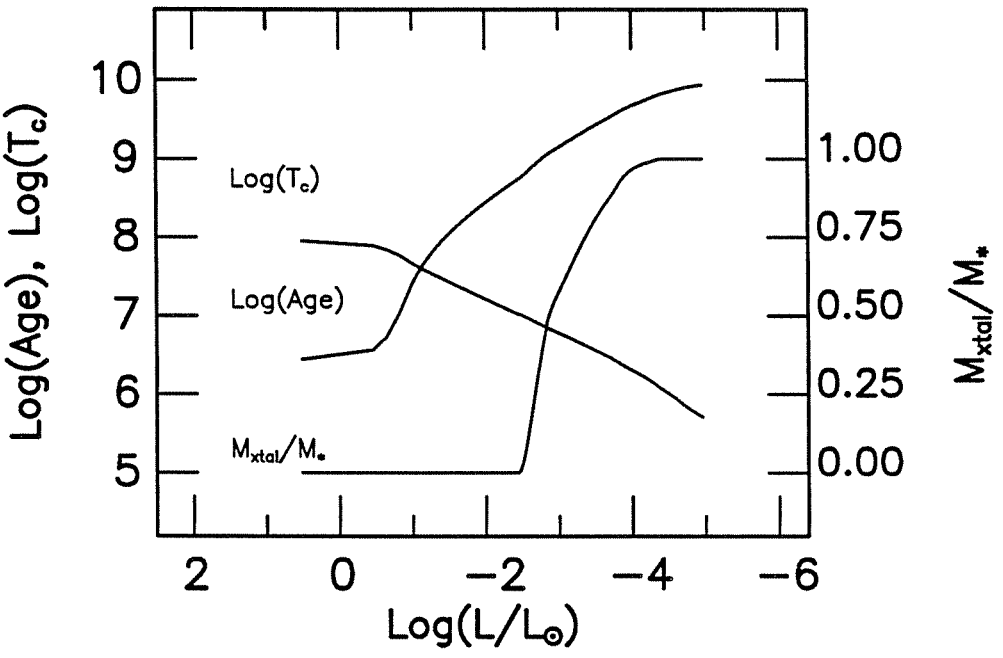

Figure 4.4: Similar to Figure 3.2, but for a 1.0 $M_\odot$ model sequence.

enhanced neutrino emissions. At $\log(L/L_\odot) \approx -0.8$, all the sequences have approximately the same effective temperature (~30,000–40,000 K) as the neutrino luminosity becomes negligible. Below this luminosity, the models are in the Mestel regime, and the core temperatures of the lower-mass models are again larger at a given luminosity as a result of both the lower overall degeneracy (and hence larger conductive opacity), and also the larger fractional mass of the non-degenerate, high-radiative-opacity surface layers. These opacity effects are also apparent in the T_c–$T_{\rm eff}$ relation (see the Tables in the Appendix) where we find that the contrast between the core and surface temperatures is larger in lower-mass models. The core temperatures of the higher-mass models remain below those of the lower-mass models through the Debye cooling regime.

Because higher-mass models have both greater neutrino and photon luminosities, they evolve very quickly at high luminosities, and so are younger at a given luminosity than the lower-mass models. There is a general crossover in the age–luminosity relations at $\log(L/L_\odot) \approx -1.5$ (*i.e.*, for a white dwarf cooling time $t_{\rm cool} \approx 7\times10^7$ Gyr) as the neutrinos cease to be an important energy-loss mechanism. In the Mestel regime, the more massive models are older at a given luminosity because first their greater mass means that their thermal reservoir is larger, and second because their radius is smaller and hence their luminosity at a given effective temperature is less.

Because the central pressures are higher and the core temperatures lower, the more massive model sequences begin (and finish) crystallizing at significantly higher luminosities than lower-mass sequences. For example, the 1.0 $M_\odot$ sequence x10400b begins crystallizing at $\log(L/L_\odot) \approx -2.5$ ($T_{\rm eff} \approx 15{,}100$ K; $t_{\rm cool} \approx 0.6$ Gyr) and is nearly completely crystallized at $\log(L/L_\odot) \approx -4.2$ ($T_{\rm eff} \approx 5800$ K; $t_{\rm cool} \approx 5.6$ Gyr). The 0.4 $M_\odot$ sequence,

on the other hand, begins crystallizing at $\log(L/L_{\odot}) \approx -4.0$ ($T_{\rm eff} \approx 4750$ K; $t_{\rm cool} \approx 3.7$ Gyr) and is nearly completely crystallized at $\log(L/L_{\odot}) \approx -5.2$ ($T_{\rm eff} \approx 2380$ K; $t_{\rm cool} \approx 16$ Gyr. At the luminosity corresponding to the onset of crystallization in the 0.4 $M_{\odot}$ model, the 1 $M_{\odot}$ sequence is already greater than 90% crystallized and bound for the Debye cooling regime. As a result, although the total latent heat released in the two sequences is comparable — scaling approximately with mass — the effect on the age–luminosity relation is greater in the lower-mass models because the energy is released at a significantly lower luminosity. In general, we find that the parameter which controls the effect of crystallization on cooling times is the luminosity at which it occurs.

Finally, we discuss the radii of the models as a function of mass. In determining mass distributions observationally, it is standard procedure to assume that the stars follow the mass–radius relation of the zero-temperature (completely degenerate) Hamada and Salpeter (1961) carbon-configurations. In general, the models all asymptotically approach the radius of a zero-temperature configuration, but on a timescale which is a function of the mass. The higher mass models have smaller radii, of course, and approach their final radii more quickly. To give a specific example the 1 $M_{\odot}$ model compresses to within ~5% of its minimum radius by $\log(L/L_{\odot}) \approx -0.5$ ($T_{\rm eff} \approx 47{,}000$ K; $t_{\rm cool} \approx 4 \times 10^6$ yr) whereas the 0.4 $M_{\odot}$ model doesn't compress to within 5% of the zero temperature radius until $\log(L/L_{\odot}) \sim -2.4$ ($T_{\rm eff} \approx 11{,}700$ K; $t_{\rm cool} \approx 0.3$ Gyr). To show the importance of finite temperature effects, consider that for an object at 15,000 K with a gravity measured to be $\log g \approx 7.7$ (*i.e.*, characteristic of a 0.4 $M_{\odot}$ object), neglecting the finite temperature effects will cause the derived mass to be systematically low by a few hundredths of a solar mass — quite significant given that the

model-independent scatter in the observed mass distributions is of order $\sigma \approx 0.10$ (Bergeron, Saffer, and Liebert 1990; McMahan 1989; Weidemann and Koester 1984; Oke, Weidemann, and Koester 1984). The mass distribution is now being determined with such precision that these deviations from the zero-temperature radii must be taken into account when converting an observed gravity distribution into a mass distribution.

4.1.2 *Variations in Core Composition*

As we discussed above, the $^{12}C(\alpha,\gamma)^{16}O$ reaction rate is not well determined (Caughlan and Fowler 1988) and so the core C/O profile is not well determined. Given this situation, we felt it best to compute parallel sequences with pure-carbon cores and pure-oxygen cores to insure bracketing the true composition. We show carbon- and oxygen-core sequences of masses 0.4, 0.6, 0.8, 1.0, and 1.2 $M_\odot$ in Figures 4.5 through 4.9, respectively. In addition, we include the evolution summary Tables in the Appendix for masses 0.4 $M_\odot$ to 1.0 $M_\odot$, inclusive, sampled at mass steps of 0.1 $M_\odot$, and also for the 1.2 $M_\odot$ sequences. These are in Tables A.8 through A.23.

In both families of sequences, we see the general behavior as a function of mass which we discussed in the previous section. The core temperatures of the high-luminosity oxygen-core sequences are slightly lower than comparable carbon-core sequences because in general the neutrino losses are greater for higher Z at a given temperature and density. After the neutrino losses cease to be important, the trend reverses, and the oxygen-core sequences have the higher core temperatures below $\log(L/L_\odot) \approx -0.5$.

Because of neutrino losses, the oxygen core sequences in general initially evolve more quickly and are younger at a given luminosity. This trend also

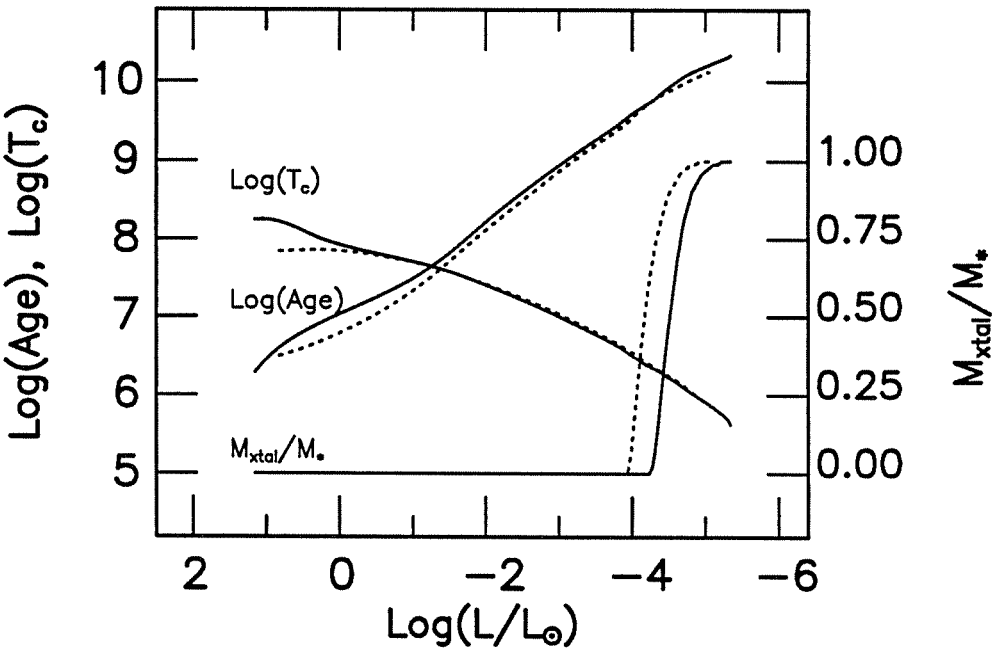

Figure 4.5: Evolutionary Summary Plot for 0.4 $M_\odot$ Carbon-Core and Oxygen-Core Sequences. These models include surface helium layers of mass 10^{-4} $M_\odot$ have the He/C and He/O transitions idealized as a discontinuities. In this and the following Figures, the carbon-core quantities are represented with a solid line, and the oxygen-core quantities with a dotted line.

reverses with the decline of the neutrino luminosity, and the carbon-core sequences remain the older until crystallization. The oxygen-core sequences crystallize at luminosities higher than those with carbon cores, and the release of latent heat slows the evolution enough that they can for a time be older than the others. The trend reverses for the final time shortly after the onset of crystallization in the carbon-core sequences. Although the energy released in carbon and oxygen crystallization is comparable, it is released at a lower luminosity in the carbon-core sequences (by a factor of $\sim \frac{1}{2.5}$ in the 0.6 $M_\odot$ models), and so has a correspondingly larger effect on the age–luminosity relations. For example, the age difference between o6400 and c6400 at $\log(L/L_\odot) = -3.4$ (just before the onset of crystallization

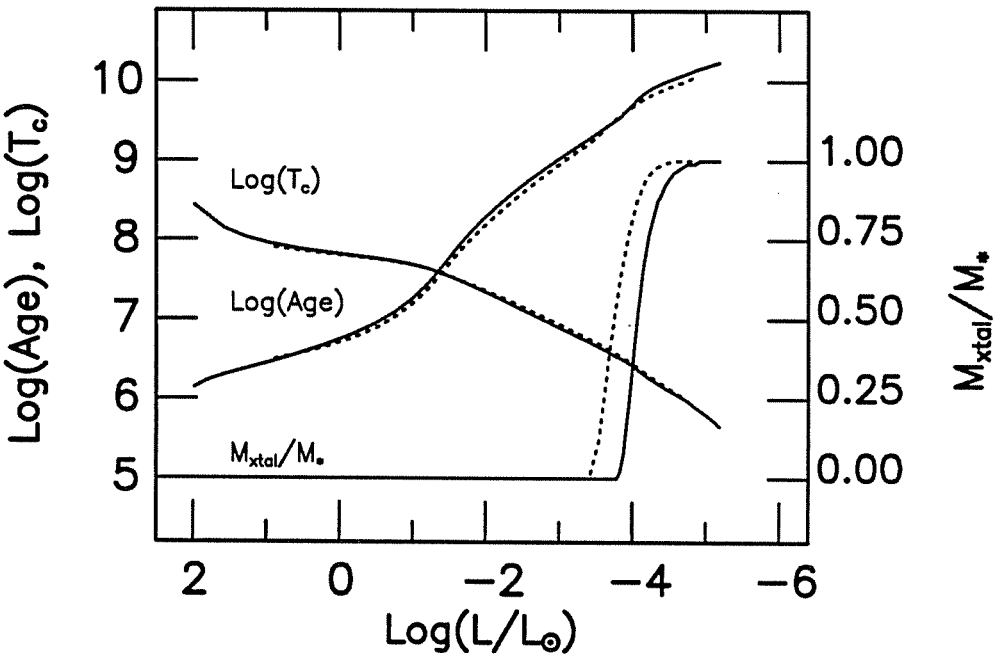

Figure 4.6: Similar to Figure 4.5, but for stellar masses of 0.6 $M_{\odot}$.

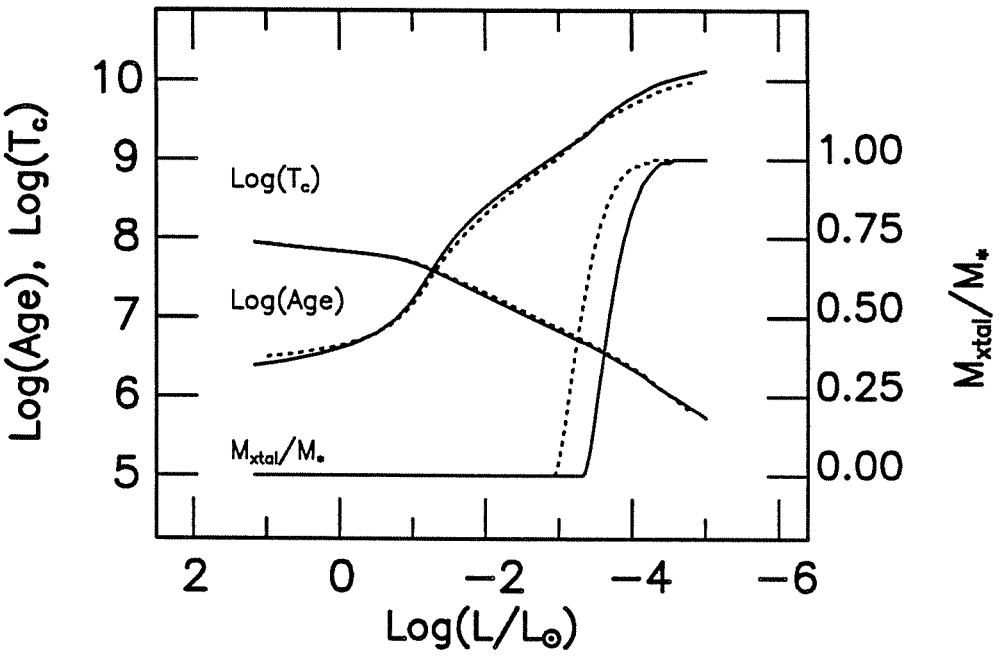

Figure 4.7: Similar to Figure 4.5, but for stellar masses of 0.8 $M_{\odot}$.

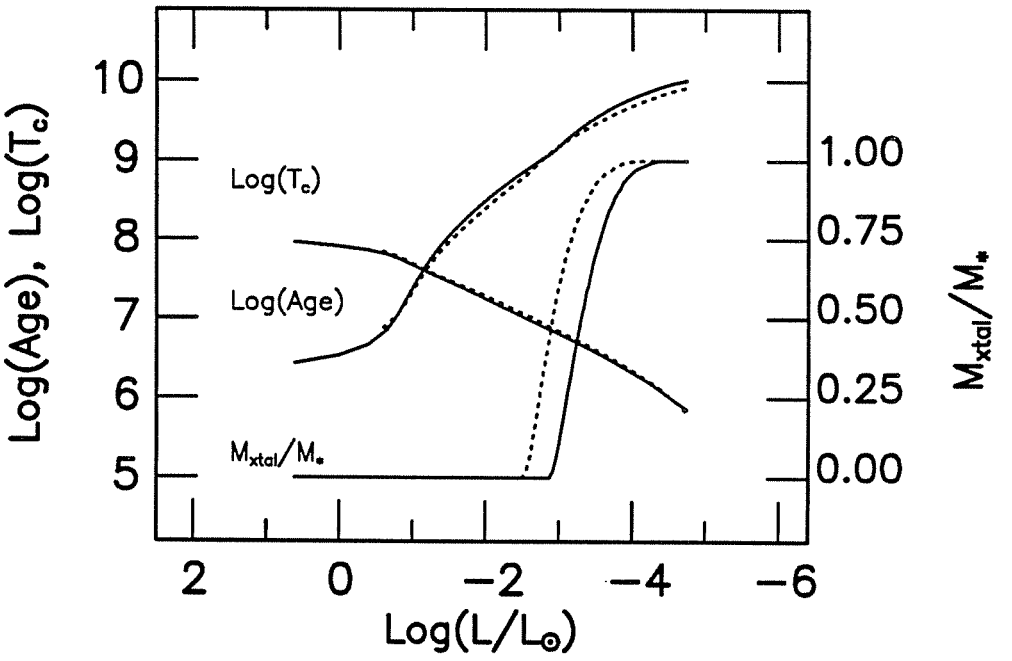

Figure 4.8: Similar to Figure 4.5, but for stellar mass of 1.0 $M_\odot$. The oxygen-core sequence has a surface helium layer mass of $M_{\rm He} = 10^{-5}\ M_\odot$.

in o6400) is $\sim 2.5 \times 10^8$ yr for a fractional age difference of $\sim$15%. At a luminosity of $\log(L/L_\odot) = -5.0$ both are fully crystallized and the age difference is $\sim 2.5 \times 10^9$ yr for a fractional age difference of $\sim$20%.

We discussed in the previous Chapter the particularly central rôles that the entropy s and heat capacity C_V played in the cooling of the models. To show the variations in these quantities as a function of mass, we present the interior surface plots for $\log(s)$ and $\log(C_V)$ for the 0.4 and 1.0 $M_\odot$ carbon-core sequences (*i.e.*, c4400 and c10500). We show the interior surface plots of $\log(s)$ and $\log(C_V)$ for the carbon-core 0.4 $M_\odot$ sequence in Figures 4.10 and 4.11, and for the 1.0 $M_\odot$ carbon-core sequence in Figures 4.12 and 4.13, respectively (comparable plots for the oxygen-core sequences look quite similar to these).

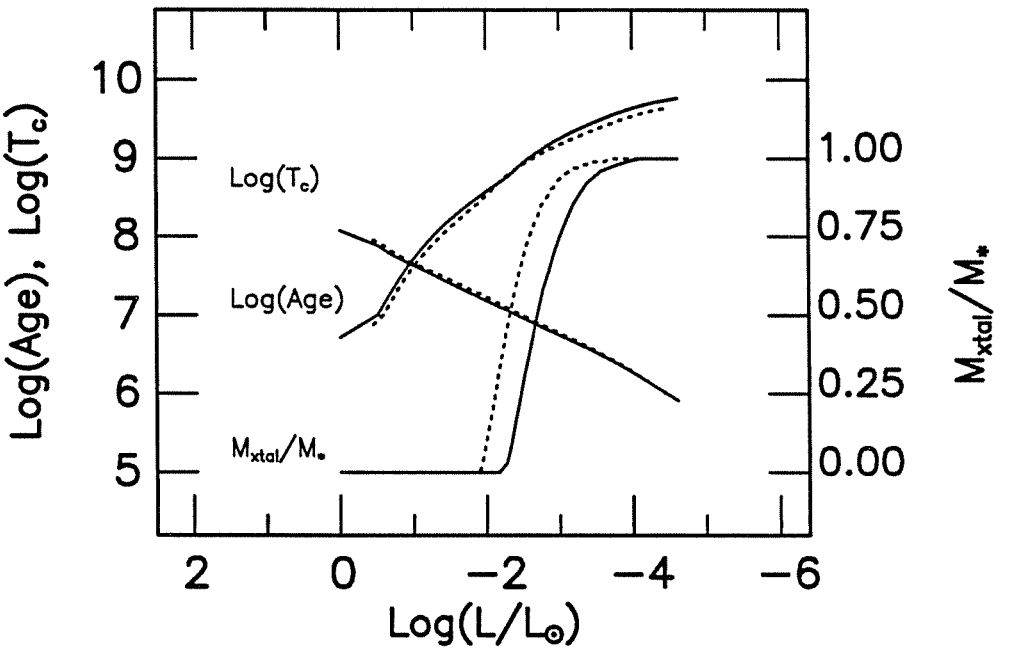

Figure 4.9: Similar to Figure 4.5, but for stellar masses of 1.2 $M_\odot$ and a helium layer masses of $M_{\rm He} = 10^{-5}\ M_\odot$.

Looking first at the run of entropy for the 0.4 $M_\odot$ sequence c4400 in Figure 4.10, we see many similarities with the fiducial sequence entropy plot shown in Figure 3.10. The entropy is only slowly decreasing with cooling in the neutrino and Mestel regimes, and crystallization again causes the jump in entropy from the release of latent heat, although here the luminosity at crystallization onset is lower and the crystallization process spans a smaller luminosity interval. In the Debye cooling regime, the entropy begins to fall off rapidly with decreasing luminosity. Up to this point we have shown only the well-behaved models in a given sequence, but in Figures 4.10 and 4.11 we show all the models down to the coldest converged. In particular, you will note the small discontinuity in the entropy near the end of the sequence (3 models from the last). This jump is non-physical and is most likely the result of the extrapolation off the equation of state for the mass shells at

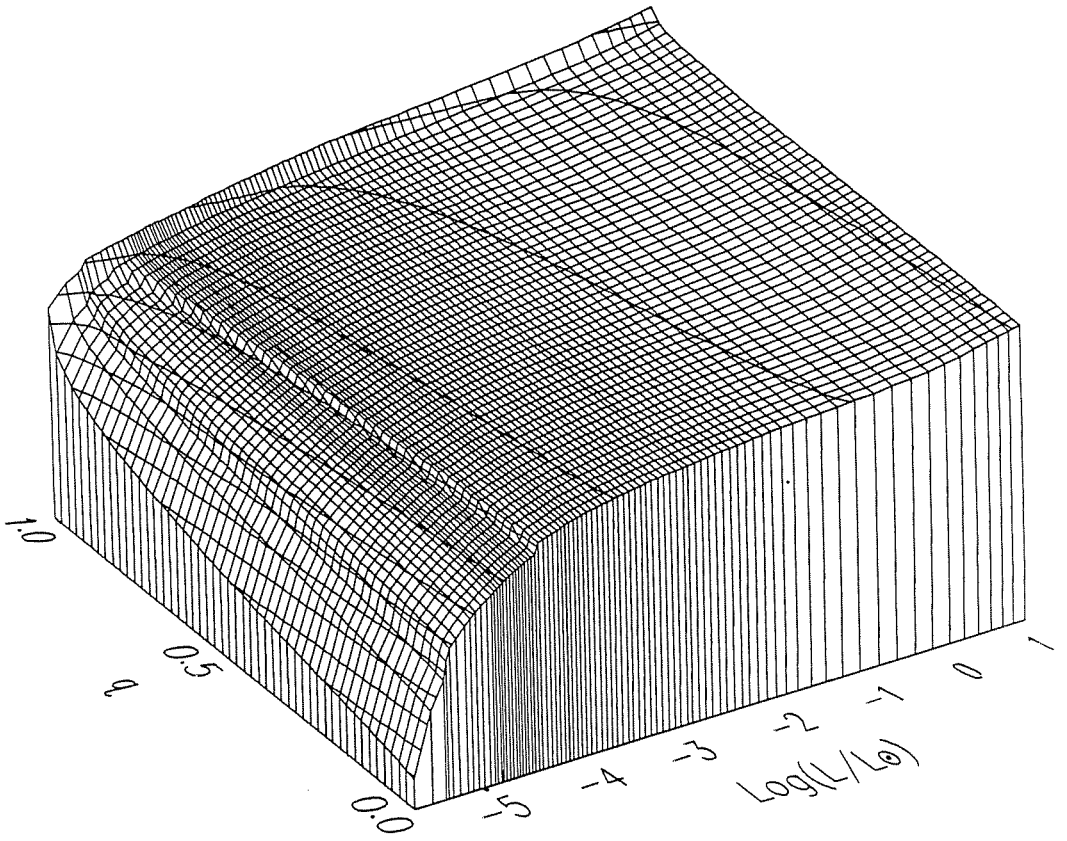

Figure 4.10: Interior Surface Plot of the Logarithm of the Entropy. Similar to Figure 3.10, but for the 0.4 $M_{\odot}$ carbon-core sequence.

the base of the envelope [the extrapolation can cause spikes in $\log(C_V)$]. A discontinuity such as this one causes a corresponding step up in the age–luminosity relation which in turn implies a bump on the luminosity function similar to the crystallization bump. All of this is to say that the evolutionary summary listings which went into making the Tables in the Appendix were truncated to avoid these non-physical features. Next, the plot of the heat capacity of sequence c4400 is shown in Figure 4.11. We find many of the same features as are in the plot of the entropy. Compared to higher-mass models the contraction phase is long-lived, and because of this the heat capacity remains high to lower luminosities. In addition, the smooth gas–liquid transition — visible as an outward-moving depression on the surface in between the two highest contour lines — has also moved to lower luminosities (cf. Figure 3.11). As before, the heat capacity rises before crystallization from that characteristic of an ideal gas to that of a high-temperature solid.

The plot of the evolution of the entropy for the 1.0 $M_\odot$ sequence c10500 is shown in Figure 4.12, and there we see again that crystallization begins at a high luminosity and spans a larger luminosity interval than for the lower-mass sequences. The jump in entropy is larger than we just saw in the 0.4 $M_\odot$ sequence, but because the release of latent heat is at a significantly higher luminosity, the effect of crystallization on the evolutionary timescale is smaller. Note the smooth decline into the Debye cooling regime. The heat capacity of sequence c10500 is shown next in Figure 4.13, and we notice first that there is little flare-up in the heat capacity in the most luminous models except for the outermost $\sim$10% of the hottest models where the Coulomb parameter $\Gamma \approx 1$. When the core begins to crystallize, there is little or no change in the heat capacity of the very-strongly degenerate interior. There

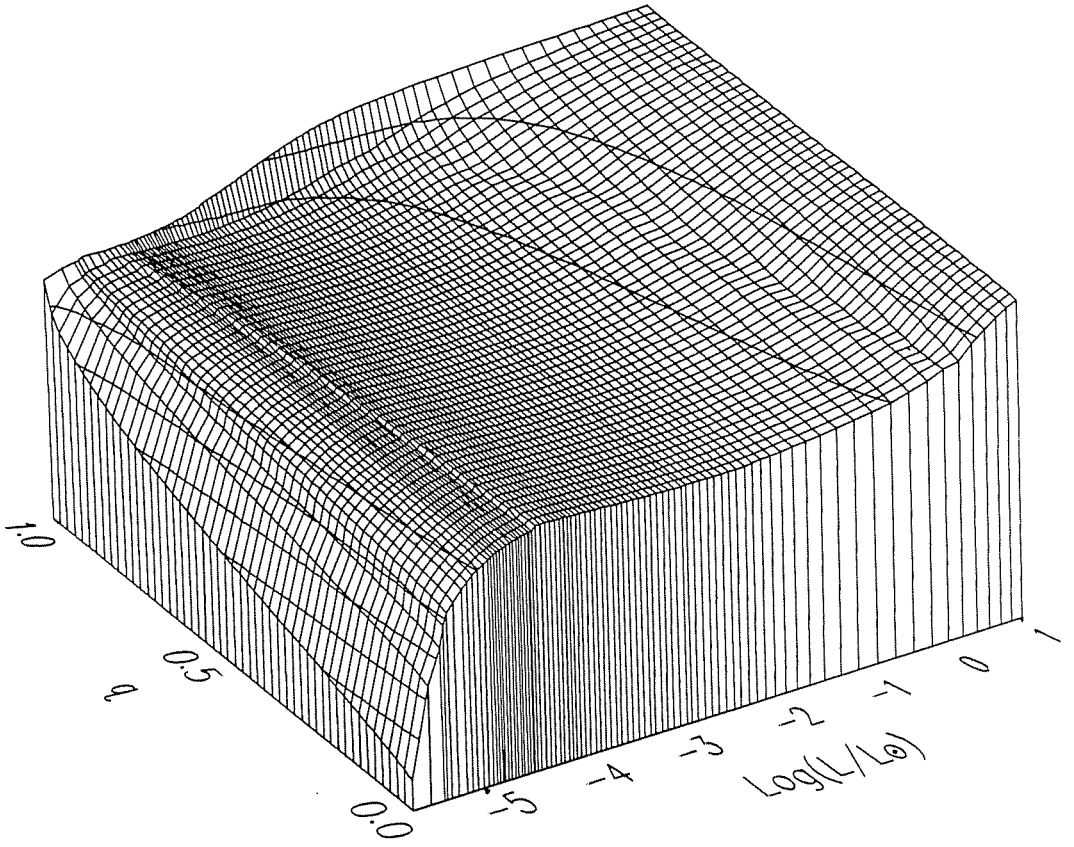

Figure 4.11: Interior Surface Plot of the Logarithm of the Heat Capacity. Similar to Figure 3.11, but for the 0.4 $M_{\odot}$ carbon-core sequence.

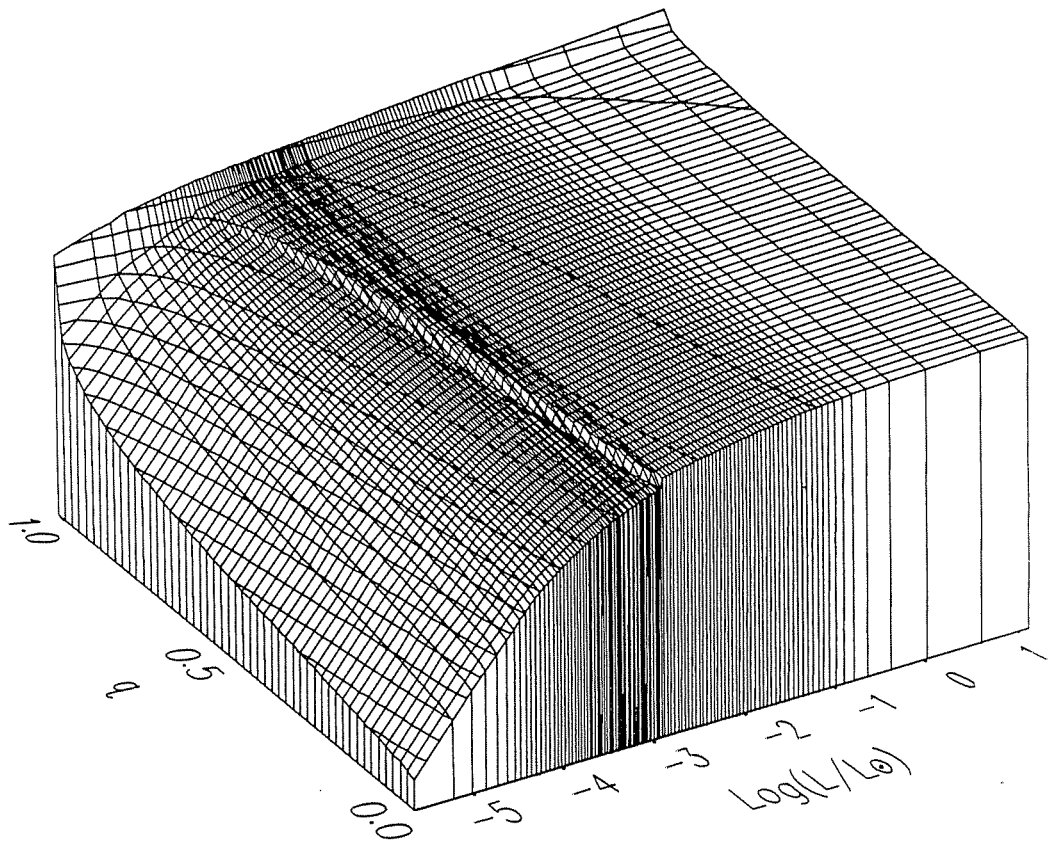

Figure 4.12: Interior Surface Plot of the Logarithm of the Entropy. Similar to Figure 3.10, but for the 1.0 $M_{\odot}$ carbon-core sequence.

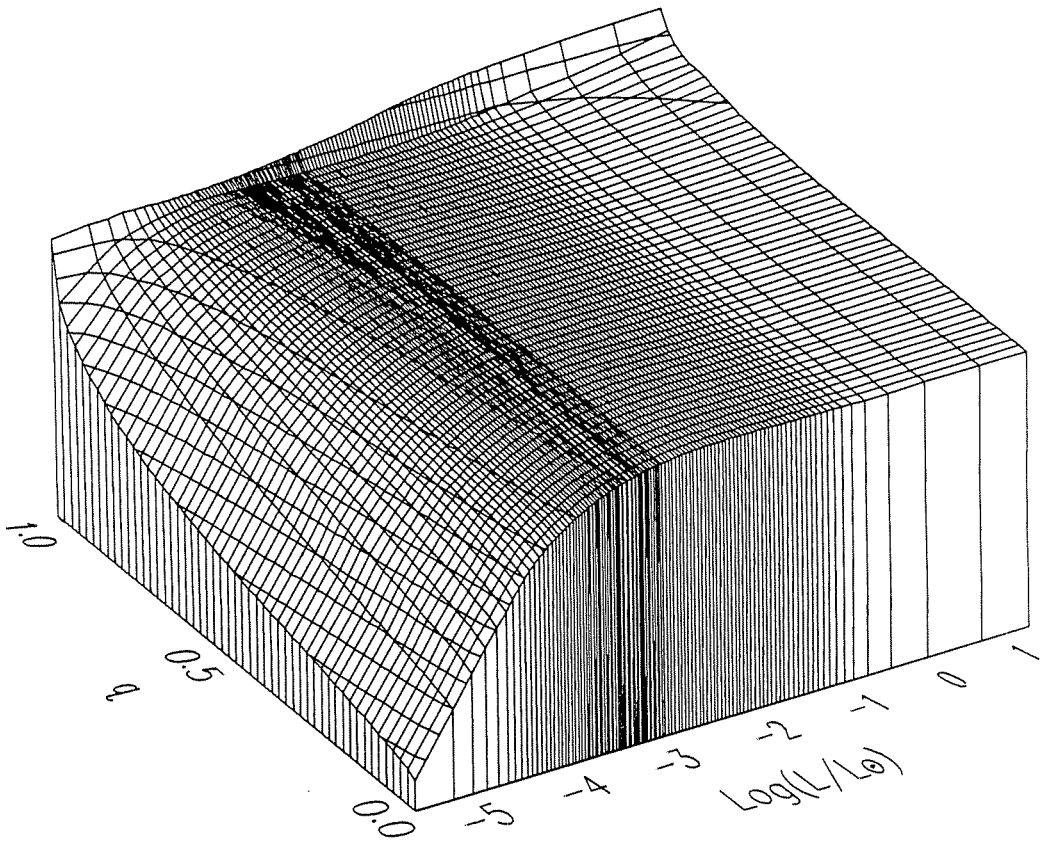

Figure 4.13: Interior Surface Plot of the Logarithm of the Heat Capacity. Similar to Figure 3.11, but for the 1.0 $M_{\odot}$ carbon-core sequence.

is a small change in the heat capacity as the crystallization front passes through the outer ~50% of the model, but the change is small.

4.1.3 *Variation of the Helium-Layer Mass*

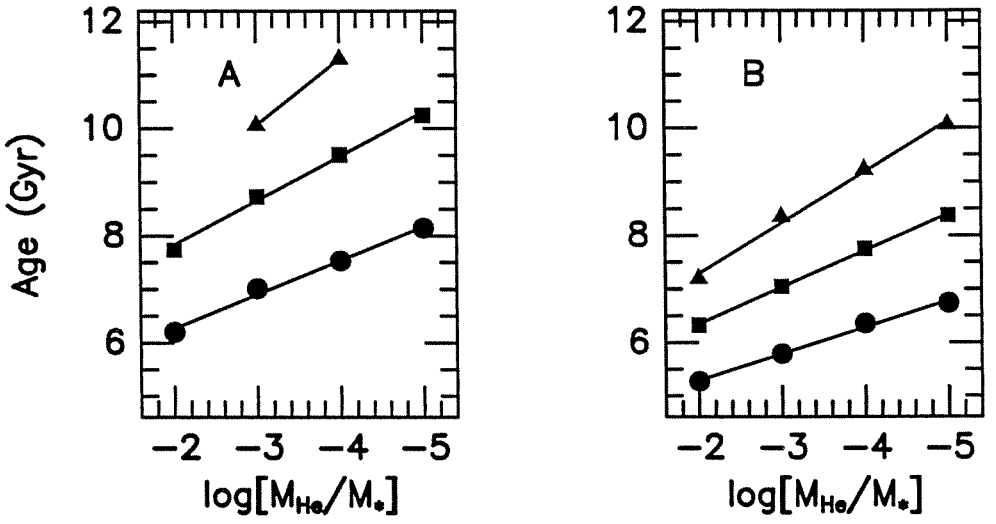

Figure 4.14: Age *vs.* Helium Layer Mass at Three Selected Luminosities for Carbon-Core and Oxygen-Core Sequences. Using model sequences c6200, c6300, c6400, and c6500, we show in panel A the effect on the age of the logarithm of the fractional helium layer mass $\log(M_{\rm He}/M_*)$ at the three luminosities $\log(L/L_\odot) = -4.2$ (*circles*), $\log(L/L_\odot) = -4.4$ (*squares*), and $\log(L/L_\odot) = -4.6$ (*triangles*). Because the carbon opacities are greater than those of helium, thinner helium layers yield older models at a given low luminosity. Panel B is similar to panel A, but for the oxygen core sequences o6200, o6300, o6400, and o6500. Note that the slopes of these fits are shallower.

The mass, or thickness, of the helium layer has a large effect on the evolutionary time scales of the model sequences (see also Wood and Winget 1989). Carbon is in general more opaque than helium, as we saw above in the opacity surface plots of He and C in Figures 2.4, 2.5, respectively, and also

in the envelope surface plot of opacity for the fiducial model in Figure 3.14). Evaluated at a luminosity typical of the turndown in the luminosity function [$\log(L/L_{\odot}) \approx -4.4$], we find that the thinner the helium layer, the older a model sequence will be at a given luminosity. To demonstrate this point, we plot the ages (in units of 1 Gyr) of 4 carbon-core and oxygen-core sequences at 3 selected luminosities in the two panels of Figure 4.14. The eight sequences all have masses of 0.6 $M_{\odot}$, and the fractional helium layer masses are $\log(M_{\rm He}/M_{\star}) = -2$, -3, -4, and -5 in each of the two groups — *i.e.*, they are c6200, c6300, c6400, c6500, o6200, o6300, o6400, and o6500 (of these, we provide abbreviated evolutionary summary Tables for the sequences c6200, c6300, o6200 and o6300 in Tables A.24 through A.27 in the Appendix).

The luminosities we have selected are in the regime of the turndown in the observed white dwarf luminosity function; specifically, they are $\log(L/L_{\odot}) = -4.2$, -4.4, and -4.6. This range in luminosity nearly spans the uncertainty in the determination of the absolute bolometric magnitudes of the coolest observed white dwarf stars (see the discussion in Liebert, Dahn, and Monet 1988), and so provides some measure of the uncertainties in the Galactic age determination. At the outside, the helium layer masses in the stars are probably not much greater than $\sim 2 \times 10^{-2}$ $M_{\odot}$ (D'Antona and Mazzitelli 1979), and recent determinations by Pelletier *et al.* (1986) suggest it is likely to be $10^{-3.5}$ $M_{\odot}$, plus or minus 0.5 in the exponent. To the extent that our 0.6 $M_{\odot}$ models are representative of the masses of the coolest stars — still a topic open for debate — we find that the ages could potentially range from a minimum of 5.3 Gyr [for sequence o6200 at $\log(L/L_{\odot}) = -4.2$] to a maximum greater than 11.3 Gyr [for sequence

c6400 at $\log(L/L_{\odot}) = -4.6$. We discuss this further in the summary section below, but note here that these two effects combined — helium layer mass and core composition — are the two major theoretical uncertainties in using the white dwarf stars as Galactic chronometers. We find that even in the most conservative picture, the uncertainties in the age determination are only roughly a factor of two. The fact that the core composition and helium-layer mass are known more accurately than we have assumed means that more detailed analyses will provide a stringent constraint on the length of time since the onset of star formation at our galactocentric radius.

Probably as important as the ages themselves are the trends in age as a function of helium layer mass for a given core composition and luminosity; a straight line fits the results extremely well at a given luminosity. At a fixed luminosity we fit the relation

$$t_{\rm cool}|_L = S_t \cdot \log(M_{\rm He}/M_{\star}) + t_{\rm o} \qquad (4.1)$$

using linear least squares on the theoretical data to obtain the magnitude of these trends. In relation (4.1), S_t is the age shift per decade change in $\log(M_{\rm He}/M_{\star})$. Starting first with the carbon-core sequences (panel A in Figure 4.14), we see that at $\log(L/L_{\odot}) = -4.2$, the age shift per decade is 0.63 Gyr. At $\log(L/L_{\odot}) = -4.4$, the age shift is 0.83 Gyr per decade, and at $\log(L/L_{\odot}) = -4.6$, 1.2 Gyr per decade (note that these three luminosities are chosen to span the observational uncertainty in the luminosity of the WDLF turndown). The oxygen-core sequences are younger, and correspondingly, the age differences are smaller. At the same three luminosities, the age differences per decade in $\log(M_{\rm He}/M_{\star})$ are 0.50 Gyr, 0.69 Gyr, and 0.95 Gyr, respectively. The rule of thumb that we use is that the age shift

per decade of helium layer mass is roughly $\frac{3}{4}$ Gyr at the luminosity function turndown.

Although we do not include summary tables for any of c5300, o5300, c7300, o7200, o7300, or o7500, we have used them to examine the effects of the helium-layer masses on sequences of masses 0.5 $M_\odot$ and 0.7 $M_\odot$. We find the age shifts in the 0.5 $M_\odot$ sequences at $\log(L/L_\odot) = -4.4$ to be 0.57 Gyr and 0.47 Gyr for the carbon- and oxygen-core sequences, respectively. For 0.7 $M_\odot$, the corresponding age shifts per decade at the same luminosity are 0.51 Gyr and 0.75 Gyr for carbon and oxygen, respectively. The carbon age is anomalous because the sequence c7400 is still crystallizing at $\log(L/L_\odot) = -4.4$.

To review, we find remarkably linear trends in the variations of age with the logarithm of the mass of the helium layer for a given stellar mass and core composition evaluated at a specified luminosity. These age variations are a direct result of the helium conductive opacities being lower than those of carbon. We find that there is a trend towards larger age shifts when evaluated at lower opacities, but the rule of thumb we apply is that *there is a* $\sim\frac{3}{4}$ *Gyr age shift towards shorter ages for a factor of 10 increase in the fractional helium-layer mass.*

4.1.4 *DA Models, No Mixing*

4.1.4.1 *The Effects of Varying the Hydrogen-Layer Mass*

As we discussed above, our primary concern is to publish a complete and homogeneous set of sequences for use in Galactic age studies. Because a number of studies have shown that white dwarf spectra below ~10,000 K

are dominated by the non-DA type, we have only discussed DB models so far. However, most of the observed white dwarfs are of spectral type DA, and so we would be remiss if we did not include discussion of these models as well.

We begin here by discussing the effects of varying the hydrogen-layer mass in compositionally stratified models that do not mix convectively with the subsurface helium layer, and which have the transition zones idealized as discontinuities. The hydrogen-layer masses that we will consider span the range $\log(M_{\rm H}/M_\star) = -4$ to -12. The specific sequences we consider are c6204, c6305, c6308, c6310, c6312, and c6410 (we include evolutionary summary Tables for sequences c6204, c6310, and c6410 in Tables A.28, A.29, and A.30 in the Appendix).

Before intercomparing the various DA sequences, we will first compare c6410 against c6400. We show the evolutionary summary plot of c6410 in Figure 4.15, and repeat in that Figure the curves from c6400 (*i.e.*, from Figure 4.6) for comparison. The first thing that we notice is that the two sequences are more similar than dissimilar. Above $\log(L/L_\odot) \approx -3.1$, the ages of the sequences are always within $\sim$1% of each other. For the hydrogen layer thickness that we chose, the surface convection zone digs inward and touches the subsurface helium convection zone at $\log(L/L_\odot) \approx -3.1$ (see Figure 4.16). The layers almost certainly mix when they touch, and the appropriate age–luminosity relation below this point will be that of the DB sequence. We note that this luminosity corresponds to an effective temperature of $T_{\rm eff} \approx 8{,}800$ K and an age of $t_{\rm cool} \approx 1.2$ Gyr and occurs well before the onset of crystallization. In other words, the observations suggest that models with thin hydrogen layers should be appropriate to most DA stars. Not only are such models indistinguishable from DB models at high effective

temperatures, they *become* DBs at lower effective temperatures Because the convection zone doesn't dig deep until $\log(L/L_{\odot}) \sim -3.5$, it is not until this luminosity that the base of the convection zone and the degeneracy boundary meet. At high luminosities, both the DA and DB envelopes have their photospheres at about the same fractional mass, because the main atmospheric components in the two cases are both fully ionized, and electron scattering is the dominant opacity source. Once the temperatures are cool enough, there exists a partial ionization regime coinciding with the convection zone. The photosphere roughly follows the top of this convection zone for the remainder of the evolution. Note that if we had allowed the layers to mix when the convection zones touched, then the plot would resemble Figure 3.4 below the mixing luminosity.

Next, we discuss the effects of varying the hydrogen layer masses over the range $\log(M_{\rm H}/M_{\star}) = -4$ to -12. Because the surface convection zone extends below the H/He interface in all but the thick hydrogen layer models [*i.e.*, $\log(M_{\rm H}/M_{\star}) = -4$], and because convection is adiabatic, we find that, excepting the case of a thick hydrogen layer, the hydrogen-layer mass itself is not likely to be a great source of uncertainty in the ages of the models. For example, comparing c6305 against c6310, we see that the age differences at $\log(L/L_{\odot}) = -4.4$ amount to roughly 0.5 Gyr. Recall that for the helium layer, a change of a single order of magnitude caused a $\sim$0.75 Gyr age shift at this luminosity. In summary, we find that the hydrogen-layer mass has only a small effect on the evolutionary time scale compared to core composition and helium-layer mass effects.

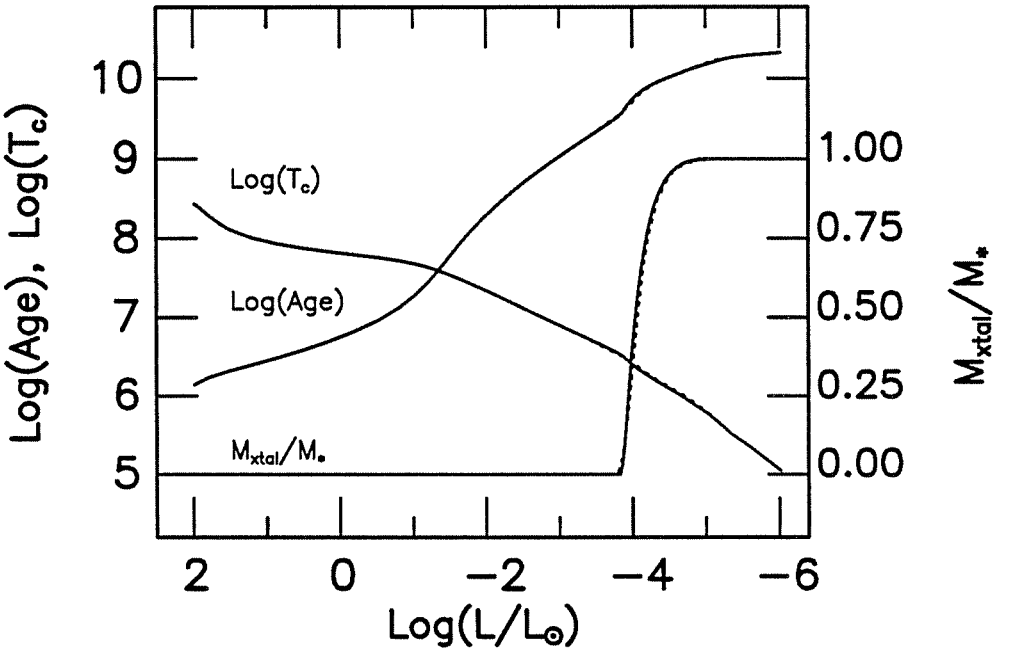

Figure 4.15: Summary Plot for Sequence c6410. We show here the summary plot for c6410 (*solid lines*) and for comparison also show the relations for c6400 (*dashed lines*). The two sets of curves are nearly indistinguishable before the onset of crystallization. The sequence c6410 would mix at $\log(L/L_{\odot}) \approx -3.1$ if we allowed it to.

4.1.4.2 *Mass Dependent Cooling Curves*

In §4.1.1 above we discussed the dependence on mass for DB model sequences with carbon and oxygen cores. Here we extend that discussion to DA sequences. We have calculated a series of models with surface hydrogen layers of $\log(M_{\rm H}/M_{\star}) = -10$ and subsurface helium layers of mass $\log(M_{\rm He}/M_{\star}) = -4$, both overlying the fiducial C/O core profile (see Figure 3.1). The sequences by name are x4410b, x6410b, x8410b, and x10410b, and are summarized in Tables A.32 through A.35 in the Appendix. The evolutionary summary plots are similar enough to the DB sequences that we do not show them. Furthermore, as we noted above, evidence suggests that

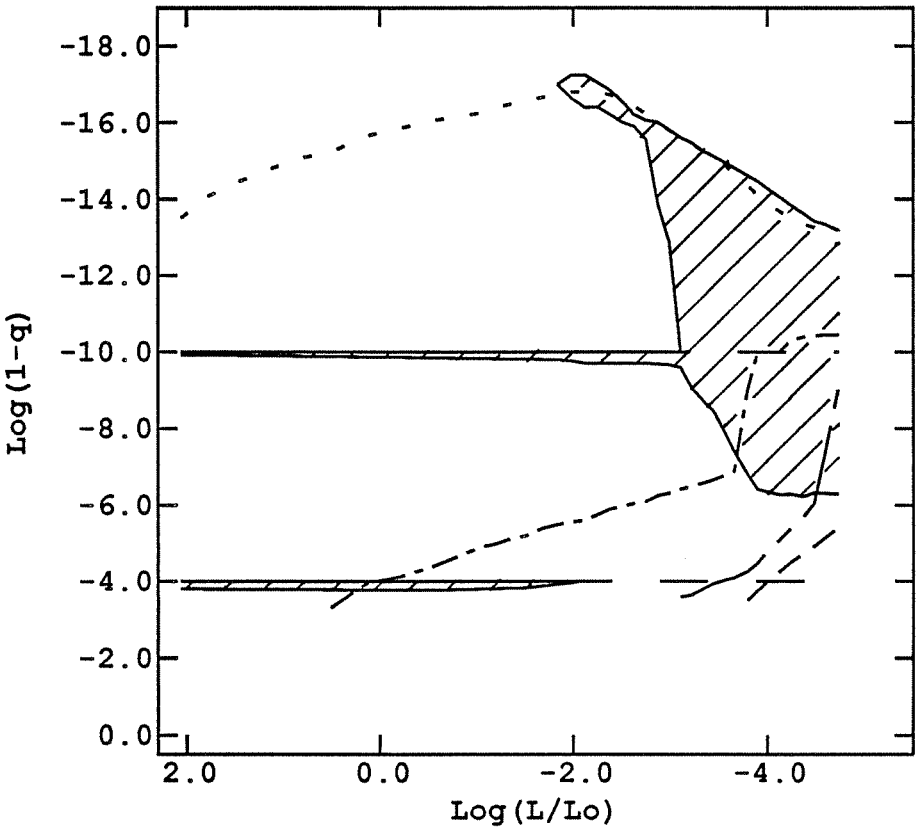

Figure 4.16: Envelope Plot for Sequence c6410. Similar to Figure 3.4. Hydrogen remains fully ionized to lower temperatures than helium, and so we see the surface convection onset shifted to much lower luminosities than in Figure 3.4. The surface convection zone touches the H/He subsurface convection zone at $\log(L/L_{\odot}) \approx -3.1$. We did not mix the two in the models that we used to generate this Figure, but if we had, it would have caused the convection-zone structure to look as it does in Figure 3.4 below the mixing luminosity.

most if not all of the coolest white dwarfs have a significant-to-dominant helium abundance at the photospheres.

We included these Tables for completeness because some researchers may prefer working from DA sequences. The radii are dependent on the

surface layer masses and composition, of course, but at 20,000 K the radii of the lower mass DA models (0.4, 0.5, 0.6) are larger than comparable DB sequences only by about 1% for these thin hydrogen layers. Thicker hydrogen layer masses do inflate the radii substantially. Sequences c6300 and c6305 suggest a radius increase of order 5% and sequences c6200 and c6204 suggest a radius increase of order 6%, again at roughly 20,000 K [$\log(L/L_{\odot}) = -1.6$]. Because thin hydrogen layers hardly affect the radii of the models, and because the evidence suggests the hydrogen layers in the stars themselves are thin, it should be sufficient to use the DB radii as a function of effective temperature for both DA and DB stars.

4.1.5 *Variations in the Composition Transition Zone Profiles*

Although we remarked that WDEC includes the ability to compute models with the H/He and He/C transition zones approximating diffusive equilibrium, all of the evolutionary summary Figures and Tables discussed so far have been computed with the composition transition zones idealized as discontinuities (for convenience, we call these "diffusive" and "discontinuity" model sequences, respectively). Figure 4.17 is the evolutionary summary plot for sequence c6400d, and shows at a glance why we chose not to use the diffusion models as the benchmark calculations. The cool models in this sequence show much larger fluctuations in the age–luminosity and T_c-luminosity relations than do the discontinuity models of c6400. The bases of the envelopes in the cool models have temperatures and densities off the EOS tables of Fontaine, Graboske, and Van Horn (1976). In this regime, we must extrapolate to obtain the necessary thermodynamic quantities. In the discontinuity models, the extrapolation is off a single table and so is tolerably stable; however, in the diffusive sequences, we are extrapolating off both the

helium and carbon EOS tables in the He/C transition region, and then interpolating between them to obtain the thermodynamic quantities for the mixture. This interpolation in quantities which are themselves interpolated is the dominant source of numerical noise in these cool models. The problem is exacerbated because the diffusive models must have the core/envelope boundary set deeper in mass to accommodate the deep tail of the helium layer.

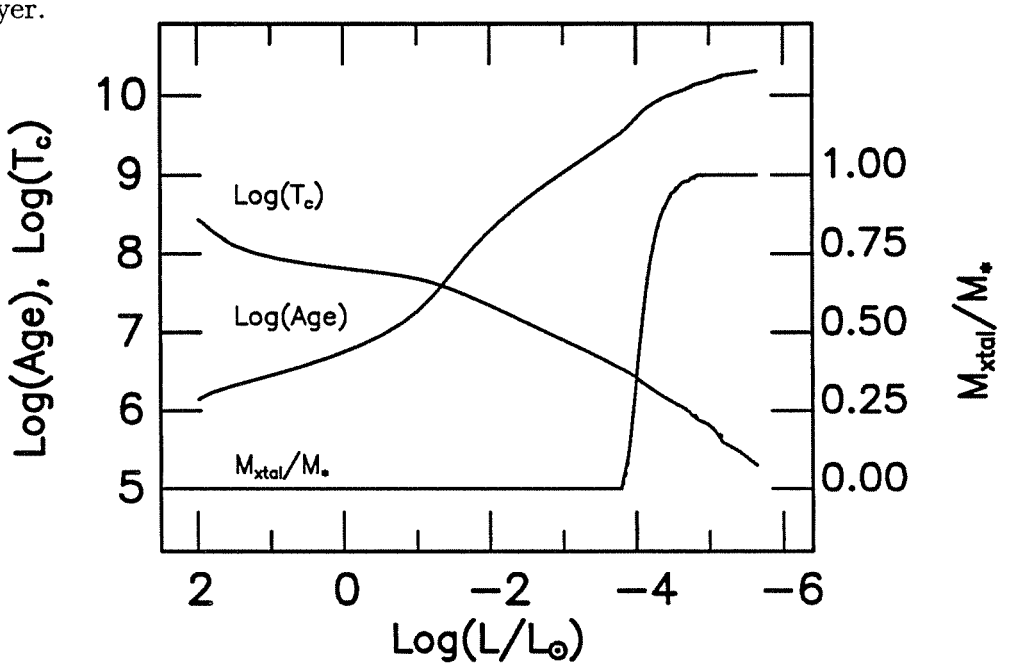

Figure 4.17: Evolutionary Summary Plot for Sequence c6400d. In the neutrino regime, this sequence (*solid line*) is nearly identical to c6400 (*dashed line*). In the Mestel regime, c6400d has a higher core temperature resulting from the higher opacities of the carbon tail which extends into the helium layer. The ages of the c6400d models are slightly younger at the beginning of the Mestel regime but are older before the onset of crystallization. The sequence c6400 crystallizes first because it has the lower core temperature.

Having discussed the problems of the cool diffusive models, we know not to rely on them below $\log(L/L_{\odot}) \approx -4.4$, depending upon the model's mass. Above this luminosity, however, the diffusive sequences are not only adequate, but also are more nearly representative of the real stars. In comparison with c6400 (see Tables A.10 and A.31), we see that the two are nearly indistinguishable during the neutrino epoch. In the Mestel regime, c6410d has core temperatures slightly higher than c6400 because of the greater integrated opacities which result from extending the carbon tail into the helium layer. Because of this, c6400 begins and ends crystallization at luminosities higher than c6400d, and so is younger by approximately 3% at $\log(L/L_{\odot}) = -4$. In summary, we find that the diffusive model sequences are quite similar to comparable sequences computed with discontinuous composition transition zones before the core is completely crystallized. In particular, the age–luminosity relations of the two sequences differ by at most a few percent over the lifetime of the model.

4.2 Variation of Adopted Constitutive Physics

4.2.1 *Uncertainties in the Conductive Opacity*

In the course of this investigation, we have had the opportunity to switch from the "workhorse" conductive opacities of Hubbard and Lampe (1969) to those of Itoh *et al.* (1983, 1984). In Figure 4.18 we show a total of four parallel 6400 sequences. Sequence c6400hl was computed with the Hubbard-Lampe opacities, and sequence c6400, one of our standards, was computed with the Itoh *et al.* opacities. The remaining two sequences are numerical experiments, and were computed with the Itoh *et al.* opacities multiplied

by a factor of two throughout (c6400it×2) and divided by a factor of two (c6400it/2), respectively. Our attention focuses first on the substantial differences among the curves at the cool end. The opacities of Itoh *et al.* are larger than those of Hubbard and Lampe by a factor of somewhat less than two in the region of interest, and this results in an overall trend toward higher core temperatures, delayed crystallization, and older model ages as a function of luminosity. At luminosities near the observed turndown in the white dwarf luminosity function, we find that there is a 6–12 percent shift to larger ages for the Itoh *et al.* opacities, and this translates to a $\sim$0.5 Gyr difference at $\log(L/L_{\odot}) = -4.2$ and a $\sim$1.3 Gyr difference at $\log(L/L_{\odot}) = -4.6$.

The behavior at cool luminosities is understandable — models with greater opacities have higher core temperatures and are older as a function of luminosity — but the behavior observed at higher luminosities is not so straightforward to understand. In the neutrino regime, we see that the sequences with higher conductive opacities have *lower* core temperatures, and this we might not have guessed. It is the core temperature inversion that is responsible. As we discussed above, in these hot models, the neutrino energy losses are a significant part of the total energy lost per unit time, and because these losses are from the interiors of the models, they cause a core temperature inversion. Because thermal energy flows from hotter to cooler regions, there is a net thermal flux *inward* in these models to compensate for the neutrino energy losses. In models with lower conductive opacities the temperature gradients are smaller as a general rule, and so the core temperatures will be higher compared to models with higher conductive opacities and hence steeper temperature gradients.

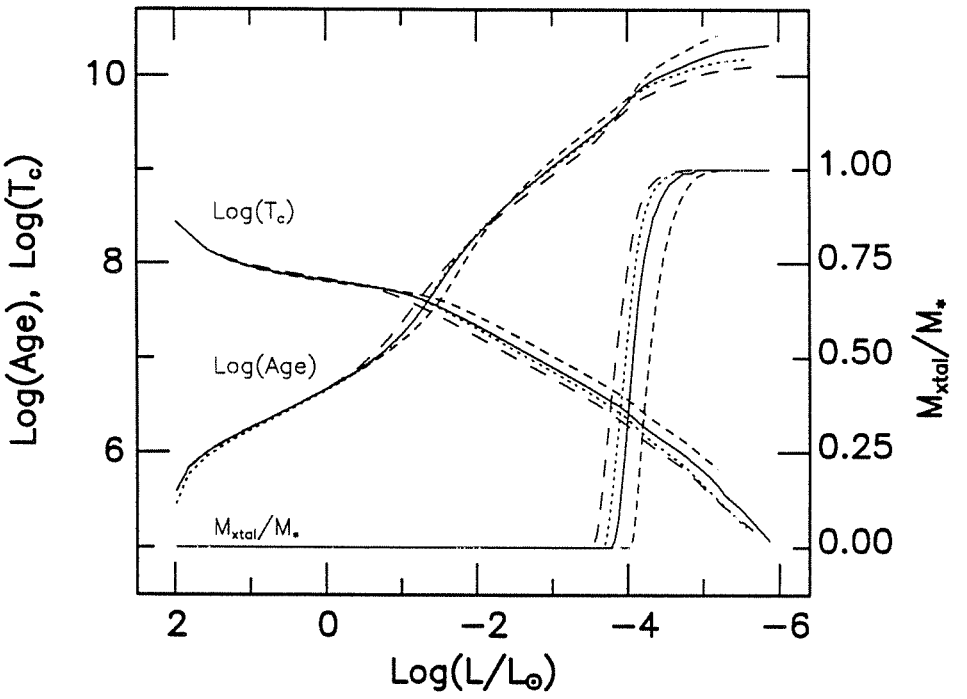

Figure 4.18: Variations in the Conductive Opacity. In this Figure we show the evolutionary relations for the sequences c6400hl (*dotted lines*), c6400 (*solid lines*), c6400it/2 (*long-dashed lines*), and c6400it×2 (*short-dashed lines*). Sequence c6400 we have already shown in Figure 4.6. Sequence c6400hl is computed using the Hubbard and Lampe (1969) conductive opacities exclusively, and comparisons between these two sequences show the upper limit to the uncertainty in the conductive opacities. Sequence c6400it/2 is computed using the standard recipe for conductive opacities, but divided arbitrarily by a factor of 2 before use to illustrate the effects of increased opacities. Sequence c6400it×2 is similar, but here the opacities are multiplied arbitrarily by a factor of two.

In the intermediate regime, near $\log(L/L_\odot) \approx -1.6$, we see that although the sequence with the highest conductive opacities (c6400it×2) already has the highest core temperature, it also has the youngest age — again contrary to what we might have naïvely guessed. The explanation again involves the neutrino energy losses. In this regime where neutrino

luminosities are declining rapidly as a function of the core temperature, the higher conductive opacities allow the neutrino processes to persist to lower photon luminosities. The enhanced energy losses cause the models to evolve more quickly through this luminosity regime than do models with lower conductive opacities. Once the neutrino energy losses become negligible in all sequences at about $\log(L/L_{\odot}) \approx -2.0$, the models with the larger opacities evolve more slowly than the others, and make the crossover to older ages at $\log(L/L_{\odot}) \approx -2.5$.

4.2.2 *Uncertainties in the Radiative Opacity*

The radiative opacities that we use are those of Huebner (1980) for the Iben I [$X(H) = 0.999$], Iben V [$X(He) = 0.999$], and Weigert V [$X(C) = 0.999$] compositions. These have been supplemented with the older Cox and Stewart (1970) opacities below $T_{\rm eff} = 12{,}000$. For our sequences, we have used a simple bi-linear interpolation (in the logarithms of all variables) on the opacity grid to determine the opacity at a particular (ρ, T) point, giving an accuracy of roughly 20%. Note that models to be used in pulsation studies provide smoother results if the opacity interpolation is smooth at the grid points, as it is if for example splines are used (see Tassoul, Fontaine, and Winget 1990).

D'Antona and Mazzitelli (1989) have suggested that the differences between the age–luminosity relations that they obtain and those that we obtain (their ages are substantially smaller, as discussed in §4.3, below) are the result of differing choices for the radiative opacities. It is therefore interesting to investigate the effects of large changes in the assumed radiative opacities. We decided to test the importance of the radiative opacities with an extreme test. We ran 4 sequences from the same starting model and with

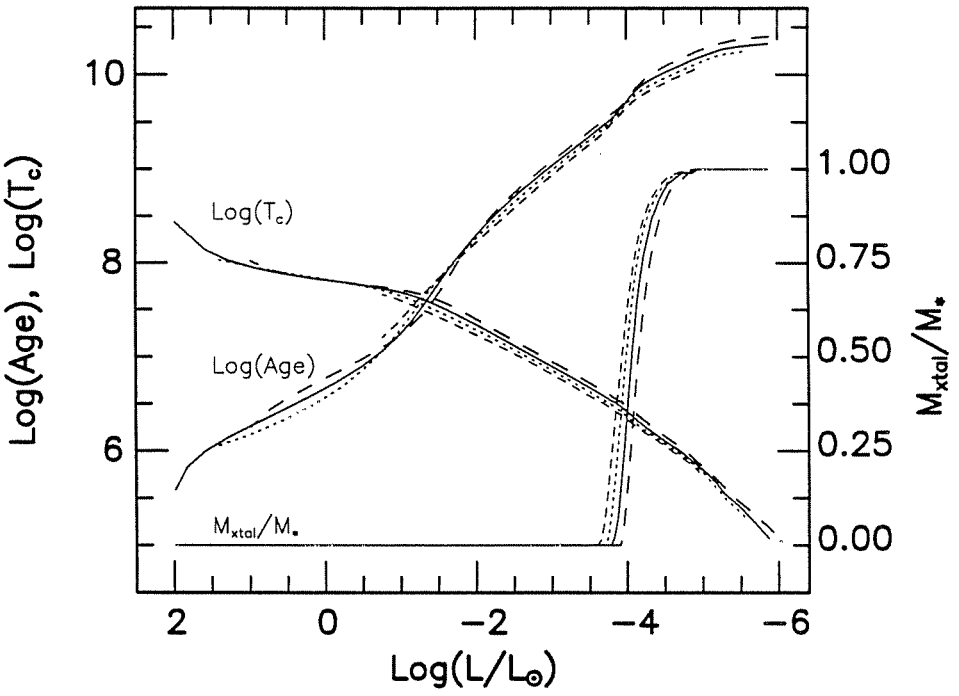

Figure 4.19: Variations in the Radiative Opacity. This Figure shows the evolutionary summary curves for sequence c6400 (*solid lines*), and for three parallel sequences. Two of these have the radiative opacities decreased, by one order of magnitude (*dotted lines*), and two orders of magnitude (*short-dashed lines*), respectively. The third has the radiative opacities increased by an order of magnitude (*long-dashed lines*). These results show that uncertainties in the radiative opacities are not likely to be the dominant uncertainty in the cooling calculations.

the same size timestep, all four c6400 sequences with discontinuities between the helium and carbon layers. The only differences between the sequences were the radiative opacities which were used in the calculations. The first sequence used the straight radiative opacities as we normally calculate them. The second had the radiative opacities increased by an order of magnitude, and the third and fourth had the radiative opacities decreased by one and

two orders of magnitude, respectively. We show the results in Figure 4.19. Although there are differences apparent among the sequences, the surprising result is that they are, in fact, small considering the extreme perturbation given the opacities. We find that the age differences between the sequences at the luminosity of the turndown in the white dwarf luminosity function $\log(L/L_\odot) \approx -4.5$ are approximately $\Delta\tau_{-4.5} = \pm 1.4$ Gyr for $\Delta \log \kappa_{\rm rad} = \pm 1$. Put another way, the fractional effect on the age is about 14% [the age of the c6400 model is 10.4 Gyr at $\log(L/L_\odot) = -4.5$]. The uncertainties in the opacity are probably more on the order of 30% or less, and straightforward scaling leads us to conclude that the real uncertainty in the ages at the turndown is roughly ± 0.4 Gyr from uncertainties in the radiative opacity.

4.2.3 *Crystallization Effects*

We explore the effects of crystallization by artificially suppressing it in WDEC. We can evolve for a time after the material is formally crystallized because our equation of state includes a broad region of overlap between the solid and liquid EOS regimes. In sequences c6400nx and o6400nx we suppressed crystallization, and we compare these against c6400 and o6400, respectively. We find that the models which suppress crystallization have only a small rise in the age–luminosity relation at the luminosity of the crystallization bump. In the carbon-core sequences, the maximum age difference is about 2 Gyr and occurs near $\log(L/L_\odot) \approx -4.5$. The oxygen-core sequence is 50% crystallized at a luminosity which is roughly twice that at which the carbon-core sequence is 50% crystallized. Accordingly, the maximum age difference is about 1 Gyr at a luminosity $\log(L/L_\odot) \approx -4.2$.

More relevant than exploring the effects of suppressing crystallization entirely was our next experiment. Recent one-component plasma calculations results by two independent groups suggest $\Gamma_m = 178 \pm 1$ (Slattery, Doolen, and DeWitt 1982) and $\Gamma_m = 180 \pm 1$ (Ogata and Ichimaru 1987). As we remarked above, when calculating the interior equation of state table, we compute the melting curve that we normally reference during the evolution to determine which portion of the EOS table (solid or liquid) is to be used to obtain the thermodynamic quantities at a given (P,T) point. This pre-computed melting curve is characterized by the critical value of the Coulomb parameter $\Gamma_m \approx 160$ (Lamb 1974, Lamb and Van Horn 1975). We also compute a broad overlap region in which we calculate the thermodynamic quantities for both the solid and liquid states, so that when interpolating the thermodynamic quantities, we reference only the solid, or only the liquid, portion of the table. To test the sensitivity of the age–luminosity relation to uncertainties in Γ_m, we modified the evolution code to read in Γ_m on startup, and to then use this value to determine which portion of the EOS table to reference, instead of using the pre-computed melting curve. We calculated a sequence where we artificially set $\Gamma_m = 180$ (*i.e.*, consistent with the recent determinations) and find that although the onset of crystallization occurs at a core temperature approximately 12% below the nominal value, the age difference at $\log(L/L_\odot) = -4.4$ ($t_{\rm cool} \approx 8.8$ Gyr) is $\sim$1% (with the $\Gamma_m = 180$ sequence the older, as expected). The maximum age difference is only $\sim$7%, and occurs at $\log(L/L_\odot) \approx -4.0$, where the $\Gamma_m = 160$ sequence is the older because it is $\sim$50% crystallized, while the $\Gamma_m = 180$ sequence is only $\sim$30% crystallized at the same luminosity.

4.3 Comparison With Others

Having discussed in detail how our models intercompare, we discuss in this section how our models compare with those of other researchers. We discuss our models in comparison to those of Mazzitelli and D'Antona (1986; hereafter MD86), D'Antona and Mazzitelli (1989; DM89), Iben and Tutukov (1984; IT84), Iben and MacDonald (1985, 1986; IM), Koester and Schönberner (1986; KS86), and Tassoul, Fontaine, and Winget (1990). We begin by highlighting the main characteristics of the sequences in question (see also D'Antona and Mazzitelli 1990):

- Mazzitelli and D'Antona (1986) compute the evolution of 5 white dwarf sequences all with masses $\sim$0.68 $M_\odot$. All start with a C/O core ($\sim$75% O) evolved from a 3 $M_\odot$ main sequence progenitor, but differ in their surface layer masses and metallicities. Of the five, their sequences D and E are the most physical. The metallicity of these two sequences is set to be $Z = 10^{-5}$, and we would classify the sequences as "7200" and "7207." The authors use a Newton-Raphson scheme (see Mazzitelli 1979) and integrate from $M_r = 0$ to the photosphere (optical depth $\tau_{\rm ph} = 2/3$) using $\sim$800–1000 shells. The thermodynamics included are from Magni and Mazzitelli (1979); crystallization and the release of latent heat are included following Hansen (1973) and Pollock and Hansen (1973), with $\Gamma_m = 155$, and they use the conductive opacities of Hubbard and Lampe (1969). The ages of the two sequences D and E at $\log(L/L_\odot) = -4.4$ are 4.9 Gyr and 6.47 Gyr, respectively.

- D'Antona and Mazzitelli (1989) compute the evolution of 4 parallel white dwarf sequences of mass $M = 0.564\ M_{\odot}$. Using the same evolution code but now using the Itoh *et al.* conductive opacities, they evolve a 1 $M_{\odot}$ Population I progenitor from the main sequence to the knee in the cooling track, where they branch to a total of 4 sequences, 3 with $Z = 10^{-5}$ ($M_H \approx 3 \times 10^{-4}$, 10^{-8}, and zero) and one with $X = 0.75$, $Z = 0.02$ ($M_H \approx 3 \times 10^{-4}$). All 4 sequences have $M_{\rm He} \approx 2 \times 10^{-2}\ M_{\star}$. The ages of the three models with $Z = 10^{-5}$ at $\log(L/L_{\odot}) = -4.4$ are 5.94 Gyr, 4.49 Gyr, and 3.36 Gyr, respectively [note that the sequence with $M_H = 10^{-8}$ mixes at $\log(L/L_{\odot}) \approx -3.6$].

- Iben and Tutukov (1984) compute the evolution of a ~0.6 $M_{\odot}$ white dwarf models of type DA and DB from PNN to fully-crystallized configurations. The input physics are the same as used in earlier publications by Iben and collaborators (Iben 1975, 1976, 1984). Although they include an analytic fit to the behavior of a Coulomb liquid after Hansen (1973), the authors do not include the release of latent heat of crystallization and more importantly do not include detailed convective envelopes. In the IT84 DA model, the helium and hydrogen shells are thick, and a hydrogen nuclear shell burning source persists well into the white dwarf regime. The ages of their DA and DB models at $\log(L/L_{\odot}) = -4.4$ are 8.04 Gyr and 9.33 Gyr, respectively.

- Iben and MacDonald (1985, 1986) use essentially the same microphysics as Iben and Tutukov; however, because here the investigation focus is the effect of diffusion on the models' evolution, the authors included detailed envelope structures with convection zones that were lacking in the calculations of IT84. Again the mass of the sequences are ~0.6 $M_{\odot}$ and the hydrogen and helium layers are thick. The initial metallicity in

the envelope is taken to be $Z = 10^{-3}$ or 0.02, and after 5×10^7 years, diffusion has reduced the metallicity to $Z \lesssim 10^{-6}$ over the outer 5×10^{-4} $M_\star$. Using the polynomial fit that Iben and Laughlin (1989) give for the Iben and MacDonald (1986) cooling curve gives an age at $\log(L/L_\odot) = -4.4$ of 6.8 Gyr.

- Koester and Schönberner (1986) compute the evolution of white dwarf models of masses 0.598 $M_\odot$ and 0.546 $M_\odot$ both with and without thick hydrogen layers, for a total of four sequences. Although nuclear burning is included, the hydrogen layer masses are roughly a factor of two lower than those of IT84, and burning contributions to the luminosity are small. The core composition is 50/50 carbon and oxygen, and the release of latent heat of crystallization is not included. The ages of the 0.598 $M_\odot$ DA and DB sequences at $\log(L/L_\odot) = -4.3$ are 4.78 and 5.24 Gyr, respectively.

- The work of Tassoul, Fontaine and Winget (1990) is quite thorough, but the models were constructed specifically for pulsation (not evolution) studies, and do not include neutrino energy losses or crystallization. These authors explicitly compare their models against those computed by WDEC in detail, and we will not repeat the exercise here.

We show the age–luminosity relations for the DA and DB sequences in KS86, MD86, and DM89 as presented in Table 2 of D'Antona and Mazzitelli (1990) in Figures 4.20 and 4.21. Also in the DA plot, we include the IM86 age–luminosity relation given by the polynomial fit presented by Iben and Laughlin (1989). We also include our sequences x6400a and x6402a ("a" $\Rightarrow$ 50/50 C/O in the core) in the Figures. In both we see that our ages are considerably larger in the neutrino regime. The other three all used

evolutionary starting models whereas our models started as polytropes, and we strongly suspect that this is the origin of the age differences in this high luminosity regime. Whatever the origin, the neutrino epoch is the great reset, and our models merge completely with the others by $\log(L/L_{\odot}) \approx -1$.

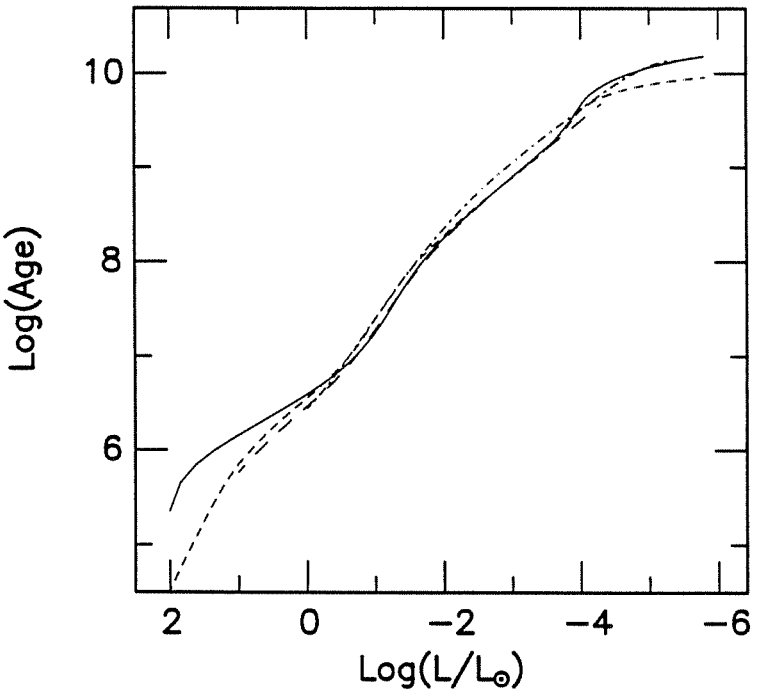

Figure 4.20: DA Age–Luminosity Relations of Various Research Groups. All models are approximately characterized as 6204 models, although there are factor-of-two differences in the layer masses. The IM86 curve (*dot-dashed line*) lies away from the relations from DM89 (*short-dashed line*), KS86 (*long-dashed line*), and our model (*solid line*). This is a result of the model's nuclear shell burning source (as an aside, note how the polynomial fit smooths the age–luminosity relation compared to the others). In the neutrino regime, our model is older than the others, probably because of the non-evolutionary starting model. Crystallization and the release of latent heat has a large effect on our models, but only a much smaller effect on the others.

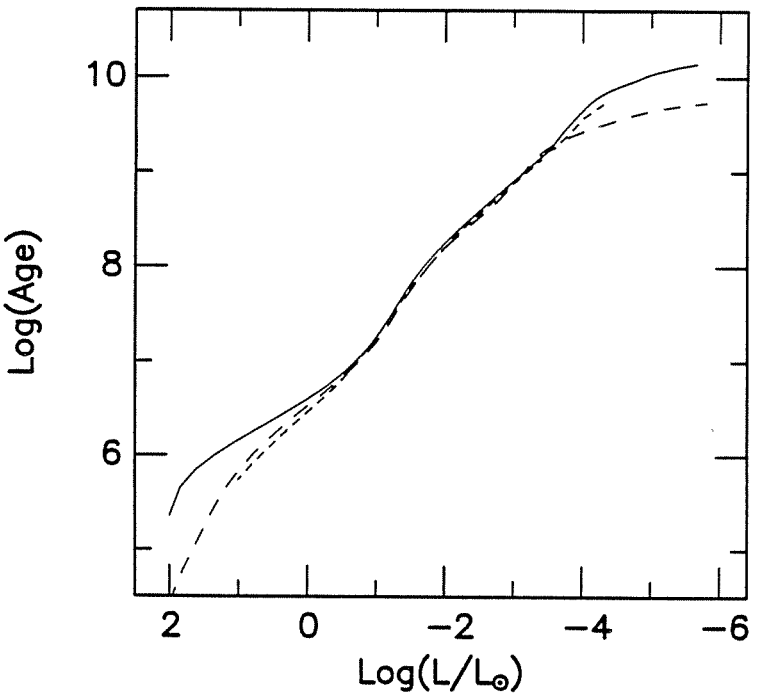

Figure 4.21: DB Age–Luminosity Relations of Various Research Groups. All models are approximately characterized as 6200 models, although again there are factor-of-two differences in the helium-layer masses. Again, in the high-luminosity regime, the ages of our models (*solid line*) are not in agreement with those of DM89 (*long-dashed line*) or KS86 (*short-dashed line*). All the models are in good agreement in the Mestel regime. The sequence of DM89 crystallizes much earlier than the others (it is mostly oxygen), and the ages at the luminosity of the turndown are several 10^9 yr younger than the other three.

In Figure 4.20 we find that the curve of IM86 lies away from the other three in the Mestel regime — their models have a significant luminosity from a hydrogen burning shell source, and this delays the cooling and lengthens the ages of the models at a given luminosity. These models were computed with the maximum hydrogen layer mass allowed by the phenomenological

Reimers' mass loss formalism. The models of KS86 and DM89 both have hydrogen layers roughly half that of the the IM86 models, and in both sets of sequences the luminosity of the shell burning source is negligible after the earliest phases of evolution. The current consensus is that the hydrogen-layer masses of the field DA white dwarfs are significantly less than $\log(M_{\rm H}/M_\star) \approx -8$ — they may in fact be as low as $\log(M_{\rm H}/M_\star) \approx -14$ — and so we can feel confident that nuclear shell burning sources do not provide significant luminosity over the white dwarf lifetime.

At low luminosities our models are the oldest of those shown in Figures 4.20 and 4.21. IM86 and KS86 did not include the release of latent heat as a luminosity source, but we all accounted for the change in internal energy as a function of the Coulomb parameter Γ, and all of the sequences are held up in their evolution when $\Gamma \approx \Gamma_m$ as a result of this change. Because KS86 do not include the release of latent heat, their models deviate only slightly from the Mestel slope as the Γ in the core passes beyond $\Gamma_m \approx 180$.

MD86 and DM89 include crystallization and the release of latent heat in their models, and although their DA model begin crystallizing at approximately the same luminosity as our model in Figure 4.20, we find that the effect of the phase transition on their model ages is evidently smaller than on ours. The result of this is that their models are much younger than ours at the luminosity of the turndown in the WD luminosity function. The disagreement between the DB sequences is worse as shown in Figure 4.21, where at $\log(L/L_\odot) = -4.4$ our models are a factor of 2.3 older than theirs. D'Antona and Mazzitelli (1989, 1990) have suggested that these age differences are the result of the opacity differences between their models and ours. They calculate using a metal abundance $Z = 10^{-5}$ compared to our

use of $Z = 10^{-3}$. As we noted in the previous section, however, our model ages are larger than theirs even when we reduce our radiative opacities by a factor of 100. Therefore, we believe that differences in opacity probably do not explain the age discrepancy. We suspect instead that it is the result of differences equation of state, although no quantitative comparison has been made.

5. *Summary of WD Evolution*

5.1 An Itemized Summary

In the preceding chapters we have discussed in detail the evolution of white dwarf model sequences. Our goal in this work was to impart a solid working "feel" for the behavior of white dwarf model sequences, and to provide a complete and homogeneous set of evolutionary sequences for use in further studies of white dwarf stars. Because there exist a number of outstanding uncertainties in the input quantities appropriate to these cooling embers, we have proceeded by computing an extensive grid of sequences which, to the extent possible, spans these uncertainties — *i.e.*, we believe that the parameters nature has chosen are embraced among the sequences presented here. We highlight our main findings as an itemized list which follows approximately the structure of the paper above, regrouped to provide a sense of continuity within the list itself. We note that the position of a given item within the list *does not* indicate the relative importance of that item (chances are excellent that if you are still reading this, you are familiar enough with the subject to know the major points), but we do give more space to those points we consider especially important. We highlight our results as follows:

- The starting models which begin the evolutionary sequence are crucial in determining the early evolution of the object — in particular the age–luminosity relation. The epoch of neutrino energy losses smooths over differences in the starting models, however, and our sequences, which begin with non-evolutionary polytropes, merge with those of other researchers who use evolutionary starting models well before $\log(L/L_{\odot}) \approx -1$.

- Neutrino luminosities can exceed the photon luminosities by factors of 5–10 in the high-temperature models. Because the neutrinos radiate from the center of the star instead of the surface, the core cools below the temperature of the surrounding material and a core temperature inversion is set up. The peak in the neutrino luminosity profile closely tracks the temperature maximum out through the star as thermal flux flows into the core. Once the neutrino epoch is over, the low conductive opacities in the core and the large radiative opacities in the outer percent (by mass) of the models cause the cores to become remarkably isothermal for the remaining evolution.

- Finite temperature effects on the radii are important down to relatively low surface temperatures for low-mass white dwarfs (*e.g.*, for $T_{\rm eff} \gtrsim 15{,}000$ K in a 0.4 $M_{\odot}$ model). We strongly recommend that future studies which require the use of white dwarf radii as input (*e.g.*, the derivation of a mass distribution from an observed gravity distribution) use these detailed model results instead of the zero-temperature C-configuration results of Hamada and Salpeter (1961). Adopting the zero-temperature results has become standard practice over the years, but the precision and accuracy of the new observations demand that the theoretical inputs be state-of-the-art as well. The current consensus is

that the surface hydrogen layers are thin, because and differences between DA and DB radii are small for thin surface hydrogen layers, the DB radii should be representative of all white dwarfs.

- In the luminosity regime where the Mestel assumptions are most closely satisfied (approximately over the range $-1 \gtrsim \log(L/L_\odot) \gtrsim -3$), *all* the sequences have the same (approximately–Mestel) slope independent of core composition, surface composition, surface-layer mass, stellar mass, or research group.

- The heat capacity rises in the Mestel regime from the value characteristic of an ideal gas ($C_V \sim \frac{3}{2}k$ per ion) to that of a high-temperature solid ($C_V \sim 3k$ per ion) before the onset of crystallization. The higher phonon energy levels are increasingly unexcitable in the Debye cooling regime, resulting in the general decline in C_V after crystallization.

- The neutrino dip in the age–luminosity relations is larger for more massive models, but these models enter the Mestel cooling regime at a higher luminosity than lower mass models. Because higher-mass models crystallize and enter the Debye cooling regime at relatively high luminosities, they are the youngest at luminosities $\log(L/L_\odot) \approx -4.5$.

- Although the total latent heat released through crystallization of less massive models is lower than that released by higher-mass models, the effect on the ages is greater because the energy is released at a substantially lower luminosity.

- Oxygen-core sequences evolve more quickly than the comparable carbon-core sequences at all stages of evolution because of slightly higher neutrino rates, lower global heat capacity, and higher crystallization tem-

perature; our models suggest that a 1.2 $M_\odot$ oxygen-core star will evolve to invisibility in less than 6 Gyr.

- The discontinuity in entropy at crystallization acts as a luminosity source through the energy generation equation relating $L_\star$ to $T\frac{\partial S}{\partial t}$ [see equation (1.20)], and slows the evolution of the models substantially. As the heat capacity drops in the Debye cooling regime, the thermal energy is necessarily lost from the star, resulting in the drop in entropy observed in the coolest models.

- The melting curve in our equation of state corresponds to $\Gamma_m \approx 160$, but recent, more sophisticated determinations of Γ_m put the critical Coulomb parameter at $\Gamma_m \approx 180$. We used the broad overlap region between the solid and liquid portions of our equation of state to artificially force $\Gamma_m = 180$, and found that the age differences between this sequence and the an otherwise parallel sequence computed with $\Gamma_m = 160$ are typically of order 1% [*i.e.*, for $\log(L/L_\odot) \lesssim -4.4$].

- In §1.3 we presented a generalized Mestel derivation, including an extension into the fully-crystallized regime. The latter should be particularly useful for studies of the white dwarf luminosity function which require the age–luminosity relations to be extended to luminosities lower than the converged models reach.

- The envelope evolution in the DB sequences is dominated by surface convection zones for temperatures lower than ~30,000 K. At a luminosity of $\log(L/L_\odot) \approx -2.7$ (for a 0.6 $M_\odot$ model) the degeneracy boundary reaches the base of the convection zone. After this point, the energy transport from core to photosphere is more efficient, and the age–luminosity relation is depressed compared to the Mestel slope.

- The helium layer mass has a strong influence on the evolutionary timescale. Roughly speaking, every decade increase in the helium layer mass changes the derived age by $\frac{3}{4}$ Gyr at the luminosity of the white dwarf luminosity function turndown. For carbon-core sequences the age shifts per decade over the luminosity interval $\log(L/L_{\odot}) = -4.2$ to -4.6 span the range 0.63 to 1.2 Gyr, and the age shift per decade for the oxygen-core sequences spans 0.50 to 0.95 Gyr over the same luminosity interval.

- In the surface convection zones of these nearly-constant radius objects, pressure as a function of mass depth is in hydrostatic equilibrium and so changes little with cooling. The temperature drops in the convection zone because of the reduced temperature gradient, and there is a corresponding density increase and radius decrease.

- The DA envelopes are radiative to much lower luminosities than the DB envelopes because of the lower ionization potential of hydrogen. Hydrogen layers less massive than $\sim 10^{-8}\ M_{\star}$ should convectively mix with the subsurface convection zone at $\log(L/L_{\odot}) \approx -2.7$. Bergeron *et al.* (1990) report convincing observational evidence that this mixing does occur, and find it to be at a temperature of $T_{\rm eff} \approx 11{,}500$ K.

- Although the thickness of the helium-layer mass strongly influences the ages of the models, variation of the hydrogen-layer mass affects the ages only marginally for layer masses of interest. Because we now believe that the stars' hydrogen layers are thin enough to mix at low luminosities, the DB age–luminosity relations are the sequences of choice for luminosity function studies.

- Although diffusive transition zones are clearly the choice for pulsation studies, the assumption of discontinuous transition zones affects the age–luminosity relation by only a few percent at luminosities characteristic of the luminosity function turndown. Because our goal here was to produce models which will be useful in studies of the white dwarf luminosity function, and because our models with diffusive composition profiles go bad at a significantly higher luminosities than the discontinuity models, we focussed on the latter.

- Artificially scaling the radiative opacities over three orders of magnitude does *not* affect the ages as much as varying the conductive opacity by only a factor of only four. In the low-luminosity regime where the models do most of their aging, the base of the convective envelope is degenerate: the energy transport is by conduction in the interior and by adiabatic convection in the envelope. The radiative opacities are important only at the photosphere. This result suggests that the differences between our models' ages and those of D'Antona and Mazzitelli (see DM90) are not the result of the radiative opacities. We suspect that the origin of the differences lies in the equation of state tables used.

5.2 Application: The WD Luminosity Function

The models that we have presented should provide working numbers for researchers in the field for some time to come. These models will be particularly useful in studies of the white dwarf luminosity function, as the major lack in these studies has been a large, internally-homogeneous set of theoretical white dwarf evolutionary sequences. These studies of the luminosity function promise to provide the age and star formation

history of the Galaxy at our galactocentric radius. Using only the 0.6 $M_{\odot}$ carbon-core and oxygen core models, we derived above (see Figure 4.14 and nearby text) conservative upper and lower limits to the age of the local disk of 5.3 and 12 Gyr. Wood (1990) using a subset of these models, has suggested that using our best values for the structures of the stars, the ages of the stars at the turndown are in the approximate range 8–10.5 Gyr. The major theoretical uncertainties in this determination are the core composition, helium-layer mass, and the mean white dwarf mass at the turndown luminosity. The observational determination of the location of the turndown is uncertain both because of small number statistics and because the bolometric correction appropriate to the few stars that *are* observed is itself quite uncertain (the latter is of course really a theoretical problem, and a tough one at that).

5.3 Observational Feedback and Future Directions

Whatever the ultimate resolution to these uncertainties, the real promise in the technique is that through asteroseismological studies of the white dwarf stars, we will eventually calibrate the theoretical sequence at the temperatures of the DA and DB instability strips (the pulsating stars are classified as type DAV and DBV, respectively. See Sion *et al.* 1983). As the stars cool, the thermodynamic structure changes, and the periods at which the star resonates changes in response. If there exists in the Fourier transform of the light curve of a given variable an isolated, single, and stable (in amplitude) peak, then evolutionary changes in the star will be observed as a secular change of phase with time relative to ephemeris time, reflecting the period change.

The hot, pulsating DOV star PG1159 was the first (pre) white dwarf object to have its rate of period change measured (Winget *et al.* 1985). Curiously, although the magnitude of the results suggests an evolutionary e–folding timescale of order 1 million years, the sign of $\dot{P} \equiv dP/dt$ disagrees with that suggested by pulsation studies of evolutionary PNN models, and agrees in sign and magnitude with the contracting polytropic models of for example (Winget and Cabot 1980).

Kepler *et al.* (1990) report that the 15 years of time-series photometric data from the DAV G117–B15A is insufficient to give a 3σ detection of $\dot{P}$, and estimated that if additional data were gathered only from a single site, then it should be another 10 years before a detection is reached. In March, 1990, S. O. Kepler and collaborators observed the star with the Whole Earth Telescope (Nather 1989, Nather *et al.* 1990), and because the data density from the Whole Earth Telescope is roughly a factor of ten greater than is typical of single-site data, they were able to make the measurement this year. The measured value is $\dot{P} = (12.0 \pm 3.5) \times 10^{-15}\mathrm{s\,s^{-1}}$ (S. O. Kepler, personal communication), and is roughly a factor of 4–10 larger than was predicted by pulsation studies of carbon-core DA models (see, for example, Wood and Winget 1988, Bradley, Winget and Wood 1989). The Whole Earth Telescope network of observers has been working as a team for only three years, but already it is clear that the new observations allow detailed seismological studies of the white dwarf stars. For an example of the wealth of information obtained using the Whole Earth Telescope on PG1159, see Winget *et al.* (1990).

The models we present here should serve the community until we have results from the next generation of white dwarf models which will include explicitly the time-dependent mixing and sorting out of the hydrogen and

helium in the envelope — our goal is to merge our interiors with the Montréal convective/diffusive envelopes into the "ultimate" white dwarf evolution code, probably using a finite element numerical formalism. The observational and theoretical advances that are currently being made by the white dwarf community are impressive, and the next 10 years should be a golden age in the study of white dwarf stars.

6. A Probe of Galactic Evolution

6.1 Background

Time began with the Big Bang, and shortly thereafter the new matter began fragmenting on progressively-smaller mass scales: from superclusters to clusters of galaxies to the galaxies themselves and eventually to the individual stars which brought it all to light. The stars and their parent structures have evolved over time to become the universe as we observe it today, and it is from this current picture that we try to reconstruct the past history of it all. Our own Galaxy is the only one in which we can study the constituent stars in three spatial dimensions (plus velocity space in many cases), and our understanding of it largely defines how we think of *all* large spirals, which as a class contain a large fraction of the luminous mass in the universe. Since the onset of star formation at our galactocentric radius, stars have formed, evolved, and died. The vast majority have left behind white dwarf remnants with masses of typically $M \approx 0.55\ M_{\odot}$ after shedding most of their mass in the giant and asymptotic giant phases preceding the final planetary nebula separation.

The mass loss process is dynamical and one of the least-well-understood processes in astrophysics, but for all the diversity of the upper right hand of the H-R diagram, the white dwarf stars are a remarkably homogeneous

class. Although stars of up to approximately 8 $M_{\odot}$ evolve to become white dwarfs (Romanishin and Angel 1980, Weidemann and Koester 1983), the observed gravity distribution (and hence mass distribution) of these stars has a central peak that is quite narrow. Over 75 percent have derived masses tightly clustered about $\langle M/M_{\odot} \rangle \approx 0.50$–$0.55$ according to two recent studies (McMahan 1989; Bergeron, Saffer, and Liebert 1990). This clustering is mfortuitous for our purposes here because it effectively removes an important degree of freedom from the problem.

Because the total thermal energy in an average white dwarf star is large enough and the rate of energy transport through the non-degenerate (insulating) surface layers meager enough, even white dwarf remnants of the earliest generation of stars formed in the local disk are still visible. These, the oldest stars in the local disk, have written in them the Galactic age and star-formation history. All but the hottest white dwarfs are necessarily nearby — certainly at the turndown luminosity the white dwarfs sample a small volume of the local disk — however, by symmetry arguments the local sample should be representative of an annulus at our galactocentric radius of $R_0 \approx 8$ kpc. Furthermore, because the ellipticities of most stellar orbits in the Galactic gravitational potential are fairly high at (typically) a few tenths (Carney, Latham, and Laird 1990), the annulus should have a breadth, of order $\frac{1}{2}\ R_0$.

It has been suspected for some time that there could be a turndown in the white dwarf luminosity function resulting from the finite age of the Galaxy (Schmidt 1959, Weidemann 1967), and D'Antona and Mazzitelli in 1978 laid out the mathematical formalism for calculating theoretical white dwarf luminosity functions within the context of a galactic evolutionary model. However, it was as recently as 1979 that Liebert demonstrated the

reality of the turndown (see also Liebert 1980) and 1987 that Winget *et al.* presented theoretical luminosity functions corresponding to ages of 6, 9, and 12 Gyr over a further updated observed luminosity function. Although their stated aim was more to demonstrate the viability of white dwarf cosmochronology than to derive a precise value for the age, they did report that their curves suggested that the onset of significant star formation in the Galaxy occurred about 9.3 ± 2 Gyr ago. The mathematical framework used by these authors was quite straightforward. They constructed their integrated luminosity functions by summing constant-birthrate luminosity functions of 0.4, 0.6, and 0.8 $M_{\odot}$ pure-carbon model sequences, weighted by the observed luminosity function of Weidemann and Koester (1984) at $\log(L/L_{\odot}) \approx -2.0$ (the mean luminosity of that observed sample). By proceeding in this manner, the authors neglected the mass dependence of the ages of the main sequence stars which give rise to the white dwarf population; however, to first order this approximation is valid because the progenitor ages are in general small compared with the white dwarf ages.

Iben and Laughlin (1989) and Yuan (1989) used the cooling curves presented in Winget *et al.* in more sophisticated luminosity function synthesis programs, and both explicitly included the main sequence evolutionary timescales. Both also found estimated disk ages in a broad range around 9 Gyr. These improved treatments of the full evolutionary picture did show some clear differences from the Winget *et al.* results, however. In particular, because of the neglect of main sequence evolutionary times, the Winget *et al.* luminosity functions predict too sharp a peak compared to the others and to the observations.

Iben and Laughlin (1989) and Yuan (1989) explored the luminosity function thoroughly using the Winget *et al.* (1987) cooling curves, but these

models are probably not as representative of the real stars as is desirable. Above, I presented the results of a large, homogeneous set of evolutionary model sequences, and I adopt them here in an extensive study of the white dwarf luminosity function, expanding upon the work presented in Wood (1990). I use the sequences discussed above to explore the effects that uncertainties in core composition and helium layer mass have on the derived luminosity function of the disk white dwarfs, and further, explore the effects on the luminosity function of changes in the assumed star formation rate as a function of time, the initial→final (I→F) mass relation, the initial mass function of white dwarf progenitors, and of possible changes as a function of age of the characteristic scale height above the Galactic plane of the stars' orbits.

In addition to the disk population, there may exist a substantial population of white dwarfs in the halo of the Galaxy. Liebert, Dahn, and Monet (1989) constructed a preliminary halo luminosity function using the high-velocity ($V_{\rm tan} \geq 250$ km s^{-1}) tail of the Luyten 8-tenths sample. The halo LF is derived using only six stars and so is subject to substantial change; however it is suggestive in that it appears that the halo LF is still increasing at the luminosity of the disk LF turndown. Previous investigations of this potential halo population of white dwarfs include those by Mochkovitch *et al.* (1990), Ryu *et al.* (1990), Tamanaha *et al.* (1990), Weidemann (1990), and Wood (1990). As in the exploration of the disk luminosity function, I explore the halo function parametrically using the model sequences tabulated in the Appendix.

The remainder of this chapter is organized as follows. In §6.2 I discuss the specifics of the LF synthesis programs, and in §6.3 the observed luminosity functions of Liebert, Dahn, and Monet (1988, 1989). I present the

resulting disk and halo luminosity functions in §§6.4 and 6.5, respectively, and then discuss these results as they apply to some of the current Galactic formation and evolution models in §6.6. Finally, I close in §6.7 with a few remarks on the future of white dwarf cosmochronology.

6.2 Theoretical Luminosity Functions

6.2.1 *Numerical Specifics*

In the simplest approximation, we consider the luminosity function that results from a constant white dwarf birthrate of stars with a specified mass. The resulting relation is

$$\Phi \propto \frac{dt_{\rm cool}}{d\log(L/L_{\odot})}, \tag{6.1}$$

where Φ is in units of $\rm pc^{-3}$ $\rm M_{bol}$. This expression allows a convenient way of examining the relative contributions that the different input evolutionary sequences make to the full integrated luminosity functions. To compare with the features of the observed luminosity function in detail, one must integrate the full expression

$$\Phi = \int_{M_L}^{M_U}\int_{L_L}^{L_U} \psi(t)\,\phi(M)\,\frac{dt_{\rm cool}}{d\log(L/L_{\odot})}\,\frac{dm}{dM}\,dL\,dM, \tag{6.2}$$

where M_L and M_U, L_L and L_U are the lower and upper mass and luminosity limits to the integration, respectively. The upper mass limit is typically 8 $\rm M_{\odot}$, and as discussed below the calculations are relatively insensitive to the specific choice. The lower mass limit is the main-sequence turnoff mass for the input disk age ($t_{\rm disk}$), and is obtained by inverting the relation for

the main-sequence evolutionary time scale, $t_{MS} = 10\left(\frac{M}{M_\odot}\right)^{-2.5}$, thus giving the mass corresponding to $t_{MS} = t_{\rm disk}$. The upper luminosity limit is $10L_\odot$ (the results are insensitive to the exact choice), and the lower luminosity is determined for each mass by interpolating between sequences for the luminosity corresponding to the age

$$t_{\rm cool}^{\rm max}[M_{\rm WD}(M_{\rm MS})] = t_{\rm disk} - t_{\rm MS}(M_{\rm MS}). \tag{6.3}$$

The other inputs to the model include the star formation rate as a function of time, [SFR $\equiv \psi(t)$], the initial mass function [IMF $\equiv \phi(M)$], the initial→final mass relation $\left(\frac{dm}{dM}\right)$, and of course the mass-dependent WD cooling curves. For these relations, I have adopted the following parameter set to define my *standard model.*

- Constant SFR,
- Mass limits: $M_U = 8\ M_\odot$, $M_L = M_{\rm turnoff}(t_{\rm disk})$,
- Salpeter IMF: $\phi(M) = (M/M_\odot)^{-2.35}$,
- Pre-WD lifetime: $t_{MS} = 10\left(\frac{M}{M_\odot}\right)^{-2.5}$,
- I→F mass relation: $M_{\rm WD} = A \cdot \exp(B \cdot M_{\rm MS})$, where $A = 0.49462$ and $B = 0.09468$ (see §6.5.2, below),
- No scale height inflation with increasing age.

For each mass sampled from M_L to M_U, I calculate the main-sequence evolutionary timescale, the weight given by the adopted IMF, the corresponding white dwarf mass, maximum age, and the minimum luminosity corresponding to this age. For each of the sampled luminosity points, I calculate $dt/d\log(L/L_\odot)$ using splines and centered differencing for each of the two input sequences which bracket the mass in question, interpolate between

these two values in the logarithm of all variables, and then multiply by the weights just discussed to obtain the LF contribution at the given mass and luminosity.

I decided to use splines after trying both simple linear interpolation as in Winget *et al.* (1987) and polynomial fitting as in Iben and Laughlin (1989). Neither of these proved to be satisfactory. Linear interpolation between models along the sequence is too sensitive to the model-to-model numerical noise in the age–luminosity relations. Polynomial fits are not constrained to pass through the points, and consistently "cuts corners." This is especially crucial at the low-luminosity end, and inspection of Figure 8 in Iben and Laughlin shows that their fit to the Winget *et al.* 1.0 $M_{\odot}$ model sequence overestimates the age at the luminosity of the dimmest fitted point and beyond (see their Figure 8), probably accounting for the high plateau they found just beyond the luminosity off the turndown (*e.g.*, their Figure 14).

6.2.2 *Extrapolating the Model Sequence Age–Luminosity Relations*

The evolutionary models detailed above terminate shortly after the crystallization boundary reaches the core/envelope transition. The age and luminosity of the final converged model in a sequence are functions of the mass and core composition — massive and oxygen-rich sequences can evolve to faint luminosities in much less than 10 Gyr. Because of this, it is necessary to extrapolate the age–luminosity relation to arbitrarily low luminosities. Although the extrapolations pick up at luminosities which are past the peak in the single-sequence luminosity functions, they are crucial in determining the shape of the LF beyond the turndown, and so should be as physically

realistic as possible. As discussed in §2.3 above, we use a Mestel-like derivation with the assumption that the heat capacity in the Debye regime may be approximated by

$$C_V \approx \langle C_V \rangle_0 \left(\frac{T}{\langle T \rangle_0} \right)^{\gamma}, \tag{6.4}$$

where nominally $\gamma = 3$, and $\langle C_V \rangle_0$ and $\langle T \rangle_0$ are the mass averages over the final model in the sequence. This leads to an age–luminosity relation of the form

$$t - t_0 = A \cdot \left[1 - \left(\frac{L}{L_0} \right)^{q} \right], \tag{6.5}$$

where t_0 and L_0 are the age and luminosity of the last converged model in a sequence, and where the exponent q is a function of the adopted opacity law and the value chosen for γ in equation (6.4). Although the Lamb (1974) equation of state does show C_V dropping approximately as T^3 as $T \rightarrow 0$ at a constant density, Figure 3.12 above shows that the integrated average heat capacity in the Debye regime scales approximately as $\langle C_V \rangle \propto T$ — *i.e.*, $\gamma = 1$. Using this and a Kramers' opacity law ($\kappa = \kappa_0 \rho^{-1} T^{4.5}$), the exponent q in equation (6.5) is $q \approx 1$. The calculation of the leading term A in the extrapolation relation nominally requires knowledge of the mean heat capacity, temperature, and controlling opacity (κ_0); however, it turns out to be sufficient to solve for A using the last two good points in the sequences. Plotted against mass these show a clear trend and can be fitted with the relation:

$$A = a \exp(b \cdot \mathcal{M}) \tag{6.6}$$

where a and b are the fitted parameters and $\mathcal{M} \equiv M/M_{\odot}$, and the fit itself is by standard non-linear least squares (see for example Press *et al.* 1986,

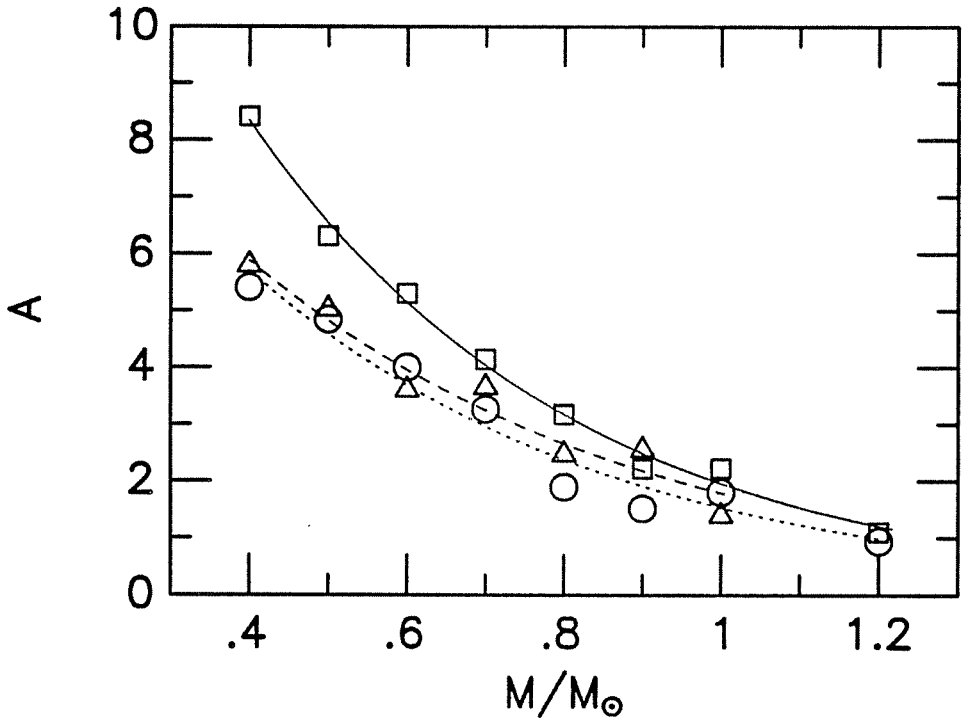

Figure 6.1: Behavior of and Fits to the Parameter A as a Function of Stellar Mass and Core Composition. The parameter A is the maximum age difference between the last converged model in a sequence and the asymptotic limit. The points shown here were from fits to the final two good models in a sequence for the carbon-core (*squares*), oxygen-core (*circles*), and mixed C/O-core (*triangles*). The fits shown over the data are of the form given by equation (6.6).

§14.4). Figure 6.1 shows the fits over the A's for the three core-composition choices.

I use these fitted values of A to calculate the extrapolations, and show the resulting age–luminosity relations for the carbon-core, oxygen-core, and carbon/oxygen-core sequences in Figures 6.2, 6.3, and 6.4, respectively. If the extrapolations were perfect, then we might expect the asymptotic age to be a smooth function of stellar mass for a given core composition. Inspection of the three Figures shows that it is not, and this is an indication of the

noise present in the process; however, even with the noise, this extrapolation relation is far superior to the simple 2-point extrapolation in the logarithm of the age and luminosity which others have used to extend cooling curves in the past. The latter completely ignores the dropping global heat capacity and so grossly overestimates the ages in the extrapolation region.

6.3 The Observed Luminosity Function

The observed disk luminosity function (LF) has been presented most recently in Liebert, Dahn, and Monet (1988; LDM88), and using the six high-velocity stars in this sample, Liebert, Dahn, and Monet (1989) constructed a halo LF. It is worthwhile to discuss these LFs and their associated uncertainties before proceeding with the theoretical results. Figure 6.5 shows the two LFs in a format which differs slightly from that in Liebert, Dahn, and Monet (1988). The data upon which the bright and faint portions of the LF are based come from two different sources, and I discuss each in turn.

The bright end of the observed LF [$M_V \leq +13$, corresponding to $\log(L/L_\odot) \gtrsim -3.3$ and ages $t_{\rm cool} \lesssim 1$ Gyr] is as determined by Fleming, Liebert, and Green (1986). Their sample was drawn from the white dwarf subset of the PG catalog, itself the result of the $U-V$ excess, magnitude-limited Palomar–Green survey, complete down to $m_V \approx 16.5$ (Green, Schmidt, and Liebert 1986). The LFs presented by Ishida *et al.* (1982) and Downes (1986) are in at least reasonable agreement with the Fleming, Liebert and Green result. Note that because the scale is logarithmic, 2σ error bars are not simply twice the standard 1 σ error bars. For working purposes, I normalize the disk LFs to the point $\log(L/L_\odot) = -2.91$,

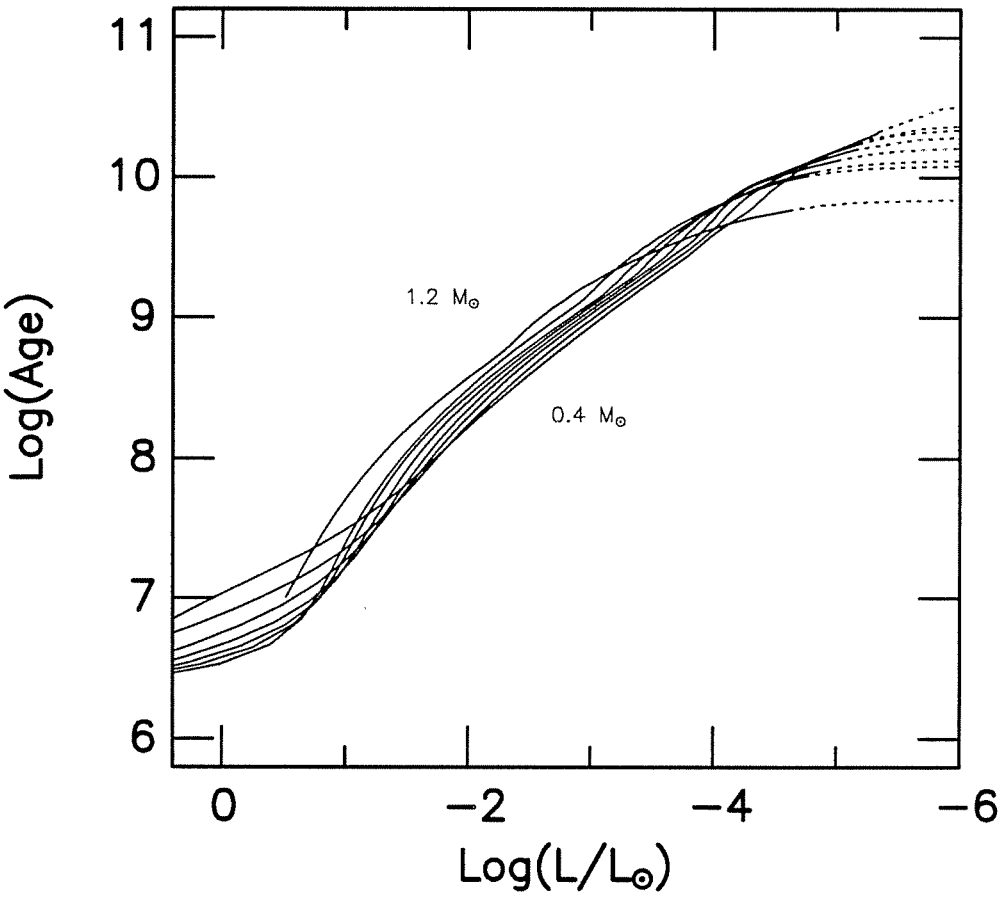

Figure 6.2: Age–Luminosity Relations for the Carbon-Core Sequences. The age–luminosity relations for the carbon-core sequences are shown (*solid lines*) including the extrapolation beyond the final converged models in the sequences (*dashed lines*). These DB sequences have masses 0.4, 0.5, 0.6, 0.7, 0.8, 0.9, 1.0, and 1.2 $M_{\odot}$. The surface helium-layer masses are typically $\log(M_{\rm He}/M_{\star}) = -4$, with the exceptions being c10500 and c12500 at $\log(M_{\rm He}/M_{\star}) = -5$. To facilitate intercomparison, this and the two following Figures are shown on the same luminosity scale as the corresponding LF Figures 6.6, 6.6, and 6.8, below.

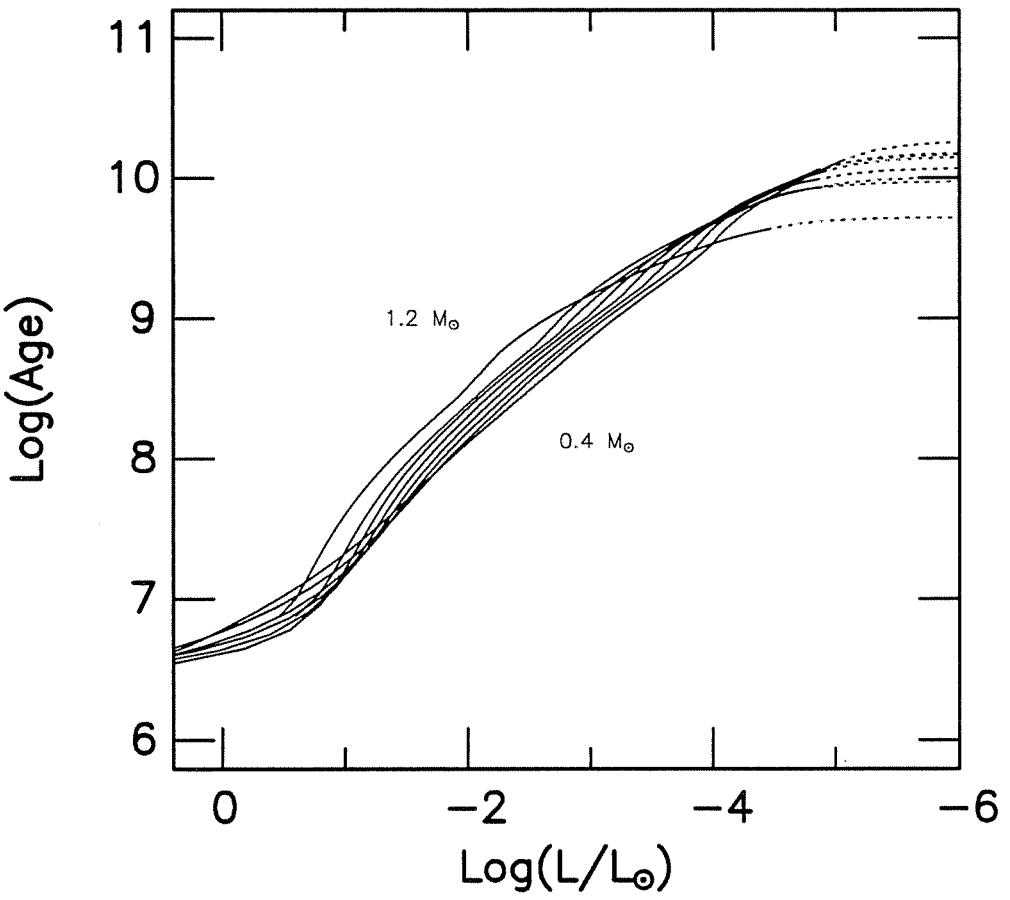

Figure 6.3: Age–Luminosity Relations for the Oxygen-Core Sequences. Similar to Figure 6.2.

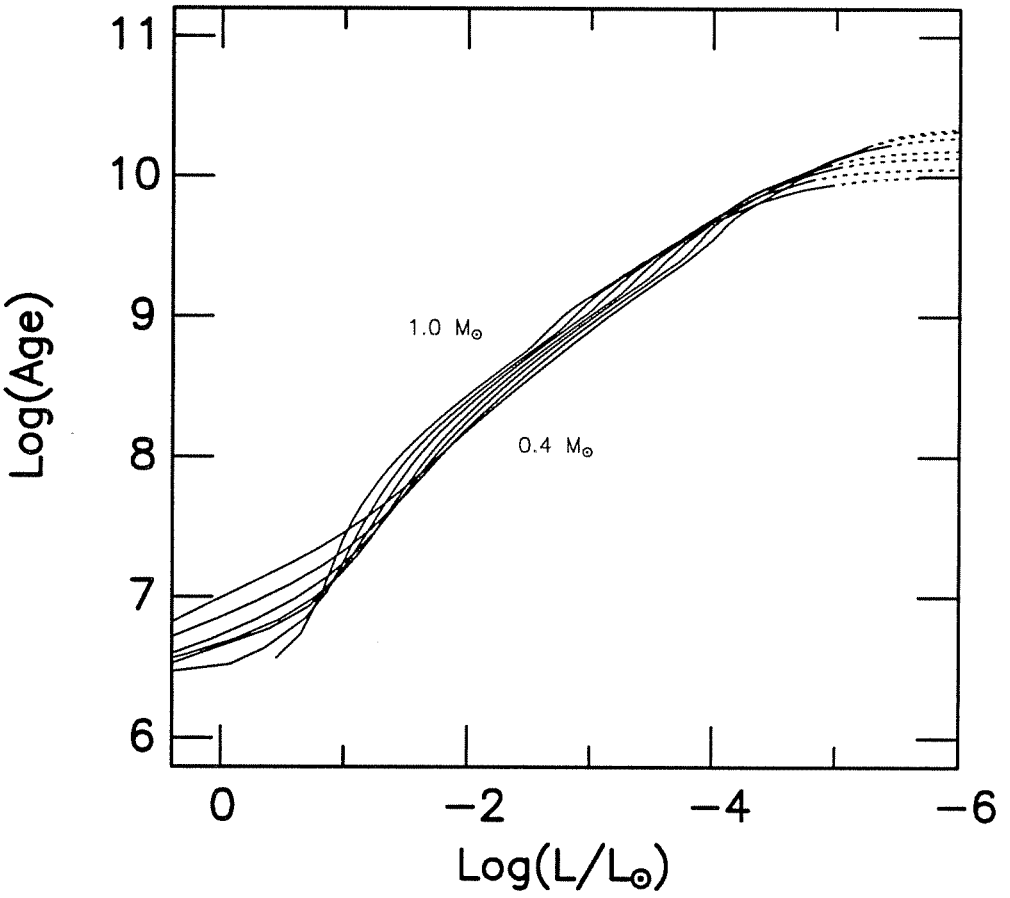

Figure 6.4: Age–Luminosity Relations for the Carbon/Oxygen-Core Sequences. Similar to Figure 6.2, these DB sequences have masses 0.4, 0.5, 0.6, 0.7, 0.8, 0.9, and 1.0 $M_{\odot}$ and all have helium layer masses of $\log(M_{\rm He}/M_{\star}) = -4$.

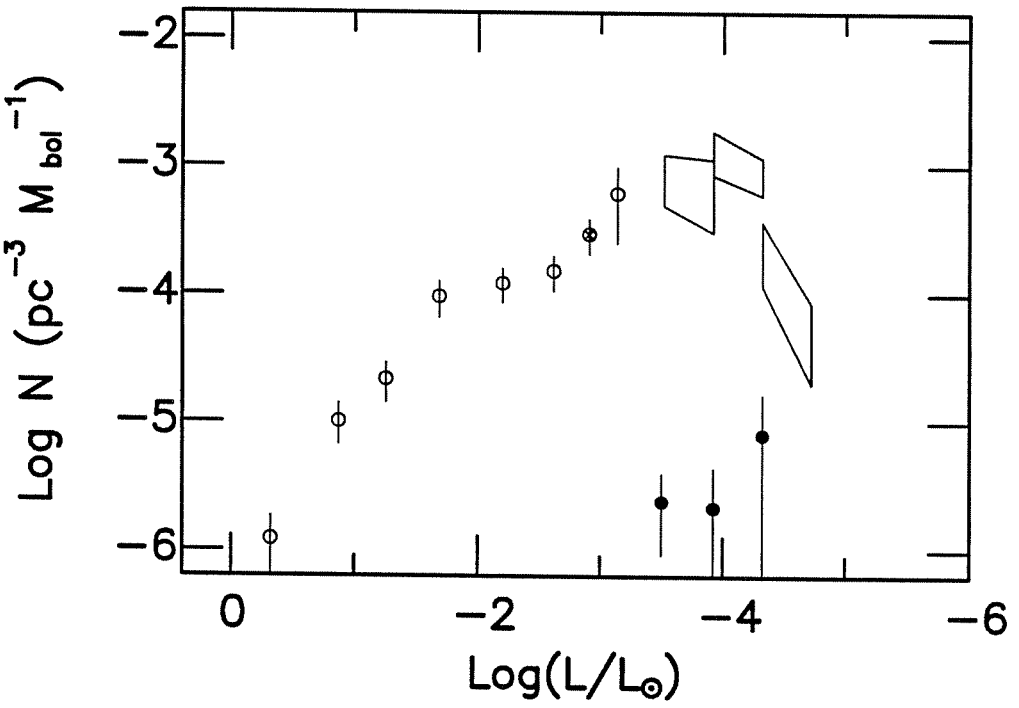

Figure 6.5: The Observed Luminosity Functions of the Disk and Halo. The disk LF is shown here in a form somewhat different from the original in Liebert, Dahn, and Monet (1988; their Figure 3). The high-luminosity points are as shown in LDM88 (o), but I combine the low-luminosity data from their Tables 6 and 7 to construct the uncertainty (or error) boxes representing the cool observed LF (see text). The normalization point used for the disk LFs is shown as a crossed circle (⊗). Also shown here is the preliminary observed halo LF as presented by Liebert, Dahn, and Monet (1989; •), constructed using the 6 high-tangential-velocity stars in their sample.

$\log N = -3.54$, which usually results in the curves not passing beyond the upper limit of any single error bar.

It is the low luminosity objects that dominate the space density of white dwarfs — the observed LF peaks at $\log(L/L_\odot) \approx -4.3$ — and these objects are usually found in proper motion studies or as binary companions to nearby stars. Luminosity functions constructed using proper motion selected

objects may have a bias introduced favoring stars with large tangential velocities. Liebert, Dahn, and Monet (1988) used the $1/V_{\rm max}$ method of Schmidt (1975), however, and because each star's contribution to the space density is itself a function of of its proper motion, the kinematic bias is removed directly. The $1/V_{\rm max}$ method requires a complete subset of the proper motion catalog. The authors drew their sample from the Luyten Half-Second (LHS) Catalog (Luyten 1979), selecting the 43 spectroscopically confirmed white dwarf stars which satisfied the criteria: proper motion $\mu \geq 0\farcs8$ yr^{-1}, absolute luminosity $M_V \geq 13$, and Galactic latitude $\delta \geq -20^0$. In making their error analysis, Liebert, Dahn, and Monet assumed that the uncertainty of a given star's contribution to the space density was equal to the value of the contribution itself. Thus, the counting uncertainties in a given luminosity interval can be dominated by a single uncertain contributing value. These uncertainties are reflected in the vertical extent of the error boxes.

In addition to the counting uncertainties, the values of the luminosities themselves are uncertain because the bolometric corrections (BCs) appropriate for the cool white dwarfs are not well known. Because of these BC uncertainties, Liebert, Dahn, and Monet (1988) analyzed and presented their data in two separate ways. First, they used the BCs predicted by cool DA (hydrogen-atmosphere) models for the cool DA stars and blackbody BCs for the cool non-DA models (no good atmosphere calculations exist for cool non-DAs). These result in corrections of a few tenths of a magnitude for the cool white dwarfs and suggest that the turndown occurs at $\log(L/L_\odot) \approx -4.3$. If the results were otherwise concordant, then this might have been the end of the story; however, the authors found that adopting the model/blackbody BCs implies that the cool white dwarfs are on average larger and hence less massive than average. In contrast, we expect that the

coolest white dwarfs should be *more* massive than average because more massive white dwarfs have shorter evolutionary timescales *and* presumably progenitors with shorter evolutionary timescales. To address this inconsistency, the authors in their second reduction simply assumed that the BC was zero for all stars. Although this has no physical basis, it does predict that the cool white dwarfs have masses near the mean. Liebert, Dahn, and Monet (1988), not knowing which of the two reductions was closer to the truth, presented both as outside limits. In this same spirit, I present them in Figure 6.5 as the left-hand and right-hand edges of the 3 uncertainty boxes (cf. their Figure 3). *Thus although we do not know observationally the exact luminosity of the turndown, we do know that it lies between* $\log(L/L_{\odot}) \approx -4.3$ *and* -4.7. This then is my criterion for acceptance in the luminosity functions presented below. Those that pass through the lowest-luminosity uncertainty box I consider to be consistent with the data, and those that do not, are not.

6.4 Single-Sequence Luminosity Functions

In the most recent discussion of nuclear reaction rates, Caughlan and Fowler (1988) estimate that the $^{12}C(\alpha,\gamma)^{16}O$ reaction rate is uncertain to a factor of 2, and this translates to correspondingly large uncertainties in the core composition that should be modelled. Above, I presented a large, homogeneous set of evolutionary sequences that were likely to bracket the "correct" parametrization of the stars themselves, and in the spirit of Liebert, Dahn, and Monet (1988), chose the 3 complete sets of sequences representing the complete range of possible core compositions: pure-carbon, pure-oxygen, and mixed carbon/oxygen cores. The mixed C/O core profiles are patterned

after C/O profiles predicted by MS→WD evolutionary calculations and so are likely to give the most reasonable ages. The profiles are parameterized by equation (3.1) and shown in Figure 3.1 above. The model sequences within the carbon and oxygen sets had masses of 0.4, 0.5, 0.6, 0.7, 0.8, 0.9, 1.0, and 1.2 $M_\odot$, and had helium envelopes and atmospheres with fractional masses typically $\log(M_{\rm He}/M_\star) = -4$ [the 1.0 and 1.2 $M_\odot$ sequences had $\log(M_{\rm He}/M_\star) = -5$]. The composition transition zones were idealized as discontinuities, but as was shown above there is not a large difference between these models and those that have the composition transition zones set to approximate diffusive equilibrium. These three sets of sequences are the inputs to the LF synthesis program unless otherwise noted.

As discussed in §7.2, the luminosity function of a single evolutionary sequence is proportional to $dt/d\log(L/L_\odot)$, and because it is a derivative it amplifies the features present in the age–luminosity functions [which are displayed as log(age) *vs.* $\log(L/L_\odot)$]. Figures 6.6, 6.7, and 6.8 show the single-sequence luminosity functions for the carbon-core, oxygen-core and mixed C/O core sequences, respectively. These are the building blocks of the integrated luminosity functions which follow, and so it is worthwhile to discuss briefly the features and their physical bases.

At high luminosities, we see the strong effects of the neutrino cooling in the interiors. The losses are immediate and are greater in higher-mass stars; the so-called neutrino dip is therefore larger for these models. Although neutrino losses are less important in lower-mass models, they persist to lower luminosities because the degeneracy is lower overall and the conductive opacities higher overall, resulting in a larger temperature contrast between interior and surface. In the Mestel regime, all the models nearly satisfy the

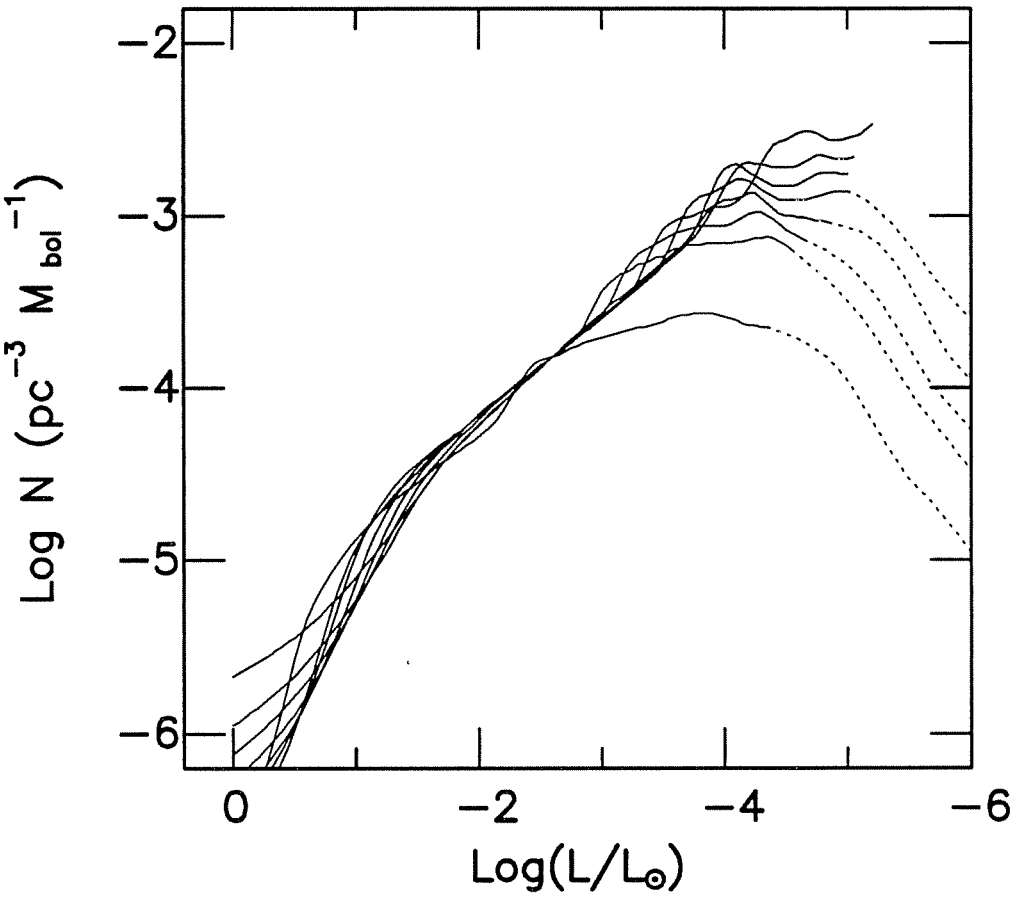

Figure 6.6: Single-Sequence Luminosity Functions for the Carbon-Core Model Sequences. See the text for a description of the mass dependence of the features. Compare with the age–luminosity relations in Figure 6.2. The LF extrapolations are shown for the sequences which are younger than 16 Gyr upon termination (*dashed lines*), calculated as described above. Note that in this and the following Figures, the ordinate axis labels read *l*og N for the quantity previously defined as log Φ in the text. I apologize for any confusion this may cause.

criteria under which the standard Mestel cooling law is derived (see above for details), and they all have slopes of approximately $\Phi \propto t^{5/7}$.

Crystallization in the interiors of white dwarfs stars is a first order phase transition with associated release of latent heat which acts as a luminosity

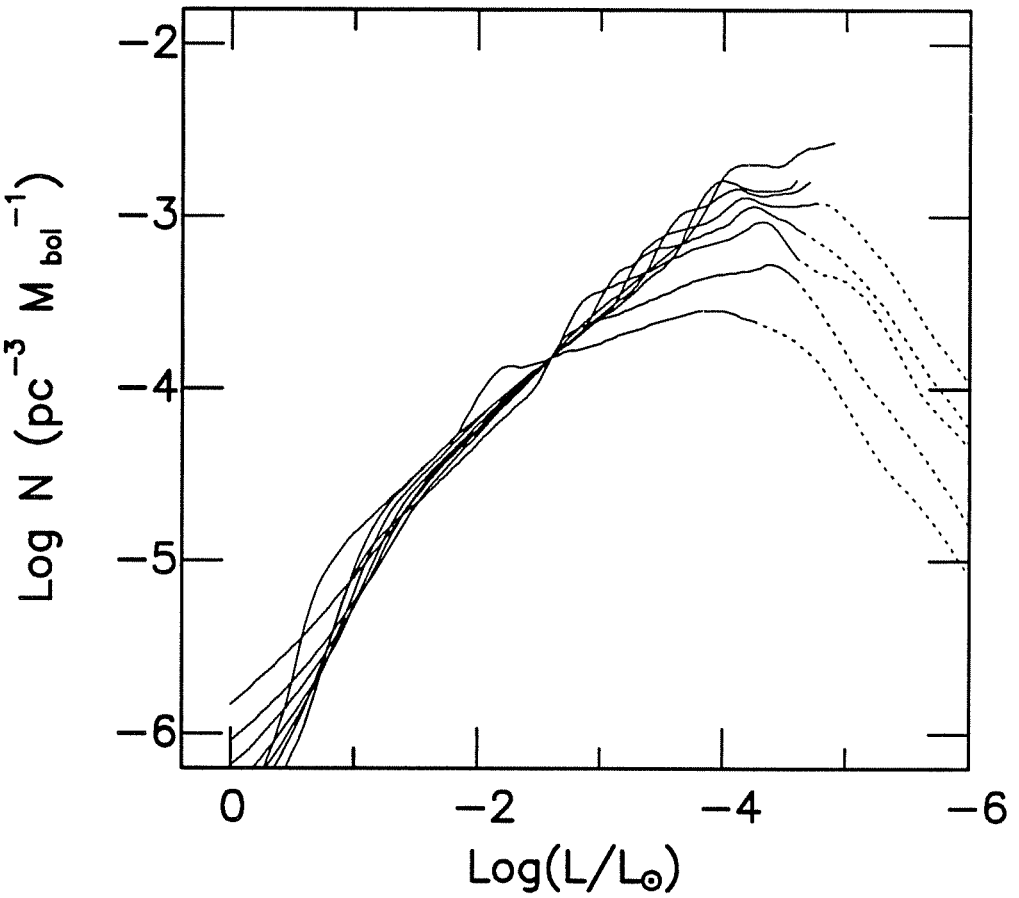

Figure 6.7: Similar to Figure 6.6, but for Oxygen-Core Sequences. Compare with the age–luminosity relations in Figure 6.3.

source through the fourth stellar structure equation relating luminosity $L_\star$ to $\frac{\partial s}{\partial t}$, where s is entropy (Van Horn 1968, Lamb and Van Horn 1975). The pressures are higher in the cores of more-massive models, and they crystallize first. The energy available in the crystallization process scales approximately with mass, but because the release begins at higher luminosities for higher-mass models and is also more spread out in luminosity, the effect on the ages is reduced. The luminosity interval spanned by crystallization is

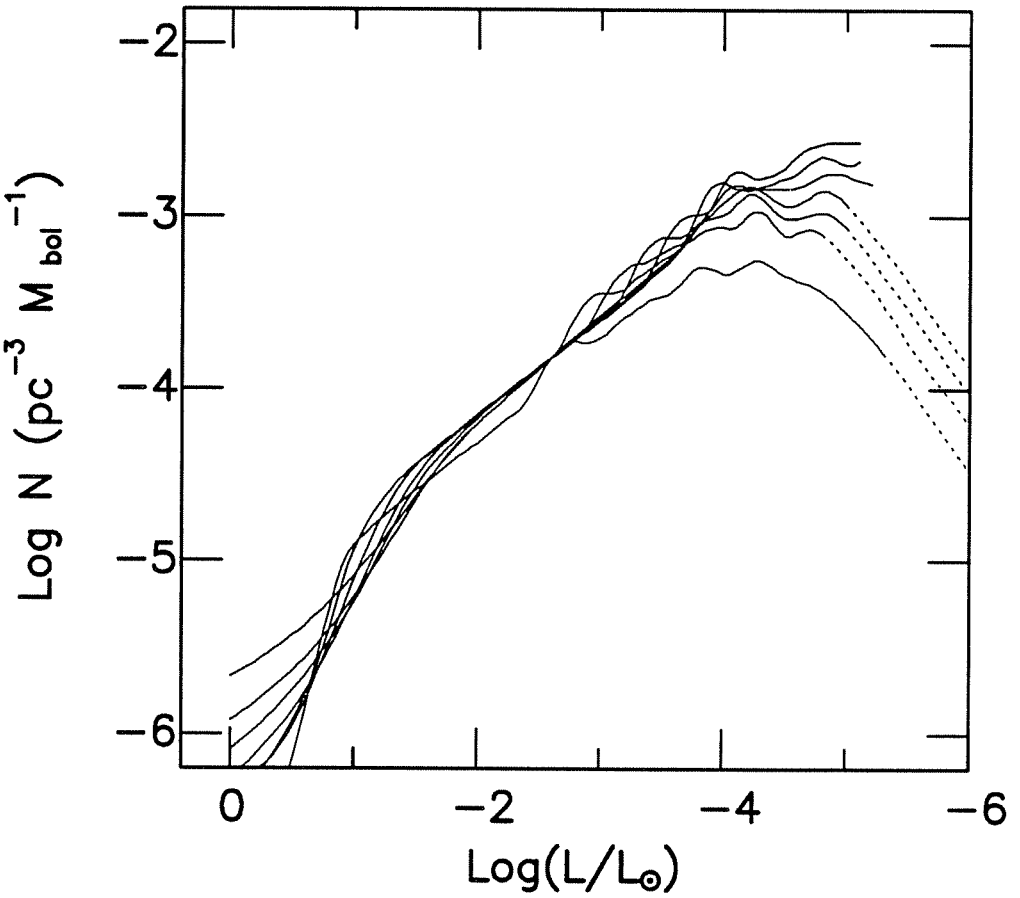

Figure 6.8: Similar to Figure 6.6, but for Mixed C/O Cores Defined by Equation (3.1). Compare with the age–luminosity relations in Figure 6.4.

larger in higher-mass models, and the onset is more gradual. Because of this, the effect on the luminosity function is smaller but more spread out. Following crystallization, the models enter the Debye cooling regime, and the global heat capacity and entropy drop with the core temperature, flattening the age–luminosity relation substantially and resulting in the cooling to microwave-background temperatures in a finite time span. The shape of the LF is also affected by core composition. Oxygen crystallizes at higher

temperatures (and hence higher luminosities) than carbon, and so for a given stellar mass the effect of crystallization is less in the oxygen-core sequences than in the carbon-core sequences. This results in a flatter peak compared to the carbon-core single-sequence LFs, and smaller leading coefficients to the extrapolation relation (6.5).

6.5 Integrated Disk Luminosity Functions

6.5.1 *Variations in Core Composition*

Probably the largest uncertainty in white dwarf evolution is the core composition of the stars themselves. Because the $^{12}C(\alpha,\gamma)^{16}O$ reaction rate is uncertain to roughly a factor of 2 (Caughlan and Fowler 1988), the core composition of the white dwarf stars as a function of progenitor mass and composition is poorly determined. The behavior of the rate as a function of temperature is non-intuitive and has been discussed recently by D'Antona and Mazzitelli (1990). They point out that the ratio $^{12}C/^{16}O$ is primarily dependent on the ratio of the cross sections for the 3α and $^{12}C+\alpha$ processes. The latter reaction is favored at lower burning temperatures, with the result that there is enhanced oxygen production in regions where the temperature is not too high. Thus, because the temperatures characteristic of core helium burning are lower than those of shell helium burning, we expect a greater fractional oxygen production in these regions. Similarly, we expect that overall the fractional oxygen production in lower-mass stars will be *greater* than that in higher-mass stars.

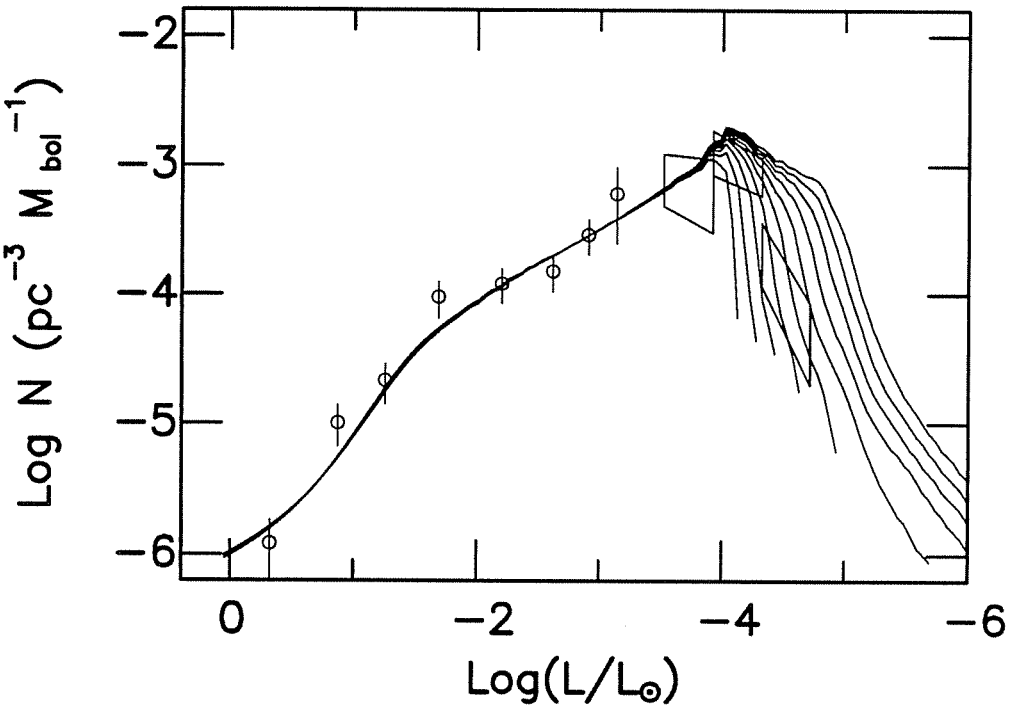

Figure 6.9: Integrated Disk Luminosity Functions for Carbon-Core Sequences using the Standard Model Parameters. Luminosity functions with input disk ages of 7–16 Gyr (at intervals of 1 Gyr) are shown over the observed luminosity function of Liebert, Dahn, and Monet (1988). Those which pass through the lowest luminosity error box have ages 9-12 Gyr.

Confronted with this uncertainty, I decided to bracket the true luminosity function by computing theoretical luminosity functions with the carbon-core and oxygen-core sequences from above in addition to the more realistic carbon/oxygen core sequences whose C/O profile was guided by the Mazzitelli and D'Antona (1986) and D'Antona and Mazzitelli (1989) results. Figure 6.9 shows the luminosity functions that result from integrating the standard-model parameters (defined in §6.2 above) with the carbon-core sequences and input disk ages of 7 to 16 Gyr. Also included for reference in this and subsequent Figures are the observational data of Liebert, Dahn,

and Monet (1988). In the Figure, note first that all of the theoretical luminosity functions converge at the high-luminosity end and that are all reasonable approximations to the data there. Because the sequences that we use start with polytropes at $\log(L/L_\odot) \approx 2$ and do not converge with the more-realistic tracks until a luminosity of order $\log(L/L_\odot) \lesssim 0$, I do not show the luminosity functions above this point.

The luminosity functions of the carbon-core models split off from each other at approximately $\log(L/L_\odot) = -3.7$, and peak shortly after this. The peak in the mass function is between 0.5 and 0.6 $M_\odot$, and because each of these individually peaks at $\log(L/L_\odot) \approx -4$, the integrated luminosity functions are fairly sharply peaked there as well. Beyond the peak, the low-age luminosity functions turndown sharply, whereas the older ones are flatter before turning down. The location of the dropoff is given approximately by the age–luminosity relation for the peak of the mass distribution, and the contributions beyond this point are from the high-mass white dwarfs, which evolve more quickly (and whose progenitors also evolved quickly). Note that the contribution of this high-mass tail to the luminosity function increases for increasing disk ages, and that the rate of falloff decreases. Focusing now on those luminosity functions which pass through the lowest-luminosity error box, we find that the acceptable fits run from an age of about 9 Gyr to slightly less than 12 Gyr. Note that Winget *et al.* (1987) fit carbon-core models to data that had the bolometric correction applied (corresponding to the left-hand sides of the low-luminosity boxes). The input sequences and galactic evolution model that went into the curves in this Figure are most similar to theirs, and interpolating by eye to the midpoint of the left-hand side of the lowest luminosity box suggests an age quite close to their estimate of 9.3 Gyr.

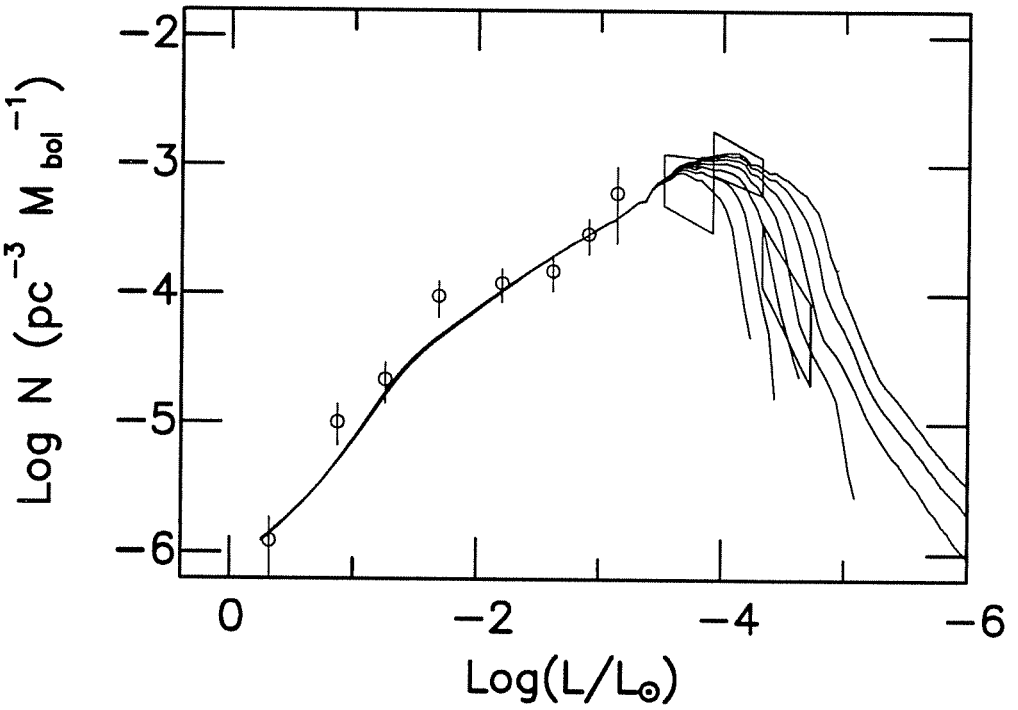

Figure 6.10: Integrated Disk Luminosity Functions for Oxygen-Core Sequences using the Standard Model Parameters. Luminosity functions with input disk ages of 6–12 Gyr (at intervals of 1 Gyr). Those which pass through the lowest-luminosity error box have ages of approximately 7-10 Gyr.

Figure 6.10 shows the LFs that result from integrating the standard-model parameters with the oxygen-core sequences as input. The ages used as input for the curves in this Figure are 6–12 Gyr, and those which satisfy the acceptance criterion have ages ranging from roughly 7 to 10 Gyr. The oxygen-core models diverge at a luminosity of $\log(L/L_\odot) = -3.4$, and the luminosity functions are flatter at the peak than the carbon-core models. Although the observational errors are too large to draw solid conclusions, the fact that these curves both rise and peak with a characteristic shape which is closer to the observed may indicate that the cores are dominated by oxygen,

as recent asymptotic giant branch calculations predict (see D'Antona and Mazzitelli 1990). In addition, because the oxygen-core models are evolving faster at the luminosity of the turndown, the spacing between the luminosity functions is larger at the turndown luminosity. The oxygen-core models give a lower limit on the disk age, especially if we consider thicker helium layer masses.

Recall Figure 4.14 which demonstrated the dependence of the ages on the adopted helium-layer mass. This Figure shows that the ages sampled at each of three luminosities within the lowest-luminosity error box are to a good approximation linear functions of the logarithm of the fractional helium layer mass, as discussed above. Because this Figure was generated using 0.6 $M_{\odot}$ sequences, it reasonably reflects the age shifts that we would expect as functions of the core composition and helium-layer mass. For example, the models I've used here have helium layer masses of $\log(M_{\rm He}/M_{\star}) = -4$. If instead I had used models with $\log(M_{\rm He}/M_{\star}) = -3$, then I might expect that the age ranges for the carbon and oxygen integrated luminosity functions would be shifted to lower ages by roughly 1.0 and 0.7 Gyr, respectively (depending on the luminosity under consideration). To the extent that the stars at the turndown luminosity have masses near 0.6 $M_{\odot}$, Figure 4.14 gives the conservative upper and lower limits to the age estimates for the local disk obtained through a comparison with the observational upper and lower limits to the lowest-luminosity error box.

Last of the standard model integrations is that using the C/O-core models. The resulting luminosity functions are shown in Figure 6.11 for ages 7-15 Gyr, and because the model sequences are the closest to the structure of the stars themselves, these LFs should provide the best estimate of the age of the local disk of the families of curves shown so far. The curves which

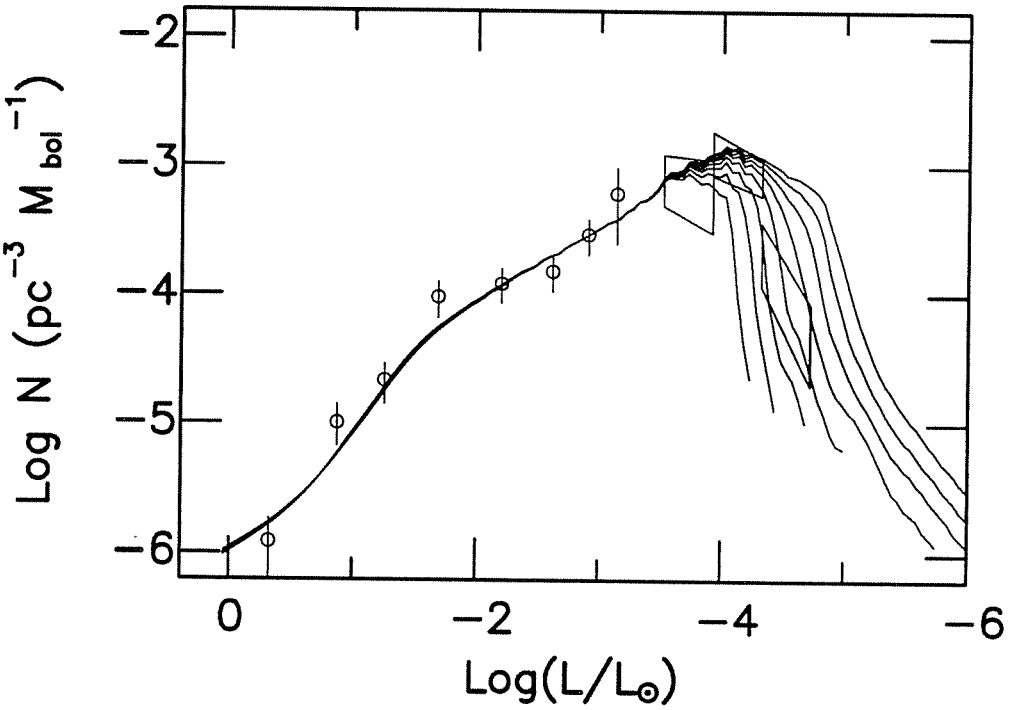

Figure 6.11: Integrated Disk Luminosity Functions for Carbon/Oxygen-Core Sequences using the Standard Model Parameters. The luminosity functions have input disk ages of 6–13 Gyr (at intervals of 1 Gyr). Those which pass through the lowest-luminosity error box have ages of approximately 7.5-10 Gyr.

pass through (or at least touch) the lowest-luminosity observational error box have ages of approximately 8-11 Gyr. Note that in each of the three cases discussed so far, the age spread is typically 3 Gyr over the observational uncertainties. By contrast, if the observed points were not uncertain because of the lack of good bolometric corrections, then the typical uncertainty of the theoretical fits would be roughly half those suggested by these fits. I will discuss this further below.

6.5.2 *Variations in the Initial Mass Function*

As reviewed recently by Scalo (1986), the determination of the initial mass function has been a long-standing problem in astrophysics, and although it is in nature intimately tied to the star formation rate (see also Tinsley 1980, and Miller and Scalo 1979), we usually separate the two as in equation (6.2) and write for the IMF, $\phi(M) = (M/M_{\odot})^{-\alpha}$. As discussed by Scalo, we find observationally that IMFs appear similar over a wide range of galactic types and metallicities, that differences among the IMF exponents α are only of order ± 0.5. Furthermore, there is no evidence for the IMF being a function of galactocentric radius or local metallicity.

Beyond these time-averaged results, however, we find that the IMF slopes are different for high-mass and low-mass stars, and that in fact the high-mass and low-mass stars form in distinctly different environments. It appears that whereas low-mass stars form in cold, dense cores typical of the Galactic inter-arm environment in the disk (see Shu, Adams, and Lizano 1987; Boss 1989), high-mass stars form in warmer environments typical of H II regions in the spiral arms — the idea being that the heating by the high mass stars raises the Jeans mass (*e.g.*, Silk 1977), and that shocks from supernova events drive a cascade of formation (see Scalo 1986). We find a significant absence of low mass stars in high-mass star forming regions, and a similar lack of high-mass stars in low-mass star forming regions (see Bash and Vissar 1981). Güsten and Mezger (1983) have suggested on the basis of their chemical evolution studies that while the slope of the IMF is the same throughout the disk, the lower mass limit, M_L, slides up and down depending on the local environment. They suggest that $M_L \approx$ 2–3 $M_{\odot}$ in the spiral arms, compared to $M_L \approx 0.1$ in the interarm region. The

progenitor clouds of the high-mass and low-mass star forming regions have differing scale heights. The dense cores in which the low-mass stars form have a larger scale height than do the giant molecular clouds in which the high-mass stars form, and as a result the low-mass stars themselves have a larger scale height than high-mass stars.

The slope of the Salpeter IMF is observationally determined to be in the range $-2.3 \geq \alpha \geq -3.4$ (see Scalo 1986), and the question is: how important are these uncertainties to the derived white dwarf luminosity functions? As a test, I computed a series of variations on the standard model with the slopes set to $\alpha = -1$, -2, -3, and -4 for the carbon-core sequences and an input disk age of 9 Gyr (see Figure 6.12). This range of IMF slopes more than spans the current observational uncertainties, and we see that even over this extreme range, the luminosity functions are relatively insensitive to variations in the IMF, and suggest a $\sim$1 Gyr uncertainty over this IMF range. Similar results are found using the oxygen-core sequences (not shown), and also by Yuan (1989) and Noh and Scalo (1990), who used the Winget *et al.* (1987) cooling curves. Noh and Scalo noted that this is one of the few cases where the effects of the IMF and the star formation rate are essentially decoupled from each other.

In addition to variations in the slope of the IMF, it is also of interest to consider the effects of variations in the adopted upper main-sequence mass limit for the integration. This was investigated by Iben and Laughlin (1989), who found little change in the resulting LF as M_U was changed from 8 $M_\odot$ to 6 $M_\odot$. Figure 6.13 shows luminosity functions calculated assuming upper mass limits of $M_U = 2$, 4, 6, and 8 $M_\odot$. Here again these are variations from the standard model for the carbon-core sequences and an input disk age of 9 Gyr. In examining the Figure, it is apparent that indeed the differences

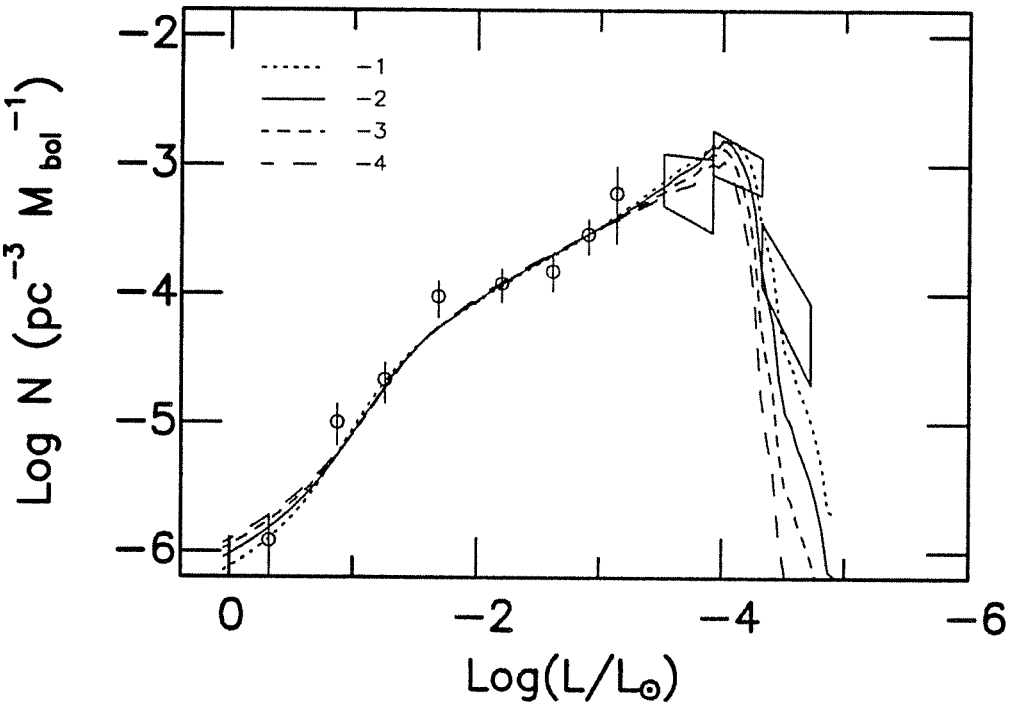

Figure 6.12: The Effects of Variations in the Initial Mass Function. The four luminosity functions shown here were computed with IMF slopes of $\alpha = -1$, -2, -3, and -4, and demonstrate conclusively that the white dwarf luminosity function is largely insensitive to uncertainties in the IMF.

among the luminosity functions with the three higher-mass limits are quite small — well within the current observational uncertainties. The curve computed with the 2 $M_\odot$ upper limit shows substantial differences from the other three; however, because the white dwarf progenitors have masses that extend *at least* to 5 $M_\odot$, this final curve is not physical. Again, the LFs calculated using the oxygen-core sequences behave similarly, but are not shown.

Finally, because the observations suggest that the lower MS mass limit for star formation is a function of time, and in particular because it has

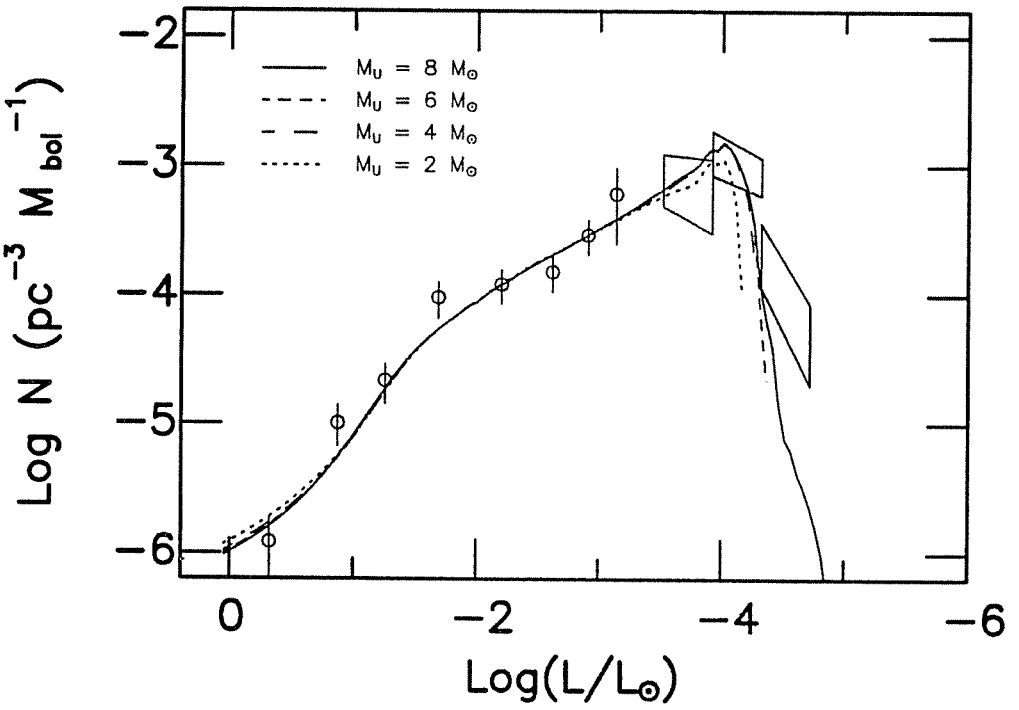

Figure 6.13: The Effects of Variations of M_U on the Luminosity Functions. The four luminosity functions shown here were computed with M_U = 2, 4, 6, and 8 $M_\odot$, as labeled. The differences among the latter three are small, and indicate that uncertainties in M_U are unlikely to be a source of uncertainty in the determination of the disk age.

been suggested that the lower mass limit was a decreasing function of time in the early Galaxy, it is worthwhile to simulate this to see the results. I have chosen three arbitrary but plausible analytical forms for the relation $M_L(t)$. Two of these are exponentially declining with time, and the third is simply a long linear decline:

$$M_L = \begin{cases} 8e^{-1.33t}, & \text{Case A,} \\ 8e^{-0.40t}, & \text{Case B,} \\ 8(1-\frac{t}{5}), & \text{Case C.} \end{cases} \tag{6.7}$$

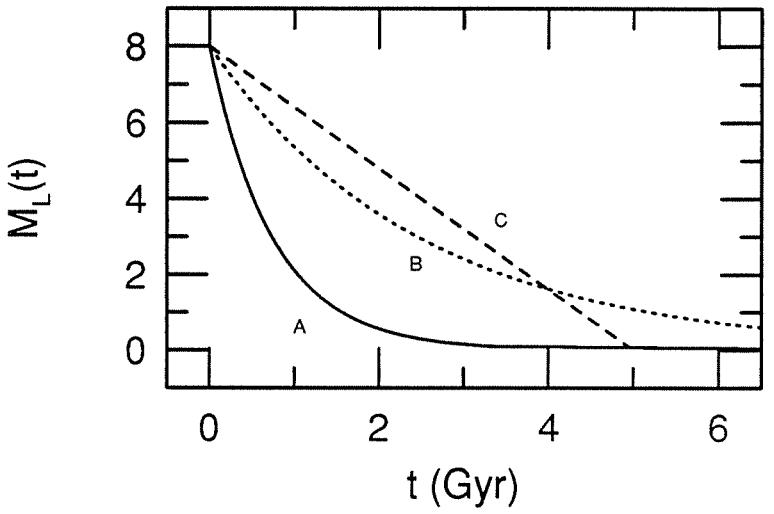

Figure 6.14: Three Test Relations Simulating the Possible Monotonic Decline in M_L with Time in the Early Galaxy. The curves in this Figure correspond to the three cases in equation (6.7) as indicated.

Of the three cases, the first is probably the most physical, as it suggests that 1 $M_\odot$ mass stars began forming approximately 1 Gyr after the onset of star formation in the disk (see Figure 6.14). The luminosity functions corresponding to these curves are shown in Figure 6.15 along with a standard-model luminosity function. They were computed using the carbon-core sequences and a disk age of 10 Gyr, with the remaining parameters according to the standard model. In the Figure, it is apparent that if in fact M_L is a function of time, then it will affect the location of the turndown. The Case A relation shows an age shift of approximately 0.5 Gyr relative to the standard-model curve (cf. Figure 6.9), and the Case B and C curves show

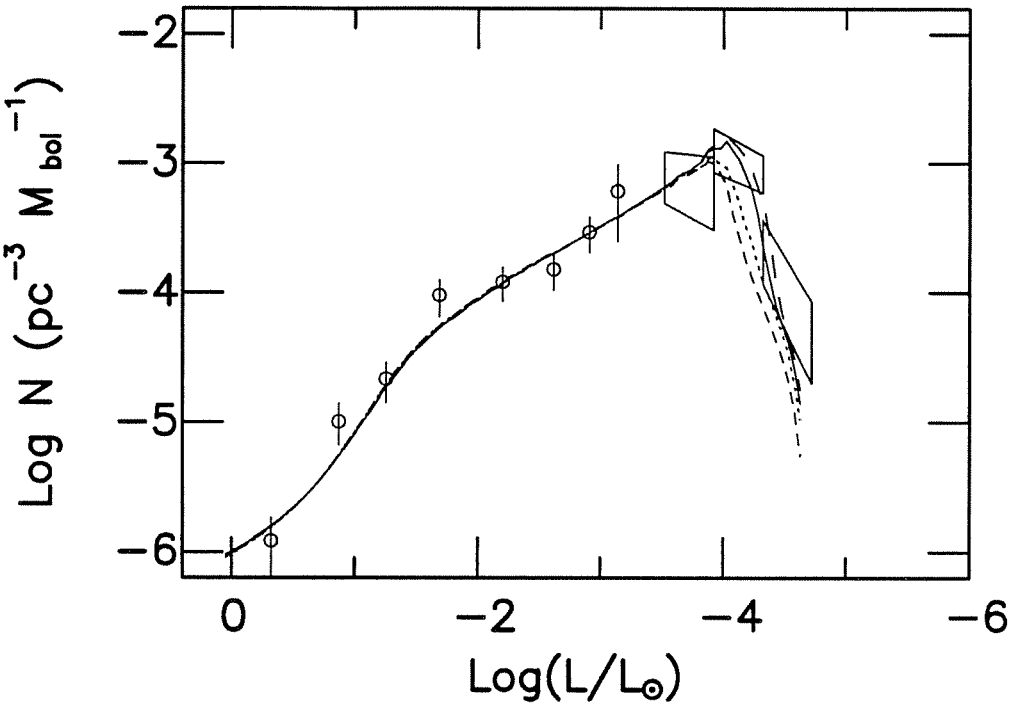

Figure 6.15: The Effects of a Monotonic Decline in $M_L(t)$ in the Early Galaxy. Three of the four luminosity functions shown here were calculated with the $M_L(t)$ relations shown in Figure 6.14, and correspond by line type.

age shifts on the order of 1 and 2 Gyr, respectively. This result again emphasizes the point that what we are measuring with the falloff is the length of time that low-mass stars have been forming in the local disk.

6.5.3 *Variations in the Star Formation Rate*

6.5.3.1 *Galactic Formation and Evolution in Brief*

As discussed in the recent comprehensive review by Gilmore, Wyse, and Kuijken (1989; GWK89), understanding the history of star formation in the

local disk of the Galaxy is an important step to understanding galactic evolution in general. To get things into context, it is worthwhile to consider the picture in an evolutionary sense, starting from $t = 0$. We know that the Big Bang occurred, and we know that matter (at least the luminous matter) is clumped into galaxies and that the galaxies are clumped on larger mass scales and so on, but that on the largest scales the universe appears smooth. As discussed by Hogan (1990), early results from COBE (**CO**smic **B**ackground **E**xplorer) satellite show that the microwave background exibits a 2.74 K blackbody spectrum with *no* apparent anisotropies other than the dipole caused by the Earth's absolute motion (see Lindley 1990). The impressive jump in sensitivity achieved with this instrument provides at last observational constraints on pre-galactic cosmology that are severe enough to seriously challenge many long-standing ideas; most dramatically, it is becoming increasingly difficult to explain the transition from the smooth background to the currently-observed large-scale structure in terms of gravitational interactions only, and string theory is all but unraveled. What this means for our purposes here is that we simply don't know the timespan between the Big Bang and the onset of star formation — estimates run from as short as 0.5 Gyr to as long as $\sim$5 Gyr (see Fowler and Meisl 1986). Furthermore, it is not clear that we will resolve the question soon.

The process of the formation of the Galaxy is also poorly known, but at least here there exist number of observational constraints. The number of suggested formation models is large, including but not limited to: rapid-collapse models (Eggen, Lynden-Bell, and Sandage 1962), pressure-supported collapse models (*e.g.*, Larson 1976), aggregate models involving the accretion of a large population of dwarf spheroidals (*e.g.*, Freeman 1987,

Searle and Zinn 1978), and nonlinear models involving cloud disruption from infall-imparted kinetic energy (Vasquez and Scalo 1989).

In the rapid collapse models, star formation starts throughout the proto-galaxy on approximately a free-fall timescale (a few 10^8 years), whereas in the pressure-supported collapse models, star formation begins in the bulge and halo of the proto-galaxy on a short timescale but then sweeps out radially through the disk over a period of a few billion years. Wyse and Gilmore (1988) suggest a variant of this picture wherein the rate of dissipation and the star formation rates increase substantially from increased cooling once the metallicity climbs to [Fe/H] ~ -1 dex, leaving behind a discrete population of stars with disk-like properties but with velocity dispersion perpendicular to the disk of order 45 km s^{-1} — the so-called thick disk. Both of these models suggest that there should exist an age–scale height relation for the oldest stars, and although such a trend is observed, it will be some time before it is clear whether the observations indicate that these stars are members of a separate thick disk population or are simply the extended tail of the old disk (see Norris and Green 1989, and Gilmore, Wyse, and Kuijken 1989 for a discussion of this). The aggregate models work from the idea that the early proto-galaxy was not stable against smaller-scale collapse in the virial collapse phase, but rather fractionated into a large number of roughly globular-cluster-mass systems which then proceeded to accrete to form the Galactic disk and globular cluster system as we observe it today. In the nonlinear one-zone models of Vasquez and Scalo (1989), infall of material onto the disk injects kinetic energy into the system of star-forming clouds, potentially disrupting them. The authors found that infall could suppress star formation for up to $\sim$5 Gyr and that the termination of this lull should be heralded by an energetic burst of star formation. The

model is crude and extrapolating from a one-zone model to the entire Galaxy is a stretch; however, it does seem plausible in view of the Vasquez and Scalo results and the discussion in the previous subsection that the infall of matter should at least heat the disk, raise the Jeans mass, and possibly enhance the high-mass star formation rate.

The very existence of a thin, cold disk suggests that the collapse was dissipative; if it was not the matter would be at the virial temperature of roughly 10^6 K with a corresponding 1-dimensional velocity dispersion of order 100 km s^{-1}. The dissipation Likely proceeded first according to the virial theorem, and then via ionizing radiative shocks and subsequent radiation upon recombination (GWK89 and references therein). Although the picture is in essence simple enough in concept, the presence of shocks makes it extremely difficult to model successfully, especially at the resolution needed to track subsequent star formation. Typically, the constant density approximation is used, thus averaging over all local perturbations and greatly simplifying the calculation (Rees and Ostriker 1977, Binney 1977, and Silk 1977). These authors have found that the calculated global cooling timescales are usually smaller than the free-fall collapse timescales for objects of roughly Galactic mass and smaller $\mathcal{M} \lesssim 10^{12}$, but not for masses characteristic of groups and clusters of galaxies. The cooling times for the shock ionized matter must be considered to be uncertain to an order of magnitude, however, and this raises the very real possibility that the Galaxy sustained an epoch of pressure supported, quasi-static collapse (*e.g.*, Larson 1976). Because the local environment suggested by this model is similar in many ways to that of the high-stellar-mass-forming H II regions we observe today, it is plausible to consider that the very early star formation history of the Galaxy was dominated by high-mass star formation, and that only with

time did significant numbers of progressively lower mass stars first form. In other words, it is plausible that the lower mass limit of the IMF monotonically decreased as the metallicity increased (see Scalo 1986). Because it is precisely these stars that the white dwarfs are tracers of, the results below may help differentiate among these early collapse models.

6.5.3.2 *Theoretical Approximations to the Star Formation Rate*

Having discussed in some detail the various models which have been suggested for the formation and evolution of the Galaxy, we now take a leap to some simple analytical approximations to the SFR, and explore further the match between the theoretical curves and the observations.

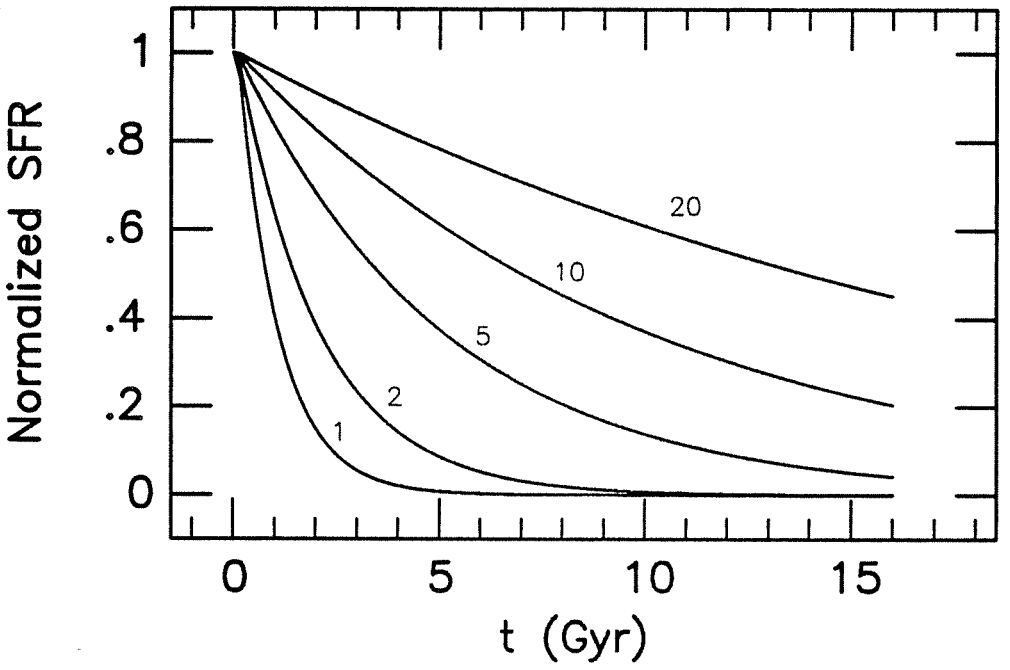

Figure 6.16: Exponentially-Decaying Star Formation Rates with Selected Decay Constants. The SFR curves are normalized to 1.0 at $t = 0$, and have their e–folding timescales printed along side.

Beyond the crudest approximation — that the SFR has been constant in time — the next step in complexity is to adopt a simple analytical approximation to the evolution of the gas density $\rho_{\rm gas}$ under the assumption that the SFR approximately obeys

$$\psi(t) \propto \rho_{\rm gas}^{\beta} \tag{6.8}$$

where β is usually assumed to be 1 or 2. An obvious choice for the functional form of the SFR is an exponential decay with time,

$$\psi(t) \propto e^{-t/\tau_{\rm SFR}}, \tag{6.9}$$

where $\tau_{\rm SFR}$ is the decay constant, typically thought to be of order a few 10^9 years. The curves in Figure 6.16 show a family of exponentially declining SFRs and Figure 6.17 shows the luminosity functions calculated using these curves, the carbon-core models, and the standard-model parameters for everything else. The luminosity functions in Figure 6.17 use the carbon-core sequences and an input disk age of 9 Gyr, and again are normalized to the observed LF at $\log(L/L_{\odot}) = -2.9$. Because the curves were all normalized to the observations in the Mestel regime, and because for all the e–folding timescales chosen the SFR is fairly constant for the most recent 1 Gyr, the curves are nearly indistinguishable above $\log(L/L_{\odot}) \approx -3$. Alternatively, the curves could be normalized at the peak in the luminosity function, and we would then find a substantial deviation from the brighter observed points for the curves calculated with the short e-folding timescales. For reference, I have also included in the figure a curve corresponding to the same model inputs, but with a constant SFR. The differences between this curve and those with e–folding timescales of 10 and 20 Gyr are quite small, and even the curve with an e–folding timescale of 5 Gyr is within the errors when

compared with the constant SFR model. Thus, it is not possible on the basis of existing observations to prefer one of these prescriptions over the others, although it is at least possible to rule out exponential-decay models that have *e*–folding timescales of order or smaller than 2 Gyr. This is consistent with other evidence that the SFR cannot have changed grossly over ~10 Gyr (see, for example, Barry and Scalo 1990).

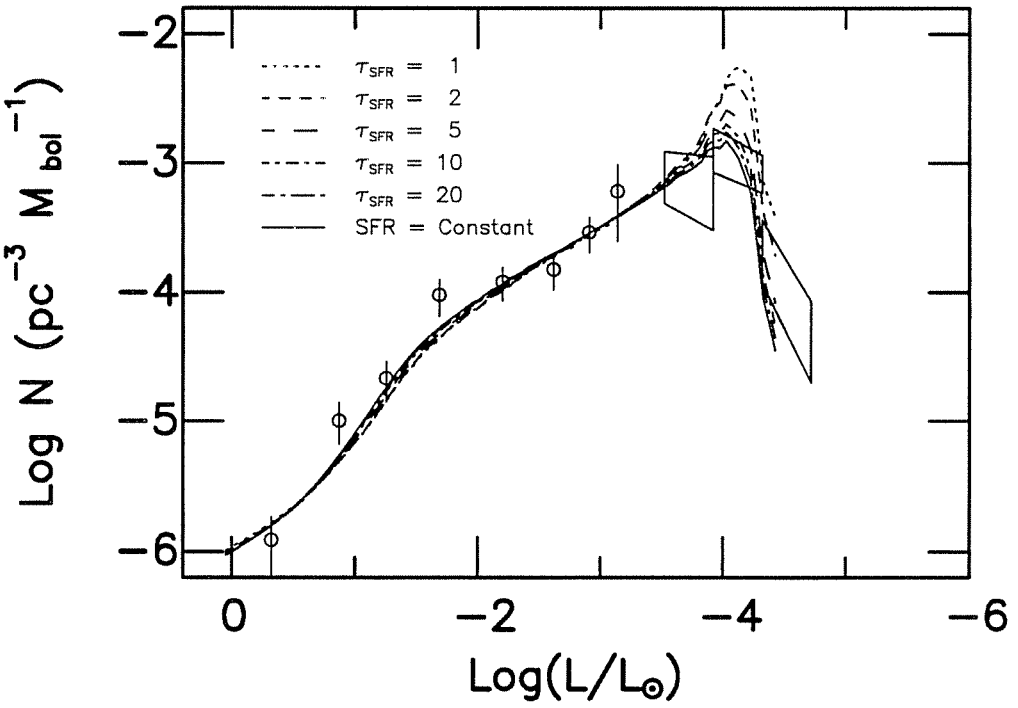

Figure 6.17: Luminosity Functions Computed with Exponentially-Decaying SFRs. The *e*–folding timescales used as input to the calculations were 1, 2, 5, 10, and 20 Gyr, and for reference the Figure also includes a luminosity function computed with a constant SFR. As discussed in the text, the models with *e*–folding timescales of order or greater than 5 Gyr are consistent with the observed data.

Clayton (1988) has quite reasonably suggested that a simple exponential decay is unphysical because there is likely to have been a sustained infall onto the disk as star formation began. Under this assumption, he derived a relation for the evolution with time of the mass of the gas $M_G(t)$, again assumed to be proportional to the SFR:

$$\frac{M_G(t)}{M_{G0}} = e^{-\omega t}\left\{1 + \frac{\omega_t}{\omega' - \omega}\left[1 - e^{-(\omega'-\omega)t}\right]\right\}, \tag{6.10}$$

where M_{G0} is the initial gas mass, ω is the gas consumption constant defined by the relation $\omega M_G = (1 - R)\psi$ where R is the gas return fraction, ω' is the exponential infall constant in $f(t) = f_0 e^{-\omega' t}$ where f_0 is the initial strength of the infall, and $\omega_f \equiv f_0/M_{G0}$ is a measure of the strength of the initial infall. Typically, the value chosen for the gas consumption constant is $\omega = 0.3$ Gyr^{-1} , and for the strength of the infall $\omega_f = 5$ (see Clayton 1985). Again assuming a linear relationship between $\rho_{\rm gas}$ and ψ, the resulting SFRs — shown in Figure 6.18 — then have maxima that occur some 1–4 Gyr after the onset of star formation. A series of 9 Gyr, carbon-core sequence luminosity functions corresponding to these SFR curves are in Figure 6.19. Alongside a constant-SFR luminosity function computed similarly, the luminosity functions show little variation as a result of the Clayton SFRs. Though the time of SFR maximum for the curve with the 5 Gyr halo-infall timescale and the 3 Gyr gas consumption timescale ($\omega' = 0.2$, $\omega = 0.3$) occurs about 4 Gyr after the onset of star formation, the relevant timescale in determining the location of the turndown for this or any SFR is the rise time to achieve a significant star formation rate, and not the time of maximum SFR. Looking at Figure 6.18, we find that the dispersion in ages at early times when the SFR first reaches 50% of its maximum is of order 1 Gyr. It is this spread of ages that the turndown

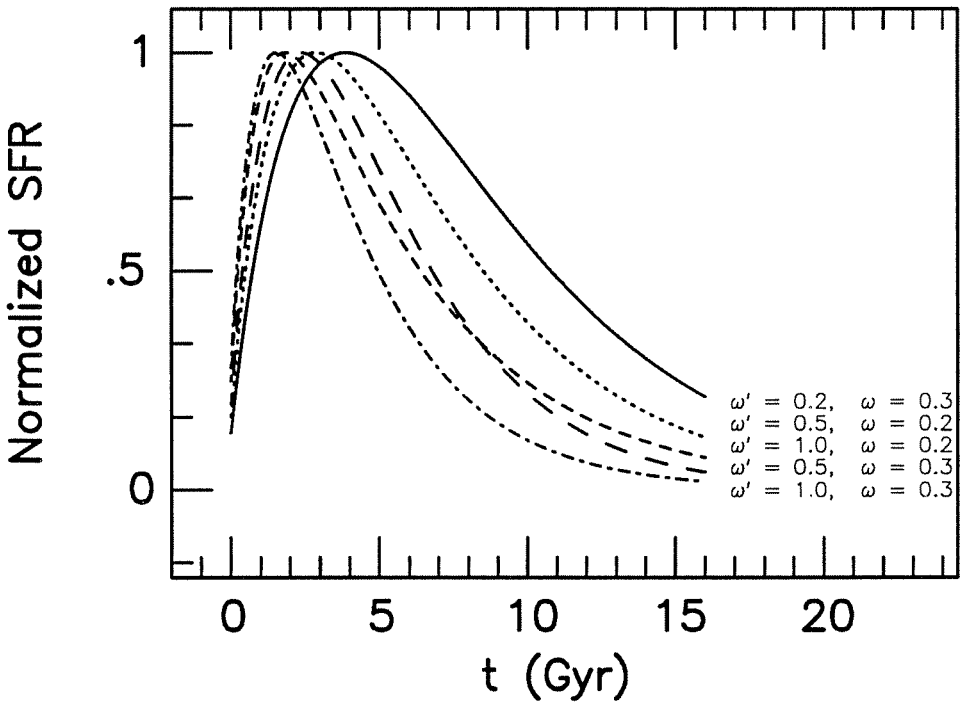

Figure 6.18: Normalized Clayton (1988) Star Formation Rates. Similar to the curves in Clayton's Figure 2, the curves shown have infall timescales ranging from 1 to 5 Gyr ($\omega' = 1$ to 0.2) and gas consumption timescales ranging from roughly 3 to 5 Gyr ($\omega = 0.2$ and 0.3). The star formation rate is assumed to be linearly proportional to the gas density. Although the peaks in these SFR relations occur as late as 4 Gyr after star formation onset, it is the age dispersion when the SFR first reaches ~50% that affects the location of the WDLF turndown.

luminosity is sensitive to, and comparison against Figure 6.9 shows that the indicated spread is of order 1 Gyr.

6.5.3.3 *Empirical Star Formation Rates*

Various authors have published empirically-obtained star formation histories for the Galaxy, among them Twarog (1980) in an age–metalicity study of a large sample of southern F dwarfs, and Barry (1988) using the observed

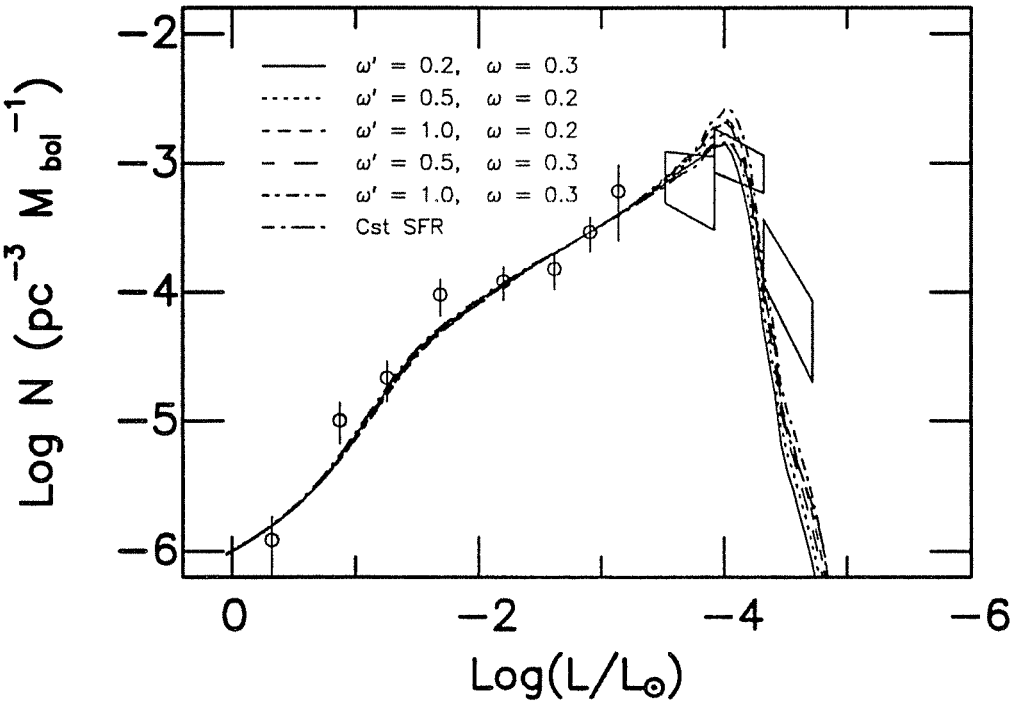

Figure 6.19: Luminosity Functions Calculated with the Clayton Star Formation Rates. The curves in this Figure correspond to the SFRs of the previous Figure, and a constant SFR is also included for reference. The spread in ages indicated by comparison with Figure 6.9 above is of order 1 Gyr. See the discussion in the previous caption.

chromospheric activity–age relation in a study of a sample of late F and G dwarfs. Figure 6.20 contains the SFR/⟨SFR⟩ values of Twarog's Table 3, and the expected SFR history of Barry as given by the outer envelope of the histogram in his Figure 4 (note that this has since been superceded by Barry and Scalo (1990), but that the adjustments are slight). In addition to showing Barry's data in the 4×10^8 yr bins he used, the Figure also shows them in 1.2 Gyr bins which smooth out the probably-spurious discontinuities and reversals indicated by the finer resolution.

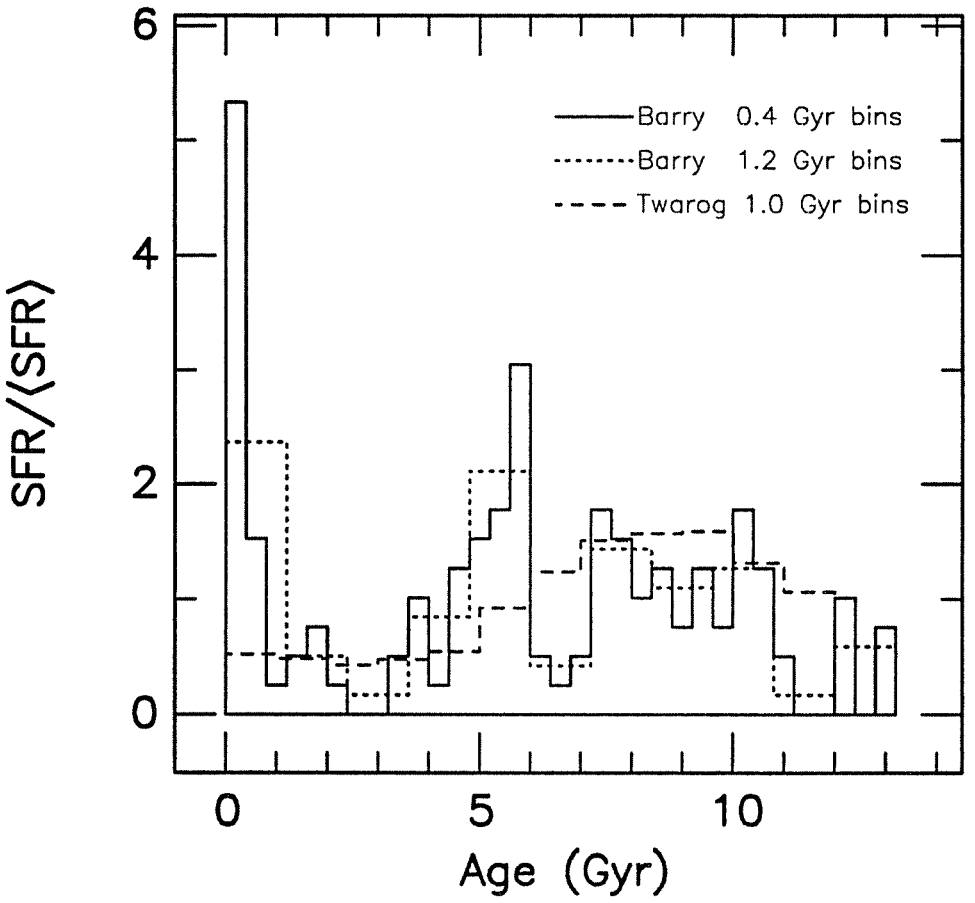

Figure 6.20: Empirical Twarog (1980) and Barry (1988) Star Formation Rates. Plotted as SFR/⟨SFR⟩, the data of Twarog are from his Table 3, and those of Barry are from the outer envelope of the histogram of his Figure 4. In addition to these histograms, I have also binned the Barry data into 1.2 Gyr steps to compare with the Twarog data.

The luminosity functions corresponding to these SFRs are shown in Figure 6.21. These models used an input disk age of 12 Gyr, the carbon-core sequences and the standard-model defaults for the remaining parameters. They show substantial differences from the comparable constant-SFR curve which is also shown in the Figure for reference. At high luminosities, the luminosity function shows an enhancement resulting from the recent

burst indicated by Barry's derived SFR. Excepting the highest-luminosity observed point, this curve is an excellent fit to the observations at high luminosities. On the basis of this curve, it is tempting to conclude that the data indicate a recent burst of star formation; it is important to realize, however, that even though the observed LF points at $\log(L/L_\odot) = -1.7$ and $\log(L/L_\odot) \approx -2.6$ lie off all the previous theoretical curves, they still lie less than 2σ away, and so the result must be considered marginally significant. The Barry data binned into 1.2 Gyr bins also cause a rise in the LF at high luminosities, but here the enhancement persists to a luminosity which is too low, and the theoretical curve is only approximately consistent with the observed points. The Twarog SFR is nearly constant over the last few billion years, and the LF reflects this at high luminosities.

The luminosity functions diverge at $\log(L/L_\odot) \approx -3.5$, and peak at $\log(L/L_\odot) \approx -4.0$. We find that all of the non-constant-SFR curves pass above the observed error box at this luminosity, and this suggests that either the SFRs overestimate the rate at early times, or that the strength of recent star formation is at least as strong as implied by Barry's burst. The Barry SFR indicates enhancements in the rate roughly 7 and 11 Gyr ago, and these are reflected in the double-peaked profile of the corresponding luminosity functions. Even though all four curves used an input age of 12 Gyr, we find that the Barry curves fall off at a luminosity higher than the other two. This is the result of the form of the Barry SFR at early times. Unlike most SFR determinations (theoretical or observational), the SFR of Barry does not simply "turn on" and stay on, but rather shows the early rate to be lower than the mean rate and non-constant. Thus, although I chose an age of 12 Gyr, the indicated rate is zero between 11.2 and 12 Gyr, giving the brighter turndown.

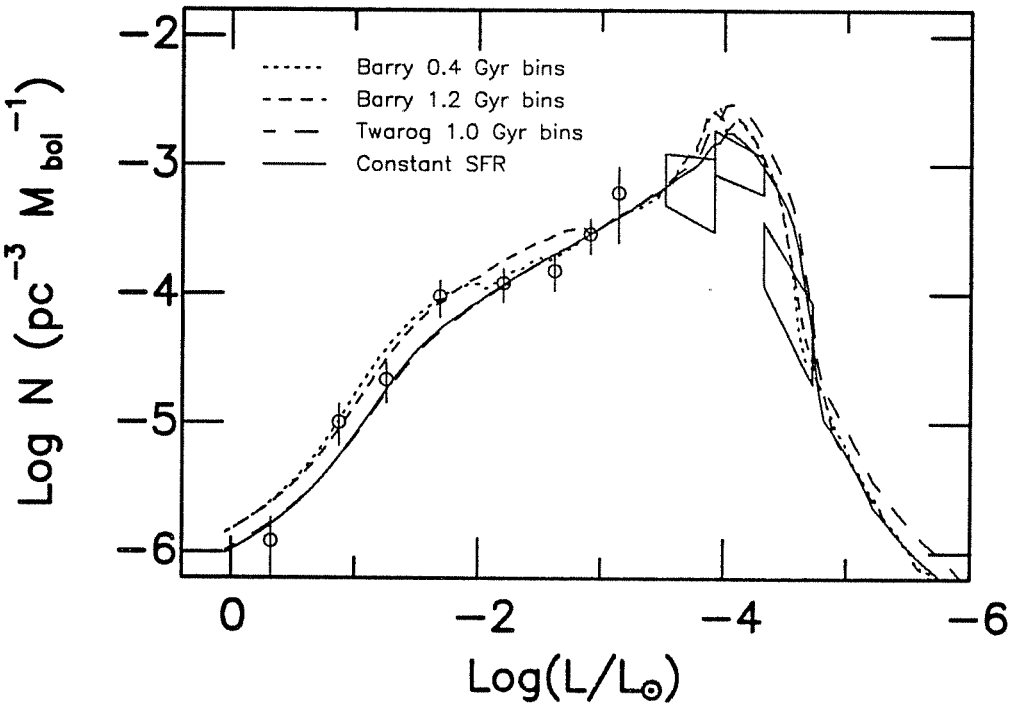

Figure 6.21: Luminosity Functions Computed with the Twarog (1980) and Barry (1988) Star Formation Rates. Shown alongside a luminosity function calculated with a constant SFR, these curves show some of the most dramatic behavior we have yet seen, particularly at the high luminosity end. Although the Barry SFR gives rise to a LF which is a better approximation to the observed point at $\log(L/L_\odot) \approx -1.7$, the error bars on the points are large enough to preclude drawing a firm conclusion on this basis.

The recent burst suggested by the Barry (1988) data motivates an exploration of the effect on the LF of a simple burst. I computed a series of luminosity functions (see Figure 6.22) which included 10^8 yr bursts of amplitude 10 times the mean SFR in the recent star formation history. I computed a total of nine such curves. The first has the burst in the most recent 10^8 yr bin, the second in the second most recent 10^8 yr bin, and so on. The final curve has the burst in the time slot extending from 1 Gyr ago to 9×10^8 yr ago. In the Figure, the curve resulting from the most

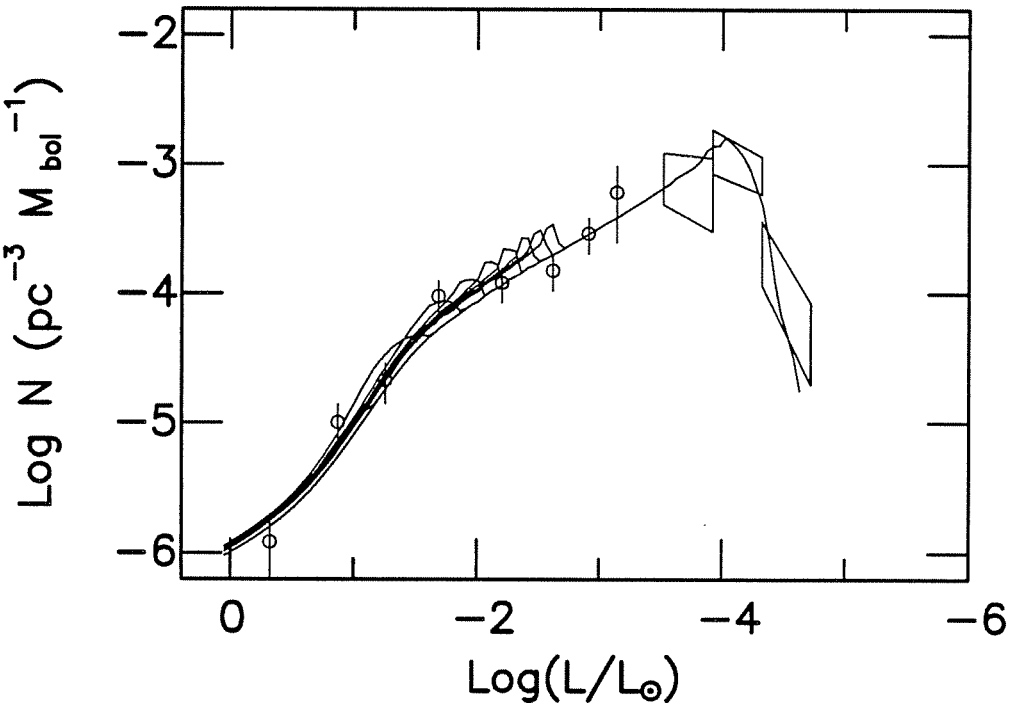

Figure 6.22: Luminosity Functions with 10^8 yr Star Formation Bursts. There are a total of 10 curves in this Figure. The carbon-core sequences were used with an input disk age of 10 Gyr. Aside from the constant–SFR curve included for comparison, each of the other nine has a SFR burst of amplitude 10 times the mean SFR and of duration 10^8 yr, with the first occupying the most recent 10^8 yr, the next occupying the next most recent 10^8 yr, and so on, until the last curve which has a SFR that bursts from 1 Gyr ago to 9×10^8 yr ago.

recent burst is hidden in among the high-luminosity tails of all the other burst LFs. Only relatively massive stars can have evolved from the main sequence to the white dwarf luminosity function in 10^8 yr, and these do not contribute much to the LF because their IMF weight is so low. The remaining curves are all easily discernible in the Figure, and as we probably could have guessed, begin to look self-similar with the overall luminosity function as they move towards low luminosities. Again comparing against

the stand-out data point near $\log(L/L_{\odot}) \approx -1.7$, the curves suggest that if it is real and not simply 2σ away from it's true location, then there probably was an enhancement in the SFR between 3 and 4×10^8 yr ago.

6.5.4 *The Effects of a Changing Disk Scale Height with Time*

The sample of old stars has a larger vertical velocity dispersion than the sample of young stars (see, for example, Freeman 1987 and references therein), and from this we infer that old stars have a larger scale height above the disk than do young stars. The cause of this is not currently known with certainty but there are two primary suggestions. First, it could be that over the history of the Galaxy stars got scattered to orbits with higher scale heights above the disk through random collisions with giant molecular clouds as suggested by Spitzer and Schwarzschild (1951, 1953), but it is not clear that such scattering can account for the entire velocity dispersion (perpendicular to the disk) which is observed (Lacey 1984). The recurrent passing of the spiral density wave through the disk and smaller scale instabilities may also scatter stars to larger scale heights (*e.g.*, Freeman 1987 and references therein), as could the accretion of a dwarf irregular galaxy similar to the Magellanics. An increase of scale height with time of this kind will be reflected as a depression in the cool end of the white dwarf luminosity function. The second suggested mechanism to account for the age–scale height relation is to assume that the stars simply *formed* at large scale heights during an initial, pressure-supported proto-Galatic collapse (*e.g.*, Gilmore, Wyse, and Kuijken 1989 and references therein). This model also predicts larger scale heights for older stars, but could be entirely consistent with an approximately constant SFR per unit time per unit volume during the phase transition from proto-Galaxy to star-filled

Galaxy. To the extent that *this* model accounts for the observed age–velocity relation, the effect on the WDLF could be minimal. Indeed, it seems reasonable that both contribute to the observed vertical velocity dispersion, and that the SFR per unit volume is approximated by the functional form of Clayton (1988).

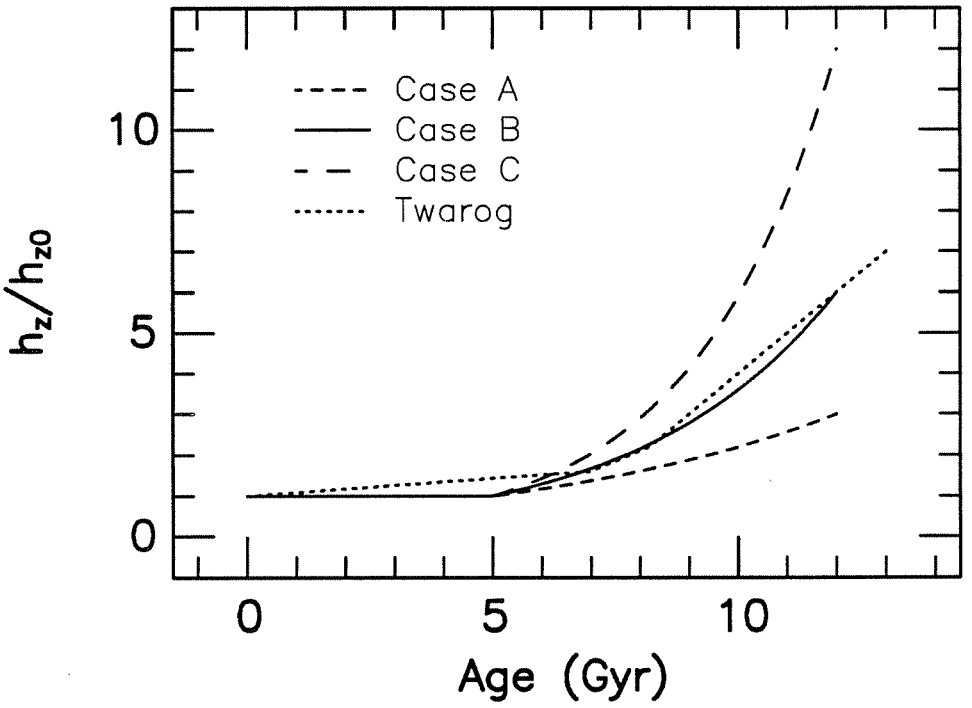

Figure 6.23: Models for the Evolution of the Scale height of the Galactic Disk as a Function of Stellar Age. This Figure includes the $h_z/\langle h_{z0}\rangle$ relation of Twarog (1980; his Figure 9) and three simple analytical models which assume an exponential decline until 5 Gyr ago, with a constant scale height since then. Each is normalized to 1 at the current epoch. The three exponential/constant inflation curves are normalized at 12 Gyr ago to have scale heights which are factors of 3, 6, and 12 times the current scale height (Cases A, B, and C, respectively).

Figure 6.23 shows a sampling of various inflation *vs.* age relations, including an approximation to that shown in Figure 6 of Twarog (1980) and three simple analytical approximations which assume an exponential decline in the scale height with time from the beginning of star formation to 5 Gyr ago, and a constant scale height since then. Of the three cases, the intermediate one (Case B) is very similarly to the curve of Twarog's Figure 9 which shows a factor of 6 inflation at the earliest times compared to the scale height of young objects. The remaining two cases have initial scale heights which are factors of 3 and 12 larger than the current scale height (Cases A and C, respectively), and they more than bracket published estimates of the early scale height of the disk. Because the white dwarf sample is drawn from an approximately cylindrically-symmetric portion of the disk and because I am considering inflation in the Spitzer and Schwarzschild sense (*i.e.*, gravitational scattering), it is handled in the WDLF integrator by simply dividing by the scale height corresponding to the total age ($t_{\rm MS}+t_{\rm WD}$) at the current luminosity and mass.

Figures 6.24, 6.25, and 6.26 show the families of luminosity functions calculated like those shown in Figure 6.9 above, but including the 3 exponential/constant SFRs shown in Figure 6.23. I also calculated similar Figures for the Twarog (1980) functions, but because they are quite similar to the intermediate analytical function, I do not show the results here. I discuss each of the three in turn.

The luminosity functions in Figure 6.24 were computed using the Case A exponential/constant inflation relation. The bright end of the luminosity function is completely unaffected as we would expect, but we see that the low-luminosity portions of the curves are somewhat depressed as compared to Figure 6.9. Using the criterion that acceptable curves pass through the

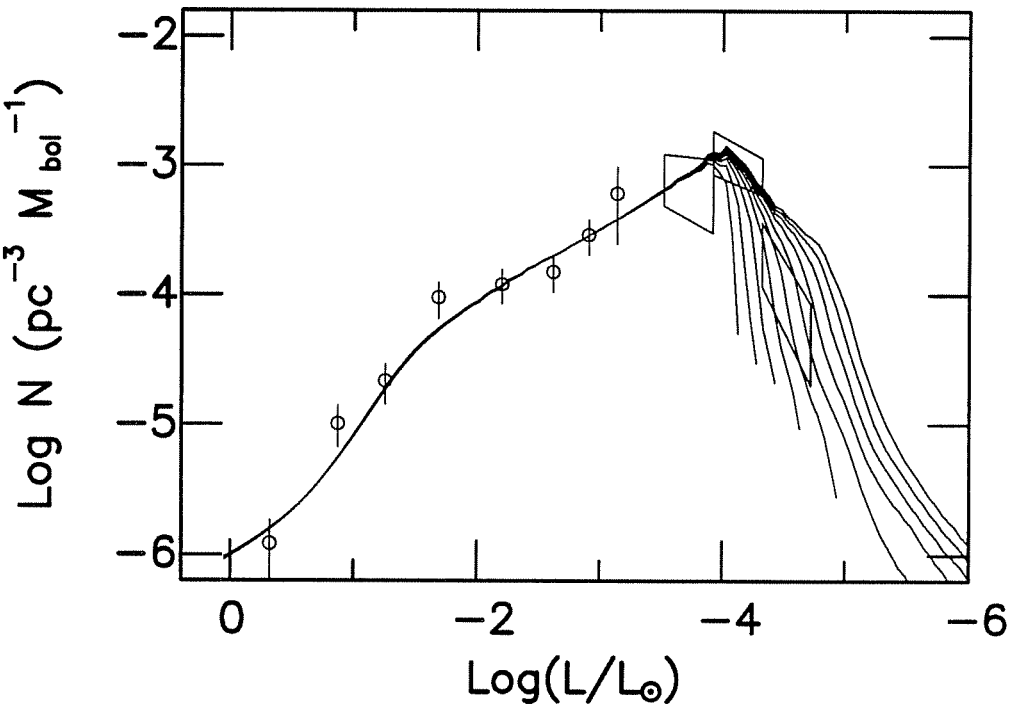

Figure 6.24: Luminosity Functions Including Disk Inflation Case A and Carbon-Core Sequences. Similar to the LFs in Figure 6.9, but with an analytical model for increased scale height as a function of age for the oldest stars as shown in Figure 6.23. The input ages for the curves run from 7 to 16 Gyr at intervals of 1 Gyr.

lowest-luminosity box, the ages suggested by these models range from ~9.3 to nearly 13 Gyr. This upper limit is consistent with the fitted ages of the the disk population of globular clusters (see, for example, the manuscripts in Philip 1988).

Figure 6.25 shows the luminosity functions calculated with the Case B inflation relation. Here the curves are further depressed, and models as old as 15 Gyr are consistent with the high-luminosity edge of the lowest luminosity box. Note, however, that because of the exponential, relation B suggests a factor-of-13 inflation over 15 Gyr, and this is larger than

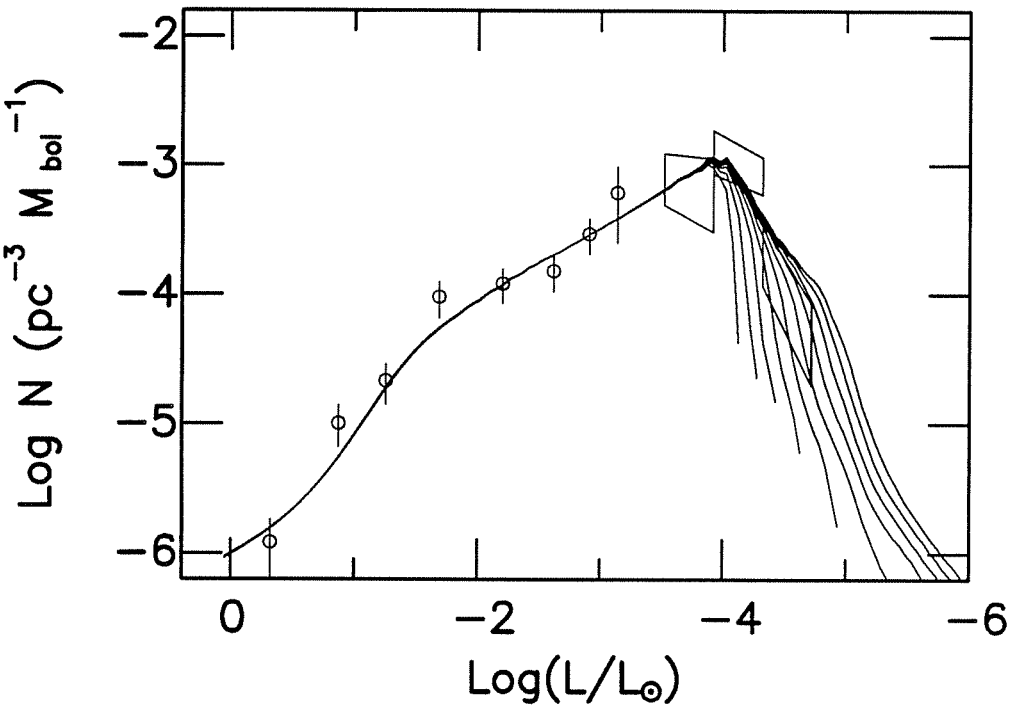

Figure 6.25: Luminosity Functions Including Disk Inflation Case B. The carbon-core sequences are used and the disk ages are as in Figure 6.24.

observational or theoretical estimates of the size of the effect. Had one of the Clayton SFRs had been used in the integration, the upper age limit would be approximately 16 Gyr, approaching the ages of the oldest globular clusters.

Last in the carbon-core models, we have the family of curves computed using the Case C inflation relation. These model an inflation in scale height by a factor of 12 over 12 Gyr (and 35 over 15 Gyr) — much larger than observations or theory suggest — and so are an extreme (*i.e.*, unphysical) test case. With that warning in mind, we see in Figure 6.26 that *all* of the curves pass well below the top of the lowest-luminosity error box, and with

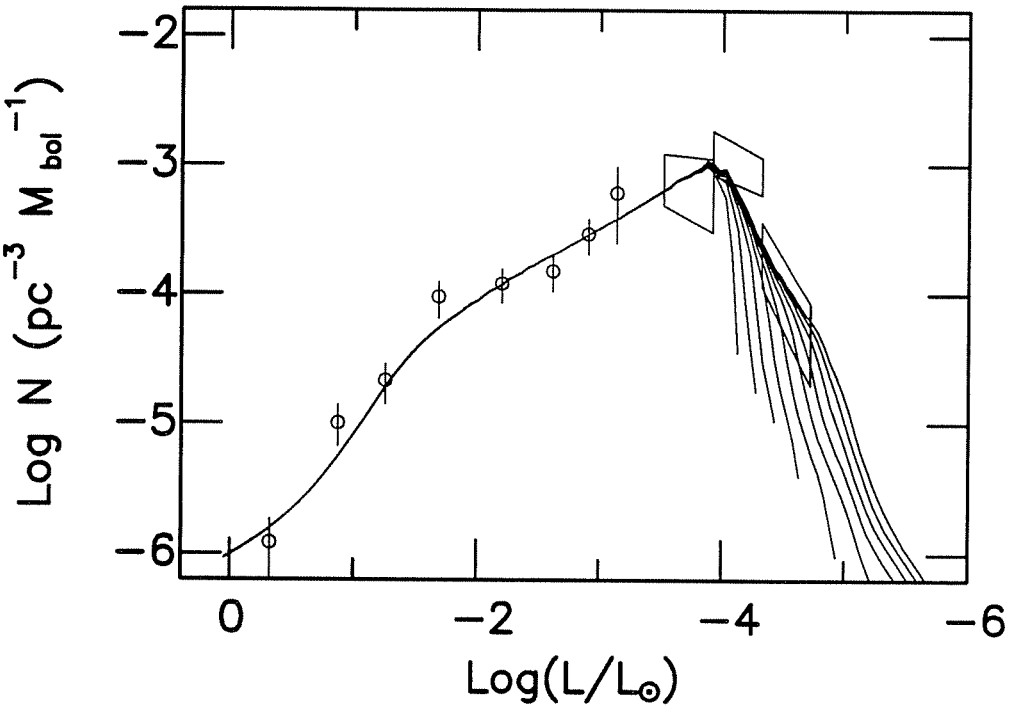

Figure 6.26: Luminosity Functions Including Disk Inflation Case C. The carbon-core sequences are used and the disk ages are as in Figure 6.24.

this inflation relation a luminosity function with an age of 18 Gyr would still be consistent with the LF observations.

In Figure 6.27 I show the family of luminosity functions computed with the Case B exponential/constant inflation relation and the oxygen-core models for input ages spanning 7–13 Gyr. As in Figure 6.10, the peaks of these curves are flatter than the comparable curves in Figure 6.25. The luminosity functions are again depressed below $\log(L/L_\odot) \sim -4$ compared to the constant-scale height models, and here the range of ages consistent with the lowest-luminosity box span the range 7.5 to just less than 11 Gyr.

6.5.5 *The Question of Mass*

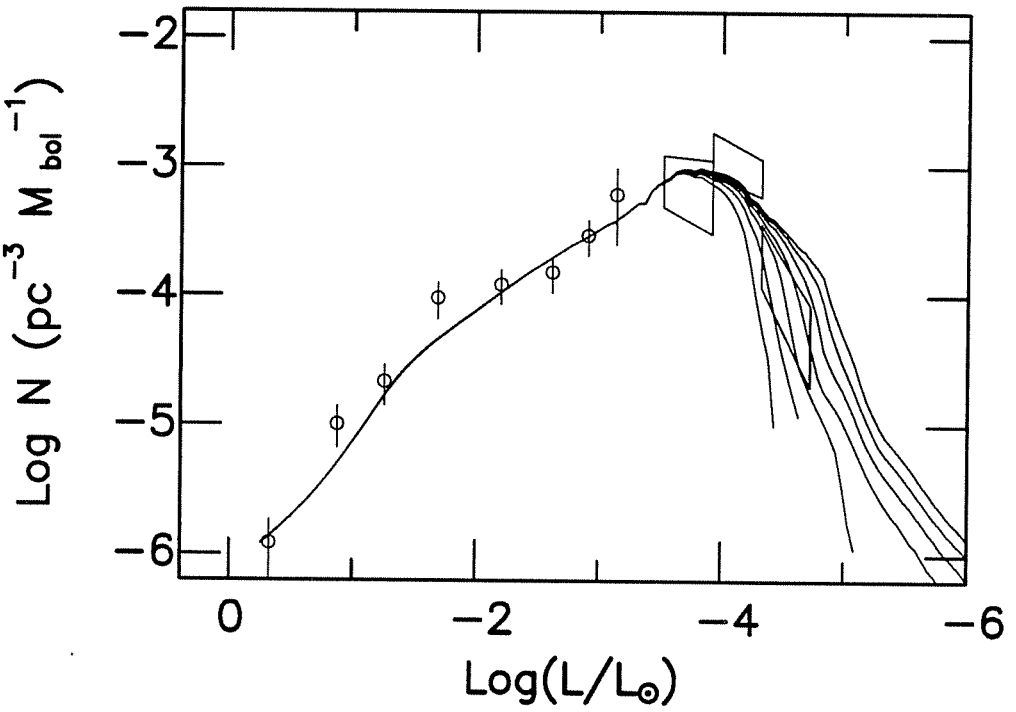

Figure 6.27: Luminosity Functions Including Disk Inflation Case B for Oxygen-Core Sequences. The ages of the curves run from 7–13 Gyr, and those consistent with the last box have ages from roughly 7.5 to 11 Gyr.

6.5.5.1 *The Observed Mass Distribution*

I mentioned above that the mass distribution of white dwarf stars is remarkably narrow, and so effectively reduces the order of complexity of the problem at hand. While this is true, it does not tell the whole story. Relative measurements are easier to make than absolute measurements, and so while we have known for some years that the distribution is narrow, there still exists some uncertainty in the mean mass of the distribution. Observationally, it is gravity that is determined directly through comparison with a grid of model atmosphere calculations spanning the range of interest in $\log g$ and $\log T_{\rm eff}$. Masses are then derived from these gravities

through an assumed mass–radius relation. The most commonly used of these have been the zero-temperature carbon-configuration results of Hamada and Salpeter (1961). Until recently, most of the gravity determinations were made using low-resolution (> 40Å) multi-channel spectrophotometry (see most recently Greenstein 1984), known to have calibration problems which cause uncertainties in the derived mean mass of approximately 0.1 $M_\odot$. Observations using these techniques suggest that the mean DA white dwarf mass is $\langle M/M_\odot \rangle = 0.58$ with a model-independent standard deviation of $\sigma = 0.1\ M_\odot$ (Koester, Shultz, and Weidemann 1979; Weidemann and Koester 1984). Using similar techniques, Oke, Weidemann and Koester (1984) derived a mean mass for DB white dwarfs of $\langle M/M_\odot \rangle = 0.55$, also with a scatter of $\sigma = 0.1\ M_\odot$.

Recently, multi-channel photometric results have been surpassed in quality by higher-resolution (~8Å) spectroscopic results compared against denser model-atmosphere grids (McMahan 1989; Bergeron, Saffer, and Liebert 1990). McMahan studied a sample of 53 DA white dwarf stars which spanned the temperature range ~5,000 to 65,000 K. He found a narrow mass distribution $\sigma \leq 0.1$ centered on $\langle M/M_\odot \rangle = 0.523$. Bergeron, Saffer, and Liebert (1990; BSL) have studied a sample of 114 DA white dwarfs with temperatures $T_{\rm eff} \geq 15{,}000$. They chose this lower temperature limit because the model atmospheres above this temperature are fully radiative and in local thermodynamic equilibrium — *i.e.*, they are comparatively simple to model. The BSL gravity determinations are good to ± 0.05 dex in $\log g$ making them the highest quality data published to date by a considerable amount.

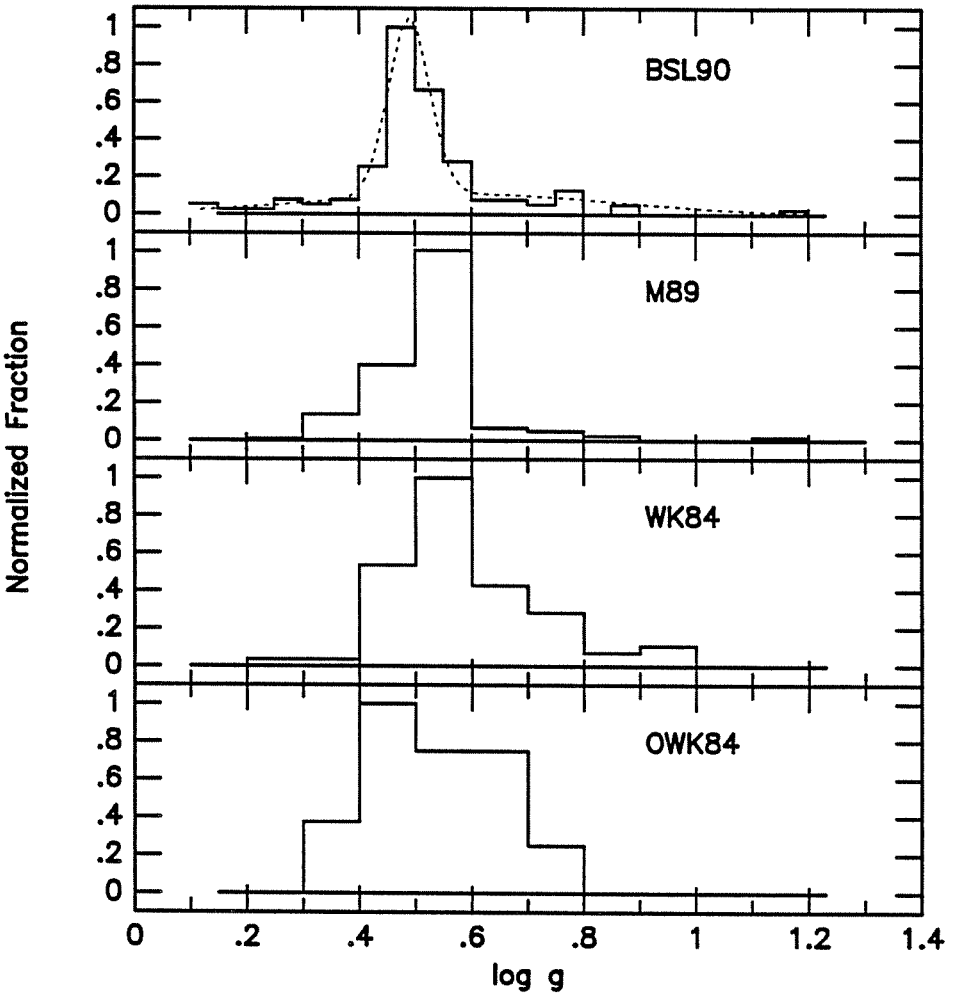

Figure 6.28: Derived White Dwarf Mass Distributions. The results of Bergeron, Saffer, and Liebert (1990; BSL90), McMahan (1989; M89), Weidemann and Koester (1984; WK84), and Oke, Weidemann, and Koester (1984; OWK84) are shown in the four panels of this Figure. Note that the recent determinations for the mean mass of the DA white dwarfs are still consistent with the DB mass distribution of OWK84, and do not suggest distinct evolutionary tracks for the DA and DB white dwarfs. Also shown over the BSL data is the 2-gaussian fit described in the text.

Starting with their gravity distribution, BSL used the mass–gravity relation given by the carbon/oxygen presented above to derive the mass distribution shown in the Figure. To accomplish this, they interpolated between the theoretical sequences at the temperature indicated for each individual star, thus fully taking into account the finite temperature effects on the radius. Although the mean, average deviation, and standard deviation of the BSL sample are similar to those of the McMahan sample, the high-resolution BSL results are really quite stunning in their detail, and the authors justly claim that it is now possible to believe mass determinations for certain individual stars. The BSL distribution shows a narrow peak skirted by extended wings to both high and low mass. As an aside we note that a (6–parameter) two-component gaussian fit gives for the central peak $\langle M/M_{\odot} \rangle = 0.49$ and $\sigma_{\rm G} = 0.052$, and for the broad component $\langle M/M_{\odot} \rangle = 0.59$ and $\sigma_{\rm G} = 0.38$ (see Figure 6.28) where $\sigma_{\rm G}$ is the Gaussian width. The ratio of the areas under the broad distribution and that portion of the narrow distribution above this is approximately 1:8, suggesting that while the great majority of white dwarf progenitors evolve into the narrow distribution, some, perhaps as the results of an external influence, evolve into the broad distribution. Interacting binary evolution seems a likely candidate for this external influence, though it is only one of many possible suggestions.

Both the BSL and the McMahan mass distributions suggest that the mean mass of the white dwarfs is closer to 0.5 $M_{\odot}$ than 0.6 $M_{\odot}$, and this is a substantial change from the value accepted until very recently. Because the two major uncertainties of atmosphere calculations — convection and non-LTE effects — are not factors in the atmospheres of the BSL hot-DA sample, it is likely the BSL determinations are quite accurate as well as being precise. These hot stars are all younger than $t_{\rm cool} \lesssim 0.5$ Gyr, however, and so may

not be representative of the mass distribution for all luminosities. It may be significant that Koester, Shultz, and Weidemann (1979) found that although their entire sample suggested a mean mass of $\langle M/M_{\odot} \rangle = 0.58$, a sub-sample with $T_{\rm eff} \gtrsim 13{,}000$ K suggested a mean mass of $\langle M/M_{\odot} \rangle = 0.47$. However, as discussed in BSL, the Kiel group's results are sensitive to the assumed convective efficiency, and they overestimate $\log g$ because they assumed ML1 convection, whereas the 13,000 K effective temperature of the blue edge of the DA instability strip is matched by pulsation models calculated under the assumption of the more efficient ML3 convection (Winget and Fontaine 1982).

It is not unreasonable that such a trend could be observed in any event, considering the effect that crystallization has on the discovery function, defined in the case of constant white dwarf birthrate (*e.g.*, Lamb 1974, Lamb and Van Horn 1975) as

$$D = \frac{dt_{\rm cool}}{d\log(L/L_{\odot})} \left(\frac{L}{L_{\odot}} \right)^{3/2} . \tag{6.11}$$

Figure 6.29 shows the discovery functions for the oxygen-core sequences. Because of the 15,000 K low-temperature cuttoff in the BSL sample, it is not expected that any of these stars will be crystallizing. In the luminosity range of the BSL sample the discovery probability as a function of mass is relatively flat at a given $T_{\rm eff}$. The other samples, however, all contain objects which *are* crystallizing, and at lower luminosities, crystallization enhances the probability of discovery of higher-mass objects, possibly accounting in part for the skew tail towards higher masses observed in the Weidemann and Koester (1984) data but not in the BSL data. As the accuracy of the mass determinations for individual stars becomes more reliable, it should be useful to apply adjustments to the derived global mass distribution based on these

discovery probabilities. Certainly the last word on the subject has not yet been written.

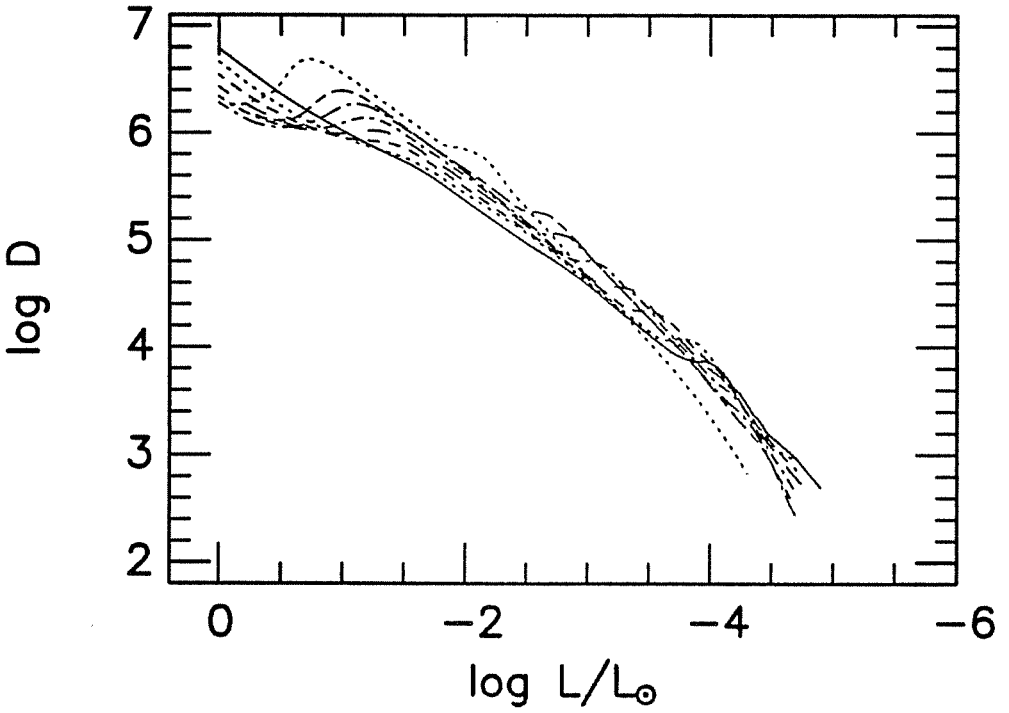

Figure 6.29: Discovery Functions for the Oxygen-Core DB Sequences. The probability of discovering crystallizing white dwarfs is enhanced compared to lower-mass white dwarfs that have yet to crystallize or higher-mass white dwarfs that already have crystallized.

6.5.5.2 *The Initial→Final Mass Relation and Theoretical Mass Distributions*

There have been a number of studies whose goal was to determine the connection between the main sequence progenitors of white dwarfs and the white dwarfs themselves. Studies of young open clusters with white dwarf members suggests that stars as massive as ~8 $M_{\odot}$evolve to become white dwarf stars (Romanishin and Angel 1980, Weidemann and Koester 1983),

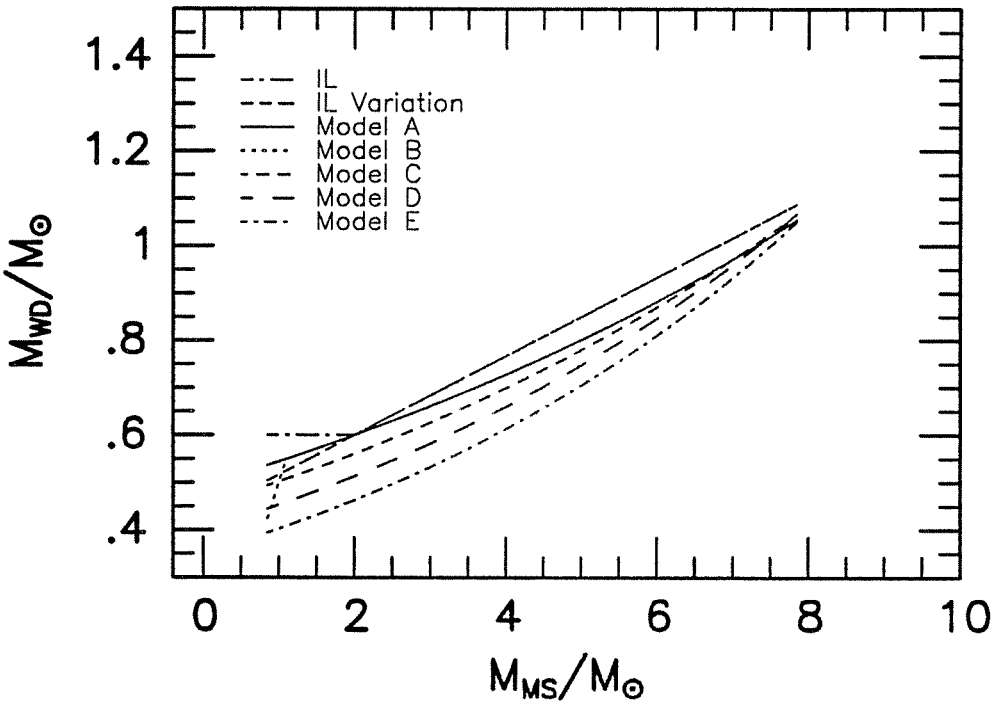

Figure 6.30: A Selection of Initial→Final Mass Relations. The relations shown here include the Iben and Laughlin (1989) relation, a variation on that relation, and a family of relations of the form given in equation (6.12).

but it is far from clear what the mapping function from main-sequence mass to white-dwarf mass is. The observations that we just discussed suggest that the mapping is quite flat, and that most stars evolve to become white dwarf stars of 0.5–0.6 $M_\odot$. Figure 6.30 shows a few sample initial→final mass relations which I've used in calculating families of luminosity functions. Several alternate relations are shown and discussed in Weidemann and Yuan (1989) and Weidemann (1987a, b). In addition to the Iben and Laughlin (1989) initial→final mass relation which has become standard for these studies I also have computed luminosity functions for a variation of the same which continues the high-mass slope to the lower-mass limit M_L. In

addition, I also present a family of initial→final mass relations based on an exponential model:

$$\mathcal{M}_{\rm WD} = A_{\rm IF} \exp(B_{\rm IF} \cdot \mathcal{M}_{\rm MS}), \tag{6.12}$$

where $A_{\rm IF}$ and $B_{\rm IF}$ are free parameters.

This functional form came to mind upon inspection of the PNN mass distribution calculated using the Schönberner method (see Schönberner and Weidemann 1983) as shown in Weidemann and Yuan (1989) — the PNN mass distribution has a distinctly exponential decline towards higher masses. Assuming that the flux of stars through this region of the H–R Diagram is at equilibrium and that a Salpeter IMF determines the relative numbers of the PN's main-sequence progenitors, we find

$$N_{\rm WD} \propto B_{\rm IF}^{\alpha} \cdot \left[\ln\left(\frac{M_{\rm WD}}{A_{\rm IF}}\right)\right]^{\alpha} \tag{6.13}$$

where again $\alpha \approx -2.3$ for low-mass stars. Using equation (6.13) it was possible to fit to the PNN mass distribution and obtain the fit shown in Figure 6.31.

As discussed in Wood (1990), this semi-empirical initial→final mass relation fits nicely the high-mass tail of the Weidemann and Koester (1984) mass distribution, but clearly does not account for the low-mass stars in that sample. Because of this, and because the Bergeron, Saffer, and Liebert (1990) and McMahan (1989) results suggest that the mean mass of the white dwarfs may be near 0.5 $M_\odot$, I also tried varying the leading term $A_{\rm IF}$ over a range from the fitted value of 0.49 down to value of 0.35, adjusting the values of $B_{\rm IF}$ such that 8 $M_\odot$ stars evolve into white dwarfs of mass $\sim$1.05 $M_\odot$, as the original fit does. The various choices are given in Table 6.1. Model B,

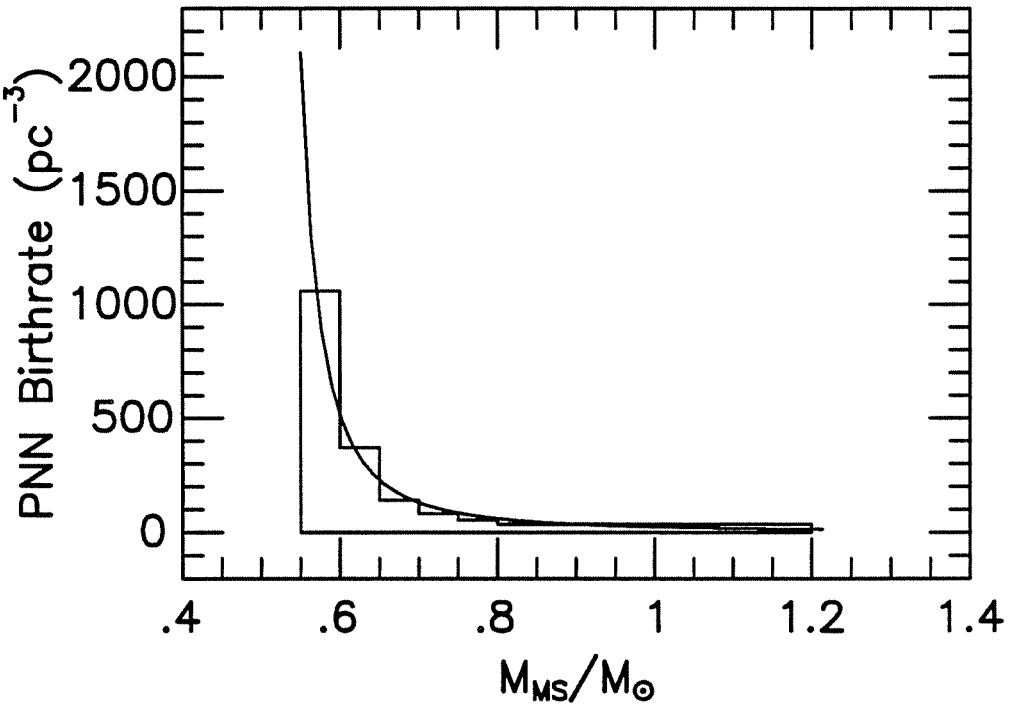

Figure 6.31: The Mass Distribution of the Planetary Nebula Nuclei with Fitted Model A. The PNN mass distribution shown in Weidemann and Yuan (1989) was fitted using equation (6.13) in a non-linear least squares formalism.

not listed in the Table, is identical to Model A above a progenitor mass of 1.1 $M_{\odot}$, but below this follows $M_{\rm WD} = \frac{1}{2} M_{\rm MS}$.

TABLE 6.1

INITIAL→FINAL

MASS RELATION PARAMETERS

Model	A_{IF}	B_{IF}
A	0.49	0.096
C	0.45	0.110
D	0.40	0.125
E	0.35	0.140

Figure 6.32 shows the family of curves calculated with the carbon-core sequences and the Iben and Laughlin (1989) I→F mass relation. The remaining parameters are according to the standard model. We find that the curves look quite similar those in Figure 6.9, and in particular they do not show the plateau just beyond the turndown in the luminosity function that Iben and Laughlin found. This plateau was not found by Yuan (1989) either, and so is probably the result of the polynomial fit to the 1.0 $M_{\odot}$ cooling curve overestimating the low-luminosity ages as discussed above, and hence the contribution of the high-mass stars to the low-luminosity end of the curve.

The white dwarf mass function which results from assuming the Iben and Laughlin I→F mass relation is nearly a delta function, and so is a poor description of the observational data. This mass function and those corresponding to the other relations just discussed are shown in Figure 6.33. It is apparent that the exponential forms yield a better approximation to the observed distributions (though they are still less than perfect). In particular,

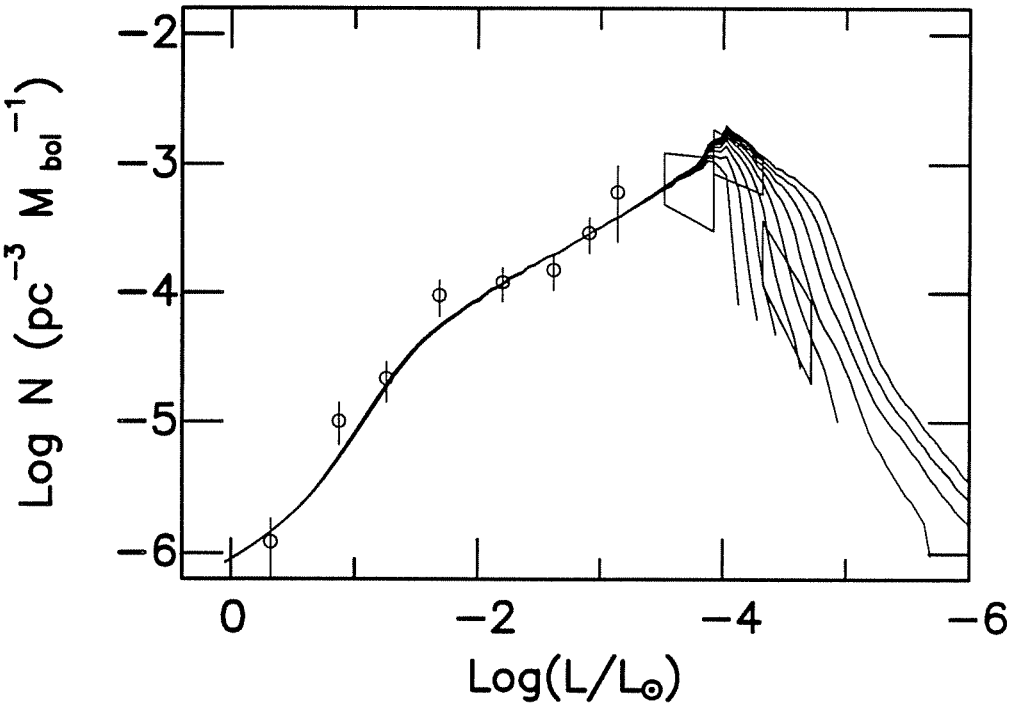

Figure 6.32: Luminosity Functions Calculated with the Iben and Laughlin (1989) I→F Mass Relation. Other parameters defining the integration are at the default standard model values. Compare with Iben and Laughlin's Figure 12.

the Model A initial→final mass relation is a particularly good fit to the high-mass tail of the Weidemann and Koester (1984) mass distribution, although it does not fit the low-mass tail. Model B includes a turnover in the I→F mass relation, and the improved fit with the observations suggests that this occurs in nature as well — although it is likely that in nature the I→F mass relation is more a probability distribution than a strict relation. The Bergeron, Saffer, and Liebert (1990) distribution suggests that an exponential relation more along the lines of Model D are more consistent with the observations.

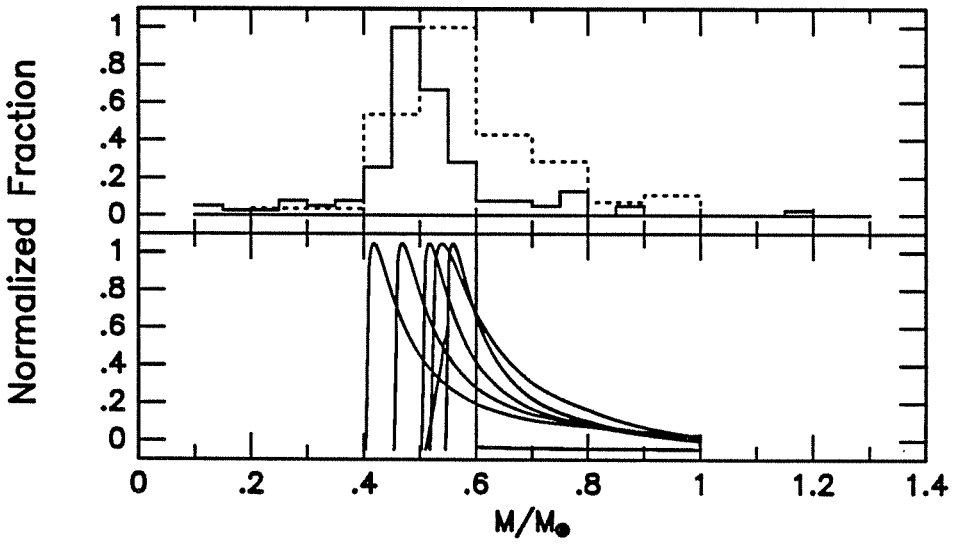

Figure 6.33: Theoretical *vs.* Observational Mass Functions. The data of BSL90 and WK84 Data are shown in the top panel for reference. The calculated mass distributions in the bottom panel result from integrating using the carbon-core sequences and an input disk age of 9 Gyr for the I→F mass relations shown in Figure 6.30.

Figure 6.34 shows the family of luminosity functions calculated with the Model D I→F mass relation. The mean mass of this sample is about 0.5 $M_{\odot}$ and the shape of the luminosity functions is changed relative to the Model A results (*i.e.*, the standard model; see Figure 6.9). However, the ages suggested by a comparison with the limits of the lowest luminosity box still suggest the range 9–12 Gyr. Figure 6.35 shows the family of luminosity functions calculated with the oxygen-core sequences and the Model D I→F mass relation. Here we see that again the curves are similar to the Model A

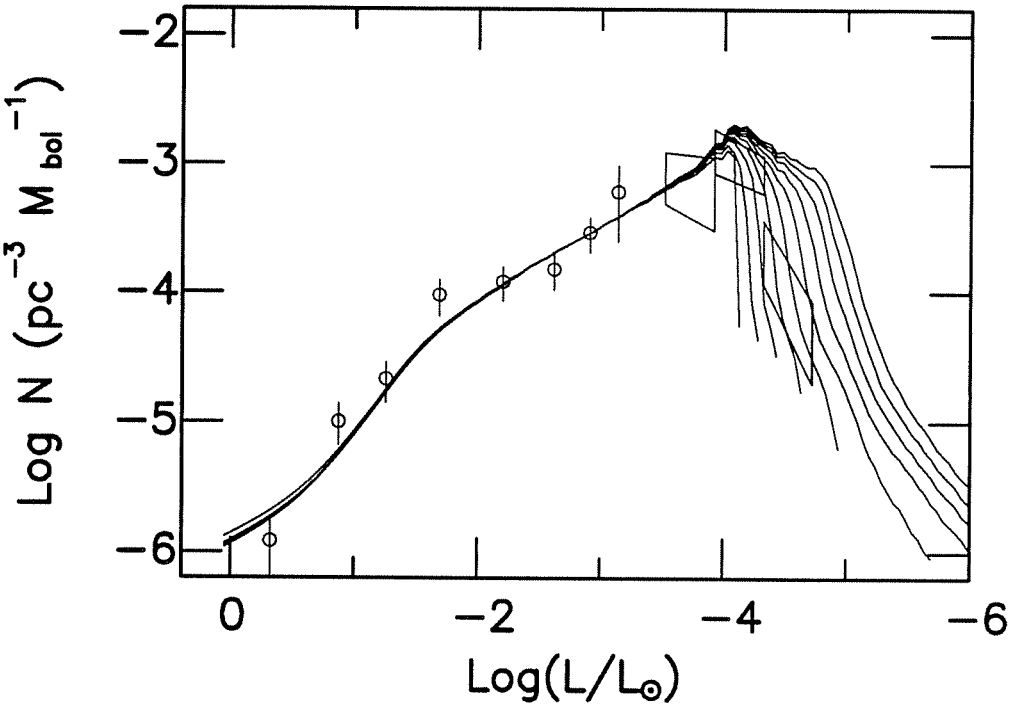

Figure 6.34: Carbon-Core Sequence Luminosity functions for Model D I→F Mass Relation. The lower mean mass of the white dwarf mass distribution changes the shape of the luminosity functions near the peak and the slope of the falloff, but do not suggest a large change in ages compared to the standard model results.

results shown in Figure 6.10 above. The disk ages implied here span the range 7.5 to 10 Gyr.

In summary then, the recent shift in the accepted mean mass of the white dwarf stars is not likely to be a source of great uncertainty in the ages of the turndown, although subtle shifts in the I→F mass relation will affect the shape of the peak of the LFs.

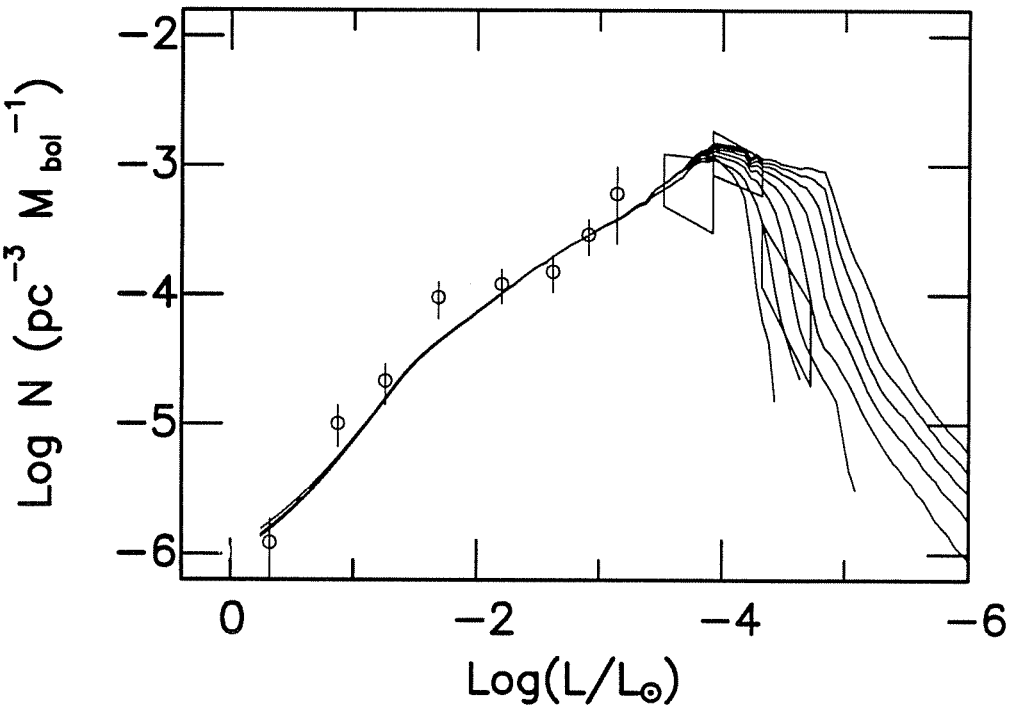

Figure 6.35: Oxygen-Core Sequence Luminosity Functions for Model D I→F Mass Relation.

6.5.6 *The Best-Guess Model*

Finally, I computed a family of luminosity functions that most closely approximate the true state of affairs (as we currently understand them). For this calculation, I used the carbon/oxygen-core sequences and assumed the parameter set:

- Clayton (1988) SFR with gas consumption timescale of 2 Gyr ($\omega' = 0.5\mathrm{Gyr}^{-1}$) and halo infall timescale of roughly 3 Gyr ($\omega = 0.3\mathrm{Gyr}^{-1}$) (*i.e.*, the long-dashed line in Figure 6.18).
- Mass limits: $M_U = 8\ M_\odot$, $M_L = M_{\mathrm{turnoff}}(t_{\mathrm{disk}})$,

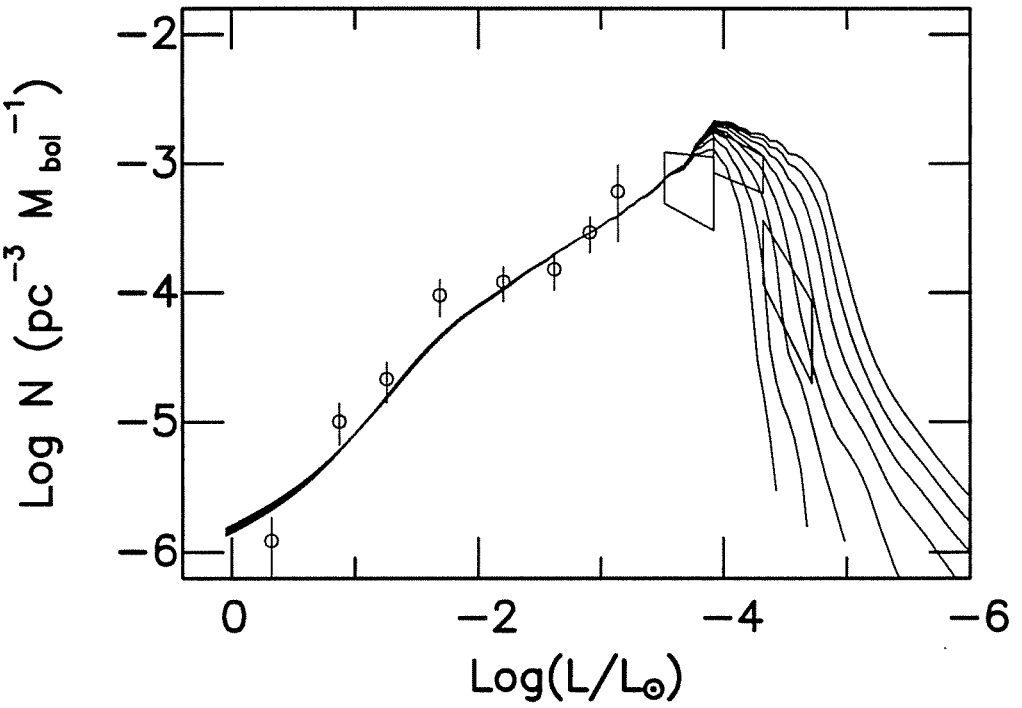

Figure 6.36: Luminosity Functions Using the C/O-Core Sequences and Best-Guess Parameter Set. The family of curves shown in this Figure should represent the true situation most closely of any shown in this work. These curves as they compare to the observations suggest that our current best estimate for the age of the local disk lies within the range 8 to less than 11 Gyr.

- Salpeter IMF: $\phi(M) = (M/M_\odot)^{-2.35}$,
- Pre-WD lifetime: $t_{MS} = 10\left(\frac{M}{M_\odot}\right)^{-2.5}$,
- I→F mass relation D: $M_{\rm WD} = 0.40\exp(0.125M_{\rm MS})$
- Scale height inflation relation B (factor of 6 inflation at an age of 12 Gyr, similar to Twarog 1980).

The resulting family of luminosity functions is shown in Figure 6.36, and shows consistency with the observations for disk ages ranging from 8 to 11 Gyr.

6.6 Halo White Dwarf Luminosity Functions

6.6.1 *Introduction*

In the previous sections I discussed the use of the white dwarf luminosity function (LF) to measure the age of the local disk. The range of ages that come out of the analysis are significantly shorter than those determined for the halo globular clusters and suggest that the onset of low-mass star formation in the disk of the galaxy was delayed by some 2–5 Gyr relative to the onset time in the halo globular clusters. This result supports the pressure-supported collapse models of Larson (1976), and further suggests that halo white dwarfs, if they can be found, will have a luminosity function that peaks at luminosities significantly lower than the disk luminosity function [*i.e.*, by roughly 0.5 dex in $\log(L/L_{\odot})$]. This being the case, and because there are at least two observational surveys currently underway which are searching for these objects (Claver *et al.* 1990; T. von Hipple, personal communication), it is worthwhile to explore briefly the theoretical luminosity functions of this suggested old population of halo white dwarf stars so that the future observations may be interpreted in context. This subject has been recently discussed by Mochkovitch *et al.* (1990), Ryu *et al.* (1990), Tamanaha *et al.* (1990), Weidemann (1990), and Wood (1990).

In the following, I will also consider the question of the halo white dwarf stars as "dark matter" candidates. Models of the rotation curves of spiral galaxies, including our own Galaxy, best fit the observations when they include the gravitational potential of a massive halo (Faber and Gallagher 1979, Bahcall and Soneira 1980, Bahcall 1984). To the limits of current

observations, this halo matter is otherwise undetected and so its exact nature is quite puzzling — we call it simply dark matter. Models fitting the Galactic rotation curve suggest that the density of the halo dark matter ($\rho_{\rm dark}$) is of order (0.01 $M_{\odot}{\rm pc}^{-3}$) at our Galactocentric radius. With only the near absence of evidence as a constraint, the number of suggested dark-matter candidates has been large, and have ranged from numerous unobservable "*-inos*" to cold objects of sub-stellar mass (*i.e.*, gas giants and brown dwarf stars) to sub-luminous stellar-mass objects (cool white dwarf stars, neutron stars, and black holes) to 10^6 $M_{\odot}$ black holes (Trimble 1987 and references therein).

Considering for the moment only baryonic matter, the current consensus is as follows: although the largest contribution to $\rho_{\rm dark}$ is possible in the form of sub-stellar mass objects, unless the initial mass function rises again below the current observed lower-mass turnover at $\sim$0.2 $M_{\odot}$ (Scalo 1986), they probably do not account for a dominant fraction of $\rho_{\rm dark}$ (Hegyi and Olive 1986); white dwarf stars are a possibility, but only marginally; neutron stars and stellar-mass black holes are effectively ruled out because their progenitors would have greatly overproduced heavy elements relative to what is observed; finally, primordial black holes of any kind, being unobservable cannot be ruled out.

6.6.2 *The Observations*

The preliminary halo WD luminosity function presented by Liebert, Dahn, and Monet (1989) was constructed using the six high-velocity stars in their sample ($V_{\rm tan} \gtrsim 250$ km s^{-1}). Because of this low number of objects, the error bars on the LF are substantial as can be seen in Figure 6.5 (or one of the following Figures). These points have had the black-body bolometric

correction applied as described in §6.3 above and in Liebert, Dahn, and Monet (1988); note that these may be overestimates, and the location in luminosity of the data should be considered as uncertain as the low-luminosity disk LF points. Of the sample of six stars, five are fainter than $M_V = +13$, and the derived space density is $(1.3 \pm 0.6) \times 10^{-5}$ pc^{-3}, which is about 3 orders of magnitude down from the space density given by the disk LF.

6.6.3 *The Calculations*

Proceeding as above, I explore the halo luminosity function by varying the input parameters to the luminosity function synthesis program: the star formation rate, the initial mass function, and of course the ages. In the following I assume that the halo and disk LFs are effectively decoupled, and further assume an exponentially declining SFR with a short decay timescale of 0.5 Gyr, a Salpeter ($\alpha = -2.35$) IMF. I use the carbon core sequences as input, because the stars formed in the early burst would have had low metallicities and so larger core-burning temperatures, and by the arguments above should be carbon rich. The sequences are extrapolated to low luminosities as described in §6.2 above. I consider halo ages of 13, 15, and 18 Gyr, and normalize the LFs to fall within the Liebert, Dahn, and Monet (1988, 1989) error estimates. A significant percentage of the models have cooling times whose asymptotic maxima are shorter than the halo ages that are considered. Although these are unobservable and therefore do not contribute to the luminosity function, they do contribute to the mass density and I account for them.

6.6.4 *The Results*

6.6.4.1 *A Full Mass Spectrum Burst*

The first case considered is an early burst of star formation with a full mass spectrum. Specifically, Figure 6.37 shows the observed halo LF of Liebert, Dahn, and Monet (1989), and the theoretical LFs computed using the carbon-core sequences under the assumptions

- SFR: $\psi(t) \propto e^{-t/0.5 \text{ Gyr}}$
- Mass limits: $M_U = 8\ M_\odot$, $M_L = M_{\text{turnoff}}(t_{\text{halo}})$,
- Salpeter IMF: $\phi(M) = (M/M_\odot)^{-2.35}$,
- Pre-WD lifetime: $t_{MS} = 10\left(\frac{M}{M_\odot}\right)^{-2.5}$,
- Initial→final mass relation: $M_{\text{WD}} = A \cdot \exp(B \cdot M_{\text{MS}})$, where $A = 0.65$ and $B = 0.08$,
- No scale-height inflation with increasing age.

A constant-SFR, 10 Gyr disk LF also computed with the carbon-core sequences is included in the Figure for reference along with the observed disk LF observations. The SFR here simulates a burst of star formation on approximately a dynamical timescale, and because the SFR timescale is short compared to the timescale implied by the luminosity steps in the integration, the computed luminosity function is fairly noisy. Normalizing the halo and disk luminosity functions relative to the observations and to each other determines the relative star formation rates, and for the 13, 15, and 18 Gyr curves shown here, the ratio of the halo-to-disk SFR is approximately 1/50 in each case, which is small enough to have been otherwise undetected. The initial→final mass relation is flat and weighted towards higher masses, giving a mean of approximately 0.7 $M_\odot$ for a full mass spectrum burst. I

chose this relation because it is expected on theoretical grounds that the efficiency with which the AGB envelope is lifted is a function of metallicity. Therefore, because the main sequence progenitors of the halo white dwarfs should have been very low in metal abundance, the white dwarfs themselves should have masses higher than the mean mass determined for the field white dwarf stars.

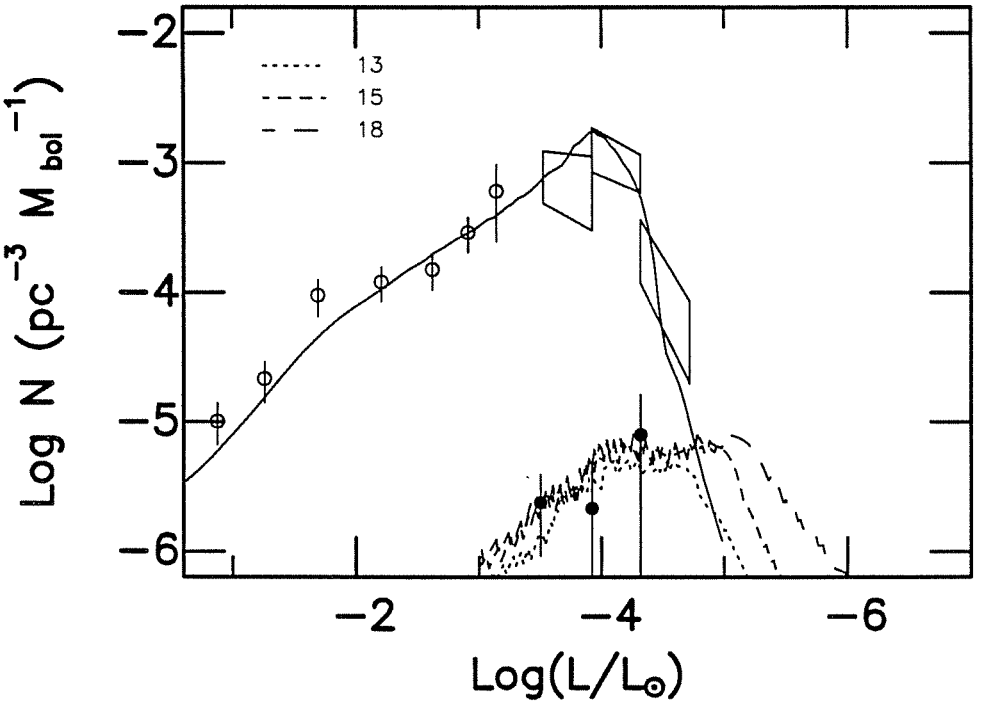

Figure 6.37: Halo Luminosity Functions from Full Mass Spectrum Burst. The three halo luminosity functions shown here were computed with carbon-core sequences and have ages of 13 (*dotted line*), 15 (*short-dashed line*), and 18 Gyr (*long-dashed line*), respectively. Also shown for comparison is a disk LF computed with the carbon-core sequences, a constant SFR, and an age of 10 Gyr. The noise in the halo LFs results from the steep drop in the SFR. The observed halo LF points from Liebert, Dahn, and Monet (1989) are also included for reference.

The luminosity functions shown in Figure 6.37 show a substantial tail to high luminosities quite similar to the trend suggested by the observations, and, as normalized, the LFs suggest only a modest space density of roughly 5×10^{-6} pc^{-3}. All of the curves roll over at low luminosities as a function of age and Debye cooling (recall the single-sequence LFs shown above in Figure 6.6). These roll over at a luminosity similar to that of the high-mass tail of the disk LF, suggesting that we must rely on observed tangential velocities to separate the two populations observationally, even if the halo is several 10^9 yr older than the disk. The same bolometric correction uncertainty that complicates the absolute disk age determination is a factor here as well, and so initially it may be difficult to determine the absolute age of the halo population; however, the relative formation epochs of the halo and disk *will* be obtainable in the near future as the number of cool white dwarfs is increased and as their proper-motions are determined.

6.6.4.2 *The Effects of Varying M_L*

As discussed above and in Scalo (1986), the evidence is strong that high-mass stars and low-mass stars form in different environments — high-mass stars in warm environments typical of H II regions in giant molecular clouds and low-mass stars in the cooler environments typical of cold dark cores. Because the local conditions in the early Galaxy were likely to have favored high-mass star formation over low-mass star formation, it is reasonable to consider luminosity functions computed with a main-sequence low-mass limit, M_L at an intermediate mass. I have computed two such sets of sequences, the first with $M_L = 1.5\ M_\odot$ and the second with $M_L = 2.0\ M_\odot$.

The first set of these is shown in Figure 6.38 with the same reference disk LF as in Figure 6.37. Again in this Figure the three curves have ages

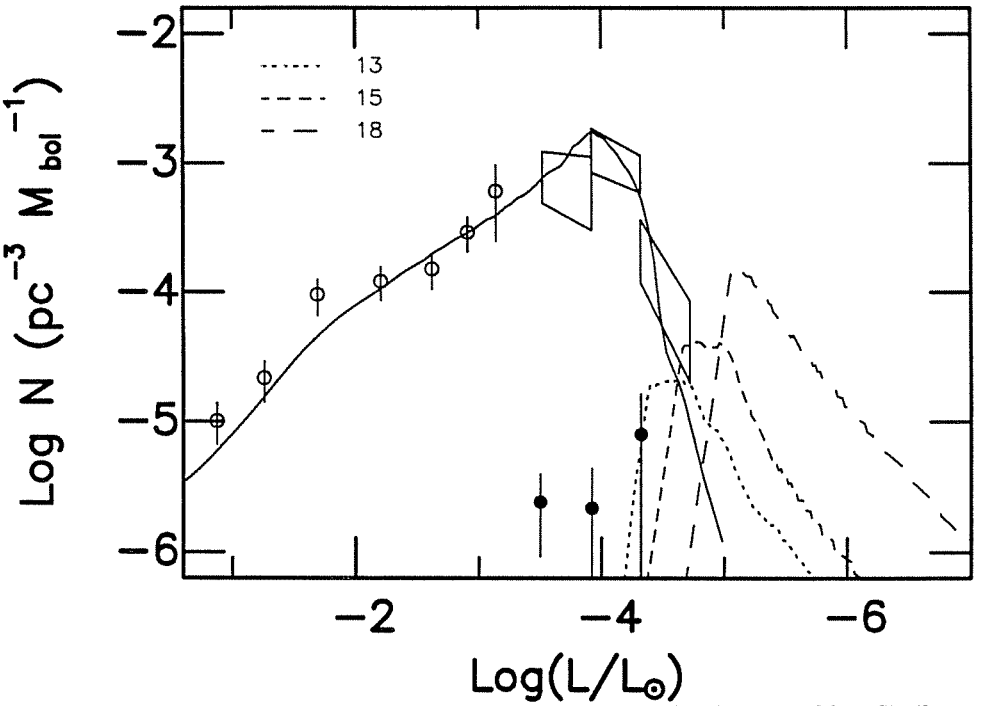

Figure 6.38: Halo Luminosity Functions Computed with $M_L = 1.5\ M_\odot$. Similar to Figure 6.37, but with a lower limit of $M_L = 1.5\ M_\odot$ to the progenitor mass spectrum.

of 13, 15, and 18 Gyr; as normalized here they have peak SFR's which are approximately factors of 1/15, 1/10, and 1 times the mean SFR of the reference disk LF. Because the total number of progenitors is again low, these SFRs are still within reason. The high luminosity tails of these curves do not show the same trend as the observations, but instead are quite steep and reflect the exponential decline in the SFR for the lowest-mass white dwarfs. A 1.5 $M_\odot$ model has a pre-white dwarf lifetime of about 3.5 Gyr, and with the initial→final mass relation used it here gives rise to a 0.73 $M_\odot$ white dwarf. The 0.7 $M_\odot$ white dwarf sequence used as input reaches a luminosity of $\log(L/L_\odot) \approx -4.7$ at $t_{\rm cool} = 12$ Gyr, and an inspection of the Figure shows that for the 15 Gyr curve this is the luminosity of the left edge of the plateau. The steep falloff to low luminosities at the right edge of the

plateau parallels the single-sequence LFs in the Debye cooling regime. The 18 Gyr curve shows almost no plateau, but only a fairly sharp peak dividing the Debye-cooling slope from the SFR slope. This curve suggests that there could be a large population of halo white dwarfs that has so far gone largely undetected.

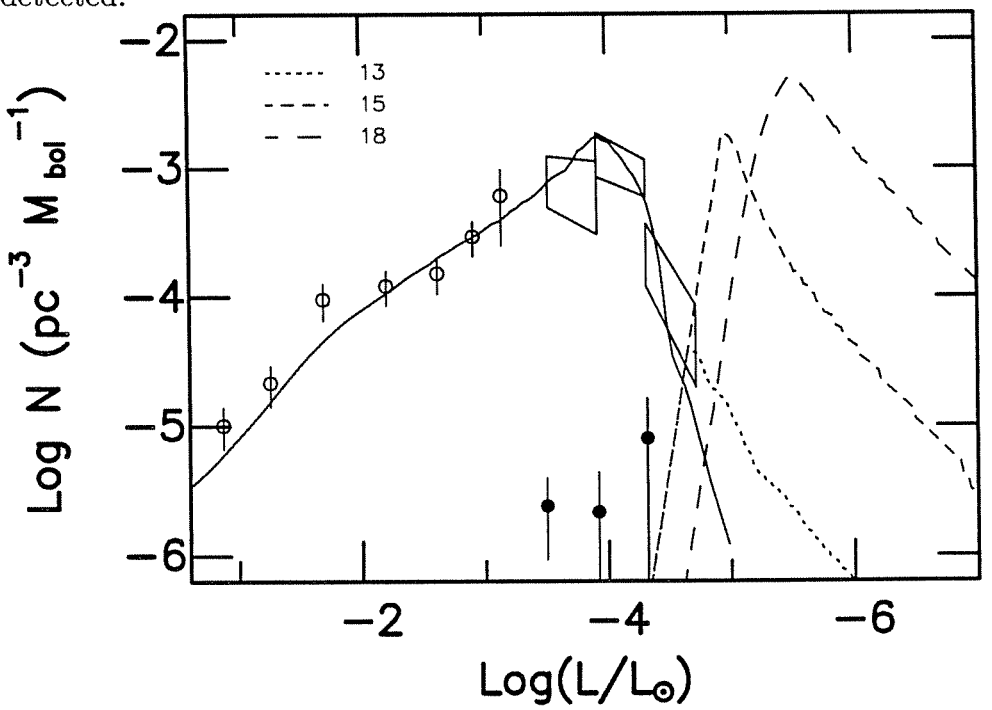

Figure 6.39: Halo Luminosity Functions Computed with $M_L = 2.0\ M_\odot$. Similar to Figure 6.37, but with a truncation of the progenitor mass spectrum at a lower limit of $M_L = 2.0\ M_\odot$.

The final Figure in this section shows three LFs calculated with $M_L = 2.0\ M_\odot$ (see Figure 6.39). These, like the LFs in the previous Figure, show a steep high-luminosity tail not suggested by the observations. All three show a sharp peak at a luminosity corresponding to the cooling time of the dominant mass in the mass distribution, which in this case is about 0.76 $M_\odot$. The 13 Gyr curve is constrained to fall below the low-luminosity

error box, and so suggests only a modest space density of halo objects. The SFR implied by this normalization is approximately $1/7^{\rm th}$ the disk SFR. The 15 and 18 Gyr curves are not tightly constrained by the observations, and so can be normalized to higher space densities, although there begins to be a problem with the SFR. The ratio of the halo-to-disk SFRs for these two curves is approximately 10 and $\gtrsim$100, respectively. Observations of starburst galaxies suggest that burst strengths can be several tens times the underlying SFR (Telesco 1988 and references therein), and so the 15 Gyr LF gives perhaps the maximum plausible space density for a halo population of white dwarfs ($\rho_{\rm halo} \approx 1 \times 10^{-3}$ pc^{-3}), or approximately 1/3 the space density of the disk white dwarfs. The high-SFR implied for the 18 Gyr curve occurs because well over 50% of the objects have evolved to invisibility; one effect of this is that the high-luminosity slope begins to roll over before the peak in the LF, unlike the behavior of the other LFs presented so far. Although many of the high-mass stars in the 18 Gyr curve shown in Figure 6.37 also would have evolved to invisibility, the lower mass limit insures that the majority will be observable.

6.6.5 *Discussion*

Given that the halo age as suggested by the globular clusters is significantly greater than the disk age as suggested by the white dwarf stars, and given that both are relatively solid determinations, it is quite possible that there is a real age difference between halo and disk. The white dwarf stars alone will eventually provide the age of the halo as they already have for the disk, and in this section I have computed a series of halo luminosity functions in preparation for the soon-to-be-realized observations of the halo population of white dwarf stars. I have explored the halo white dwarf luminosity

function using ages of 13, 15 and 18 Gyr, the carbon-core input sequences, and three different assumptions for the main-sequence lower-mass limit.

The results show that if there was a burst of star formation of all masses in the early Galaxy, the halo luminosity function will show only a modest space density consistent with the six-star luminosity function of Liebert, Dahn, and Monet (1989). Because the halo and disk LFs suggest similar contributions at luminosities of $\log(L/L_{\odot}) \approx -5$, the two populations will have to be separated observationally on the basis of their proper motions. Removing the constraint that all masses must have formed in the halo burst and instead truncating the progenitor mass distribution at either 1.5 or 2.0 $M_{\odot}$ allows a greater halo space density to be consistent with the observations; however, LFs computed under this assumption fit the observed halo LF extremely poorly. These curves suggest that if there was an early burst of star-formation in the halo preceding the onset of star formation in the disk, and if that burst only produced stars above 2 $M_{\odot}$, then for plausible burst star formation rates ($\lesssim$ 80 times the mean disk SFR; see Telesco 1988) there could exist a population of halo white dwarf stars at luminosities just beyond the current practical observational limits with a space density of $\sim\frac{1}{3}$ the disk space density ($\rho_{\rm halo} \lesssim 1 \times 10^{-3}$ pc^{-3} $M_{\odot}$ pc^{-3}), but small compared to the inferred halo dark matter density of $\rho_{\rm dark} \approx 0.01$ $M_{\odot}$ pc^{-3}.

The LFs which I have presented here are meant to serve more as guides to interpreting future observations than as predictions of the detailed shape of the halo LF at luminosities below current observational limits. There are several theoretical uncertainties whose effects are difficult to gauge *a priori*. The $^{12}C(\alpha,\gamma)^{16}O$ reaction rate suggests that high-temperature nuclear burning should produce a relatively higher mass fraction of carbon (see D'Antona

and Mazzitelli 1990, and Caughlan and Fowler 1988), and because the progenitors of the halo white dwarfs should have had very low metal abundances and so should have burned hot while on the main sequence, I used carbon-core model sequences to represent the halo population. If instead oxygen-core sequences are more representative of the halo white dwarfs (as they are of the disk white dwarfs), then the LFs would have approximately the same character, but would be moved to lower luminosities for comparable ages. Furthermore, for comparable ages, the oxygen-core sequences would suggest that a larger fraction of the white dwarf population would have cooled to invisibility. The initial→final mass relation that I used gives a higher mean mass than the observed mass distribution of field white dwarfs, again because of the low metallicities of these objects. If the mean mass of the halo population is lower than assumed here, then again the curves will have the same general character, but will be shifted only slightly to higher luminosities.

6.7 SUMMARY

In this Chapter I have discussed the white dwarf luminosity function and the information available from it. It has been a long read getting to this point, and a quick look back is in order before discussing the results within the context of evolutionary models of the early Galaxy.

It has been ten years that we've known of the turndown in the white dwarf luminosity function (Liebert 1979, 1980), but only in the most recent three years has there been a flurry of activity in the community with several parallel attempts to decode the historical record of the luminosity function. The pioneering work on the problem was presented by Winget *et al.* (1987),

who used a simple but sufficient method of constructing theoretical luminosity functions and who showed that the luminosity of the turndown suggested an age of the local disk of (9.3 ± 2) Gyr.

The observational results of Liebert, Dahn, and Monet (1988) show an unambiguous decline at low luminosities, but the precise luminosity of the turndown is not well determined because of bolometric correction uncertainties for cool white dwarfs. Realizing that they could not get around these uncertainties, the authors chose to present their results such that they *bracketed* the true luminosity function. In this study, I adopted the same philosophy, and have calculated a large number of luminosity functions in order to bracket the true luminosity function.

The spread in ages just from the observational uncertainty in the luminosity of the turndown is about 3 Gyr, or about *half* of the total uncertainty in the local disk age determination. This uncertainty is from the lack of good bolometric correction estimates from cool non-DA white dwarf atmosphere calculations. A new grid of cool helium-dominated atmospheres needs to be computed. In addition, the question of the bolometric correction uncertainties can be addressed observationally using multi-wavelength observations to determine the deviations of the spectra of individual objects from blackbody spectra corresponding to their effective temperatures.

The age corresponding to the luminosity function turndown is given approximately by the age-luminosity relation appropriate to the peak mass for the mass distribution at the adopted turndown luminosity, plus roughly 0.5 Gyr contributed by main sequence evolution. There is currently some debate on what the mean mass of the white dwarfs is, but within the

suggested range of 0.5–0.6 $M_{\odot}$ the turndown ages are only a very weak function of mass.

The derived ages are a function of core composition such that pure-carbon core sequences give ages roughly 2 Gyr larger than comparable oxygen-core sequences. Sequences with mixed carbon-oxygen cores, not surprisingly, suggest ages that are intermediate between these extremes. Integrated luminosity functions that use the oxygen-core sequences as input are marginally more consistent with the observations at the peak of the luminosity function than are those using the carbon-core sequences. The former suggest a flatter peak and an earlier crystallization bump compared to the latter. On the basis of the $^{12}C(\alpha,\gamma)^{16}O$ reaction rate (Caughlan and Fowler 1988), it is expected that the white dwarf interiors contain more than 50% oxygen by mass, but because the reaction rate is only claimed to be accurate to a factor of two, the precise C/O profile is currently unknown. We must wait for asteroseismological determinations of the actual abundance determinations to pin down these uncertainties further.

In addition to the uncertainty in the C/O profile of Population I composition stars, there is the added uncertainty of the evolution of the earliest generation of low-mass stars. Unless the early evolution of the Galaxy was dominated by high-mass star formation which enriched the interstellar medium before low-mass stars began forming, the first generation of white dwarf progenitors should have had near-zero metallicities. Because of lower opacities throughout, low-metallicity stellar models evolve quickly off the main sequence and have significantly higher core temperatures than comparable Pop I stars. Because of the behavior of the $^{12}C(\alpha,\gamma)^{16}O$ reaction rate with temperature, we might expect these stars to have formed white dwarfs that are more carbon-rich than do later-formed progenitors (cf. D'Antona

and Mazzitelli 1990), suggesting that the ages appropriate to the stars at the turndown are the carbon-core model ages. However, the initial→final mass relation is almost certainly a function of metallicity also — the ease with which the envelope is lifted off an asymptotic giant branch star is a function of opacity (see Kwok 1987) — and this suggests that the upper mass limit for white dwarf progenitors may have been much lower in the past than the current estimate of 8 $M_{\odot}$. Because the interstellar medium was enriched in metals on a timescale of order 1 Gyr, the effects just described should provide at most a $\sim$1 Gyr uncertainty to the ages derived using the white dwarf stars.

Given the observed dichotomy of high-mass and low-mass star formation environments, it is not unreasonable to consider that the lower mass limit of forming stars was a monotonically declining function of time in the early Galaxy. If this did occur, then the ages obtained through fitting the white dwarf luminosity functions will be short by approximately half the time it took the lower mass limit to reach $\sim$1 $M_{\odot}$. Realistically, this is probably no more than a $\sim$2 Gyr effect.

As was shown in Part I of this thesis, the mass of the helium layer is nearly as important to the age determination as is the core composition. Increasing the mass of the helium layer by an order of magnitude causes a roughly 0.75 Gyr shift towards younger ages at the luminosity of the turndown. The models that I used here typically had helium layer masses of $\log(M_{\rm He}/M_{\star}) = -4$, and the determined mean (Pelletier *et al.* 1986) is $\langle\log(M_{\rm He}/M_{\star})\rangle = -3.5 \pm 0.5$, suggesting a roughly 0.5 Gyr shift to younger ages.

The combined facts that the majority of white dwarfs are tightly clustered around the mean mass of 0.50–0.55 (Bergeron, Saffer, and Liebert 1990) and that the main sequence progenitors have masses up to $\sim$8 $M_\odot$ imply that the initial $\rightarrow$final mass relation is quite flat. Because of this, dramatic changes in the slope of the IMF have little affect on the luminosity functions. As Noh and Scalo (1990) discuss, this is one of the few probes of the star-formation history where the effects of the IMF and SFR are essentially decoupled.

The luminosity function is sensitive to the star formation rate both in terms of onset and also for the most recent $\sim$2 Gyr. The theoretical curves all cluster tightly at high luminosities, suggesting that as the error bars are reduced, it should be possible to decode the recent star formation history in great detail. A non-constant star formation rate within the most recent $\sim$2 Gyr is perhaps already suggested, because the luminosity functions of the individual sequences and the integrated sequences all show a Mestel slope in the luminosity range $-2.0 \gtrsim \log(L/L_\odot) \gtrsim -3.5$, but the observations *may* indicate a different slope (it is marginal, given the error bars). It could be that the observed points will move towards the Mestel relation as the error bars are reduced, but if they do not, then the observed LF points at $\log(L/L_\odot) \approx -1.7$, -2.2, and -2.6 may suggest that there was a recent burst of star formation some 3–4 $\times$ 10^8 yr ago, preceded by a lull approximately 1 Gyr ago. Both of these are consistent with the chromospheric age data of Barry (1988).

The Galactic disk ages that the white dwarfs suggest range conservatively from a low obtained from fitting the high-luminosity turndown limit using oxygen-core models with thick helium layers [$\log(M_{\rm He}/M_\star) = -2$], to a high obtained from fitting the low-luminosity turndown limit using

carbon-core models with thin helium layers [$\log(M_{\rm He}/M_\star) = -4$] and using the case A disk scale height inflation relation (factor of 3 over 12 Gyr) and a Clayton (1988) SFR. With these assumptions, the conservative estimates for the ages consistent with the observations range from a low of $\sim$6 Gyr to a high of $\sim$13.5 Gyr. Using the best estimates for the core composition [see equation (3.1)], a thin helium-layer mass, and one of the Clayton (1988) infall star-formation rates, the age estimates run from roughly 8-11 Gyr.

The oldest stars in the disk may have been scattered to larger scale heights above the disk through gravitational interactions with giant molecular clouds or through a satellite-galaxy accretion event. Carlberg *et al.* (1985) have re-investigated the Twarog (1980) results using the VandenBerg (1985) isochrones and several other refinements, and find Twarog overestimated the scale height inflation. In addition, Liebert, Dahn, and Monet (1988) found no correlation between tangential velocity with decreasing luminosity for the coolest white dwarfs, which further suggests that if there is a scale height inflation with age, it is modest. As we saw above, modest scale height inflation (*e.g.*, Case A) has only a small effect on the low-luminosity end of the luminosity function. Although it is well established that older stars are observed to have a larger scale height statistically than are young stars, an alternative explanation is that these stars were formed during an early pressure-supported collapse phase. Once formed, the stars would no longer be supported against the galactic gravitational potential, and would orbit on a highly-elliptical path with a mean scale height well above that of stars formed later when the disk had settled to its current thickness (see Gilmore, Wyse, and Kuijken 1989). In this picture, the SFR per volume could be approximately constant, and so might cause *no* change

in the white dwarf luminosity function. Undoubtedly both processes contribute to the observed trend of age *vs.* scale height, but sorting out the relative importance of the two explanations is going to be difficult and time consuming. For now, it seems likely that even the Case B relation is an overestimate for the increase of scale height by scattering processes, and so scale height inflation is not likely to strongly affect the derived ages of the oldest white dwarfs.

7. Concluding Remarks

We discussed the age limits for the local Galactic disk in great detail in the previous Chapter, and now compare those results against the age estimates obtained from other cosmochronological techniques. There are some serious inconsistancies among the results, and it is currently not possible to select unambiguously from among these various results to obtain the age of the Galaxy and universe. However, based on the success of white dwarf cosmochronology in determining the age of the local disk, we suggest that the continuing study of the white dwarf disk and halo luminosity functions may provide the solution to the problem within a few years.

Estimates for the age of the universe, Galaxy, and Solar System come from a number of sources. Traditional estimates come from measurements of the Hubble expansion constant H_0, which together with a cosmological model gives an age estimate for the length of time that the galaxies have been receding from each other. In the most recent major review of the cosmic distance scale, van den Bergh (1989) estimates that $H_0 = 67 \pm 8$ km s^{-1} Mpc^{-1}, which, if the inflationary model (Guth 1981; Guth and Steinhardt 1984) is correct and the universe is flat, suggests an age $t_U = \frac{2}{3}H_0^{-1} \approx 10$ Gyr (see Fowler 1987). Using Type Ia supernovae as standard candles, Arnett, Branch and Wheeler (1985) and Wheeler and Harkness (1986) use the apparent luminosity and redshift of SN Ia's in galaxies with $z \gtrsim 0.01$ to determine the Hubble time $T_0 \equiv H_0^{-1}$. They find $T_0 =$

16.8±1.4 Gyr, which again if Einstein's curvature constant and cosmological constant are zero (the Einstein–De Sitter model, 1932), gives $t_U = \frac{2}{3}T_0 = 11.2$.

Within our own Galaxy, it is common to fit isochrones to the halo globular clusters and to the disk globular and open clusters (where "disk globulars" refers to the higher-metallicity, lower-scale-height population discussed by Zinn 1985). The isochrones are constructed using the numerical results of standard stellar evolution calculations (VandenBerg and Bell 1985; Green, Demarque, and King 1987), and have associated with them a number of inherent uncertainties, such as mixing length, nuclear reaction rates, meridonal circulation, and magnetic field effects. Ages derived in this way are typically ~15 Gyr and Green (1988) suggests that there is a real spread in ages in the globular cluster system, ranging from about 13 Gyr for 47 Tuc and NGC 362 to almost 18 Gyr for M 92 and NGC 288.

The oldest of these ages are taken to be the age of the Galaxy t_G. To find the age of the Universe the formation timescale t_F (*i.e.*, Big Bang to star-formation onset timescale) must be added:

$$t_U = t_F + t_G. \tag{7.1}$$

The values adopted for t_F are typically near 1 Gyr, but with estimates that range up to ~5 Gyr. The recent COBE (Cosmic Background Explorer) satellite results show the microwave background to be described by a 2.74 K blackbody to exceptional accuracy, and in light of these results it is becoming increasingly clear that $t_F \approx 1$ Gyr may be too short a time to evolve from the smooth background to galactic structures if gravity is the sole force at work.

Also dependent upon isochronal calibration are the ages determined by Barry (1988) in his study of 115 nearby chromospherically-active stars. He suggests that the ages of the oldest object in his sample are ~13 Gyr old, with estimated accidental errors of 15% and systematic errors (possibly) as large as 20% at an age of 10 Gyr. These results are challenged by Norris and Green (1989), however, who in their study of core-helium-burning giants with distances above the galactic plane $z \lesssim 3$ kpc find that there is no compelling reason to believe that the Galactic disk in the solar neighborhood has any major stellar component as old as the disk globular clusters (*i.e.*, 47 Tuc at ~13 Gyr), by at least 3–6 Gyr.

Fowler (1987) and Fowler and Meisl (1986) describe their preferred method for dating the Galaxy: nucleocosmochronology. They use the ratios of radioactive decay product in the Solar System to derive the length of time Δ preceding the formation of the Solar System, and then add to that the age of the solar system (*e.g.*, Wasserburg *et al.* 1977):

$$t_{SS} = 4.6 \pm 0.1 \text{ Gyr}. \tag{7.2}$$

Fowler (1987) finds the pre-Solar System timespan to be $\Delta = 5.4 \pm 1.5$ Gyr for a Galactic age of $t_G = 10.0 \pm 1.5$ Gyr. Fowler's results have been brought into question by Cowan, Thielemann, and Truran (1986) who found $7.8 < \Delta < 10.1$ Gyr, suggesting a Galactic age of of $12.4 < t_G < 14.7$ Gyr, after introducing beta-delayed fission into the r–process network of reactions.

The local sample of white dwarf stars suggests that the first white dwarf progenitors began forming at our galactocentric radius some 9.5 Gyr ago, with the best estimates ranging from 8–11 Gyr. These results are consistent with those of Norris and Green (1989) and Fowler and Meisl (1986), and with the Hubble ages derived under the assumption of the inflationary model

with a zero cosmological constant, using recent determinations for H_0 and T_0. The white dwarf results are perhaps inconsistent with the globular cluster ages, the nucleocosmochronological ages of Cowan, Thielemann, and Truran (1986), and are marginally inconsistent with the chromospheric ages of Barry (1988).

If the Hubble ages as discussed above are essentially correct, then the globular cluster ages are wrong. The white dwarf ages and the nucleocosmochronological ages of Fowler are consistent with this picture, and within this context support the idea that the proto-Galaxy collapsed on roughly a dynamical timescale (*e.g.*, Eggen, Lynden-Bell, and Sandage 1962).

If instead the globular cluster ages are essentially correct (and it should be noted that there is good agreement among the calculations), then either the inflationary cosmological model is incorrect or the cosmological constant is (or was) non-zero. The results of Fowler (but not those of Cowan, Thielemann, and Truran) are inconsistent with this picture, because the r-process nuclei formed in an early generation of high-mass halo stars should have fallen onto the disk and then have be incorporated into forming disk stars — the nucleocosmochronological ages should lie between the disk and halo ages. If the globular cluster ages are correct, then it is possible to conclude that the time of onset of low-mass star formation occured 2–5 Gyr earlier in the halo globular clusters than in the local disk. This is an important result because it suggests that the Galaxy formed *via* an epoch of pressure supported collapse wherein the more-massive halo globular clusters and the bulge of the galaxy formed first, followed by the disk globular clusters and the stars in the disk itself. In other words, this result favors the pressure-supported collapse model of Larson (1976).

Whether there is or is not an age difference between disk and halo, observations of the halo and disk populations of white dwarf stars will trace the relative ages of the two, and will provide the solution to the problem within the next few years.

As discussed above, the main uncertainties in the age of the local disk as given by the white dwarf stars are the bolometric corrections appropriate to the cool stars, and the core composition and helium layer mass of the coolest stars. Roughly half of the age uncertainty is the result of the bolometric correction uncertainties, and the remaining uncertainty is in the white dwarf models. There are currently at least two observational campaigns whose goal is to reduce significantly the error bars for the lowest luminosity objects, and these efforts should produce results within the next two years (Claver *et al.* 1990; Von Hipple, personal communication).

In addition, our knowledge of the core composition and surface-layer structure is growing at an accelerated pace because of the advent of the Whole Earth Telescope (Nather 1989, Nather *et al.* 1990). With the Whole Earth Telescope, it is at last possible to observe the pulsating white dwarf stars and to obtain nearly continuous ~2-week photometric time-series measurements. Because the data density is roughly a factor of 10 higher than is obtainable from a typical single site, the Whole Earth Telescope Team are finding results which are different not by degree but by kind. For example, through comparison with theoretical models of pulsating white dwarf stars, they have been able to determine the mass of the DOV star PG1159 to two significant figures, the rotation period, the inclination angle, a limit to the magnetic field strength, and the composition of the surface layer masses (see Winget *et al.* 1990). In short, the observers are finding that they can use the Whole Earth Telescope time-series data as a fine seismological probe of the

structure of the star, and they are finding a wealth of information — stunning in its detail — with every run of the instrument. Because the pulsating DA and DB white dwarf stars are otherwise normal white dwarfs, these seismological observations will allow us to measure the physical parameters of the populations — especially the core composition and stratification — and to eliminate these uncertainties.

Over the next few years, as the results come in from the both the low-luminosity-white-dwarf surveys and the Whole Earth Telescope, our understanding of the shape of the low-temperature end of the luminosity function, and our understanding of the properties of the stars observed at the turndown, will improve greatly. The results promise to reveal the age of the local disk to greater accuracy than is possible with other methods, and will answer the question of the relative ages of the disk and halo of the Galaxy. In doing so, they will shape how we think about the formation and evolution of *all* galaxies.

Appendix: Model Sequence Summary Tables

Before listing the sequence summary tables discussed in the text, we should describe in some detail our method of naming the sequences. Examples of sequence names are c6310, c6410d, and x10400b. The leading character in the name indicates the core composition: **C**arbon, **O**xygen, or mi**X**ture. The following character(s) denote the core mass; for example "6" implies a core mass of 0.6 $M_\odot$, and "10" a core mass of 1.0 $M_\odot$ (note the use of two places for models with mass of 1.0 $M_\odot$ and greater). Following this is the character which denotes the logarithm of the helium-layer mass; for example "4" implies $\log(M_{He}/M_\star) = -4$. The following two characters denote the hydrogen layer mass in the same sense as we just discussed. Because we calculate sequences with hydrogen-layer masses below 10^{-10} $M_\star$ must use two characters in the name.

For most of these carbon- and oxygen-core sequences, the naming convention just described is sufficient. Implicit in these most basic names is that the He/C and H/He transitions are idealized as discontinuities. For those sequences calculated with the transition regions set to approximate the equilibrium diffusion profile, we tag a "d" onto the tail end of the name, and then specify the details of the transition zone thicknesses in the footnotes to the individual tables.

A number of our sequences have mixed C/O cores, and as we noted above, we lead these sequences' names with the letter "x." Because the number of C/O profiles which could be adopted approaches infinity, we chose to compute families of sequences, where each member of the family

has the same core C/O profile as a function of $M_r/M_\star$ as its siblings. For example, the sequences with mixed C/O profiles we present here we denote with a trailing "b" specifying the profile defined by equation (3.1) and shown in Figure 3.1. Not published here, but available upon request, we have computed a family of sequences with 50/50 C/O cores which we have defined as family "a" (e.g., x6300a). Similarly, we have another family of sequences computed with an approximation to the C/O profile in Mazzitelli and D'Antona (1986; their Figure 5) and thin diffusive equilibrium composition-transition zones; these we define with a trailing "c," for the core composition, followed by "d," for the diffusive transition zones. These sequences were used in a preliminary study of the white dwarf luminosity function by Wood (1990), and are also available upon request.

In the Tables that follow, we list the luminosity $\log(L/L_\odot)$, the Age the core temperature $\log(T_c)$, the effective temperature $\log(T_{\rm eff})$, the radius $\log(R_\star)$, the neutrino luminosity $\log(L_\nu/L_\odot)$, and the crystallization mass fraction $M_{\rm xtal}/M_\star$. Typical model sequences have $\sim$90 models in them, and so would take up too much space if published "raw." For this reason, and also to facilitate the intercomparison of the various sequences, we have interpolated (using splines) all of the sequences onto a uniform luminosity grid whose maximum is $\log(L/L_\odot) = +1.0$ and whose minimum is a function of the specific sequence. The stepsize in luminosity between table entries is 0.2 dex. Finally, we note that beyond a point in the evolution of the models, neutrino energy losses become unimportant, and we stop calculating them. In the Tables these models have ellipses in the $\log(L_\nu/L_\odot)$ column.

TABLE A.1
X6400B SUMMARY LISTING

$\log(L/L_\odot)$	Age	$\log(T_c)$	$T_{\rm eff}$	$\log(R_\star)$	$\log(L_\nu/L_\odot)$	$M_{\rm xtal}/M_\star$
+1.0	2.636 (6)	7.941	79924	9.065	+1.326	0.
+0.8	2.981 (6)	7.905	72940	9.043	+1.133	0.
+0.6	3.394 (6)	7.874	66249	9.026	+0.942	0.
+0.4	3.897 (6)	7.847	59971	9.013	+0.751	0.
+0.2	4.524 (6)	7.824	54167	9.002	+0.561	0.
0.0	5.318 (6)	7.803	48811	8.992	+0.366	0.
−0.2	6.348 (6)	7.783	43906	8.983	+0.166	0.
−0.4	7.722 (6)	7.762	39475	8.976	−0.045	0.
−0.6	9.659 (6)	7.739	35453	8.970	−0.274	0.
−0.8	1.259 (7)	7.714	31780	8.964	−0.535	0.
−1.0	1.739 (7)	7.682	28520	8.959	−0.848	0.
−1.2	2.592 (7)	7.638	25532	8.954	−1.243	0.
−1.4	4.218 (7)	7.580	22874	8.950	−1.763	0.
−1.6	7.137 (7)	7.507	20503	8.947	−2.414	0.
−1.8	1.162 (8)	7.428	18329	8.943	−3.143	0.
−2.0	1.790 (8)	7.345	16397	8.940	−3.889	0.
−2.2	2.645 (8)	7.258	14670	8.936	−4.583	0.
−2.4	3.793 (8)	7.169	13104	8.933	−5.201	0.
−2.6	5.270 (8)	7.079	11727	8.931	−5.758	0.
−2.8	7.139 (8)	6.991	10468	8.930	−6.283	0.
−3.0	9.578 (8)	6.903	9329	8.929	−6.804	0.
−3.2	1.276 (9)	6.814	8325	8.928	−7.361	0.
−3.4	1.694 (9)	6.725	7430	8.927	...	0.
−3.6	2.430 (9)	6.635	6632	8.926	...	0.188
−3.8	3.526 (9)	6.529	5913	8.925	...	0.526
−4.0	4.737 (9)	6.417	5278	8.924	...	0.662
−4.2	6.392 (9)	6.281	4707	8.924	...	0.810
−4.4	7.992 (9)	6.161	4195	8.923	...	0.904
−4.6	9.565 (9)	6.054	3743	8.923	...	0.964
−4.8	1.132(10)	5.936	3331	8.923	...	0.991
−5.0	1.324(10)	5.801	2972	8.924	...	1.000
−5.2	1.520(10)	5.637	2648	8.923	...	1.000
−5.4	1.666(10)	5.474	2356	8.924	...	1.000

TABLE A.2
X4400B SUMMARY LISTING

$\log(L/L_\odot)$	Age	$\log(T_c)$	$T_{\rm eff}$	$\log(R_\star)$	$\log(L_\nu/L_\odot)$	$M_{\rm xtal}/M_\star$
+1.0	2.920 (6)	8.258	55030	9.388	+0.471	0.
+0.8	4.033 (6)	8.205	53455	9.313	+0.527	0.
+0.6	5.255 (6)	8.125	50842	9.256	+0.493	0.
+0.4	6.592 (6)	8.037	47583	9.214	+0.377	0.
+0.2	8.108 (6)	7.967	44019	9.182	+0.212	0.
0.0	9.886 (6)	7.911	40376	9.157	+0.031	0.
−0.2	1.203 (7)	7.863	36886	9.136	−0.164	0.
−0.4	1.467 (7)	7.821	33502	9.120	−0.369	0.
−0.6	1.803 (7)	7.782	30320	9.106	−0.580	0.
−0.8	2.248 (7)	7.744	27381	9.094	−0.808	0.
−1.0	2.871 (7)	7.704	24673	9.084	−1.062	0.
−1.2	3.780 (7)	7.660	22256	9.075	−1.356	0.
−1.4	5.146 (7)	7.611	20002	9.067	−1.703	0.
−1.6	7.268 (7)	7.553	17995	9.059	−2.126	0.
−1.8	1.058 (8)	7.487	16156	9.053	−2.642	0.
−2.0	1.539 (8)	7.414	14504	9.046	−3.241	0.
−2.2	2.198 (8)	7.339	13020	9.039	−3.902	0.
−2.4	3.084 (8)	7.261	11681	9.035	−4.594	0.
−2.6	4.269 (8)	7.181	10446	9.031	−5.260	0.
−2.8	5.876 (8)	7.096	9349	9.028	−5.872	0.
−3.0	8.012 (8)	7.009	8354	9.025	−6.434	0.
−3.2	1.082 (9)	6.918	7466	9.023	−6.983	0.
−3.4	1.448 (9)	6.826	6670	9.021	−7.582	0.
−3.6	1.925 (9)	6.732	5959	9.019	...	0.
−3.8	2.569 (9)	6.633	5319	9.018	...	0.
−4.0	3.604 (9)	6.519	4748	9.016	...	0.041
−4.2	5.288 (9)	6.390	4242	9.015	...	0.498
−4.4	6.781 (9)	6.279	3776	9.015	...	0.646
−4.6	8.533 (9)	6.169	3364	9.014	...	0.773
−4.8	1.085(10)	6.044	3002	9.015	...	0.885
−5.0	1.332(10)	5.921	2673	9.014	...	0.966
−5.2	1.576(10)	5.800	2379	9.015	...	0.993

TABLE A.3
X5400B SUMMARY LISTING

$\log(L/L_\odot)$	Age	$\log(T_c)$	$T_{\rm eff}$	$\log(R_\star)$	$\log(L_\nu/L_\odot)$	$M_{\rm xtal}/M_\star$
+1.0	3.235 (6)	8.059	69994	9.179	+1.174	0.
+0.8	3.789 (6)	7.993	65021	9.143	+0.996	0.
+0.6	4.422 (6)	7.938	59784	9.117	+0.811	0.
+0.4	5.172 (6)	7.895	54616	9.095	+0.622	0.
+0.2	6.076 (6)	7.860	49650	9.077	+0.429	0.
0.0	7.188 (6)	7.829	44979	9.063	+0.233	0.
−0.2	8.585 (6)	7.800	40663	9.051	+0.032	0.
−0.4	1.038 (7)	7.774	36695	9.041	−0.175	0.
−0.6	1.279 (7)	7.747	33034	9.031	−0.395	0.
−0.8	1.619 (7)	7.719	29673	9.024	−0.636	0.
−1.0	2.132 (7)	7.685	26664	9.017	−0.915	0.
−1.2	2.945 (7)	7.645	23961	9.011	−1.247	0.
−1.4	4.306 (7)	7.595	21451	9.006	−1.659	0.
−1.6	6.642 (7)	7.533	19254	9.001	−2.177	0.
−1.8	1.042 (8)	7.461	17233	8.996	−2.802	0.
−2.0	1.601 (8)	7.383	15457	8.991	−3.514	0.
−2.2	2.354 (8)	7.302	13858	8.986	−4.238	0.
−2.4	3.377 (8)	7.218	12398	8.982	−4.924	0.
−2.6	4.744 (8)	7.130	11089	8.979	−5.535	0.
−2.8	6.567 (8)	7.040	9898	8.977	−6.105	0.
−3.0	8.863 (8)	6.950	8843	8.975	−6.641	0.
−3.2	1.183 (9)	6.861	7901	8.974	−7.151	0.
−3.4	1.574 (9)	6.771	7051	8.973	−9.441	0.
−3.6	2.096 (9)	6.678	6285	8.972	...	0.
−3.8	2.885 (9)	6.588	5609	8.971	...	0.084
−4.0	4.431 (9)	6.458	5009	8.970	...	0.518
−4.2	5.953 (9)	6.330	4474	8.969	...	0.681
−4.4	7.473 (9)	6.218	3979	8.969	...	0.801
−4.6	9.182 (9)	6.110	3551	8.968	...	0.891
−4.8	1.132(10)	5.990	3163	8.970	...	0.966
−5.0	1.358(10)	5.860	2817	8.969	...	0.993
−5.2	1.559(10)	5.743	2505	8.971	...	1.000

TABLE A.4

X7400B SUMMARY LISTING

$\log(L/L_\odot)$	Age	$\log(T_c)$	$T_{\rm eff}$	$\log(R_\star)$	$\log(L_\nu/L_\odot)$	$M_{\rm xtal}/M_\star$
+1.0	2.661 (6)	7.914	87326	8.989	+1.447	0.
+0.8	2.947 (6)	7.884	79100	8.971	+1.214	0.
+0.6	3.288 (6)	7.857	71263	8.956	+0.996	0.
+0.4	3.661 (6)	7.838	63959	8.946	+0.817	0.
+0.2	4.119 (6)	7.821	57278	8.939	+0.640	0.
0.0	4.719 (6)	7.803	51230	8.932	+0.449	0.
−0.2	5.531 (6)	7.785	45775	8.926	+0.247	0.
−0.5	6.698 (6)	7.766	40858	8.921	+0.026	0.
−0.7	8.517 (6)	7.744	36446	8.916	−0.230	0.
−0.9	1.173 (7)	7.714	32579	8.911	−0.551	0.
−1.1	1.803 (7)	7.672	29052	8.908	−0.971	0.
−1.3	3.130 (7)	7.610	25884	8.904	−1.532	0.
−1.5	5.784 (7)	7.532	23079	8.900	−2.243	0.
−1.7	1.020 (8)	7.445	20553	8.897	−3.047	0.
−1.9	1.643 (8)	7.354	18294	8.894	−3.835	0.
−2.1	2.486 (8)	7.261	16297	8.891	−4.529	0.
−2.3	3.572 (8)	7.169	14518	8.889	−5.123	0.
−2.5	5.007 (8)	7.076	12903	8.887	−5.685	0.
−2.7	6.850 (8)	6.984	11482	8.886	−6.225	0.
−2.9	9.272 (8)	6.894	10197	8.885	−6.759	0.
−3.1	1.246 (9)	6.804	9048	8.884	−7.329	0.
−3.3	1.774 (9)	6.716	8045	8.883	−9.998	0.167
−3.6	2.642 (9)	6.613	7144	8.882	...	0.502
−3.8	3.557 (9)	6.511	6341	8.883	...	0.634
−4.0	4.733 (9)	6.401	5634	8.882	...	0.755
−4.2	6.315 (9)	6.271	4992	8.882	...	0.870
−4.4	8.021 (9)	6.136	4440	8.882	...	0.958
−4.6	9.388 (9)	6.027	3931	8.884	...	0.986
−4.8	1.092(10)	5.910	3488	8.884	...	1.000

TABLE A.5
X8400B SUMMARY LISTING

$\log(L/L_\odot)$	Age	$\log(T_c)$	$T_{\rm eff}$	$\log(R_\star)$	$\log(L_\nu/L_\odot)$	$M_{\rm xtal}/M_\star$
+0.6	2.941 (6)	7.899	77989	8.906	+1.359	0.
+0.4	3.336 (6)	7.867	67905	8.893	+1.042	0.
+0.2	3.886 (6)	7.842	61128	8.883	+0.784	0.
0.0	4.516 (6)	7.822	55253	8.877	+0.567	0.
−0.2	5.213 (6)	7.805	49269	8.872	+0.364	0.
−0.4	6.135 (6)	7.787	43758	8.868	+0.150	0.
−0.6	7.688 (6)	7.765	39009	8.864	−0.112	0.
−0.9	1.104 (7)	7.730	34850	8.860	−0.488	0.
−1.1	1.900 (7)	7.676	30963	8.857	−1.027	0.
−1.3	3.702 (7)	7.598	27573	8.854	−1.732	0.
−1.5	7.036 (7)	7.508	24593	8.851	−2.544	0.
−1.7	1.202 (8)	7.415	21910	8.848	−3.365	0.
−1.9	1.863 (8)	7.322	19467	8.846	−4.076	0.
−2.1	2.727 (8)	7.229	17313	8.844	−4.685	0.
−2.3	3.856 (8)	7.136	15409	8.842	−5.245	0.
−2.5	5.332 (8)	7.045	13696	8.841	−5.789	0.
−2.7	7.242 (8)	6.955	12172	8.840	−6.319	0.
−2.9	9.764 (8)	6.865	10793	8.839	−6.848	0.
−3.1	1.405 (9)	6.779	9591	8.838	−7.936	0.206
−3.3	2.059 (9)	6.682	8508	8.838	...	0.506
−3.5	2.763 (9)	6.584	7571	8.837	...	0.629
−3.8	3.635 (9)	6.483	6705	8.838	...	0.740
−4.0	4.825 (9)	6.373	5959	8.837	...	0.841
−4.2	6.200 (9)	6.257	5274	8.839	...	0.924
−4.4	7.859 (9)	6.110	4687	8.838	...	0.982
−4.6	9.069 (9)	5.999	4149	8.841	...	0.998
−4.8	1.039(10)	5.875	3691	8.839	...	1.000
−5.0	1.164(10)	5.744	3261	8.842	...	1.000

TABLE A.6
X9400B SUMMARY LISTING

$\log(L/L_\odot)$	Age	$\log(T_c)$	$T_{\rm eff}$	$\log(R_\star)$	$\log(L_\nu/L_\odot)$	$M_{\rm xtal}/M_\star$
+1.0	2.524 (6)	7.962	104858	8.858	+1.752	0.
+0.8	2.660 (6)	7.934	90827	8.844	+1.476	0.
+0.6	2.737 (6)	7.917	79682	8.834	+1.316	0.
+0.4	2.800 (6)	7.909	71212	8.829	+1.239	0.
+0.2	2.926 (6)	7.902	64239	8.826	+1.160	0.
0.0	3.213 (6)	7.887	57958	8.823	+0.996	0.
−0.2	3.798 (6)	7.859	51906	8.818	+0.688	0.
−0.5	4.805 (6)	7.828	46309	8.813	+0.347	0.
−0.7	6.637 (6)	7.795	41286	8.809	−0.005	0.
−0.9	1.090 (7)	7.745	36741	8.807	−0.515	0.
−1.1	2.402 (7)	7.659	32699	8.804	−1.297	0.
−1.3	4.973 (7)	7.565	29138	8.802	−2.135	0.
−1.5	8.927 (7)	7.470	25927	8.799	−2.961	0.
−1.7	1.422 (8)	7.376	23079	8.797	−3.680	0.
−1.9	2.116 (8)	7.283	20510	8.795	−4.295	0.
−2.1	3.008 (8)	7.193	18227	8.794	−4.848	0.
−2.3	4.185 (8)	7.101	16204	8.793	−5.388	0.
−2.5	5.728 (8)	7.012	14394	8.792	−5.918	0.
−2.7	7.780 (8)	6.943	13027	8.791	−6.437	0.
−2.9	1.152 (9)	6.834	11373	8.790	−6.962	0.276
−3.1	1.629 (9)	6.742	10091	8.790	−9.997	0.523
−3.3	2.182 (9)	6.650	8963	8.790	...	0.636
−3.6	2.855 (9)	6.552	7952	8.789	...	0.741
−3.8	3.722 (9)	6.451	7050	8.791	...	0.832
−4.0	4.821 (9)	6.339	6267	8.789	...	0.912
−4.2	5.947 (9)	6.233	5543	8.793	...	0.966
−4.4	7.385 (9)	6.085	4928	8.790	...	0.992
−4.6	8.388 (9)	5.970	4358	8.795	...	1.000
−4.8	9.511 (9)	5.826	3882	8.791	...	1.000

TABLE A.7

X10400B SUMMARY LISTING

$\log(L/L_\odot)$	Age	$\log(T_c)$	$T_{\rm eff}$	$\log(R_\star)$	$\log(L_\nu/L_\odot)$	$M_{\rm xtal}/M_\star$
+1.0	2.465 (6)	8.006	114412	8.790	+1.911	0.
+0.8	2.589 (6)	7.986	103414	8.784	+1.695	0.
+0.6	2.731 (6)	7.961	89088	8.775	+1.427	0.
+0.4	2.774 (6)	7.946	77126	8.768	+1.268	0.
+0.2	2.742 (6)	7.942	68214	8.763	+1.221	0.
0.0	2.768 (6)	7.939	61153	8.760	+1.187	0.
−0.2	2.993 (6)	7.927	55111	8.758	+1.060	0.
−0.5	3.637 (6)	7.897	49513	8.754	+0.739	0.
−0.7	5.549 (6)	7.840	44150	8.750	+0.159	0.
−0.9	1.330 (7)	7.749	39266	8.749	−0.659	0.
−1.1	3.508 (7)	7.630	34931	8.747	−1.680	0.
−1.3	6.635 (7)	7.532	31136	8.744	−2.526	0.
−1.5	1.079 (8)	7.438	27681	8.742	−3.249	0.
−1.7	1.624 (8)	7.346	24585	8.741	−3.863	0.
−1.9	2.346 (8)	7.253	21895	8.739	−4.430	0.
−2.1	3.275 (8)	7.163	19418	8.739	−4.964	0.
−2.3	4.493 (8)	7.074	17284	8.738	−5.490	0.
−2.5	6.184 (8)	6.994	15338	8.737	−5.998	0.046
−2.7	9.219 (8)	6.897	13628	8.736	−6.528	0.335
−2.9	1.284 (9)	6.804	12104	8.736	−7.110	0.545
−3.1	1.687 (9)	6.717	10728	8.737	...	0.647
−3.3	2.205 (9)	6.624	9527	8.736	...	0.744
−3.6	2.869 (9)	6.529	8449	8.736	...	0.828
−3.8	3.657 (9)	6.428	7487	8.738	...	0.898
−4.0	4.646 (9)	6.313	6669	8.736	...	0.961
−4.2	5.545 (9)	6.208	5888	8.740	...	0.985
−4.4	6.632 (9)	6.072	5248	8.737	...	1.000
−4.6	7.515 (9)	5.943	4615	8.744	...	1.000
−4.8	8.340 (9)	5.795	4122	8.739	...	1.000

TABLE A.8
C4400 SUMMARY LISTING

$\log(L/L_\odot)$	Age	$\log(T_c)$	$T_{\rm eff}$	$\log(R_\star)$	$\log(L_\nu/L_\odot)$	$M_{\rm xtal}/M_\star$
+1.0	2.788 (6)	8.251	52934	9.421	+0.264	0.
+0.8	4.089 (6)	8.218	52051	9.336	+0.390	0.
+0.6	5.506 (6)	8.151	49891	9.273	+0.405	0.
+0.4	7.049 (6)	8.061	46882	9.227	+0.328	0.
+0.2	8.756 (6)	7.986	43506	9.191	+0.180	0.
0.0	1.071 (7)	7.928	40073	9.164	+0.009	0.
−0.2	1.302 (7)	7.878	36588	9.142	−0.178	0.
−0.4	1.584 (7)	7.833	33306	9.125	−0.378	0.
−0.6	1.937 (7)	7.793	30157	9.110	−0.588	0.
−0.8	2.404 (7)	7.752	27287	9.098	−0.816	0.
−1.0	3.062 (7)	7.710	24624	9.087	−1.072	0.
−1.2	4.030 (7)	7.663	22173	9.077	−1.370	0.
−1.4	5.493 (7)	7.610	19955	9.069	−1.724	0.
−1.6	7.788 (7)	7.550	17917	9.061	−2.156	0.
−1.8	1.136 (8)	7.481	16123	9.054	−2.679	0.
−2.0	1.652 (8)	7.409	14481	9.048	−3.281	0.
−2.2	2.362 (8)	7.333	12990	9.041	−3.948	0.
−2.4	3.317 (8)	7.256	11652	9.037	−4.651	0.
−2.6	4.602 (8)	7.175	10437	9.033	−5.337	0.
−2.8	6.347 (8)	7.091	9329	9.029	−5.964	0.
−3.0	8.649 (8)	7.004	8336	9.027	−6.527	0.
−3.2	1.174 (9)	6.913	7443	9.025	−7.080	0.
−3.4	1.578 (9)	6.821	6650	9.023	−7.672	0.
−3.6	2.103 (9)	6.729	5947	9.021	−9.988	0.
−3.8	2.819 (9)	6.629	5304	9.020	...	0.
−4.0	3.935 (9)	6.503	4740	9.018	...	0.
−4.2	5.181 (9)	6.387	4227	9.017	...	0.
−4.4	7.181 (9)	6.287	3776	9.016	...	0.259
−4.6	9.850 (9)	6.169	3367	9.016	...	0.647
−4.8	1.292(10)	6.037	2998	9.015	...	0.888
−5.0	1.563(10)	5.914	2676	9.015	...	0.968
−5.2	1.862(10)	5.777	2383	9.015	...	0.994

TABLE A.9
c5400 SUMMARY LISTING

$\log(L/L_\odot)$	Age	$\log(T_c)$	$T_{\rm eff}$	$\log(R_\star)$	$\log(L_\nu/L_\odot)$	$M_{\rm xtal}/M_\star$
+1.0	3.470 (6)	8.090	68959	9.192	+1.154	0.
+0.8	4.077 (6)	8.016	64250	9.154	+0.982	0.
+0.6	4.765 (6)	7.958	59286	9.124	+0.806	0.
+0.4	5.559 (6)	7.914	54235	9.101	+0.626	0.
+0.2	6.502 (6)	7.876	49351	9.082	+0.437	0.
0.0	7.651 (6)	7.845	44784	9.067	+0.244	0.
−0.2	9.086 (6)	7.815	40491	9.055	+0.046	0.
−0.4	1.093 (7)	7.786	36529	9.043	−0.161	0.
−0.6	1.339 (7)	7.758	32935	9.034	−0.381	0.
−0.8	1.690 (7)	7.726	29619	9.027	−0.626	0.
−1.0	2.226 (7)	7.691	26604	9.019	−0.910	0.
−1.2	3.091 (7)	7.647	23927	9.012	−1.252	0.
−1.4	4.577 (7)	7.592	21422	9.007	−1.682	0.
−1.6	7.163 (7)	7.527	19227	9.002	−2.222	0.
−1.8	1.128 (8)	7.453	17216	8.997	−2.861	0.
−2.0	1.720 (8)	7.376	15432	8.992	−3.568	0.
−2.2	2.529 (8)	7.296	13820	8.987	−4.300	0.
−2.4	3.636 (8)	7.213	12385	8.984	−5.003	0.
−2.6	5.130 (8)	7.125	11073	8.981	−5.629	0.
−2.8	7.116 (8)	7.035	9891	8.979	−6.201	0.
−3.0	9.620 (8)	6.947	8831	8.977	−6.732	0.
−3.2	1.291 (9)	6.857	7885	8.976	−7.266	0.
−3.4	1.722 (9)	6.767	7029	8.974	...	0.
−3.6	2.303 (9)	6.673	6284	8.973	...	0.
−3.8	3.081 (9)	6.576	5607	8.972	...	0.
−4.0	4.276 (9)	6.456	4998	8.971	...	0.
−4.2	6.451 (9)	6.332	4462	8.970	...	0.385
−4.4	8.700 (9)	6.216	3978	8.970	...	0.722
−4.6	1.085(10)	6.107	3544	8.969	...	0.892
−4.8	1.334(10)	5.979	3160	8.969	...	0.975
−5.0	1.576(10)	5.851	2821	8.969	...	0.990

TABLE A.10
c6400 SUMMARY LISTING

$\log(L/L_\odot)$	Age	$\log(T_c)$	$T_{\rm eff}$	$\log(R_\star)$	$\log(L_\nu/L_\odot)$	$M_{\rm xtal}/M_\star$
+1.0	2.809 (6)	7.960	79240	9.071	+1.350	0.
+0.8	3.174 (6)	7.921	72470	9.049	+1.160	0.
+0.6	3.605 (6)	7.890	65914	9.032	+0.966	0.
+0.4	4.130 (6)	7.863	59699	9.018	+0.778	0.
+0.2	4.780 (6)	7.840	53898	9.006	+0.590	0.
0.0	5.601 (6)	7.817	48560	8.995	+0.397	0.
−0.2	6.661 (6)	7.796	43737	8.987	+0.196	0.
−0.4	8.082 (6)	7.774	39381	8.980	−0.016	0.
−0.6	1.009 (7)	7.750	35338	8.973	−0.246	0.
−0.8	1.316 (7)	7.722	31682	8.967	−0.511	0.
−1.0	1.827 (7)	7.686	28455	8.962	−0.831	0.
−1.2	2.759 (7)	7.640	25486	8.957	−1.239	0.
−1.4	4.558 (7)	7.577	22812	8.952	−1.772	0.
−1.6	7.769 (7)	7.503	20445	8.949	−2.429	0.
−1.8	1.267 (8)	7.424	18295	8.945	−3.162	0.
−2.0	1.956 (8)	7.342	16363	8.942	−3.923	0.
−2.2	2.893 (8)	7.256	14648	8.938	−4.641	0.
−2.4	4.147 (8)	7.167	13096	8.936	−5.271	0.
−2.6	5.797 (8)	7.077	11692	8.934	−5.840	0.
−2.8	7.872 (8)	6.989	10440	8.932	−6.366	0.
−3.0	1.059 (9)	6.900	9317	8.930	−6.890	0.
−3.2	1.412 (9)	6.812	8316	8.929	−7.444	0.
−3.4	1.882 (9)	6.723	7415	8.928	−9.947	0.
−3.6	2.519 (9)	6.630	6616	8.927	...	0.
−3.8	3.382 (9)	6.531	5899	8.927	...	0.
−4.0	5.077 (9)	6.421	5269	8.926	...	0.342
−4.2	7.530 (9)	6.282	4697	8.925	...	0.732
−4.4	9.513 (9)	6.162	4191	8.925	...	0.897
−4.6	1.130(10)	6.054	3737	8.925	...	0.968
−4.8	1.331(10)	5.935	3326	8.925	...	0.990
−5.0	1.547(10)	5.799	2968	8.925	...	1.000

TABLE A.11
C7400 SUMMARY LISTING

$\log(L/L_\odot)$	Age	$\log(T_c)$	$T_{\rm eff}$	$\log(R_\star)$	$\log(L_\nu/L_\odot)$	$M_{\rm xtal}/M_\star$
+1.0	2.668 (6)	7.923	87428	8.988	+1.465	0.
+0.8	2.910 (6)	7.897	79208	8.974	+1.270	0.
+0.6	3.208 (6)	7.874	71444	8.961	+1.079	0.
+0.4	3.571 (6)	7.855	64347	8.951	+0.895	0.
+0.2	4.028 (6)	7.836	57939	8.943	+0.708	0.
0.0	4.621 (6)	7.818	52132	8.936	+0.515	0.
−0.2	5.408 (6)	7.799	46799	8.929	+0.314	0.
−0.4	6.509 (6)	7.779	41942	8.924	+0.097	0.
−0.6	8.165 (6)	7.757	37599	8.918	−0.147	0.
−0.8	1.092 (7)	7.728	33661	8.914	−0.439	0.
−1.0	1.611 (7)	7.689	30173	8.910	−0.814	0.
−1.2	2.708 (7)	7.632	26980	8.907	−1.321	0.
−1.4	4.987 (7)	7.559	24157	8.902	−1.981	0.
−1.6	8.843 (7)	7.477	21618	8.899	−2.734	0.
−1.8	1.447 (8)	7.392	19329	8.897	−3.521	0.
−2.0	2.213 (8)	7.304	17278	8.894	−4.255	0.
−2.2	3.231 (8)	7.215	15463	8.891	−4.892	0.
−2.4	4.556 (8)	7.125	13791	8.889	−5.455	0.
−2.6	6.252 (8)	7.036	12311	8.888	−5.986	0.
−2.8	8.437 (8)	6.949	10988	8.886	−6.503	0.
−3.0	1.129 (9)	6.862	9824	8.886	−7.020	0.
−3.2	1.501 (9)	6.775	8763	8.885	−9.681	0.
−3.4	2.004 (9)	6.686	7811	8.884	...	0.
−3.6	2.700 (9)	6.596	6968	8.883	...	0.017
−3.8	4.105 (9)	6.493	6210	8.883	...	0.350
−4.0	5.817 (9)	6.383	5539	8.882	...	0.657
−4.2	7.863 (9)	6.250	4942	8.882	...	0.874
−4.4	9.658 (9)	6.121	4407	8.881	...	0.965
−4.6	1.123(10)	6.008	3923	8.881	...	0.991
−4.8	1.280(10)	5.896	3498	8.881	...	1.000
−5.0	1.457(10)	5.759	3113	8.882	...	1.000

TABLE A.12
C8400 SUMMARY LISTING

$\log(L/L_\odot)$	Age	$\log(T_c)$	$T_{\rm eff}$	$\log(R_\star)$	$\log(L_\nu/L_\odot)$	$M_{\rm xtal}/M_\star$
+1.0	2.583 (6)	7.922	93668	8.918	+1.538	0.
+0.8	2.747 (6)	7.904	84862	8.909	+1.362	0.
+0.6	2.958 (6)	7.887	76694	8.902	+1.186	0.
+0.4	3.236 (6)	7.869	68898	8.894	+1.000	0.
+0.2	3.594 (6)	7.851	61785	8.887	+0.811	0.
0.0	4.058 (6)	7.834	55436	8.881	+0.618	0.
−0.2	4.695 (6)	7.817	49725	8.876	+0.414	0.
−0.4	5.635 (6)	7.797	44549	8.872	+0.189	0.
−0.6	7.166 (6)	7.772	39842	8.868	−0.077	0.
−0.8	1.003 (7)	7.740	35645	8.864	−0.414	0.
−1.0	1.639 (7)	7.690	31892	8.861	−0.879	0.
−1.2	3.159 (7)	7.618	28561	8.857	−1.524	0.
−1.4	6.084 (7)	7.536	25550	8.855	−2.282	0.
−1.6	1.073 (8)	7.446	22830	8.852	−3.105	0.
−1.8	1.703 (8)	7.356	20432	8.849	−3.863	0.
−2.0	2.509 (8)	7.268	18217	8.847	−4.493	0.
−2.2	3.565 (8)	7.179	16272	8.845	−5.054	0.
−2.4	4.931 (8)	7.090	14540	8.844	−5.583	0.
−2.6	6.709 (8)	7.002	12977	8.843	−6.104	0.
−2.8	9.008 (8)	6.916	11581	8.842	−6.615	0.
−3.0	1.201 (9)	6.829	10326	8.841	−7.117	0.
−3.2	1.596 (9)	6.742	9215	8.840	−9.983	0.
−3.4	2.157 (9)	6.660	8216	8.840	...	0.049
−3.6	3.264 (9)	6.560	7326	8.839	...	0.357
−3.8	4.579 (9)	6.457	6531	8.838	...	0.650
−4.0	6.061 (9)	6.350	5830	8.838	...	0.835
−4.2	7.687 (9)	6.228	5189	8.838	...	0.938
−4.4	9.393 (9)	6.088	4633	8.838	...	0.990
−4.6	1.073(10)	5.972	4128	8.838	...	1.000
−4.8	1.202(10)	5.854	3678	8.838	...	1.000
−5.0	1.325(10)	5.733	3275	8.838	...	1.000

TABLE A.13
c9400 SUMMARY LISTING

$\log(L/L_\odot)$	Age	$\log(T_c)$	$T_{\rm eff}$	$\log(R_\star)$	$\log(L_\nu/L_\odot)$	$M_{\rm xtal}/M_\star$
+1.0	2.519 (6)	7.967	105730	8.860	+1.782	0.
+0.8	2.676 (6)	7.940	91819	8.848	+1.514	0.
+0.6	2.865 (6)	7.917	80403	8.838	+1.278	0.
+0.4	3.082 (6)	7.900	72149	8.832	+1.098	0.
+0.2	3.368 (6)	7.884	65071	8.828	+0.924	0.
0.0	3.778 (6)	7.866	58146	8.823	+0.714	0.
−0.2	4.399 (6)	7.844	51726	8.819	+0.474	0.
−0.5	5.410 (6)	7.819	46136	8.816	+0.206	0.
−0.7	7.378 (6)	7.785	41178	8.813	−0.134	0.
−0.9	1.226 (7)	7.734	36626	8.809	−0.625	0.
−1.1	2.586 (7)	7.652	32637	8.806	−1.334	0.
−1.3	5.387 (7)	7.561	29061	8.803	−2.162	0.
−1.5	9.782 (7)	7.466	25857	8.800	−3.012	0.
−1.7	1.568 (8)	7.372	23033	8.798	−3.756	0.
−1.9	2.339 (8)	7.279	20459	8.797	−4.383	0.
−2.1	3.336 (8)	7.187	18225	8.795	−4.941	0.
−2.3	4.643 (8)	7.097	16198	8.794	−5.479	0.
−2.5	6.374 (8)	7.006	14388	8.793	−6.014	0.
−2.7	8.629 (8)	6.917	12775	8.792	−6.540	0.
−2.9	1.159 (9)	6.828	11352	8.791	−7.053	0.
−3.1	1.572 (9)	6.746	10083	8.790	−9.979	0.043
−3.3	2.357 (9)	6.649	8963	8.790	...	0.326
−3.6	3.376 (9)	6.551	7965	8.789	...	0.596
−3.8	4.555 (9)	6.446	7058	8.789	...	0.796
−4.0	5.816 (9)	6.334	6277	8.789	...	0.914
−4.2	7.119 (9)	6.221	5564	8.789	...	0.967
−4.4	8.643 (9)	6.077	4940	8.788	...	0.989
−4.6	9.867 (9)	5.944	4383	8.789	...	1.000
−4.8	1.088(10)	5.820	3892	8.789	...	1.000

TABLE A.14
c10500 SUMMARY LISTING

$\log(L/L_\odot)$	Age	$\log(T_c)$	$T_{\rm eff}$	$\log(R_\star)$	$\log(L_\nu/L_\odot)$	$M_{\rm xtal}/M_\star$
+1.0	2.464 (6)	8.007	114668	8.790	+1.912	0.
+0.8	2.559 (6)	7.987	102160	8.784	+1.700	0.
+0.6	2.704 (6)	7.963	88323	8.776	+1.438	0.
+0.4	2.880 (6)	7.943	78071	8.770	+1.223	0.
+0.2	3.103 (6)	7.927	70303	8.767	+1.041	0.
0.0	3.407 (6)	7.910	63498	8.764	+0.854	0.
−0.2	3.863 (6)	7.889	56903	8.761	+0.631	0.
−0.4	4.672 (6)	7.862	50830	8.758	+0.355	0.
−0.6	6.381 (6)	7.824	45478	8.755	−0.002	0.
−0.8	1.115 (7)	7.762	40593	8.752	−0.532	0.
−1.0	2.431 (7)	7.676	36285	8.749	−1.242	0.
−1.2	4.912 (7)	7.590	32441	8.747	−1.985	0.
−1.4	8.664 (7)	7.508	28968	8.745	−2.702	0.
−1.6	1.390 (8)	7.424	25864	8.743	−3.356	0.
−1.8	2.121 (8)	7.337	23118	8.741	−3.958	0.
−2.0	3.084 (8)	7.249	20619	8.740	−4.505	0.
−2.2	4.380 (8)	7.158	18412	8.739	−5.050	0.
−2.4	6.057 (8)	7.068	16434	8.738	−5.585	0.
−2.6	8.168 (8)	6.980	14668	8.737	−6.103	0.
−2.8	1.091 (9)	6.892	13074	8.736	−6.622	0.
−3.0	1.516 (9)	6.808	11650	8.736	−7.172	0.109
−3.2	2.205 (9)	6.716	10409	8.735	...	0.376
−3.4	3.037 (9)	6.625	9272	8.735	...	0.602
−3.6	3.949 (9)	6.529	8261	8.734	...	0.783
−3.8	5.048 (9)	6.425	7380	8.734	...	0.899
−4.0	6.161 (9)	6.318	6575	8.734	...	0.962
−4.2	7.291 (9)	6.207	5857	8.733	...	0.988
−4.4	8.490 (9)	6.083	5221	8.733	...	1.000
−4.6	9.597 (9)	5.947	4653	8.733	...	1.000

TABLE A.15
c12500 SUMMARY LISTING

$\log(L/L_\odot)$	Age	$\log(T_c)$	$T_{\rm eff}$	$\log(R_\star)$	$\log(L_\nu/L_\odot)$	$M_{\rm xtal}/M_\star$
+0.6	2.697 (6)	7.964	88915	8.776	+1.450	0.
+0.4	3.075 (6)	7.994	87047	8.741	+1.492	0.
+0.2	4.018 (6)	8.045	82325	8.673	+1.518	0.
0.0	5.191 (6)	8.072	75672	8.613	+1.395	0.
−0.2	6.063 (6)	8.038	68078	8.593	+1.019	0.
−0.4	7.652 (6)	7.952	60642	8.599	+0.414	0.
−0.6	1.331 (7)	7.835	54160	8.603	−0.354	0.
−0.8	2.732 (7)	7.727	48459	8.599	−1.139	0.
−1.0	5.035 (7)	7.637	43239	8.597	−1.865	0.
−1.2	8.469 (7)	7.547	38647	8.595	−2.545	0.
−1.4	1.323 (8)	7.454	34487	8.593	−3.167	0.
−1.6	1.926 (8)	7.365	30804	8.592	−3.720	0.
−1.8	2.717 (8)	7.274	27446	8.591	−4.262	0.
−2.0	3.716 (8)	7.186	24513	8.590	−4.786	0.
−2.2	4.995 (8)	7.100	21875	8.590	−5.307	0.
−2.4	7.115 (8)	7.013	19510	8.589	−5.813	0.168
−2.6	1.020 (9)	6.924	17379	8.588	−6.327	0.391
−2.8	1.361 (9)	6.834	15517	8.588	−6.887	0.599
−3.0	1.763 (9)	6.748	13822	8.587	−9.701	0.744
−3.2	2.206 (9)	6.660	12322	8.587	...	0.854
−3.4	2.681 (9)	6.571	10995	8.587	...	0.925
−3.6	3.194 (9)	6.478	9799	8.586	...	0.963
−3.8	3.769 (9)	6.377	8736	8.586	...	0.980
−4.0	4.341 (9)	6.270	7784	8.586	...	0.994
−4.2	4.899 (9)	6.154	6940	8.586	...	1.000
−4.4	5.390 (9)	6.035	6192	8.586	...	0.999
−4.6	5.799 (9)	5.921	5517	8.586	...	1.000

TABLE A.16
o4400 SUMMARY LISTING

$\log(L/L_\odot)$	Age	$\log(T_c)$	$T_{\rm eff}$	$\log(R_\star)$	$\log(L_\nu/L_\odot)$	$M_{\rm xtal}/M_\star$
+1.0	2.735 (6)	7.824	66842	9.247	+0.105	0.
+0.8	3.153 (6)	7.839	60330	9.207	+0.118	0.
+0.6	3.599 (6)	7.850	55257	9.182	+0.101	0.
+0.4	4.184 (6)	7.855	50581	9.163	+0.056	0.
+0.2	4.997 (6)	7.855	46020	9.143	−0.019	0.
0.0	6.061 (6)	7.847	41874	9.126	−0.126	0.
−0.2	7.482 (6)	7.829	37942	9.112	−0.261	0.
−0.4	9.390 (6)	7.805	34305	9.100	−0.419	0.
−0.6	1.200 (7)	7.775	30948	9.088	−0.602	0.
−0.8	1.572 (7)	7.741	27886	9.078	−0.818	0.
−1.0	2.120 (7)	7.703	25102	9.069	−1.072	0.
−1.2	2.934 (7)	7.660	22578	9.062	−1.373	0.
−1.4	4.176 (7)	7.609	20252	9.055	−1.735	0.
−1.6	6.111 (7)	7.549	18204	9.049	−2.174	0.
−1.8	8.983 (7)	7.484	16312	9.045	−2.682	0.
−2.0	1.298 (8)	7.417	14651	9.038	−3.238	0.
−2.2	1.846 (8)	7.348	13134	9.033	−3.831	0.
−2.4	2.603 (8)	7.277	11751	9.029	−4.449	0.
−2.6	3.653 (8)	7.203	10518	9.026	−5.065	0.
−2.8	5.162 (8)	7.121	9404	9.024	−5.666	0.
−3.0	7.251 (8)	7.034	8397	9.020	−6.239	0.
−3.2	1.000 (9)	6.942	7508	9.019	−6.794	0.
−3.4	1.353 (9)	6.851	6701	9.017	−7.330	0.
−3.6	1.816 (9)	6.757	5981	9.015	...	0.
−3.8	2.433 (9)	6.658	5339	9.014	...	0.
−4.0	3.460 (9)	6.547	4772	9.012	...	0.089
−4.2	5.125 (9)	6.419	4256	9.011	...	0.549
−4.4	6.777 (9)	6.302	3799	9.010	...	0.814
−4.6	8.428 (9)	6.189	3388	9.010	...	0.934
−4.8	1.051(10)	6.050	3020	9.010	...	0.989
−5.0	1.274(10)	5.904	2688	9.010	...	1.000

TABLE A.17
o5400 SUMMARY LISTING

$\log(L/L_\odot)$	Age	$\log(T_c)$	$T_{\rm eff}$	$\log(R_\star)$	$\log(L_\nu/L_\odot)$	$M_{\rm xtal}/M_\star$
+1.0	3.188 (6)	7.912	74192	9.124	+0.880	0.
+0.8	3.517 (6)	7.896	67753	9.103	+0.778	0.
+0.6	3.959 (6)	7.877	61517	9.084	+0.645	0.
+0.4	4.517 (6)	7.857	55565	9.068	+0.494	0.
+0.2	5.194 (6)	7.836	50112	9.055	+0.334	0.
0.0	6.068 (6)	7.814	45089	9.044	+0.162	0.
−0.2	7.230 (6)	7.792	40447	9.034	−0.023	0.
−0.5	8.829 (6)	7.767	36230	9.026	−0.225	0.
−0.7	1.114 (7)	7.740	32488	9.018	−0.452	0.
−0.9	1.464 (7)	7.710	29048	9.011	−0.714	0.
−1.1	2.019 (7)	7.673	25971	9.005	−1.024	0.
−1.3	2.939 (7)	7.628	23163	9.000	−1.402	0.
−1.5	4.555 (7)	7.570	20704	8.995	−1.881	0.
−1.7	7.242 (7)	7.502	18439	8.991	−2.457	0.
−1.9	1.123 (8)	7.431	16456	8.987	−3.087	0.
−2.1	1.693 (8)	7.356	14658	8.983	−3.750	0.
−2.3	2.517 (8)	7.278	13064	8.979	−4.431	0.
−2.5	3.717 (8)	7.190	11647	8.976	−5.096	0.
−2.7	5.354 (8)	7.099	10351	8.974	−5.700	0.
−2.9	7.521 (8)	7.004	9208	8.972	−6.275	0.
−3.1	1.032 (9)	6.910	8195	8.970	−6.835	0.
−3.3	1.394 (9)	6.817	7282	8.969	−7.405	0.
−3.6	1.882 (9)	6.720	6473	8.968	−9.949	0.
−3.8	2.632 (9)	6.627	5757	8.967	...	0.103
−4.0	4.116 (9)	6.500	5109	8.966	...	0.546
−4.2	5.756 (9)	6.361	4544	8.965	...	0.845
−4.4	7.224 (9)	6.239	4034	8.964	...	0.950
−4.6	8.734 (9)	6.122	3583	8.964	...	0.988
−4.8	1.074(10)	5.974	3179	8.964	...	1.000

TABLE A.18
o6400 SUMMARY LISTING

$\log(L/L_\odot)$	Age	$\log(T_c)$	$T_{\rm eff}$	$\log(R_\star)$	$\log(L_\nu/L_\odot)$	$M_{\rm xtal}/M_\star$
+1.0	2.977 (6)	7.922	84069	9.039	+1.272	0.
+0.8	3.328 (6)	7.885	74402	9.016	+1.048	0.
+0.6	3.646 (6)	7.863	67293	9.003	+0.875	0.
+0.4	4.034 (6)	7.843	60687	8.994	+0.705	0.
+0.2	4.547 (6)	7.822	54331	8.984	+0.524	0.
0.0	5.206 (6)	7.802	48630	8.976	+0.337	0.
−0.2	6.094 (6)	7.782	43556	8.969	+0.140	0.
−0.5	7.369 (6)	7.761	38966	8.963	−0.076	0.
−0.7	9.312 (6)	7.737	34766	8.958	−0.323	0.
−0.9	1.245 (7)	7.707	31004	8.954	−0.615	0.
−1.1	1.790 (7)	7.669	27655	8.949	−0.973	0.
−1.3	2.817 (7)	7.619	24666	8.946	−1.437	0.
−1.5	4.789 (7)	7.551	22004	8.942	−2.038	0.
−1.7	8.010 (7)	7.475	19581	8.939	−2.721	0.
−1.9	1.263 (8)	7.398	17426	8.936	−3.418	0.
−2.1	1.908 (8)	7.320	15516	8.933	−4.089	0.
−2.3	2.812 (8)	7.238	13826	8.931	−4.705	0.
−2.5	4.079 (8)	7.150	12307	8.929	−5.274	0.
−2.7	5.801 (8)	7.060	10940	8.927	−5.822	0.
−2.9	8.088 (8)	6.968	9715	8.926	−6.366	0.
−3.1	1.111 (9)	6.876	8644	8.925	−6.913	0.
−3.3	1.514 (9)	6.782	7685	8.924	−7.649	0.
−3.6	2.191 (9)	6.689	6816	8.923	−9.966	0.147
−3.8	3.327 (9)	6.581	6064	8.922	...	0.520
−4.0	4.609 (9)	6.467	5378	8.921	...	0.789
−4.2	6.196 (9)	6.326	4778	8.921	...	0.939
−4.4	7.652 (9)	6.198	4244	8.920	...	0.985
−4.6	9.171 (9)	6.072	3770	8.920	...	1.000
−4.8	1.087(10)	5.937	3349	8.920	...	1.000

TABLE A.19
o7400 SUMMARY LISTING

$\log(L/L_\odot)$	Age	$\log(T_c)$	$T_{\rm eff}$	$\log(R_\star)$	$\log(L_\nu/L_\odot)$	$M_{\rm xtal}/M_\star$
+1.0	3.250 (6)	7.912	89446	8.961	+1.401	0.
+0.8	3.440 (6)	7.888	80575	8.950	+1.203	0.
+0.6	3.672 (6)	7.868	72607	8.942	+1.024	0.
+0.4	3.983 (6)	7.848	65026	8.934	+0.844	0.
+0.2	4.377 (6)	7.829	58113	8.927	+0.660	0.
0.0	4.881 (6)	7.810	51945	8.921	+0.470	0.
−0.2	5.588 (6)	7.792	46385	8.916	+0.267	0.
−0.5	6.656 (6)	7.771	41364	8.911	+0.038	0.
−0.7	8.371 (6)	7.746	36899	8.907	−0.228	0.
−0.9	1.135 (7)	7.716	32905	8.903	−0.551	0.
−1.1	1.716 (7)	7.673	29317	8.900	−0.968	0.
−1.3	2.972 (7)	7.613	26101	8.897	−1.538	0.
−1.5	5.401 (7)	7.535	23246	8.894	−2.238	0.
−1.7	9.117 (7)	7.455	20674	8.892	−2.959	0.
−1.9	1.433 (8)	7.375	18378	8.890	−3.645	0.
−2.1	2.167 (8)	7.293	16361	8.887	−4.273	0.
−2.3	3.202 (8)	7.204	14554	8.885	−4.854	0.
−2.5	4.616 (8)	7.113	12954	8.883	−5.412	0.
−2.7	6.480 (8)	7.021	11510	8.882	−5.961	0.
−2.9	8.923 (8)	6.928	10231	8.881	−6.505	0.
−3.1	1.214 (9)	6.836	9092	8.880	−7.025	0.
−3.3	1.780 (9)	6.745	8085	8.879	−9.952	0.210
−3.6	2.649 (9)	6.643	7179	8.879	...	0.549
−3.8	3.642 (9)	6.536	6369	8.878	...	0.783
−4.0	4.752 (9)	6.425	5657	8.878	...	0.914
−4.2	6.193 (9)	6.289	5033	8.877	...	0.980
−4.4	7.651 (9)	6.146	4466	8.877	...	0.995
−4.6	9.021 (9)	6.012	3966	8.877	...	1.000
−4.8	1.044(10)	5.864	3515	8.877	...	1.000

TABLE A.20
o8400 SUMMARY LISTING

$\log(L/L_\odot)$	Age	$\log(T_c)$	$T_{\rm eff}$	$\log(R_\star)$	$\log(L_\nu/L_\odot)$	$M_{\rm xtal}/M_\star$
+1.0	3.166 (6)	7.934	96681	8.900	+1.561	0.
+0.8	3.324 (6)	7.908	86076	8.889	+1.336	0.
+0.6	3.489 (6)	7.889	77463	8.883	+1.153	0.
+0.4	3.718 (6)	7.872	69427	8.878	+0.974	0.
+0.2	4.031 (6)	7.853	61940	8.872	+0.789	0.
0.0	4.446 (6)	7.834	55192	8.868	+0.593	0.
−0.2	5.027 (6)	7.814	49201	8.863	+0.381	0.
−0.5	5.948 (6)	7.793	43829	8.860	+0.138	0.
−0.7	7.553 (6)	7.767	39039	8.857	−0.153	0.
−0.9	1.065 (7)	7.731	34847	8.854	−0.523	0.
−1.1	1.775 (7)	7.677	30993	8.851	−1.035	0.
−1.3	3.444 (7)	7.600	27591	8.848	−1.729	0.
−1.5	6.370 (7)	7.516	24564	8.846	−2.480	0.
−1.7	1.058 (8)	7.434	21864	8.844	−3.191	0.
−1.9	1.650 (8)	7.351	19448	8.842	−3.840	0.
−2.1	2.482 (8)	7.262	17269	8.840	−4.433	0.
−2.3	3.616 (8)	7.170	15375	8.838	−4.997	0.
−2.5	5.116 (8)	7.077	13660	8.837	−5.548	0.
−2.7	7.075 (8)	6.985	12157	8.836	−6.092	0.
−2.9	9.640 (8)	6.894	10785	8.835	−6.633	0.
−3.1	1.430 (9)	6.802	9584	8.834	−7.250	0.258
−3.3	2.095 (9)	6.705	8507	8.834	−9.999	0.561
−3.6	2.901 (9)	6.605	7559	8.833	...	0.782
−3.8	3.779 (9)	6.498	6717	8.833	...	0.908
−4.0	4.779 (9)	6.386	5966	8.832	...	0.969
−4.2	5.977 (9)	6.261	5288	8.832	...	0.991
−4.4	7.397 (9)	6.104	4702	8.832	...	1.000
−4.6	8.595 (9)	5.957	4173	8.832	...	1.000
−4.8	9.597 (9)	5.814	3705	8.832	...	1.000

TABLE A.21
o9400 SUMMARY LISTING

$\log(L/L_\odot)$	Age	$\log(T_c)$	$T_{\rm eff}$	$\log(R_\star)$	$\log(L_\nu/L_\odot)$	$M_{\rm xtal}/M_\star$
+1.0	3.071 (6)	7.973	105651	8.842	+1.745	0.
+0.8	3.216 (6)	7.943	92392	8.831	+1.480	0.
+0.6	3.346 (6)	7.923	82328	8.825	+1.277	0.
+0.4	3.506 (6)	7.906	73880	8.821	+1.100	0.
+0.2	3.746 (6)	7.889	66055	8.817	+0.916	0.
0.0	4.100 (6)	7.870	58856	8.813	+0.714	0.
−0.2	4.611 (6)	7.849	52382	8.810	+0.489	0.
−0.5	5.429 (6)	7.825	46633	8.807	+0.228	0.
−0.7	7.012 (6)	7.793	41527	8.804	−0.098	0.
−0.9	1.068 (7)	7.746	37003	8.801	−0.545	0.
−1.1	2.072 (7)	7.673	32903	8.799	−1.198	0.
−1.3	4.265 (7)	7.584	29287	8.796	−1.977	0.
−1.5	7.651 (7)	7.497	26051	8.794	−2.724	0.
−1.7	1.242 (8)	7.411	23181	8.793	−3.400	0.
−1.9	1.907 (8)	7.321	20594	8.791	−4.010	0.
−2.1	2.807 (8)	7.229	18323	8.790	−4.577	0.
−2.3	3.998 (8)	7.137	16298	8.788	−5.129	0.
−2.5	5.557 (8)	7.044	14462	8.787	−5.674	0.
−2.7	7.643 (8)	6.961	12857	8.787	−6.207	0.019
−2.9	1.166 (9)	6.862	11417	8.786	−6.739	0.313
−3.1	1.655 (9)	6.766	10152	8.785	−8.849	0.594
−3.3	2.230 (9)	6.671	9003	8.785	...	0.783
−3.6	2.892 (9)	6.572	8007	8.784	...	0.896
−3.8	3.682 (9)	6.464	7109	8.784	...	0.956
−4.0	4.582 (9)	6.350	6301	8.784	...	0.991
−4.2	5.572 (9)	6.231	5598	8.783	...	1.000
−4.4	6.792 (9)	6.073	4971	8.783	...	1.000
−4.6	7.792 (9)	5.911	4415	8.783	...	1.000
−4.8	8.413 (9)	5.793	3912	8.784	...	1.000

TABLE A.22

o10500 SUMMARY LISTING

$\log(L/L_\odot)$	Age	$\log(T_c)$	$T_{\rm eff}$	$\log(R_\star)$	$\log(L_\nu/L_\odot)$	$M_{\rm xtal}/M_\star$
−0.2	5.242 (6)	7.926	57901	8.751	+0.789	0.
−0.4	5.896 (6)	7.898	53035	8.749	+0.544	0.
−0.6	7.601 (6)	7.845	45904	8.746	+0.083	0.
−0.8	1.117 (7)	7.783	41025	8.744	−0.432	0.
−1.0	2.186 (7)	7.694	36660	8.741	−1.150	0.
−1.2	4.285 (7)	7.605	32691	8.739	−1.901	0.
−1.4	7.334 (7)	7.523	29211	8.738	−2.573	0.
−1.6	1.143 (8)	7.445	26065	8.736	−3.152	0.
−1.8	1.701 (8)	7.367	23261	8.735	−3.672	0.
−2.0	2.478 (8)	7.286	20748	8.734	−4.172	0.
−2.2	3.562 (8)	7.199	18543	8.733	−4.684	0.
−2.4	5.032 (8)	7.111	16536	8.732	−5.209	0.
−2.6	7.140 (8)	7.027	14741	8.731	−5.728	0.061
−2.8	1.089 (9)	6.932	13158	8.731	−6.260	0.351
−3.0	1.537 (9)	6.839	11746	8.730	−6.796	0.605
−3.2	2.038 (9)	6.747	10460	8.730	...	0.777
−3.4	2.608 (9)	6.654	9337	8.729	...	0.884
−3.6	3.271 (9)	6.556	8315	8.729	...	0.952
−3.8	4.041 (9)	6.452	7418	8.729	...	0.983
−4.0	4.897 (9)	6.341	6605	8.728	...	0.997
−4.2	5.797 (9)	6.226	5890	8.728	...	1.000
−4.4	6.769 (9)	6.097	5259	8.728	...	1.000
−4.6	7.713 (9)	5.942	4680	8.728	...	1.000

TABLE A.23

o12500 SUMMARY LISTING

$\log(L/L_\odot)$	Age	$\log(T_c)$	$T_{\rm eff}$	$\log(R_\star)$	$\log(L_\nu/L_\odot)$	$M_{\rm xtal}/M_\star$
0.0	5.239 (6)	8.083	77241	8.599	+1.422	0.
−0.2	5.624 (6)	8.055	71314	8.598	+1.161	0.
−0.4	6.894 (6)	7.985	61654	8.595	+0.592	0.
−0.6	1.019 (7)	7.884	54845	8.592	−0.106	0.
−0.8	2.116 (7)	7.760	48969	8.590	−0.930	0.
−1.0	3.997 (7)	7.663	43768	8.588	−1.647	0.
−1.2	6.703 (7)	7.577	39062	8.586	−2.270	0.
−1.4	1.041 (8)	7.494	34864	8.585	−2.823	0.
−1.6	1.549 (8)	7.408	31095	8.584	−3.351	0.
−1.8	2.240 (8)	7.319	27752	8.583	−3.880	0.
−2.0	3.285 (8)	7.235	24786	8.582	−4.400	0.101
−2.2	5.085 (8)	7.139	22109	8.581	−4.934	0.355
−2.4	7.224 (8)	7.045	19702	8.580	−5.478	0.586
−2.6	9.493 (8)	6.953	17574	8.580	−6.012	0.751
−2.8	1.204 (9)	6.863	15676	8.579	−6.543	0.859
−3.0	1.482 (9)	6.774	13974	8.579	−7.384	0.932
−3.2	1.796 (9)	6.684	12453	8.579	...	0.970
−3.4	2.146 (9)	6.592	11109	8.579	...	0.983
−3.6	2.538 (9)	6.495	9900	8.578	...	0.989
−3.8	2.971 (9)	6.392	8816	8.578	...	1.000
−4.0	3.424 (9)	6.279	7865	8.578	...	1.000
−4.2	3.860 (9)	6.158	7010	8.578	...	1.000
−4.4	4.239 (9)	6.030	6246	8.578	...	1.000

TABLE A.24

c6200 ABBREVIATED SUMMARY LISTING

$\log(L/L_\odot)$	Age	$\log(T_c)$	$T_{\rm eff}$	$\log(R_\star)$	$\log(L_\nu/L_\odot)$	$M_{\rm xtal}/M_\star$
+1.0	2.808 (6)	7.966	77278	9.093	+1.363	0.
0.0	5.596 (6)	7.820	48214	9.003	+0.408	0.
−1.0	2.162 (7)	7.663	28322	8.965	−1.074	0.
−2.0	1.921 (8)	7.256	16321	8.944	−4.723	0.
−3.0	8.618 (8)	6.839	9272	8.934	−7.301	0.
−4.0	4.643 (9)	6.365	5230	8.933	...	0.527
−4.2	6.608 (9)	6.220	4628	8.937	...	0.838
−4.4	8.195 (9)	6.087	4157	8.932	...	0.953
−4.6	9.422 (9)	5.986	3664	8.941	...	0.981
−4.8	1.097(10)	5.859	3245	8.946	...	0.980
−5.0	1.249(10)	5.722	2886	8.949	...	0.980

TABLE A.25

c6300 ABBREVIATED SUMMARY LISTING

$\log(L/L_\odot)$	Age	$\log(T_c)$	$T_{\rm eff}$	$\log(R_\star)$	$\log(L_\nu/L_\odot)$	$M_{\rm xtal}/M_\star$
+1.0	2.779 (6)	7.958	78599	9.079	+1.349	0.
0.0	5.410 (6)	7.818	48387	9.000	+0.410	0.
−1.0	1.817 (7)	7.684	28348	8.964	−0.855	0.
−2.0	2.019 (8)	7.297	16339	8.942	−4.351	0.
−3.0	9.544 (8)	6.866	9309	8.932	−7.101	0.
−4.0	4.863 (9)	6.390	5253	8.928	...	0.445
−4.2	7.013 (9)	6.248	4676	8.929	...	0.794
−4.4	8.773 (9)	6.123	4179	8.928	...	0.935
−4.6	1.026(10)	6.018	3712	8.929	...	0.974
−4.8	1.206(10)	5.893	3306	8.930	...	0.989
−5.0	1.395(10)	5.747	2941	8.931	...	1.000
−5.2	1.551(10)	5.605	2623	8.932	...	1.000
−5.4	1.668(10)	5.483	2327	8.935	...	1.000
−5.6	1.764(10)	5.364	2071	8.937	...	1.000
−5.8	1.850(10)	5.219	1830	8.944	...	1.000

TABLE A.26

o6200 ABBREVIATED SUMMARY LISTING

$\log(L/L_\odot)$	Age	$\log(T_c)$	$T_{\rm eff}$	$\log(R_\star)$	$\log(L_\nu/L_\odot)$	$M_{\rm xtal}/M_\star$
+1.0	2.953 (6)	7.924	82203	9.061	+1.283	0.
0.0	5.038 (6)	7.807	48869	8.990	+0.383	0.
−1.0	1.684 (7)	7.675	28535	8.958	−0.937	0.
−2.0	1.660 (8)	7.285	16421	8.939	−4.435	0.
−3.0	7.562 (8)	6.859	9332	8.929	−7.036	0.
−4.0	3.993 (9)	6.367	5265	8.926	...	0.908
−4.2	5.271 (9)	6.209	4685	8.928	...	0.984
−4.4	6.328 (9)	6.071	4181	8.926	...	0.990
−4.6	7.191 (9)	5.967	3707	8.931	...	0.990
−4.8	8.140 (9)	5.861	3280	8.937	...	0.990
−5.0	9.295 (9)	5.729	2913	8.940	...	0.990
−5.2	1.018(10)	5.618	2589	8.943	...	0.990
−5.4	1.111(10)	5.496	2292	8.947	...	0.990
−5.6	1.184(10)	5.395	2032	8.953	...	0.990

TABLE A.27

o6300 ABBREVIATED SUMMARY LISTING

$\log(L/L_\odot)$	Age	$\log(T_c)$	$T_{\rm eff}$	$\log(R_\star)$	$\log(L_\nu/L_\odot)$	$M_{\rm xtal}/M_\star$
+1.0	2.976 (6)	7.922	83473	9.045	+1.273	0.
0.0	5.073 (6)	7.806	49288	8.983	+0.372	0.
−1.0	1.565 (7)	7.683	28657	8.954	−0.840	0.
−2.0	1.654 (8)	7.336	16460	8.936	−3.980	0.
−3.0	8.488 (8)	6.897	9355	8.926	−6.802	0.
−4.0	4.392 (9)	6.406	5287	8.922	...	0.872
−4.2	5.792 (9)	6.259	4719	8.922	...	0.970
−4.4	7.046 (9)	6.124	4207	8.921	...	0.989
−4.6	8.347 (9)	5.986	3746	8.921	...	1.000
−4.8	9.466 (9)	5.865	3336	8.922	...	1.000
−5.0	1.074(10)	5.720	2977	8.922	...	1.000
−5.2	1.167(10)	5.603	2643	8.925	...	1.000
−5.4	1.256(10)	5.474	2357	8.924	...	1.000

TABLE A.28

c6204 ABBREVIATED SUMMARY LISTING

$\log(L/L_\odot)$	Age	$\log(T_c)$	$T_{\rm eff}$	$\log(R_\star)$	$\log(L_\nu/L_\odot)$	$M_{\rm xtal}/M_\star$
+1.0	2.772 (6)	7.966	73955	9.132	+1.373	0.
0.0	5.510 (6)	7.820	46411	9.036	+0.412	0.
−1.0	2.139 (7)	7.663	27383	8.995	−1.070	0.
−2.0	1.921 (8)	7.254	15878	8.967	−4.736	0.
−3.0	8.424 (8)	6.849	9076	8.953	−7.197	0.
−4.0	4.641 (9)	6.405	5155	8.944	...	0.396
−4.2	7.059 (9)	6.245	4580	8.947	...	0.797
−4.4	8.911 (9)	6.106	4112	8.941	...	0.942
−4.6	1.043(10)	5.986	3624	8.951	...	0.977
−4.8	1.205(10)	5.842	3224	8.953	...	0.977
−5.0	1.340(10)	5.718	2859	8.957	...	0.977
−5.2	1.450(10)	5.618	2530	8.962	...	0.977
−5.4	1.568(10)	5.500	2237	8.970	...	0.977

TABLE A.29

c6310 ABBREVIATED SUMMARY LISTING

$\log(L/L_\odot)$	Age	$\log(T_c)$	$T_{\rm eff}$	$\log(R_\star)$	$\log(L_\nu/L_\odot)$	$M_{\rm xtal}/M_\star$
+1.0	2.808 (6)	7.961	78291	9.082	+1.349	0.
0.0	5.570 (6)	7.819	48318	9.001	+0.408	0.
−1.0	1.881 (7)	7.683	28286	8.966	−0.857	0.
−2.0	2.055 (8)	7.296	16297	8.944	−4.358	0.
−3.0	9.632 (8)	6.866	9286	8.934	−7.102	0.
−4.0	5.328 (9)	6.365	5259	8.928	...	0.523
−4.2	7.185 (9)	6.232	4685	8.928	...	0.820
−4.4	8.825 (9)	6.108	4175	8.927	...	0.941
−4.6	1.024(10)	6.003	3717	8.929	...	0.981
−4.8	1.204(10)	5.866	3309	8.930	...	0.995
−5.0	1.374(10)	5.722	2944	8.931	...	0.995
−5.2	1.501(10)	5.604	2621	8.933	...	0.995
−5.4	1.614(10)	5.492	2329	8.935	...	0.995
−5.6	1.714(10)	5.380	2071	8.936	...	0.995

TABLE A.30

C6410 ABBREVIATED SUMMARY LISTING

$\log(L/L_\odot)$	Age	$\log(T_c)$	$T_{\rm eff}$	$\log(R_\star)$	$\log(L_\nu/L_\odot)$	$M_{\rm xtal}/M_\star$
+1.0	2.807 (6)	7.960	79043	9.073	+1.348	0.
0.0	5.602 (6)	7.817	48565	8.997	+0.397	0.
−1.0	1.828 (7)	7.687	28424	8.963	−0.831	0.
−2.0	1.951 (8)	7.342	16327	8.943	−3.922	0.
−3.0	1.061 (9)	6.900	9284	8.933	−6.891	0.
−4.0	5.480 (9)	6.402	5266	8.926	...	0.409
−4.2	7.659 (9)	6.268	4697	8.925	...	0.760
−4.4	9.510 (9)	6.151	4189	8.925	...	0.911
−4.6	1.127(10)	6.039	3730	8.925	...	0.971
−4.8	1.324(10)	5.913	3328	8.925	...	0.993
−5.0	1.512(10)	5.790	2965	8.924	...	0.999
−5.2	1.717(10)	5.639	2643	8.925	...	1.000
−5.4	1.881(10)	5.474	2357	8.925	...	1.000
−5.6	1.980(10)	5.353	2100	8.926	...	1.000
−5.8	2.055(10)	5.218	1866	8.928	...	1.000
−6.0	2.123(10)	5.066	1657	8.931	...	1.000

TABLE A.31

C6400D ABBREVIATED SUMMARY LISTING

$\log(L/L_\odot)$	Age	$\log(T_c)$	$T_{\rm eff}$	$\log(R_\star)$	$\log(L_\nu/L_\odot)$	$M_{\rm xtal}/M_\star$
+1.0	2.807 (6)	7.960	79277	9.072	+1.348	0.
0.0	5.599 (6)	7.817	48586	8.996	+0.397	0.
−1.0	1.825 (7)	7.687	28439	8.962	−0.830	0.
−2.0	1.949 (8)	7.343	16373	8.942	−3.905	0.
−3.0	1.063 (9)	6.902	9309	8.930	−6.881	0.
−4.0	5.216 (9)	6.422	5270	8.926	...	0.341
−4.2	7.527 (9)	6.285	4697	8.925	...	0.731
−4.4	9.576 (9)	6.162	4189	8.925	...	0.900
−4.6	1.125(10)	6.060	3730	8.925	...	0.967
−4.8	1.375(10)	5.908	3325	8.925	...	0.997
−5.0	1.529(10)	5.811	2963	8.925	...	1.000
−5.2	1.812(10)	5.572	2638	8.926	...	1.000
−5.4	1.904(10)	5.478	2351	8.927	...	1.000
−5.6	2.002(10)	5.341	2091	8.928	...	1.000

TABLE A.32

X4410B SUMMARY LISTING

$\log(L/L_\odot)$	Age	$\log(T_c)$	$T_{\rm eff}$	$\log(R_\star)$	$\log(L_\nu/L_\odot)$	$M_{\rm xtal}/M_\star$
+1.0	2.924 (6)	8.258	54913	9.389	+0.472	0.
+0.8	4.038 (6)	8.205	53407	9.314	+0.527	0.
+0.6	5.262 (6)	8.124	50747	9.258	+0.492	0.
+0.4	6.601 (6)	8.036	47569	9.215	+0.376	0.
+0.2	8.121 (6)	7.966	43969	9.183	+0.211	0.
0.0	9.903 (6)	7.910	40328	9.157	+0.029	0.
−0.2	1.205 (7)	7.862	36821	9.137	−0.167	0.
−0.4	1.470 (7)	7.821	33449	9.120	−0.371	0.
−0.6	1.807 (7)	7.781	30325	9.107	−0.583	0.
−0.8	2.255 (7)	7.743	27374	9.095	−0.811	0.
−1.0	2.881 (7)	7.704	24665	9.084	−1.066	0.
−1.2	3.794 (7)	7.660	22249	9.075	−1.360	0.
−1.4	5.168 (7)	7.610	19993	9.067	−1.708	0.
−1.6	7.306 (7)	7.552	17983	9.060	−2.133	0.
−1.8	1.060 (8)	7.485	16142	9.054	−2.652	0.
−2.0	1.545 (8)	7.412	14482	9.048	−3.254	0.
−2.2	2.208 (8)	7.337	12970	9.044	−3.919	0.
−2.4	3.098 (8)	7.259	11614	9.039	−4.614	0.
−2.6	4.287 (8)	7.179	10386	9.035	−5.281	0.
−2.8	5.889 (8)	7.094	9299	9.032	−5.887	0.
−3.0	8.008 (8)	7.007	8334	9.028	−6.441	0.
−3.2	1.086 (9)	6.916	7450	9.025	−6.997	0.
−3.4	1.443 (9)	6.827	6652	9.022	−7.545	0.
−3.6	1.904 (9)	6.738	5946	9.020	...	0.
−3.8	2.703 (9)	6.614	5322	9.017	...	0.
−4.0	3.694 (9)	6.506	4760	9.016	...	0.085
−4.2	5.241 (9)	6.381	4233	9.015	...	0.521
−4.4	6.669 (9)	6.270	3778	9.015	...	0.657
−4.6	8.515 (9)	6.152	3369	9.014	...	0.790
−4.8	1.061(10)	6.036	2999	9.015	...	0.893
−5.0	1.289(10)	5.920	2677	9.015	...	0.966
−5.2	1.530(10)	5.802	2380	9.015	...	0.974
−5.4	1.850(10)	5.639	2118	9.016	...	1.000

TABLE A.33
X6410B SUMMARY LISTING

$\log(L/L_\odot)$	Age	$\log(T_c)$	$T_{\rm eff}$	$\log(R_*)$	$\log(L_\nu/L_\odot)$	$M_{\rm xtal}/M_*$
+1.0	2.632 (6)	7.945	79857	9.067	+1.331	0.
+0.8	2.982 (6)	7.905	72759	9.045	+1.133	0.
+0.6	3.395 (6)	7.873	66080	9.028	+0.941	0.
+0.4	3.897 (6)	7.848	59831	9.014	+0.752	0.
+0.2	4.524 (6)	7.824	54026	9.003	+0.561	0.
0.0	5.319 (6)	7.803	48731	8.993	+0.366	0.
−0.2	6.348 (6)	7.783	43905	8.985	+0.166	0.
−0.4	7.722 (6)	7.762	39434	8.978	−0.045	0.
−0.6	9.659 (6)	7.739	35371	8.971	−0.274	0.
−0.8	1.259 (7)	7.714	31774	8.965	−0.535	0.
−1.0	1.738 (7)	7.682	28475	8.960	−0.847	0.
−1.2	2.593 (7)	7.638	25509	8.955	−1.243	0.
−1.4	4.218 (7)	7.580	22867	8.951	−1.763	0.
−1.6	7.135 (7)	7.507	20463	8.948	−2.414	0.
−1.8	1.161 (8)	7.428	18304	8.944	−3.143	0.
−2.0	1.792 (8)	7.344	16354	8.941	−3.891	0.
−2.2	2.638 (8)	7.259	14647	8.938	−4.578	0.
−2.4	3.791 (8)	7.169	13078	8.936	−5.198	0.
−2.6	5.269 (8)	7.079	11685	8.934	−5.755	0.
−2.8	7.135 (8)	6.991	10432	8.932	−6.280	0.
−3.0	9.567 (8)	6.904	9314	8.931	−6.800	0.
−3.2	1.272 (9)	6.816	8318	8.929	−7.357	0.
−3.4	1.685 (9)	6.728	7415	8.928	...	0.
−3.6	2.345 (9)	6.647	6625	8.927	...	0.148
−3.8	3.458 (9)	6.547	5906	8.926	...	0.491
−4.0	5.057 (9)	6.397	5279	8.924	...	0.686
−4.2	6.602 (9)	6.266	4712	8.924	...	0.821
−4.4	8.092 (9)	6.151	4194	8.923	...	0.912
−4.6	9.629 (9)	6.039	3743	8.923	...	0.971
−4.8	1.135(10)	5.914	3337	8.923	...	0.993
−5.0	1.303(10)	5.789	2973	8.924	...	0.998
−5.2	1.479(10)	5.641	2645	8.923	...	1.000
−5.4	1.632(10)	5.470	2356	8.924	...	1.000

TABLE A.34
x8410B SUMMARY LISTING

$\log(L/L_\odot)$	Age	$\log(T_c)$	$T_{\rm eff}$	$\log(R_\star)$	$\log(L_\nu/L_\odot)$	$M_{\rm xtal}/M_\star$
+0.8	2.856 (6)	7.911	88236	8.910	+1.444	0.
+0.6	3.099 (6)	7.884	77311	8.898	+1.187	0.
+0.4	3.411 (6)	7.861	68179	8.888	+0.955	0.
+0.2	3.774 (6)	7.845	61573	8.882	+0.777	0.
0.0	4.234 (6)	7.829	55754	8.878	+0.601	0.
−0.2	4.865 (6)	7.811	50004	8.873	+0.394	0.
−0.4	5.800 (6)	7.791	44682	8.869	+0.160	0.
−0.6	7.315 (6)	7.767	39985	8.865	−0.105	0.
−0.8	1.009 (7)	7.737	35795	8.862	−0.438	0.
−1.0	1.601 (7)	7.691	32013	8.858	−0.890	0.
−1.2	2.984 (7)	7.622	28646	8.855	−1.517	0.
−1.4	5.722 (7)	7.538	25616	8.852	−2.284	0.
−1.6	9.877 (7)	7.450	22921	8.849	−3.070	0.
−1.8	1.556 (8)	7.360	20451	8.847	−3.798	0.
−2.0	2.297 (8)	7.270	18277	8.845	−4.423	0.
−2.2	3.255 (8)	7.181	16336	8.843	−4.979	0.
−2.4	4.490 (8)	7.092	14561	8.843	−5.508	0.
−2.6	6.079 (8)	7.005	13013	8.841	−6.024	0.
−2.8	8.161 (8)	6.918	11609	8.840	−6.540	0.
−3.0	1.094 (9)	6.841	10352	8.839	−7.036	0.026
−3.2	1.608 (9)	6.747	9233	8.838	−9.903	0.312
−3.4	2.239 (9)	6.657	8232	8.838	...	0.538
−3.6	2.916 (9)	6.570	7343	8.837	...	0.646
−3.8	3.753 (9)	6.481	6548	8.836	...	0.743
−4.0	5.081 (9)	6.368	5847	8.836	...	0.846
−4.2	6.835 (9)	6.215	5213	8.835	...	0.949
−4.4	8.212 (9)	6.082	4649	8.835	...	0.986
−4.6	9.392 (9)	5.963	4140	8.835	...	0.997

TABLE A.35
X10410B SUMMARY LISTING

$\log(L/L_\odot)$	Age	$\log(T_c)$	$T_{\rm eff}$	$\log(R_\star)$	$\log(L_\nu/L_\odot)$	$M_{\rm xtal}/M_\star$
+1.0	2.465 (6)	8.006	115215	8.790	+1.905	0.
+0.8	2.559 (6)	7.986	103506	8.784	+1.702	0.
+0.6	2.705 (6)	7.961	89473	8.776	+1.437	0.
+0.4	2.872 (6)	7.940	78193	8.770	+1.208	0.
+0.2	3.074 (6)	7.923	69927	8.766	+1.028	0.
0.0	3.371 (6)	7.907	63175	8.762	+0.849	0.
−0.2	3.845 (6)	7.887	56912	8.760	+0.624	0.
−0.4	4.724 (6)	7.858	50900	8.757	+0.323	0.
−0.6	6.651 (6)	7.818	45486	8.754	−0.070	0.
−0.8	1.205 (7)	7.753	40627	8.752	−0.647	0.
−1.0	2.651 (7)	7.660	36345	8.748	−1.424	0.
−1.2	5.210 (7)	7.567	32488	8.746	−2.233	0.
−1.4	8.831 (7)	7.475	29029	8.744	−2.980	0.
−1.6	1.355 (8)	7.385	25899	8.742	−3.617	0.
−1.8	1.960 (8)	7.296	23120	8.741	−4.174	0.
−2.0	2.742 (8)	7.209	20638	8.740	−4.697	0.
−2.2	3.761 (8)	7.121	18431	8.739	−5.212	0.
−2.4	5.086 (8)	7.033	16427	8.738	−5.722	0.
−2.6	7.263 (8)	6.953	14652	8.737	−6.214	0.156
−2.8	1.039 (9)	6.863	13052	8.737	−6.716	0.429
−3.0	1.401 (9)	6.775	11654	8.736	−8.042	0.579
−3.2	1.808 (9)	6.688	10385	8.736	−9.995	0.677
−3.4	2.334 (9)	6.603	9269	8.735	...	0.764
−3.6	2.952 (9)	6.516	8273	8.735	...	0.838
−3.8	3.707 (9)	6.428	7366	8.734	...	0.898
−4.0	4.635 (9)	6.333	6566	8.734	...	0.952
−4.2	5.880 (9)	6.203	5860	8.734	...	0.986
−4.4	7.058 (9)	6.050	5215	8.734	...	0.998

List of Symbols

The following list defines the notation used in this work. Units will either be *c.g.s.*, primarily for thermodynamic quantities, or *solar* for stellar masses, radii, luminosities, etc. Also included in this table are the white dwarf spectral types following Sion *et al.* (1983).

Symbol	Description
a	radiation constant (7.5646×10^{-15} erg cm^{-3} deg^{-4})
A	Atomic Mass
C_V	heat capacity
DA	hydrogen-dominated spectra (DAV $\Rightarrow$ pulsating)
DB	helium-dominated atmosphere (DBV $\Rightarrow$ pulsating)
DO	hottest class of white dwarfs (DOV $\Rightarrow$ pulsating)
DQ	strong carbon features
DZ	strong metal features (other than carbon)
DC	featureless continuum spectra
∇	true temperature gradient
∇_{ad}	adiabatic temperature gradient
∇_{rad}	radiative temperature gradient
ϵ_X	nuclear burning rate of process X
ϵ_ν	neutrino emission rate
η	electron degeneracy parameter
g	local gravity

G	gravitational constant (6.670×10^{-8} dyn cm^2 g^{-2})
h	Plank's constant (6.6262×10^{-27} erg s)
$\hbar$	$h/2\pi$
H	atomic mass unit (1.6604×10^{-24} g)
H_P	pressure scale height
Γ	ratio of Coulomb to thermal energy
Γ_m	Γ at solid/liquid interface
k	Boltzmann constant (1.3806×10^{-16}erg deg^{-1})
κ	total opacity
κ_c	conductive opacity
κ_r	radiative opacity
κ_0	constant in Kramer's opacity law
ℓ	mixing length
L	stellar luminosity
L_r	luminosity within radius r
$L_\odot$	solar luminosity (3.826×10^{33} erg s^{-1})
M	stellar mass
$M_{\rm H}$	hydrogen layer mass
$M_{\rm He}$	helium layer mass
M_r	mass contained within radius r
$M_\odot$	Solar mass (1.989×10^{33} g)
$M_{\rm xtal}$	crystallized mass
μ	mean molecular weight
μ_e	mean molecular weight per electron
$N_{\rm WD}$	number density of white dwarf stars
P_c	central pressure
P_r	relativistic degeneracy pressure

P_{nr}	non-relativistic degeneracy pressure
$\phi(M)$	initial mass function
Φ	luminosity function
$\Psi(t)$	star formation rate
r	radius
R	stellar radius
$R_\odot$	solar radius (6.9559×10^{10} cm)
R_0	galactocentric radius (≈ 8 kpc)
ρ_c	central density
s	entropy
σ	Stephan–Boltzmann constant ($= \frac{ac}{4} = 5.6696 \times 10^{-5}$ erg cm^{-2} deg^{-4} s^{-1})
t	time
$t_{\rm cool}$	white dwarf cooling age
$t_{\rm disk}$	age of the local Galactic disk
$t_{\rm MS}$	main sequence evolutionary timescale
T	temperature
T_c	core temperature
$T_{\rm eff}$	effective temperature
τ	optical depth
X_i	mass fraction of element i
Z	atomic number

REFERENCES

Adams, W. S. 1914, *P.A.S.P.*, **26**, 198.

Adams, W. S. 1915, *P.A.S.P.*, **27**, 236.

Allen, C. W., 1973, *Astrophysical Quantities, Third Ed.*, (The Athlone Press: London).

Anthonny-Twarog, B. J. 1982, *Ap. J.*, **255**, 245.

Arcouragi, J.-P., and Fontaine, G. 1980, *Ap. J.*, **242**, 1208.

Arnett, W. D., Branch, D., and Wheeler, J. C. 1985, *Nature*, **314**, 337.

Bahcall, J. N. 1984, *Ap. J.*, **287**, 926.

Bahcall, J. N. and Soneira, R. M. 1980, *Ap. J. Suppl.*, **44**, 73.

Baglin, A., and Vauclair, G. 1973, *Astron. Astrophys.*, **27**, 307.

Barkat, Z., and Tuchman, Y. 1980, *Ap. J.*, **237**, 105.

Barrat, J. L., Hansen, J. P., and Mochkovitch, R. 1988, *Astron. Astrophys.*, **199**, L15.

Barry, D. C. 1988, *Ap. J.*, **334**, 436.

Barry, D. C., and Scalo, J. M., 1990, in preparation.

Bash, F. H., and Vissar, H. C. D. 1981, *Ap. J.*, **247**, 488.

Beaudet, G., Petrosian, V. and Salpeter, E. E. 1967, *Ap. J.*, **150**, 979.

Beaudet, G., Salpeter, E. E., and Silvestro, M. L. 1972, *Ap. J.*, **174**, 79.

Bergeron, P., Saffer, R. A., and Liebert, J., 1990, *in preparation.*

Bergeron, P., Wesemael, F., Fontaine, G., and Liebert, J., 1990, *Ap. J. (Letters)*, in press.

Binney, J. J. 1977, *M.N.R.A.S.*, **181**, 735.

Böhm, K.-H. 1968, *Ap. and Space Sci.*, **2**, 375.

Böhm–Vitense, E. 1958, *Zs. f. Ap.*, **46**, 108.

Boss, A. P. 1989, *P.A.S.P.*, **101**, 767.

Bradley, P. A., Winget, D. E., and Wood, M. A., 1989, in *IAU Colloquium #114: White Dwarfs*, ed. G. Wegner (Berlin: Springer-Verlag) p. 286.

Carlberg, R. G., Dawson, P. C., Hsu, T., and VandenBerg, D. A. 1985, *Ap. J.*, **294**, 674.

Carney, B. W., Aguilar, L., Latham, D. W., and Laird, J. B. 1990, *A.J.*, **99**, 201.

Carney, B. W., Latham, D. W., and Laird, J. B. 1990, *A. J.*, **99**, 572.

Carr, W. J., Jr. 1961, *Phys. Rev.*, **122**, 1437.

Caughlan, G. R., and Fowler, W. A. 1988, *Atomic Data and Nuclear Data Tables*, **40**, 334.

Chandrasekhar, S. 1931a, *Phil. Mag.*, **11**, 592.

Chandrasekhar, S. 1931b, *Ap. J.*, **74**, 81.

Chandrasekhar, S., 1939, *An Introduction to the Study of Stellar Structure*, (Chicago: University of Chicago Press).

Chandrasekhar, S. 1984, *Rev. Mod. Phys.*, **56**, 137.

Claver, C. F., Cornell, M. E., and Opal, C. B., 1990, in *S.P.I.E. Procedings: Astronomical Telescopes and Instrumentation for the 21st Century*, in press.

Clayton, D. D., 1968, *Principles of Stellar Evolution and Nucleosynthesis*, (Chicago: The University of Chicago Press).

Clayton, D. D., 1985, in *Challenges and New Developments in Nucleosynthesis*, eds. W. D. Arnett and J. W. Truran, (Chicago: Univ. Chicago Press).

Clayton, D. D. 1988, *M.N.R.A.S.*, **234**, 1.

Cohen, M. H., and Keffer, F. 1955, *Phys. Rev.*, **99**, 1128.

Cowan, J. J., Thielemann, F.-K. and Truran, J. W., 1986, in *Proceedings of the Second IAP Recontre (Nuclear Astrophysics).*, .

Cox, A. N., and Stewart, J. N. 1970, *Ap. J. (Suppl.)*, **19**, 261.

Cox, J. P., and Giuli, R. T., 1968, *Principles of Stellar Structure*, (New York: Gordon and Breach).

D'Antona, F., and Mazzitelli, I. 1978, *Astron. Astrophys.*, **66**, 453.

D'Antona, F., and Mazzitelli, I. 1979, *Astron. Astrophys.*, **74**, 161.

D'Antona, F., and Mazzitelli, I. 1989, *Ap. J.*, **347**, 934.

D'Antona, F., and Mazzitelli, I., 1990, *Ann. Rev. Astron. Astrophys.*, in press.

DeZotti, G. 1972, *Estratto dalle Memorie della Società Astronomica Italiana*, **43**, 89.

Dicus, D. 1973, *Phys. Rev. D*, **6**, 941.

Dirac, P. A. M. 1926, *Proc. Roy. Soc. London Ser. A.*, **112**, 660.

Downes, R. A. 1986, *Ap. J. (Suppl.)*, **61**, 569.

Eddington, A. S. 1926, *The Internal Constitution of the Stars,* (Cambridge, England: Cambridge University Press).

Eggen, O. J., Lynden-Bell, D., and Sandage, A. R. 1962, *Ap. J.*, **163**, 748.

Eggleton, P. P., Faulkner, J., and Flannery, B. P. 1973, *Astron. Astrophys.*, **23**, 325.

Einstein, A., and de Sitter, W. 1932, *Proc. Nat. Acac. Sci.*, **18**, 213.

Faber, S. M. and Gallagher, J. S. 1979, *Ann. Rev. Astr. Ap.*, **17**, 135.

Fleming, T. A., Liebert, J., and Green, R. F. 1986, *Ap. J.*, **308**, 176.

Fontaine, G. 1973, Ph.D. thesis, University of Rochester.

Fontaine, G., Bergeron, P., Lacombe, P., Lamontagne, R., and Talon, A. 1985, *A. J.*, **90**, 1094.

Fontaine, G., Graboske, H. C., Jr., and Van Horn, H. M. 1977, *Ap. J. Suppl.*, **35**, 293.

Fontaine, G., McGraw, J. T., Dearborn, D. S. P., Gustafson, J., and Lacombe, P. 1982, *Ap. J.*, **258**, 651.

Fontaine, G., and Michaud, G. 1979, *Ap. J.*, **231**, 826.

Fontaine, G., and Van Horn, H. M. 1976, *Ap. J. (Suppl.)*, **31**, 467.

Fontaine, G., Van Horn, H. M., Böhm, K. H., and Grenfell, T., C. 1974, *Ap. J.*, **193**, 205.

Fontaine, G., and Wesemael, F., 1987, in *IAU Colloquium 95, The Second Conference on Faint Blue Stars*, ed. A. G. D. Philip, D. S. Hayes, and J. Liebert (Schenectady: Davis Press), p. 319.

Fowler, R. H. 1926, *M.N.R.A.S.*, **87**, 114.

Fowler, W. A. 1987, *Q.J.R.A.S.*, **28**, 87.

Fowler, W. A., Caughlan, G. R., and Zimmerman, B. A. 1975, *Ann. Rev. Astron. Astrophys.*, **13**, 69.

Fowler, W. A., and Meisl, C. C. 1986, in *Cosmogenical Processes*, ed. W. D. Arnett, C. J. Hansen, J. W. Truran, and S. Tsuruta (Utrech: VNU Sci. Press).

Freeman, K. C. 1987, *Ann. Rev. Astr. Ap.*, **25**, 603.

Garcia-Berro, E., Hernanz, M, Mochkovitch, R., Isern, J 1988, *Astron. Astrophys.*, **66**, 453.

Gilmore, G., Wyse, R. F. G., and Kuijken, K. 1989, *Ann. Rev. Astron. Astrophys.*, **27**, 555.

Green, E. M., 1988, in *Calibration of Stellar Ages*, ed. A. D. G. Philip (Schenectady: L. Davis Press), p. 81.

Green, E. M., Demarque, P., and King, C. R., 1987, *The Revised Yale Isochrones and Luminosity Functions*, (New Haven: Yale University Observatory).

Green, R. G., Schmidt, M., and Liebert., J. 1986, *Ap. J. (Suppl.)*, **61**, 305.

Greenstein, J. L. 1984, *Ap. J.*, **276**, 602.

Güsten, R. and Mezger, P. G. 1983, *Vistas in Astron.*, **26**, 159.

Guth, A. H. 1981, *Phys. Rev. D*, **23**, 347.

Guth, A. H., and Steinhardt, P. J. 1984, *Scientific American*, **250**, 116.

Hamada, T., and Salpeter, E. E. 1961, *Ap. J.*, **134**, 683.

Hansen, C. J., and Kawaler, S. D., 1990, in *Introduction to Stellar Structure and Evolution*, (Springer-Verlag: Berlin).

Hansen, J. P. 1973, *Phys. Rev. A*, **8**, 3096.

Harris, M. J., Fowler, W. A., Caughlan, G. R., and Zimmerman, B. A. 1983, *Ann. Rev. Astron. Astrophys.*, **21**, 165.

Hegyi, D., and Olive, K. A. 1986, *Ap. J.*, **303**, 56.

Hertzsprung, E. 1915, *Ap. J.*, **42**, 116.

Hogan, C. 1990, *Nature*, **344**, 107.

Hubbard, W. B., and Lampe, M. 1969, *Ap. J. Suppl.*, **163**, 297.

Huebner, W. B. 1980, private communication.

Iben, I., Jr. 1967, *Ann. Rev. Astron. Astrophys.*, **5**, 571.

Iben, I., Jr. 1975, *Ap. J.*, **196**, 525.

Iben, I., Jr. 1976, *Ap. J.*, **208**, 165.

Iben, I., Jr. 1984, *Ap. J.*, **277**, 333.

Iben, I., Jr., and Laughlin, G. 1989, *Ap. J.*, **341**, 312.

Iben, I., Jr., and MacDonald, J. 1985, *Ap. J.*, **296**, 540.

Iben, I., Jr., and MacDonald, J. 1986, *Ap. J.*, **301**, 164.

Iben, I., Jr., and Renzini, A. 1984, *Ann. Rev. Astron. Astrophys.*, **21**, 271.

Iben, I., Jr., and Tutukov, A. V. 1984, *Ap. J.*, **282**, 615.

Ichimaru, S., Iyetomi, H., and Mitake, S. 1983, *Ap. J. (Letters)*, **265**, L83.

Ichimaru, S., Iyetomi, H., Ogata, S. 1988, *Ap. J. Letts.*, **334**, L17.

Ishida, K., Mikami, T., Noguchi, T., and Maehara, H. 1982, *P.A.S.P.*, **34**, 381.

Itoh, N., Kahyama, Y., Matsumoto, N., and Seki M. 1984, *Ap. J.*, **285**, 758.

Itoh, N., Mitake, S., Iyetomi, H., and Ichimaru, S. 1983, *Ap. J.*, **273**, 774.

Kawaler, S. D. 1986, Ph.D. thesis, The University of Texas at Austin.

Kepler, S. O., Vauclair, G., Dolez, N., Chevreton, M., Barstow, M. A., Nather, R. E., Winget, D. E., Provencal, J. L., Clemens, J. C., and Fontaine, G., 1990, *Ap. J.*, in press.

Kippenhahn, R., Weigert, A., and Hofmeister, E. 1967, *Methods in Computational Physics*, **7**, 129.

Knapp, G. R., 1990, in *Frontiers of Stellar Evolution*, ed. D. L. Lambert, in press.

Koester, D. 1972, *Astron. Astrophys.*, **16**, 459.

Koester, D. 1976, *Astron. Astrophys.*, **52**, 415.

Koester, D., and Chanmugam, G., 1990, *Reports on Progress in Physics*, in press.

Koester, D., and Schöenberner, D. 1986, *Astron. Astrophys.*, **154**, 125.

Koester, D., Shultz, H., and Weidemann, V. 1979, *Astron. Astrophys.*, **76**, 262.

Kovetz, A., Lamb, D. Q., and Van Horn, H. M. 1972, *Ap. J.*, **174**, 109.

Kovetz, A., and Shaviv, G. 1970, *Astron. Astrophys.*, **8**, 398.

Kovetz, A., and Shaviv, G. 1976, *Astron. Astrophys.*, **52**, 403.

Kugler, A. A. 1969, *Ann. Phys.*, **53**, 133.

Kwok, S., 1987, in *IAU Coll. #131: Planetary Nebulae*, ed. S. Torres-Peimbert (Springer-Verlag: Berlin), p. 401.

Lacey, C. G. 1984, *M.N.R.A.S.*, **208**, 687.

Lamb, D. Q. 1974, Ph.D. thesis, University of Rochester.

Lamb, D. Q., and Van Horn, H. M. 1975, *Ap. J.*, **200**, 306.

Landau, L. D., and Lifshitz, E. M., 1980, *Statistical Physics, 3rd Ed. Pt. 1*, (Oxford: Permagon Press).

Larson 1976, *M.N.R.A.S.*, **176**, 31.

Liebert, J., 1979, in *IAU Coll. #53: White Dwarfs and Variable Degenerate Stars*, ed. H. M. Van Horn and V. Weidemann (Rochester: University of Rochester Press), p. 146.

Liebert, J. 1980, *Ann. Rev. Astron. Astrophys.*, **18**, 363.

Liebert, J., Dahn, C. C., and Monet, D. G. 1988, *Ap. J.*, **332**, 891.

Liebert, J., Dahn, C. C., and Monet, D. G., 1989, in *IAU Coll. #114: White Dwarfs*, ed. G. Wegner (Berlin: Springer-Verlag) p. 15.

Liebert, J., Wesemael, F., Hansen, C. J., Fontaine, G., Shipman, H. L., Sion, E. M., Winget, D. E., and Green, R. F. 1986, *Ap. J.*, **309**, 241.

Luyten, W. J. 1979, LHS Catalogue (Minneapolis: University of Minnesota Press).

Magni, G., and Mazzitelli, I. 1979, *Astron. Astrophys.*, **72**, 134.

Mazzitelli, I. 1979, *Astron. Astrophys.*, **79**, 251.

Mazzitelli, I., 1989, in *IAU Coll. #114: White Dwarfs*, ed. G. Wegner, (Springer-Verlag: Berlin), p. 341.

Mazzitelli and D'Antona 1986, *Ap. J.*, **308**, 706.

McGraw, J. T. 1979, *Ap. J.*, **229**, 203.

McMahan, R. K. 1989, *Ap. J.*, **336**, 177.

Mestel, L. 1952, *M.N.R.A.S.*, **112**, 583.

Mestel, L., and Ruderman, M. A. 1967, *M.N.R.A.S.*, **136**, 27.

Michaud, G., Fontaine, G., and Charland, Y. 1984, *Ap. J.*, **280**, 247.

Miller, G. E., and Scalo, J. M. 1979, *Ap. J. Suppl.*, **41**, 513.

Mochkovitch, R. 1983, *Astron. Astrophys.*, **122**, 212.

Mochkovitch, R., Garcia–Berro, E., Hernanz, M., Isern, J., and Panis, J. F., 1990, *Astron. Astrophys.*, in press.

Muchmore, D. 1982, *Ap. J.*, **259**, 749.

Muchmore, D. 1984, *Ap. J.*, **278**, 769.

Nandkumar, R., and Pethick, C. J. 1984, *M.N.R.A.S.*, **209**, 511.

Nather, R. E., 1989, in *IAU Coll. #114: White Dwarfs*, ed. G. Wegner, (Springer-Verlag: Berlin), p. 109..

Nather, R. E., Clemens, J. C., Winget, D. E., Hansen, C. J., and Hine, B. P., III, 1990, *Ap. J.*, submitted.

Noh, H.-R., and Scalo, J. 1990, *Ap. J.*, **352**, 605.

Norris and Green 1989, *Ap. J.*, **337**, 272.

O'Donoghue, D., and Warner, B. 1987, *M.N.R.A.S.*, **228**, 949.

Ogata, S., and Ichimaru, S. 1987, *Physical Review A*, **36**, 5451.

Oke, J. B., Weidemann, V., and Koester, D. 1984, *Ap. J.*, **281**, 276.

Paquette, C., Pelletier, C., Fontaine, G., and Michaud, G. 1986, *Ap. J. (Suppl.)*, **61**, 197.

Pelletier, C., Fontaine, G., Wesemael, F., Michaud, G., and Wegner, G. 1986, *Ap. J.*, **307**, 242.

Philip, A. D. G. (Editor), 1988, *Calibration of Stellar Ages*, (Schenectady: L. Davis Press).

Pollock, E. L., and Hansen, J. P. 1973, *Phys Rev A*, **8**, 310.

Press, W. H., Flannery, B. P., Teukolsky, S. A., and Vetterling, W. T., 1986, *Numerical Recipes*, (Cambridge: Cambridge University Press).

Rees, M. J., and Ostriker, J. P. 1977, *M.N.R.A.S.*, **179**, 541.

Reif, F., 1965, *Statistical and Thermal Physics*, (New York: McGraw Hill).

Romanishin, W., and Angel, J. 1980, *Ap. J.*, **235**, 992.

Ryu, D., Olive, K. A., and Silk, J., 1990, *Ap. J.*, in press.

Salpeter, E. E. 1961, *Ap. J.*, **134**, 669.

Scalo, J. M. 1986, *Fund. Cos. Phys.*, **11**, 1.

Schatzman, E., 1958, *White Dwarfs*, Amsterdam: North Holland Publishing Co.).

Schild, H. 1989, *M.N.R.A.S.*, **240**, 63.

Schmidt, M. 1959, *Ap. J.*, **129**, 243.

Schmidt, M. 1975, *Ap. J.*, **202**, 22.

Schönberner, D. 1981, *Astron. Astrophys.*, **103**, 119.

Schönberner, D. 1983, *Ap. J.*, **272**, 708.

Schönberner, D., and Weidemann, V., 1983, in *Planetary Nebulae*, ed. D. Flower (Reidel: Dorrdrecht), p. 359.

Schwarzschild, M., 1958, *Structure and Evolution of the Stars*, (Princeton: Princeton University Press).

Searle, L., and Zinn, R. 1978, *Ap. J.*, **225**, 357.

Shapiro, I. I., and Teukolsky, S. A. 1983, *Black Holes, White Dwarfs, and Neutron Stars,* (Ithaca, New York: Wiley and Sons).

Shipman, H. L., and Sass, C. A. 1980, *Ap. J.*, **235**, 177.

Shu, F. H., Adams, F. C., and Lizano, S. 1987, *Ann. Rev. Astr. Ap.*, **25**, 23.

Silk, J. 1977, *Ap. J.*, **214**, 718.

Sion, E. M., Greenstein, J. L., Landstreet, J., Liebert, J., Shipman, H. L., and Wegner, G. 1983, *Ap. J.*, **269**, 253.

Slattery, W. L., Doolen, G. D., and DeWitt, H. E. 1982, *Physical Review A*, **26**, 2255.

Spitzer, L, and Schwarzschild, M. 1951, *Ap. J.*, **114**, 385.

Spitzer, L, and Schwarzschild, M. 1953, *Ap. J.*, **118**, 106.

Stevenson, D. J. 1980, *J. de Phys. (Paris) Suppl.*, **41**, C2-61.

Strittmatter, P. A., and Wickramasinghe, D. T. 1971, *M.N.R.A.S.*, **152**, 47.

Sweeney, M. A. 1976, *Astron. Astrophys.*, **49**, 375.

Tamanaha, C. M., Silk, J., Wood, M. A., and Winget, D. E., 1989, *Ap. J.*, in press.

Tassoul, M., Fontaine, G., and Winget, D. E. 1990, *Ap. J. (Suppl.)*, **72**, 335.

Telesco, C. M. 1988, *Ann. Rev. Astr. Ap.*, **26**, 343.

Tinsley, B. A. 1980, *Fund. Cos. Phys.*, **5**, 287.

Trimble, V. 1987, *Ann. Rev. Astr. Ap.*, **25**, 425.

Twarog, B. A. 1980, *Ap. J.*, **242**, 242.

van den Berg, S. 1989, *Astron. Astrophys. Rev.*, **1**, 111.

VandenBerg, D. A. 1985, *Ap. J. (Suppl.)*, **58**, 711.

VandenBerg, D. A., and Bell, R. A. 1985, *Ap. J. (Suppl.)*, **58**, 561.

Van Horn, H. M. 1968, *Ap. J.*, **151**, 227.

Van Horn, H. M., 1971, in *IAU Symp. #42: White Dwarfs*, ed. W. Luyten (Dordrecht: Reidel), p. 97.

Van Maanan, A. 1913, *P.A.S.P.*, **29**, 258.

Vasquez, E. C. and Scalo, J. M. 1989, *Ap. J.*, **343**, 644.

Vauclair, G., and Reisse, C. 1977, *Astron. Astrophys.*, **61**, 415.

Vauclair, G., Vauclair, S., and Greenstein, J. L. 1979, *Astr. Ap.*, **80**, 79.

Vennes, S., Pelletier, C., Fontaine, G., and Wesemael, F. 1988, *Ap. J.*, **331**, 876.

Vila, S. C. 1971, *Ap. J.*, **170**, 153.

Wasserburg, G. J., Papanastassiou, D. A., Tera, F., and Huneke, J. C. 1977, *Phil. Trans. R. Soc. London, Ser. A.*, **285**, 7.

Weidemann, V. 1967, *Z. f. Astrophysik*, **67**, 286.

Weidemann, V. 1987a, *Astron. Astrophys.*, **188**, 74.

Weidemann, V., 1987b, in *6th European Workshop on White Dwarfs. Mem. Soc. Astr. Ital.* **58**, 33.

Weidemann, V., 1990, *Astron. Astrophys.*, in press.

Weidemann, V., and Koester, D. 1983, *Astron. Astrophys.*, **121**, 77.

Weidemann, V., and Koester, D. 1984, *Astron. Astrophys.*, **132**, 195.

Weidemann, V. and Yuan, J. W., 1989, in *IAU Coll. #114: White Dwarfs*, ed. G. Wegner (Berlin: Springer-Verlag) p. 1.

Weinberg, S. 1974, *Rev. Mod. Phys.*, **46**, 255.

Wesemael, F., Winget, D. E., Cabot, W., Van Horn, H. M. and Fontaine, G. 1982, *Ap. J.*, **254**, 221.

Wheeler, J. C., and Harkness, R. P., 1986, in *Galaxy Distances and Deviations from Universal Expansion*, eds. B. F. Madore, and R. B. Tully (Dordrecht: Reidel).

Wigner, E. 1932, *Phys. Rev.*, **40**, 749.

Winget, D. E., and Cabot, W. 1980, *Ap. J.*, **242**, 1166.

Winget *et al.*, 1990, *Ap. J.*, submitted.

Winget, D. E., and Fontaine, G., 1982, in *Pulsations in Classical and Cataclysmic Variable Stars*, ed. J. P. Cox and C. J. Hansen (Boulder: University of Colorado Press), p. 46.

Winget, D. E., Hansen, C. J., Liebert, J., Van Horn, H. M., Fontaine, G., Nather, R. E., Kepler, S. O., and Lamb, D. Q. 1987, *Ap. J. (Letters)*, **315**, L77.

Winget, D.E., Kepler, S.O., Robinson, E.L., Nather, R.E., and O'Donoghue, D. 1985, *Ap. J.*, **292**, 606.

Winget, D. E., and Van Horn, H. M., 1987, in *IAU Coll. #95: The Second Conference on Faint Blue Stars*, eds. A. G. D. Philip, D. S. Hayes, and J. Liebert (Schenectady: Davis Press), p. 363.

Wood, M. A., 1990, *J.R.A.S.C.*, in press.

Wood, M. A., and Winget, D. E., 1988, in *Multimode Stellar Pulsations*, eds. G. Kovács, L. Szabados, and B. Szeidl (Konkoly Observatory · Kultura: Budapest), p. 199..

Wood, M. A., and Winget, D. E., 1989, in *IAU Colloquium #114: White Dwarfs*, ed. G. Wegner (Berlin: Springer-Verlag) p. 282.

Wood, M. A., Winget, D. E., and Van Horn, H. M., 1987, in *IAU Colloquium #95: The Second Conference on Faint Blue Stars*, ed. A. G. D. Philip, D. S. Hayes, and J. Liebert (Schenectady: Davis Press), p. 639.

Wood, P. R., and Faulkner, D. J. 1986, *Ap. J.*, **307**, 659.

Wyse, R. F. G., and Gilmore, G. 1988, *Astron. J.*, **95**, 1404.

Yakovlev, D. G., and Urpin, V. A. 1980, *Soviet. Astr.*, **24**, 303.

Yuan, J. W. 1989, *Astron. Astrophys.*, **224**, 108.

Zinn, R. 1985, *Ap. J.*, **293**, 424.